AD-766 766

AN INVESTIGATION OF LASER-SUPPORTED DETONATION WAVES

Boeing Aerospace Co.

Prepared for

Air Force Weapons Laboratory

Advanced Research Projects Agency
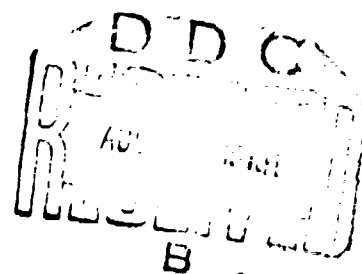
June 1973

AN INVESTIGATION OF LASER-SUPPORTED DETONATION WAVES

R. B. Hall

W. E. Maher

P. S. P. Wei

Boeing Aerospace Company

TECHNICAL REPORT NO. AFWL-TR-73-28

June 1973

AD766766

AIR FORCE WEAPONS LABORATORY

Air Force Systems Command

Kirtland Air Force Base

New Mexico

DOCUMENT CONTROL DATA - R & D

(Security classification of title, body of abstract and indexing annotation must be entered when the overall report is classified)

1. ORIGINATING ACTIVITY (Corporate author)	2a. REPORT SECURITY CLASSIFICATION
The Boeing Company, Aerospace Group P.O. Box 3999 Seattle, Washington 98124	UNCLASSIFIED
	2b. GROUP

3. REPORT TITLE

AN INVESTIGATION OF LASER-SUPPORTED DETONATION WAVES

4. DESCRIPTIVE NOTES (Type of report and inclusive dates)

24 February 1972 through 23 March 1973

5. AUTHOR(S) (First name, middle initial, last name)

R. B. Hall, W. E. Maher, and P.S.P. Wei

6. REPORT DATE	7a. TOTAL NO. OF PAGES	7b. NO. OF REFS
June 1973	~~266~~ 269	77

8a. CONTRACT OR GRANT NO.	9a. ORIGINATOR'S REPORT NUMBER(S)
F29601-72-C-0064	
b. PROJECT NO.	AFWL-TR-73-28
1256	
c. Task 09	9b. OTHER REPORT NO(S) (Any other numbers that may be assigned this report)
d.	

10. DISTRIBUTION STATEMENT

Approved for public release; distribution unlimited.

11. SUPPLEMENTARY NOTES	12. SPONSORING MILITARY ACTIVITY
	AFWL (DYT) Kirtland AFB, NM 87117

13. ABSTRACT

(Distribution Limitation Statement A)

A pulsed 10.6 micron laser emitting 20 joules energy at a peak power of 3 megawatts has been used to study laser-supported detonation waves in air. The thresholds for igniting these absorption waves have been determined for various metals, plastics, and painted surfaces in air. It is found that the intensity thresholds vary from 6×10^6 watts/cm^2 for painted surfaces to 4.5×10^7 watts/cm^2 for silica at standard atmospheric pressure. Such a detonation wave is found to change features late in the laser pulse becoming a subsonic absorption wave with a long luminous column of plasma filling the laser beam. Time resolved interferometry with an argon laser and interferograms with a pulsed ruby laser show the ignition, growth, and decay of both the detonation wave itself and of the radial shock waves which are produced. These interferograms have been transformed to determine the spatial variation of the densities. Spectroscopic studies have been made showing both time-integrated and time-resolved temperatures. The most prominent lines are those of singly ionized nitrogen and oxygen when detonation waves are ignited from reflective metals. At lower intensities, however, target species are observed. Impulse and pressure measurements were made with a linear velocity transducer and an acousto-optic pressure transducer. These measurements indicate the radial and time-dependence of the shock waves on the target surface. Theoretical calculations of the propagation of subsonic laser-supported combustion waves have been performed using analytical techniques and approximations to thermodynamic and transport properties of air. Threshold laser intensities greater than 10^4 watts/cm^2 are needed in order to overcome radiation losses, and in addition, higher thresholds are found to be beam diameter   (over)

DD FORM 1473 (1 NOV 65)

14 KEY WORDS	LINK A		LINK B		LINK C	
	ROLE	WT	ROLE	WT	ROLE	WT
Laser-supported detonation						
Laser-supported combustion						
Ignition thresholds						
Target response						
Target-induced breakdown						

dependent.   The analysis includes the decrease
with distance of the intensity of the laser beam
through the plasma and considers effects of
boundaries on the observed propagation velocities.

AN INVESTIGATION OF LASER-SUPPORTED
DETONATION WAVES

R. B. Hall
W. E. Maher
P. S. P. Wei

Boeing Aerospace Company

TECHNICAL REPORT NO. AFWL-TR-73-28

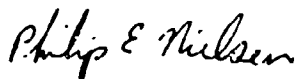Approved for public release; distribution unlimited.

$i b$

FOREWORD

This technical report has been reviewed and is approved.

Philip E. Nielsen

PHILIP E. NIELSEN
Captain, USAF
Project Officer

Jay R. Roland

JAY R. ROLAND
Major, USAF
Chief, Theoretical Branch

John K. Lerohl

JOHN K. LEROHL
Colonel, USAF
Chief, Technology Division

ABSTRACT
(Distribution Limitation Statement A)

A pulsed 10.6 micron laser emitting 20 joules energy at a peak
power of 3 megawatts has been used to study laser-supported detonation
waves in air. The thresholds for igniting these absorption waves
have been determined for various metals, plastics, and painted surfaces
in air. It is found that the intensity thresholds vary from 6×10^6
watts/cm^2 for painted surfaces to 4.5×10^7 watts/cm^2 for silica at
standard atmospheric pressure. Such a detonation wave is found to
change features late in the laser pulse becoming a subsonic absorption
wave with a long luminous column of plasma filling the laser beam.
Time-resolved interferometry with an argon laser and interferograms
with a pulsed ruby laser show the ignition, growth, and decay of both
the detonation wave itself and of the radial shock waves which are
produced. These interferograms have been transformed to determine
the spatial variation of the densities. Spectroscopic studies have
been made showing both time-integrated and time-resolved temperatures.
The most prominent lines are those of singly ionized nitrogen and
oxygen when detonation waves are ignited from reflective metals. At
lower intensities, however, target species are observed. Impulse
and pressure measurements were made with a linear velocity transducer
and an acousto-optic pressure transducer. These measurements indicate
the radial and time-dependence of the shock waves on the target surface.
Theoretical calculations of the propagation of subsonic laser-supported
combustion waves have been performed using analytical techniques and
approximations to thermodynamic and transport properties of air.
Threshold laser intensities greater than 10^4 watts/cm^2 are needed in
order to overcome radiation losses, and in addition, higher thresholds
are found to be beam diameter dependent. The analysis includes the
decrease with distance of the intensity of the laser beam through the
plasma and considers effects of boundaries on the observed propagation
velocities.

TABLE OF CONTENTS

TABLE OF CONTENTS (Continued)

LIST OF ILLUSTRATIONS

SECTION I

INTRODUCTION

1.1 OBJECTIVE

The ultimate limit to the power densities which can be propagated from a laser to a target is caused by air or particulate induced breakdown. Recent experimental work[1] indicates that the cold air breakdown threshold under standard conditions is about $q = 2 \times 10^9$ watts/cm^2, and we will regard this as the ultimate limit for propagation of 10.6μ energy in the atmosphere. It appears, however, that the most serious limitation to laser energy transfer to targets is not caused by breakdown but is, in fact, caused by the ignition of various types of laser-supported absorption waves. At high intensities ($10^7 < q < 10^9$ watts/cm^2) supersonic laser-supported detonation waves are formed while subsonic laser-supported combustion waves can propagate at even lower intensities ($10^4 < q < 10^6$ watts/cm^2). The purpose of this investigation is to experimentally determine ignition thresholds and to provide sufficient diagnostics on the spatial and temporal development of laser-supported detonation waves to allow a comparison between theory and experiment. In addition, however, a theoretical study is made of the propagation of laser-supported combustion waves. Laser-supported detonation waves were first observed experimentally by Ramsden and Savic[2] while laser-supported combustion waves were first observed by Bunkin[3] as stationary optical discharges.

The importance of laser-supported detonation waves (LSD waves) and laser-supported combustion waves (LSC waves) arises because they can absorb a large fraction of the laser power incident on target. When a high-power 10.6μ laser beam interacts with a solid target, however, it may or may not ignite such laser-supported absorption waves. The determination of whether ignition occurs depends on many factors including: (1) atmospheric pressure and species, (2) target material and state of the surface, (3) laser wavelength and pulse length, and (4) laser intensity. In the absence of any significant ionization in the vapor produced at the solid surface, the laser beam is transmitted without attenuation and reaches the solid. As pointed

out by Raizer[4,5,6], however, a high-temperature plasma (such as vaporized metal) can ignite LSD or LSC waves which then travel down the collimated laser beam absorbing most of the power.

1.2 APPROACH

Because of the complexity of the physics of laser interaction with solids, a number of experiments (several thousand laser shots) were performed with the Boeing Marx Bank Laser. After passing through various optics, such as wedges, lenses, and mirror required for beam diagnostics and steering, between 15 and 18 joules of laser energy at 10.6μ wavelength is available for target interaction experiments. Further data on characteristics of the beam and laser reliability are given in Appendix A.

Section II discusses some of the general features of laser interaction with solid targets and indicates the classes of waves that exist. In particular, high-speed photographs of laser-supported detonation waves are shown as well as certain slower waves. These include various laser-supported vapor jets from the target as well as laser-supported combustion waves[6]. The dependence of LSD wave velocity on both laser intensity and ambient pressure is determined by use of streak photography and a vacuum system where absorption waves are found down to pressures of 8 Torr. A cross beam absorption experiment is described in which an auxiliary CO_2 laser beam is refracted and absorbed by the plasma produced by the LSD wave.

Section III discusses interferometric data and shadow graphs of LSD waves and target jets taken with a ruby laser synchronized with the Marx Bank high power CO_2 laser. By counting fringes of these interferograms, one determines, by an Abel inversion, the variation of the index of refraction of the plasma with radius. Time-resolved interferometry is also performed with an argon laser in conjunction with the streak image converter camera.

Section IV discusses both time-integrated and time-resolved spectroscopy of laser-supported absorption waves. Various target materials are examined as well as viewing the "wave" at various positions from the target surfaces. By identification of spectral lines, one can determine that LSD waves contain mainly singly ionized air species. At lower intensities one can "see" both target spectra and air spectra.

Section V discusses the laser intensity required to ignite absorption waves from over twenty different target materials including metals, plastics, and painted surfaces. The laser ignition thresholds are also determined as a function of ambient pressure.

Section VI discusses measurements of target response in terms of impulse, material removal, and target surface pressures. Impulse is measured with a linear velocity transducer and it is observed, confirming previous measurements[7,8] and theoretical predictions[9], that impulse is nearly proportional to target area when LSD waves are ignited. An acousto-optical pressure transducer was used to make pressure measurements in the vicinity of the LSD wave.

Section VII is a theoretical discussion of laser-supported combustion waves (LSC waves) determining velocities of propagation in the presence of radial conduction losses, optical emission, and solid boundaries.

3

SECTION II

GENERAL FEATURES OF LASER-SUPPORTED ABSORPTION WAVES

Different ry laser-supported absorption waves (LSA waves)[4,6,10,11] are generated and account for luminous phenomena which occur near solid targets placed at the focus of a high-power laser beam. At intensities an order of magnitude below the breakdown intensity[12] for the gaseous medium (usually air) traveling plasmas propagate away from the target along the incident laser beam and are called laser-supported detonation waves (LSD waves). At even lower intensities, slower laser-supported combustion waves (LSC waves) appear.

Several techniques have been used to analyze these LSA waves and these are discussed in separate subsections below. The most heavily used technique of visible optical observation using the TRW image converter camera with streak and framing capability has produced a wealth of data, some of which will be presented here.

2.1 OPTICAL OBSERVATIONS

Typically, one observes for high intensities a clearly defined isolated supersonic spark traveling up the laser beam. At lower intensities near threshold, one observes with the image converter camera slower waves with a luminous column extending to the target surface. These near-threshold conditions are probably some variant of an absorption wave. (Perhaps a laser-supported combustion wave?) In any case, the laser energy appears to be absorbed in the plasma as discussed below.

Most of the photographs have been made with an inclined target which allowed a clear discrimination of an LSA wave from vapor jets of target material as the latter move along a normal to the target surface. Spherical shock waves also appear with the vapor jets and are called laser-supported blast waves (LSB waves). On the other hand, LSA waves move backwards along the beam, which makes an angle (typically 30°) with the target normal. Figure 1 shows a typical
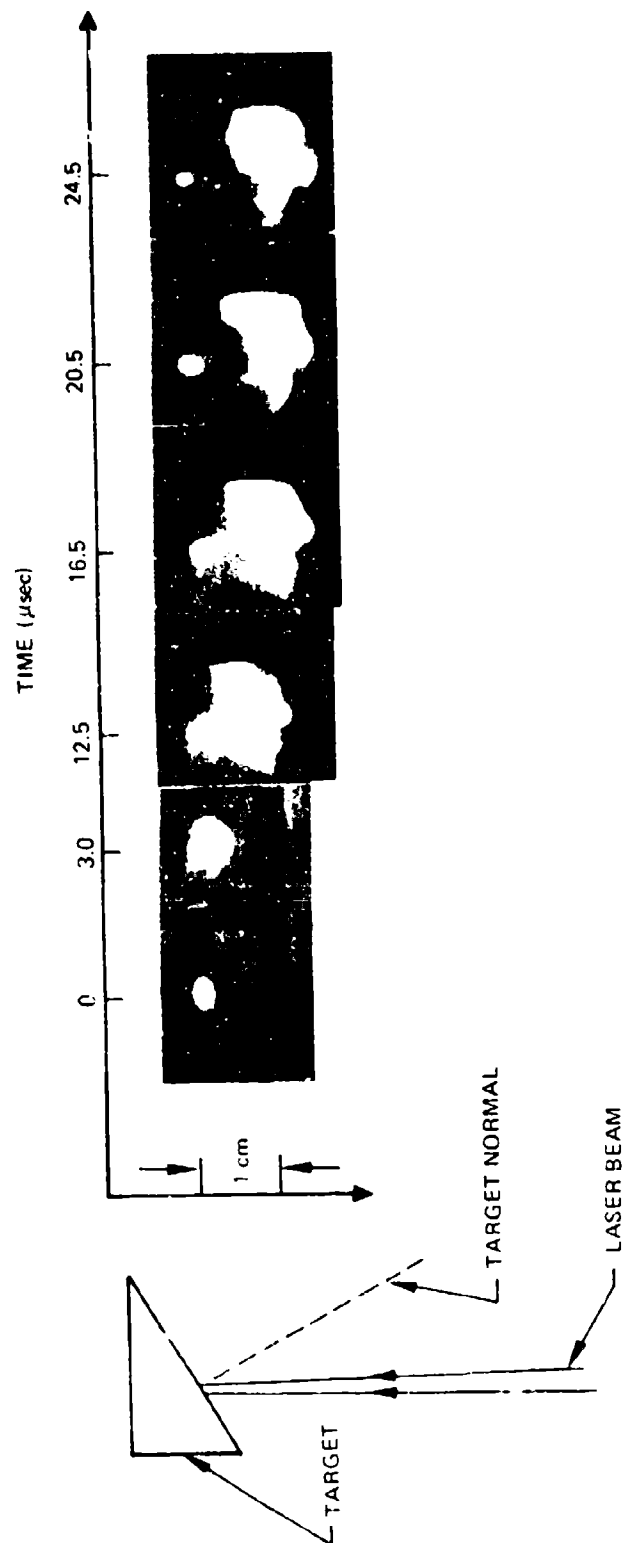
Figure 1: LASER-SUPPORTED BLAST WAVES IGNITED FROM SILICA AT A POWER DENSITY OF 3×10^7 WATTS/CM^2. ENERGY $\approx$ 14 JOULES, SPOT SIZE $\approx$ .04 CM^2.

5

blast wave, while figure 2 shows a typical LSA wave.

Not all targets ignite LSA waves even at very high-power densities incident on the target. The formation of a LSB wave, shown in figure 1, from a silica target occurred at 25 MW/cm^2. Note that the blast waves do not travel up the laser beam. The photos shown in figure 1 were made after a "preliminary" laser pulse was incident on the target surface and did ignite a laser-supported detonation wave equivalent to the one shown in figure 2. Apparently, the first laser pulse "cleans" the target surface sufficiently that no surface-induced breakdown occurs.

Figure 2 shows the propagation of a laser-supported detonation wave traveling up the laser beam. This particular wave was ignited from a metallic target and shows detonation waves for times less than about 7 sec. These LSD waves are characterized by a narrow supersonic absorption front. As the LSD wave moves up the focused beam, the laser intensity drops both due to the increasing beam area and due to the laser power decrease with time. At some critical laser intensity, the propagation maintenance conditions are not satisfied and the LSD wave degenerates into a long lumirous column eventually extending to the target.

The first observations of detonation waves were performed using a 40-cm focal length mirror. The materials to be examined were attached to an aluminum block set so that the laser beam axis made an angle of 30° with the target normal. The axial target position was adjusted so that the focal spot occurred at the surface of the tested material. Under these conditions, an elliptical laser spot of the 4 mm major axis by the 3 mm minor axis appears at the target. When the specularly reflected laser light from the target is collected and focused on a gold-doped germanium detector, one can determine when shielding of the surface exists. This kind of measurement of the laser power reaching the target surface is very useful in determining the presence of absorbing plasmas since weakly absorbing laser

6
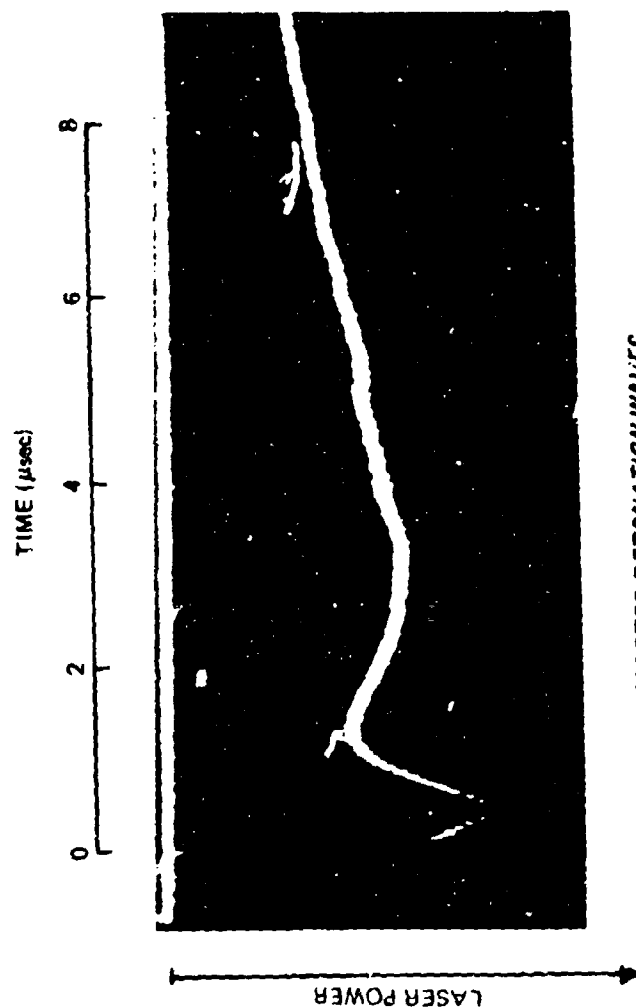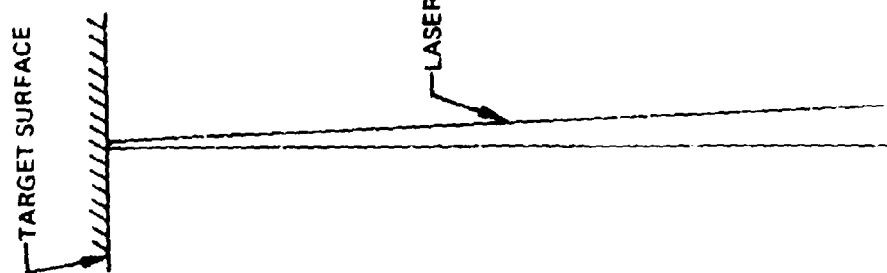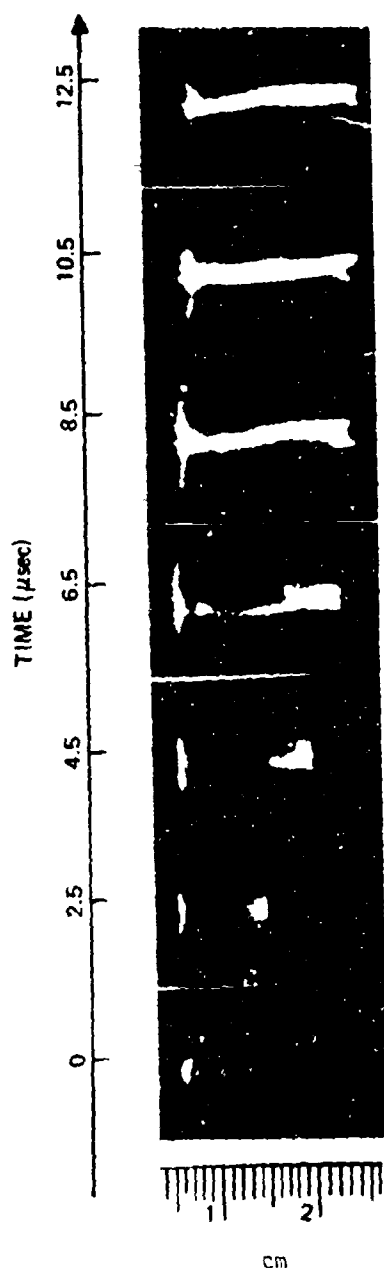
Figure 2: LASER-SUPPORTED DETONATION WAVES.

sparks can also be produced at target surfaces. For our available laser energy, the craters produced in either metals or opaque targets are not deep enough to reflect the laser beam out of the collecting optics.

When the laser intensity at the target is very high (greater than threshold), LSD waves are ignited in less than .5 microsecond. On the other hand, when the intensity is too low, one observes a target reflected signal nearly identical to the incident laser pulse. The detector that monitors the target reflected laser radiation shows that, near threshold, the ignition of a LSD wave occurs later in the laser pulse. Because of this, it appears that target heating is important and that either surface impurities or target material is vaporized leading to ignition of a LSD wave. This obviously indicates that metallic reflectivity is important.

The existence of LSA waves was confirmed by observing the direction which the luminous fronts leaving the target material traveled. There is no ambiguity concerning the existence of detonation waves ignited at high laser intensities from metallic targets. For absorbing targets such as Lucite, Lexan and other plastic and organic materials, however, a more complicated situation exists. For laser intensities below or near the threshold for igniting LSD waves, these opaque materials are vaporized and the vapor jets interact with the background gas (air) to produce luminous blast waves. As mentioned previously, these vapor jets tend to be ejected in the direction of the target normal. Near threshold for ignition of LSD waves, however, it becomes difficult to distinguish between the blast wave and the detonation wave since both have similar appearances. The image converter camera shows that both events can be present at different times in the same laser pulse.

In order to observe laser-supported absorption waves at lower pressures, a vacuum chamber was constructed and is shown in figure 3.

8

INCIDENT

REFLECTED

30°
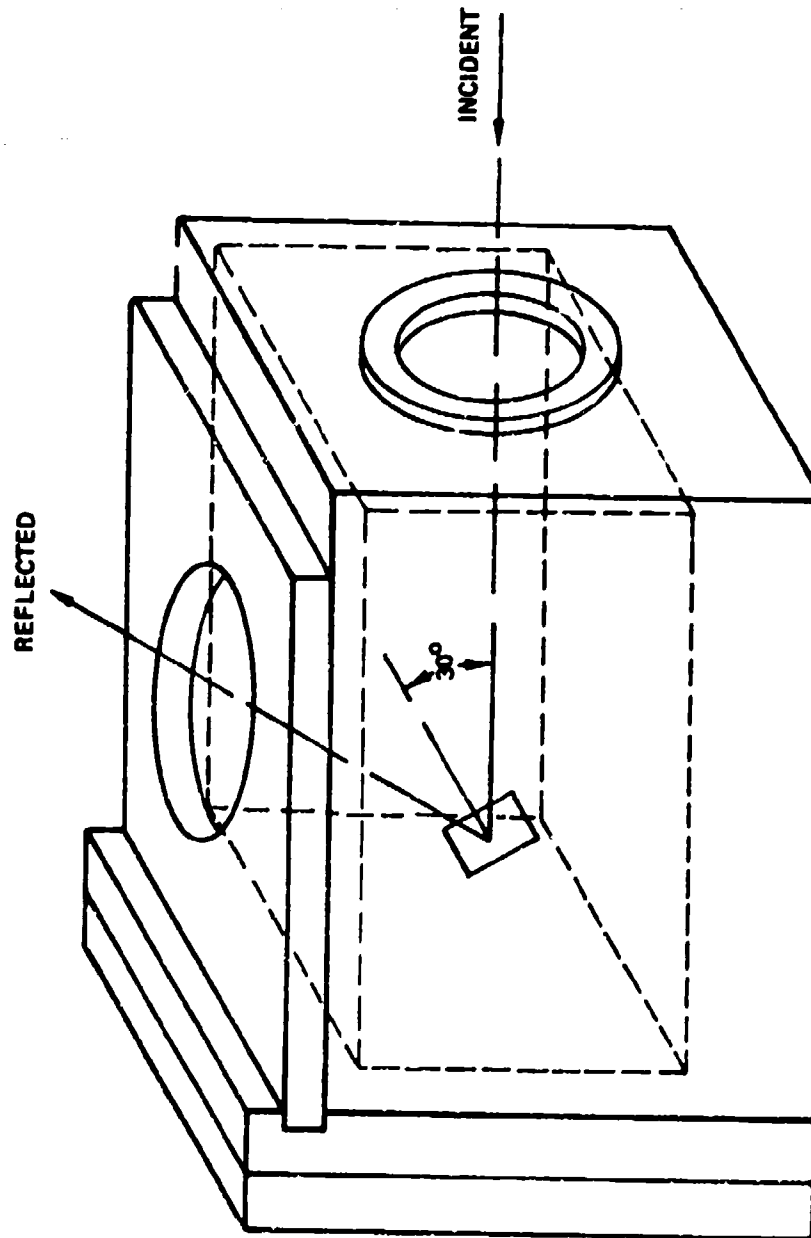
Figure 3: CELL FOR PRESSURE DEPENDENCE TESTS OF LSDW.

9

It has two NaCl windows, one to admit the incident beam and one to
allow a detector to monitor the reflected beam. A Kistler pressure
transducer was inserted to measure the pressure transients which
occur during and after the LSD wave ignition. Such transition pressure
measurements were studied in detail at 1 atmosphere for a titanium
specimen, and many multiple sound wave reflections are seen as indicated
in figure 4. The "DC" pressure rise of .1 atm is consistent with
the chamber volume, specific heat, and laser energy and indicates
most of the laser energy is absorbed by the LSD wave.

As the air pressure in the vacuum chamber is reduced, the
boundaries of the LSD waves become increasingly less clear. At
pressures below .1 atmosphere, image converter photographs of the
laser-supported absorption waves gradually tend to appear more and
more like "blast waves" as seen in figure 5. In addition, one observes
by monitoring the specularly reflected beam, that complete plasma
blocking occurs for shorter and shorter times as the ambient gas
pressure decreases.

For a target such as silica, one can observe both laser-supporrted
absorption waves and laser-supported blast waves during the same
laser pulse. An example is shown in figure 6 for which the peak
laser intensity was 2.8×10^7 watts/cm^2. During the initial high-
intensity part of the laser pulse, a LSA wave was ignited but also
quickly extinguished. By the time of 5μsec, a silica vapor jet
has been formed and has produced a laser-supported blast wave as
indicated by the spreading of the luminous zone perpendicular to the
laser beam.

Non-highly absorbing plasmas can also be formed when laser beams
interact with targets at peak intensities less than 1.2×10^7 watts/cm^2.
An example of such a case is shown in figure 7 where one observes sub-
sonic laser-supported absorption waves traveling both in the usual
direction (opposite to the laser propagation direction) and in the
direction of the specularly reflected beam. These LSC waves, traveling in
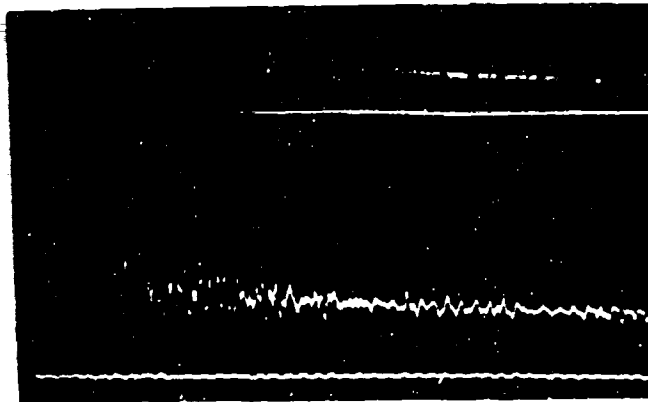
Figure 4 : PRESSURE TRANSIENTS AFTER A LASER-SUPPORTED DETONATION WAVE: TITANIUM
SPECIMEN, AIR AT 0.2 ATMOSPHERES (UPPER TRACE 5 MS/DIV, 0.10 ATMOSPHERES/DIV,
LOWER TRACE 1 MS/DIV, 0.10 ATMOSPHERES/DIV) 346 J/CM^2.

LASER BEAM →

Figure 5: *LASER-SUPPORTED BLAST WAVE PRODUCED FROM A TITANIUM TARGET AT 0.01 ATMOSPHERE WITH 230 J/CM² AFTER 10 μSECONDS. SPECIMEN NORMAL IS 30° ABOVE HORIZONTAL.*

LASER BEAM →

Figure 6: *LASER-SUPPORTED DETONATION WAVE AND A BLAST WAVE PRODUCED FROM A FUSED SILICA TARGET AT 0.05 ATMOSPHERE WITH 194 J/CM² AFTER 5 μSECONDS. SPECIMEN NORMAL IS 30° ABOVE HORIZONTAL.*

LASER BEAM →

Figure 7: REFLECTED BEAM LASER-SUPPORTED ABSORPTION WAVES PRODUCED FROM AN ANODIZED ALUMINUM SPECIMEN AT ONE ATMOSPHERE AND 67 J/CM² AT 13 μSECS. SPECIMEN NORMAL IS 30° BELOW HORIZONTAL

LASER BEAM →

SPECIMEN NORMAL IS
30° ABOVE HORIZONTAL

LASER BEAM →
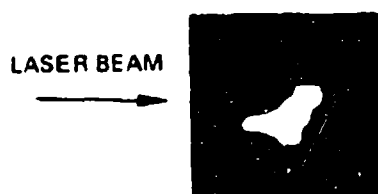
SPECIMEN NORMAL IS
30° BELOW HORIZONTAL

Figure 8: SURFACE PHENOMENA ACCOMPANY LASER-SUPPORTED ABSORPTION WAVES PRODUCED FROM AN ALUMINUM SPECIMEN WITH A 0.001 CM GLOSS BLACK LACQUER PAINT COATING. ONE ATMOSPHERE AND 173 J/CM² AT 15 μSECS

13

both directions, are evidence for low laser beam absorption. Additional
evidence for the formation of LSC waves is shown in figure 8 which
indicates the long absorption lengths that occur at lower laser
intensities. In this case, an LSD wave was initially ignited but
had degenerated into an LSC wave as the laser intensity decreased
later in time (15µsec) during the pulse. One can clearly note
the luminous column tending to follow the contour of the target.
This type of behavior is discussed in Section VII, where one notes
that heated air in a LSC wave accelerated in the beam direction.

Soda glass is an interesting example of a target which ignites
laser-supported detonation waves easily and also is very absorbing.
Figure 9 shows a late-time photograph of the luminosity produced
at such a target by a beam energy much larger than that required to
just reach the threshold of ignition. At this last time, the initially
ignited detonation wave has degenerated into a long luminuous column
of plasma extending to the target surface. This, in turn, indicates
that laser energy reaches the surface and can vaporize the target
material. In this case, the resultant vapor jet has produced a blast
wave by interacting hydrodynamically with the air. A blast wave
is again observable as the bright vertical line in figure 9.

Occasionally other anomalies occur in the appearance of laser-
supported absorption waves. As an example, one sometimes observes
a forked shaped appearance of the absorption front as seen
in figure 10. This may indicate some form of instability related to
the temperature or density profile.

As indicated previously in figure 8, the hot gas ejected in the
laser beam direction and toward the target, when LSC waves are ignited,
tends to follow the target contour. This effect is also shown in figure
11, but in addition, one observes that the ejected hot gas appears
not to actually reach the target surface. The smallest bright spots
on the target surface were obtained as the result of an earlier, short

14

LASER BEAM →
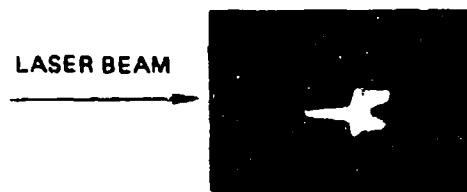
Figure 9 : *LASER-SUPPORTED BLAST WAVE WHICH DEVELOPS AFTER THE DECAY OF A LASER-SUPPORTED DETONATION WAVE. SODA GLASS SPECIMEN AT ONE ATMOSPHERE IS NORMAL TO THE INCIDENT BEAM WITH 233 J/CM^2 AFTER 20 μSECS.*

LASER BEAM →
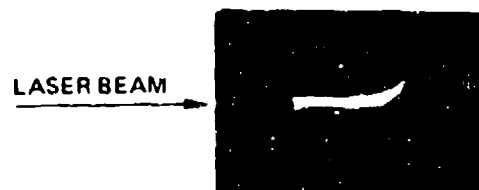
Figure 10: *LASER-SUPPORTED ABSORPTION WAVF WITH A FORKED FRONT WHICH DEVELOPED FROM A LUCITE SPECIMEN AT ONE ATMOSPHERE WITH 346 J/CM^2 AFTER 10 μSECONDS. SPECIMEN NORMAL IS 30° ABOVE HORIZONTAL.*

t = 15.5 μS

t = 15 μS

t = 0.5 μS

LASER BEAM
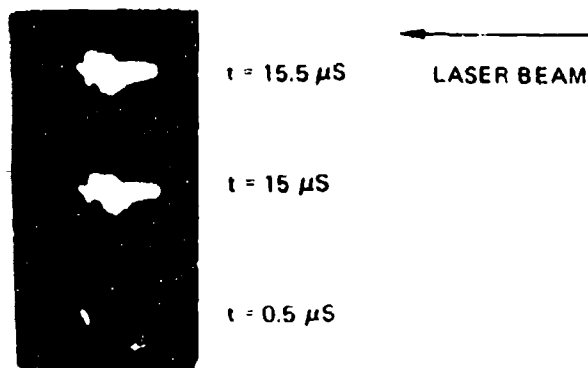
Figure 11: DOUBLE EXPOSURE SHOWING LASER SUPPORTED COMBUSTION WAVE EXHAUST DOES
NOT REACH THE SPECIMEN AFTER IGNITION. 0.001 CM GLOSS BLACK LACQUER ON
ALUMINUM SPECIMEN. 166 J/CM² AT ONE ATMOSPHERE. SURFACE IS SHOWN BY LOW
INTENSITY BEAM IN SECOND EXPOSURE. SPECIMEN NORMAL 30° ABOVE HORIZONTAL.

INCIDENT POWER

REFLECTED POWER

TIME   (μSECONDS AFTER
TRW CAMERA TRIGGER)

t = 5.5 μS
C

t = 5 μS
P

t = 0.5 μS
A

LASER
BEAM
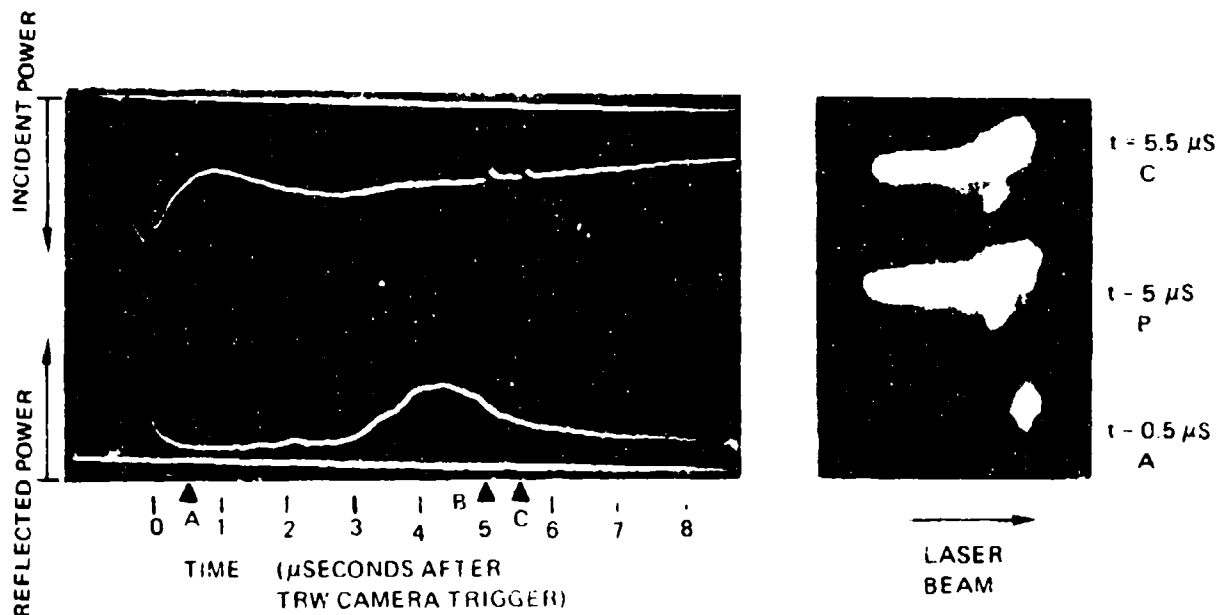
Figure 12: REIGNITION. THE OSCILLOSCOPE PICTURE ON THE LEFT SHOWS THE INCIDENT POWER
INVERTED ON THE UPPER TRACE AND THE REFLECTED POWER ON THE LOWER TRACE.
TRIANGLES SHOW THE TIMES WHEN TRW FRAMING CAMERA PICTURES WERE TAKEN.
THESE PICTURES ARE SHOWN AT THE RIGHT. THE LEAD SPECIMEN NORMAL IS 30°
ABOVE THE HORIZONTAL. REIGNITION OCCURS AT C. 302 J/CM² AT 0.1 ATMOSPHERE.

16

time-delay photograph. A double exposure was then made with a second laser pulse showing the indicated structure of the luminous hot gas. Apparently, heat conduction at the target surface causes this flowing gas to cool and, as a consequence, stop radiating.

Laser-supported detonation waves ignited and traveling away from a solid target "see" a continually decreasing laser intensity. This is due both to the focused laser beam geometry which leads to an increasing beam area as well as due to the decrease of the laser power for times greater than 3μsec. At some critical laser intensity, the LSD wave will not be maintained as the absorption length of the plasma becomes too great. This increase of the absorption length is clearly observable by the increased luminosity of the plasma column. This "bleaching" wave[13] is the effect of heating the plasma originally formed by the passage of the LSD wave.

When the laser intensity reaches the target surface for the second time , a re-ignition of laser-supported absorption waves can occur as shown by figure 12. This is observed by the time variation of the reflected power from the target. This reflected power is seen to first increase at about 3.5μsec and then abruptly decreases at about 4.5μsec as re-ignition of the absorption wave occurs. Re-ignition of absorption waves is more evident in the streak photograph of figure 13. This re-ignition occurs simultaneously with an increase in surface luminosity indicating that either target vaporization or desorption of atmospheric gases leads to ignition.

2.2 LSD WAVE VELOCITY DEPENDENCE ON BACKGROUND PRESSURE

As mentioned previously, there is a clearly defined luminous LSD wave shock front for intensities well above ignition threshold. A streak photograph (figure 14) taken with the TRW image converter camera shows this narrow absorption zone. In addition, however, one notes a number of striations in the luminosity which are similar to those observed by Alcock[14] in studies of gas breakdown by high-

17

intensity laser beams. From figure 13 one notes a nearly constant velocity of the absorption zone of the laser-supported detonation wave. Thus, slope measurement leads to an accurate determination of velocity of the LSD wave. This approach was used to determine the dependence on both intensity and ambient pressure. The tests were conducted with both aluminum and lead targets because their ignition thresholds were low and, hence, allowed observation of LSD waves under wider variations in both laser intensity and ambient pressure. Velocities were determined by the initial slope found on the streak photographs. Streak photographs taken at lower image magnification such as shown in figure 14 show both the initial fast velocity (approximately Mach 10) as well as the final deceleration of the absorption wave.

Re-ignition of laser-supported absorption waves is evident in the streak photograph shown in figure 15 where one also notes the appearance of a hot and luminous target surface. This indicates that the plasma formed after re-ignition is of low absorptivity.

The velocity of LSD waves is plotted in figures 16 and 17 versus (I/ρ) where I is laser intensity and ρ is background mass density in g/cm^3. Theory[4,5] predicts a velocity dependence of $(I/\rho)^{1/3}$, and these predictions are dicated, showing a good agreement with experiment. A more useful comparison between theory and experiment can be obtained by numerically integrating the theoretical dependence of velocity, v, as dependent on laser intensity as given by Raizer[15].

$$v(t,z) = \frac{dz}{dt} = \left[2(\gamma^2 - 1)I/\rho\right]^{1/3} \tag{1}$$

In equation 1, z is the axial position of the LSD wave along the laser beam, γ is the ratio of specific heats, I is the laser intensity, and ρ is the ambient gas background density. Using $\rho = 1.22 \times 10^{-3} \ g/cm^3$ and $\gamma = 1.17$ for T = 15,000 K as discussed by Zel'dovich and Raizer[16], one obtains
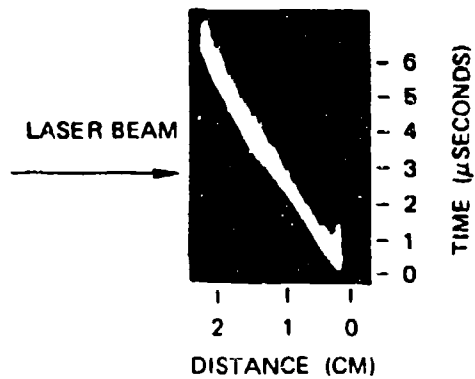
Figure 13: *TRW STREAK CAMERA PICTURE OF A LASER-SUPPORTED DETONATION WAVE DEVELOPED FROM A 7075 ALUMINUM SPECIMEN AT 311 J/CM^2 AND ONE ATMOSPHERE. SPECIMEN NORMAL IS 30° ABOVE HORIZONTAL.*
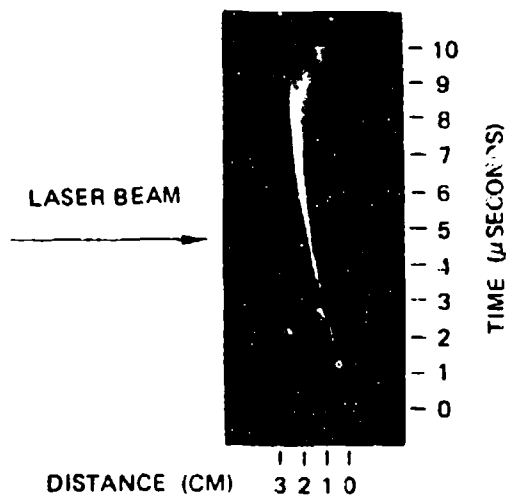
Figure 14: *TRW STREAK CAMERA PICTURE OF A LASER-SUPPORTED DETONATION WAVE DEVELOPED FROM A LEAD SPECIMEN AT 302 J/CM^2 AND ONE ATMOSPHERE. SPECIMEN NORMAL IS 30° ABOVE HORIZONTAL.*

19
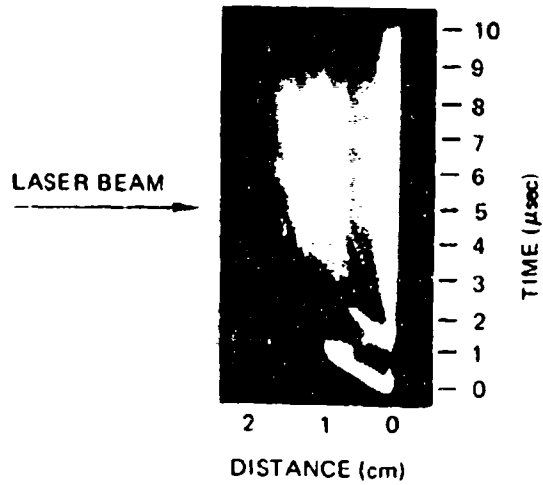
Figure 15: *TRW STREAK CAMERA PICTURE OF A LASER-SUPPORTED DETONATION WAVE WHICH EXHIBITS REIGNITION AND LATER SPECIMEN HEATING. LEAD SPECIMEN HAS ITS NORMAL 30° ABOVE HORIZONTAL WITH 180 J/CM² AT 0.05 ATMOSPHERE.*
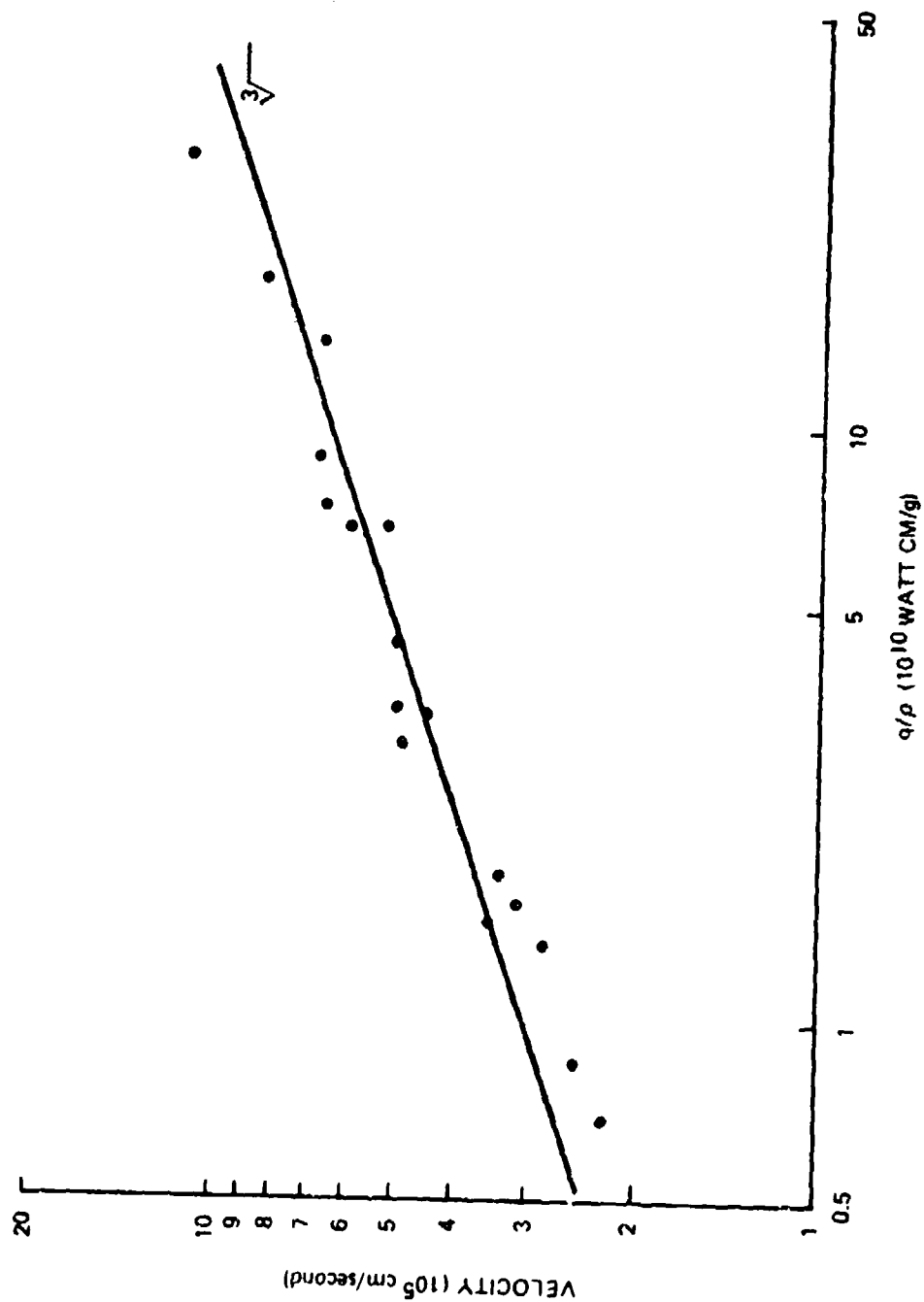
Figure 16: LASER-SUPPORTED DETONATION WAVE VELOCITIES AS A FUNCTION OF LASER-BEAM INTENSITY DIVIDED BY MEDIUM DENSITY. LEAD SPECIMEN.
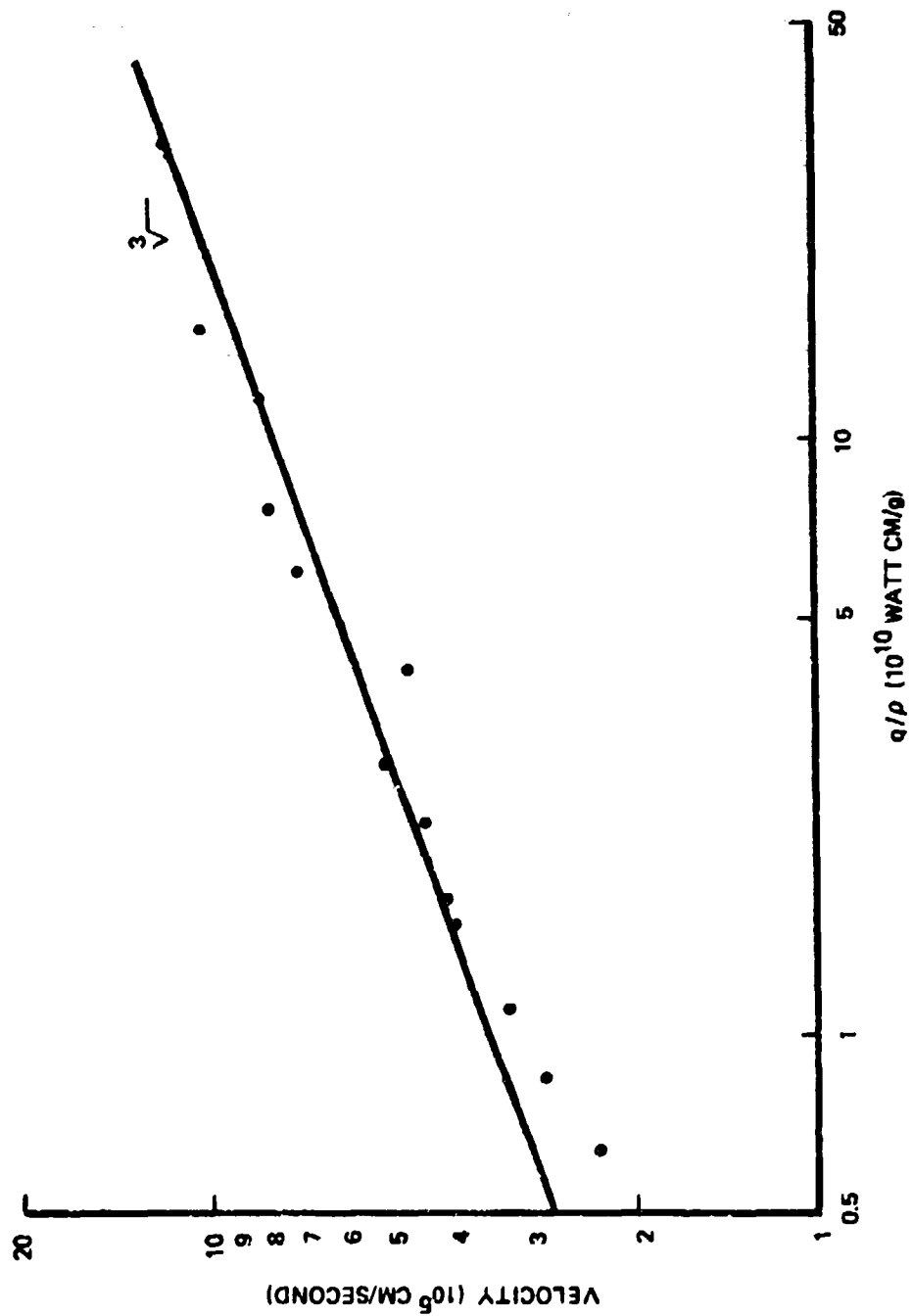
Figure 17. LASER-SUPPORTED DETONATION WAVE VELOCITIES AS A FUNCTION OF LASER BEAM INTENSITY DIVIDED BY MEDIUM DENSITY. 7075 ALUMINUM SPECIMEN.

22

$$\frac{dz}{dt} = \left[6.05 \times 10^{-9} \; I(z,t)\right]^{1/3} \qquad cm/\mu sec \qquad (2)$$

where t is time in μsec, z is position in cm, and $I(z,t)$ is laser
intensity in watts/cm. As noted from figure 2, the laser power versus
time consists of two pulses with peak powers occurring approximately
at .5μsec and 3.1μsec.

Analytical approximations to the power versus time, $P(t)$, are
defined by

$$P(t) = \left[A(t) + B(t)\right] \quad \text{Megawatts}$$

where $A(t)$ represents the earliest pulse with a peak of 2.6 at
.5μsec while $B(t)$ has a peak of 1.8 at approximately 3.1μsec.

$$\left.\begin{array}{l} A(t) = \dfrac{8.36 \; e^{1.2/t}}{t^2 \, (1 + e^{1.2/t})^2} \\[6mm] B(t) = \dfrac{194 \; e^{7.44/t}}{t^2 \, (1 + e^{7.44/t})^2} \end{array}\right\} \qquad \text{Megawatts} \qquad (3)$$

The numerical results given in equation 3 are for a total delivered
energy of 15.4 joules. This result is shown in figure 18 and is used
only in solving equation 2.

This laser beam is focused on targets to produce LSD waves.
In our case, the beam converges from 7.6 cm to .24 cm diameter with
a 28-cm focal length lens. The focal area as a function of axial
position z from the minimum focal area is

$$\text{beam area} = (.045 + .058z^2)cm^2$$

and the laser intensity is

POWER
RELATIVE
UNITS
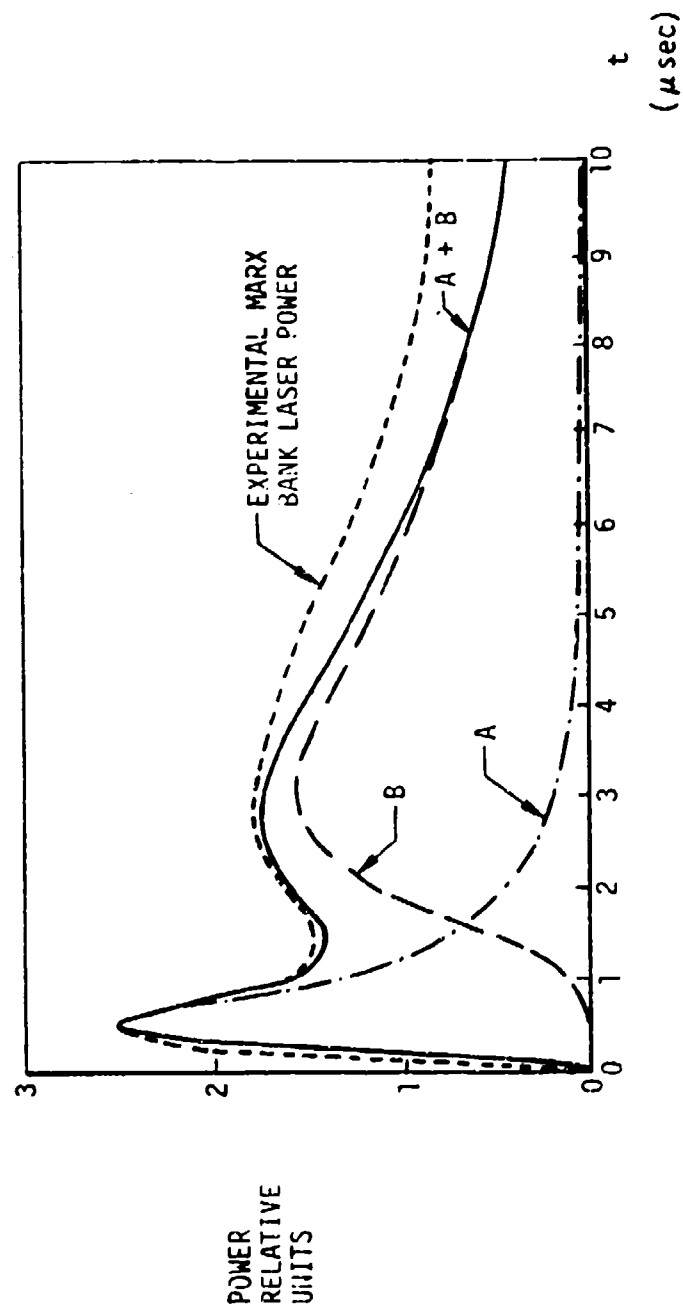
FIGURE 18 : ANALYTIC FUNCTION A + B FITTED TO MARX BANK LASER POWER

24

$$I(z,t) = \frac{P(t)}{\text{beam area}} \qquad \text{Megawatts/cm}^2 \qquad (4)$$

Equation 2 has been numerically integrated for our laser pulse and the result plotted in figure 19, where the experimental results are also indicated. The initial LSD wave velocity is approximately 3.8×10^5 cm/sec showing good agreement with experiment.

2.3 REFRACTION

Laser-supported detonation waves can produce a significant free electron density[15]. The local index of refraction will increase with the electron density and may become large enough to cause measurable refraction. If the absorption length is not too large and if the front of the laser-supported detonation wave has some radial curvature, some of the incident beam will be refracted.

We attempted to find if such refraction is important in the detonation wave geometry used in our experiments. The focal spot diameter of the Marx Bank laser beam is 0.24 cm when the beam is focused by the 28-cm focal length KCl lens. A target was prepared whose diameter is 0.5 cm and which was supported at the beam waist (minimum focal area) by a narrow arm. Laser-supported detonation waves were formed in front of it in the usual way and the beam which was neither absorbed nor refracted was blocked by the target. A 15-cm diameter focal length mirror was placed behind this target so that it imaged the target on a Au:Ge detector. As the laser-supported detonation wave moved away from the target, its image moved closer to the mirror. The detector was placed to intercept the entire beam which originates from the LSD wave for positions from the target surface to 2 cm away from the target as shown in figure 20.

The beam can possibly be refracted in angle between 0 and 180°, however, the 15-cm diameter mirror could collect only refraction angles between 0 and 22°. The maximum half-angle of the converging
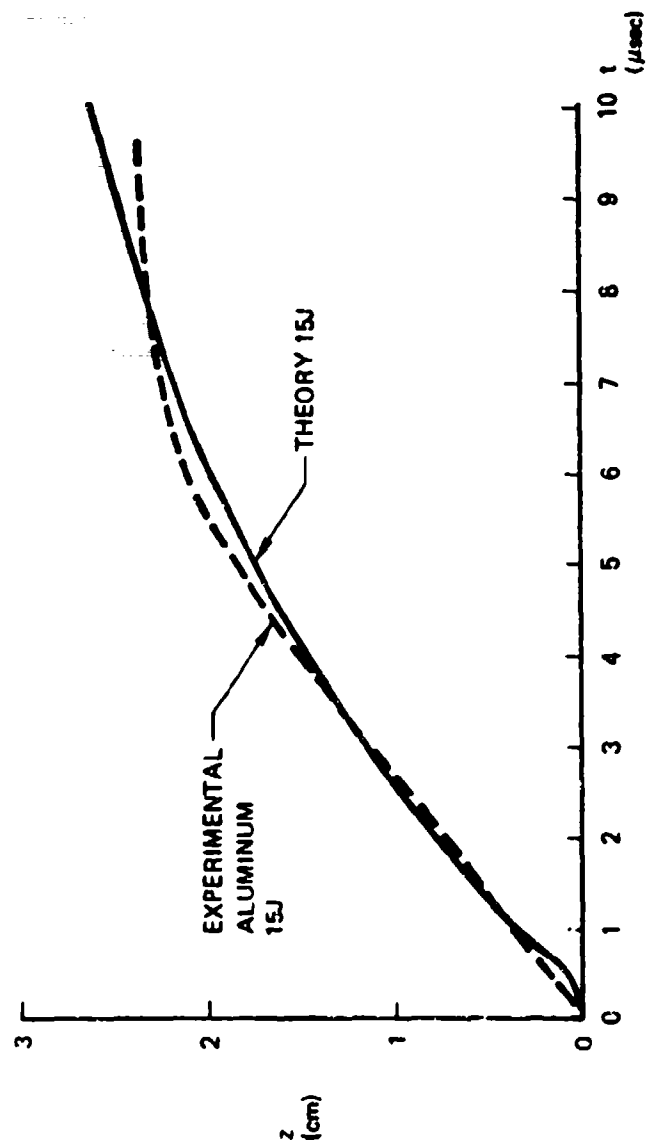
Figure 19: *THEORETICAL LASER-SUPPORTED DETONATION WAVE MOTION COMPARED WITH EXPERIMENT.*
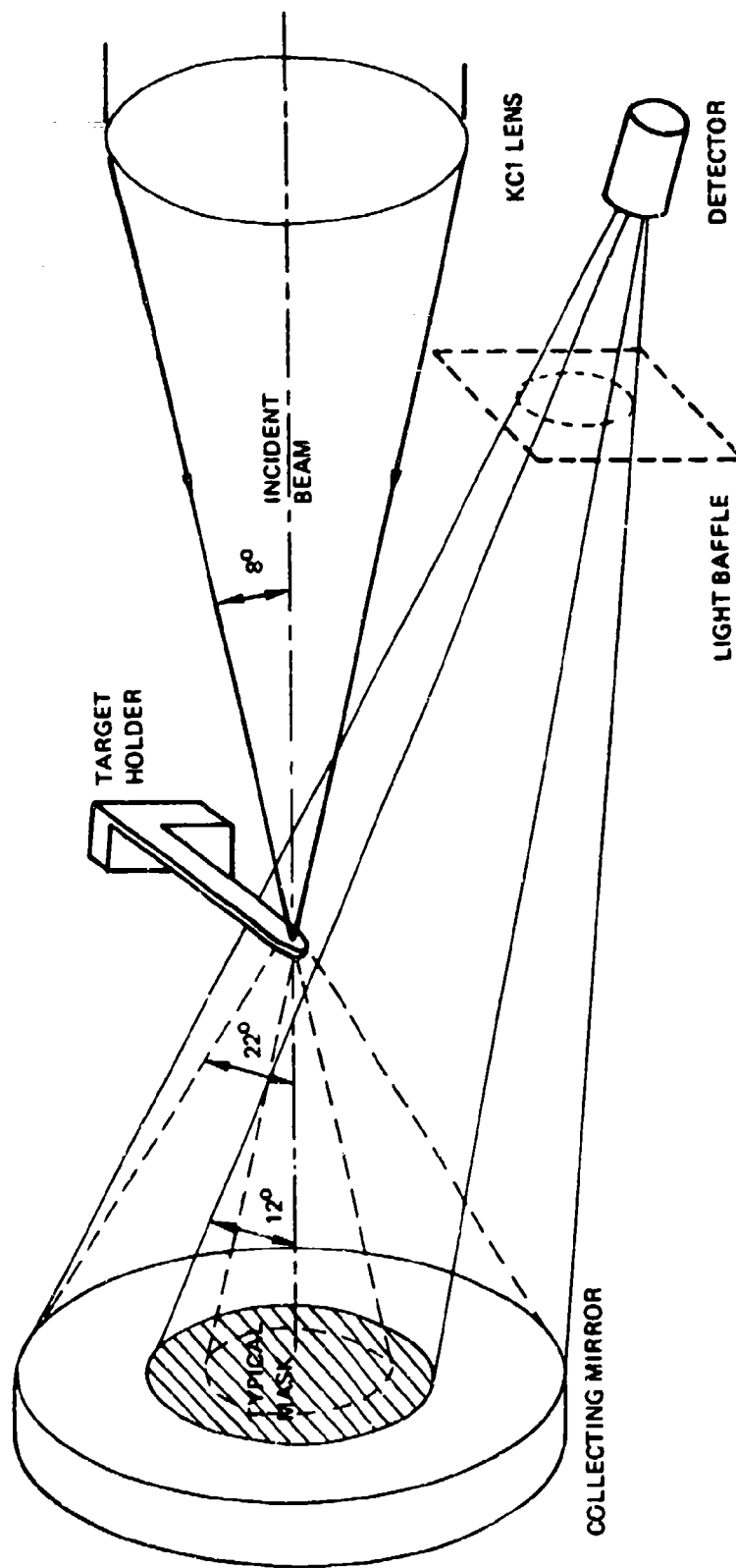
Figure 20: *LASER — SUPPORTED DETONATION WAVE REFRACTION MEASUREMENT APPARATUS.*

laser beam was 8°. A series of disks was prepared which masked
off the center of the mirror in steps of 8°, 10°, 12°, 15°, and
18°. This arrangement permitted the quantities of radiation
refracted between 0°-22°, 8°-22°, 10°-22°, 12°-22°, 15°-22° and
18°-22° to be measured by the detector. A narrow-band filter
centered at 10.6μ was placed in front of the detector which allowed
differention between the refracted laser beam power and the LSD
wave black body or line spectra.

Results, which have not been thoroughly subjected to tests
for systematic errors, showed refraction of laser beam power of the
order of a few percent within the 22° acceptance cone of our apparatus.
Temporal behavior in each angular zone was different from the other
zones but was repeatable. A contribution from black body or line
spectra was seen at all angles in addition to the refraction 10.6μ
radiation. Figure 21 shows both the total IR seen by the detector
and the radiation passed by the narrow-band filter when the mirror
annulus defining the acceptance cone has half angles of 8° and 10°.
The broad-band radiation peaked at 4-8 microseconds, but the 10.6μ
radiation didn't peak until 10μsec. This late refraction seems
sensible only if the refraction was occurring well in front of the
target and the actual angle was close to or less than the beam
convergence angle. Figure 22 shows the radiation passed by the
narrow 10.6μ filter for each mask. In general, at higher angles
the peak occurred later. Note that the radiation seen inside the
8° cone is appreciable and occurs early in the laser pulse.

The incremental energy refracted per unit solid angle is
shown in figure 23. This is narrow-band, 10.6μ radiant energy,
and there is a falloff with increasing solid angle. Similar behavior
would be expected for refraction by a convex lens whose index of
refraction is always less than one and which as a function of radius
monotonically reaches a minimum at the center. This is equivalent
to a plasma core with a radial electron density which peaks at $r = 0$.

28
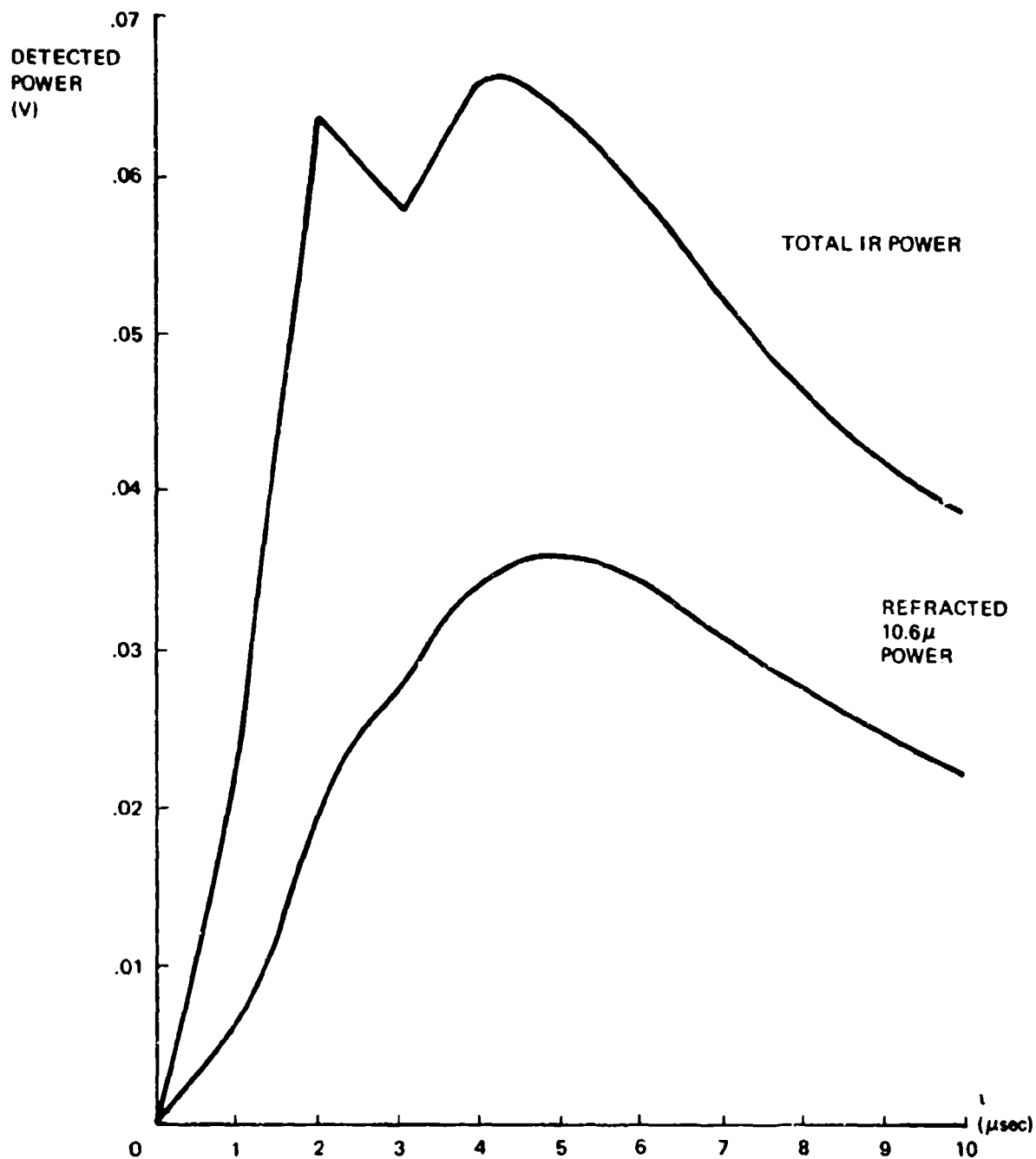
Figure 21: POWER COLLECTED FROM 8° -10° ANNULAR CONE
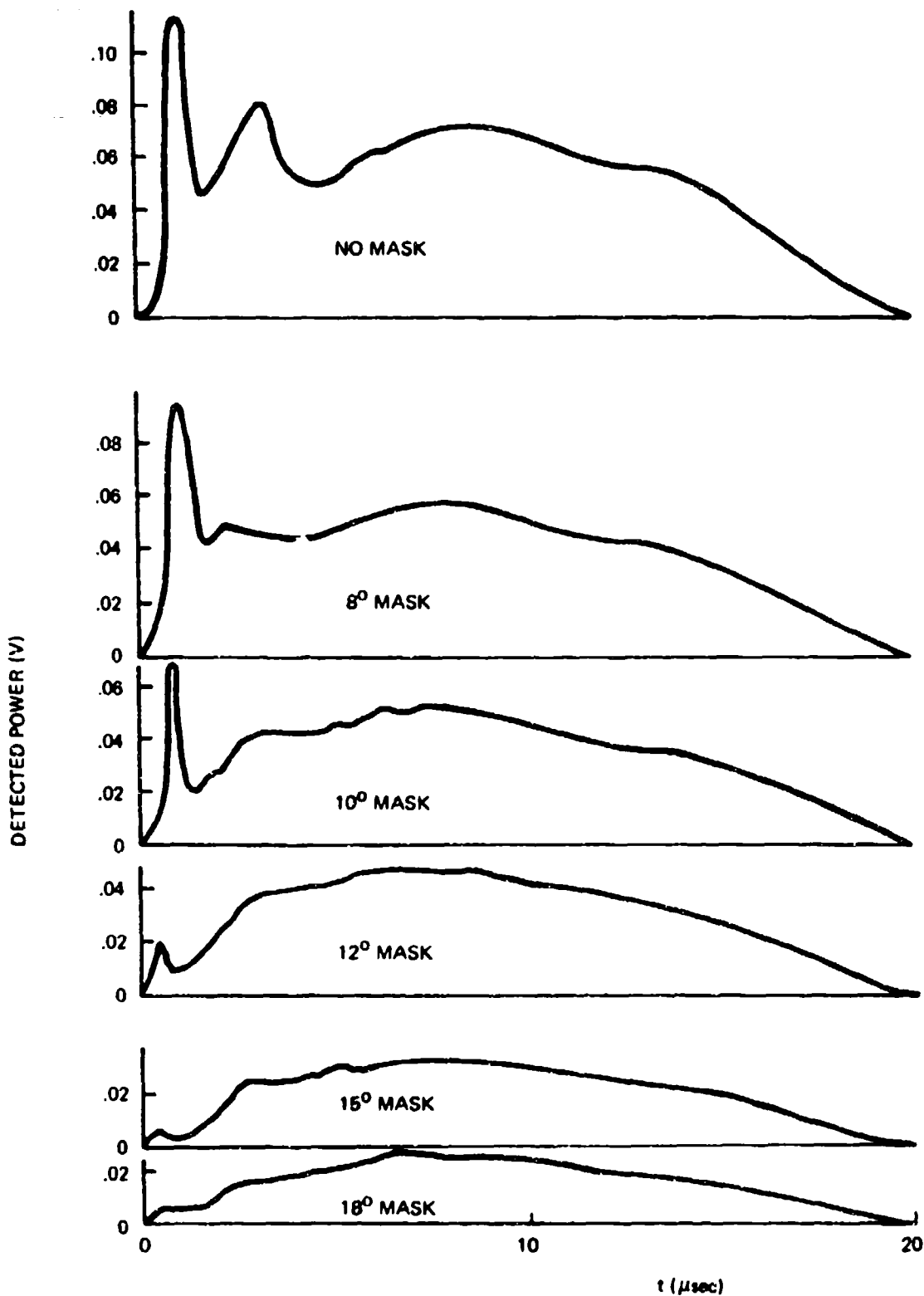
Figure 22: 10.6μ POWER COLLECTED WITH ANNULAR ACCEPTANCE CONES
N -22° WHERE N = 0°, 8°, 10°, 12°, 15°, AND 18°.
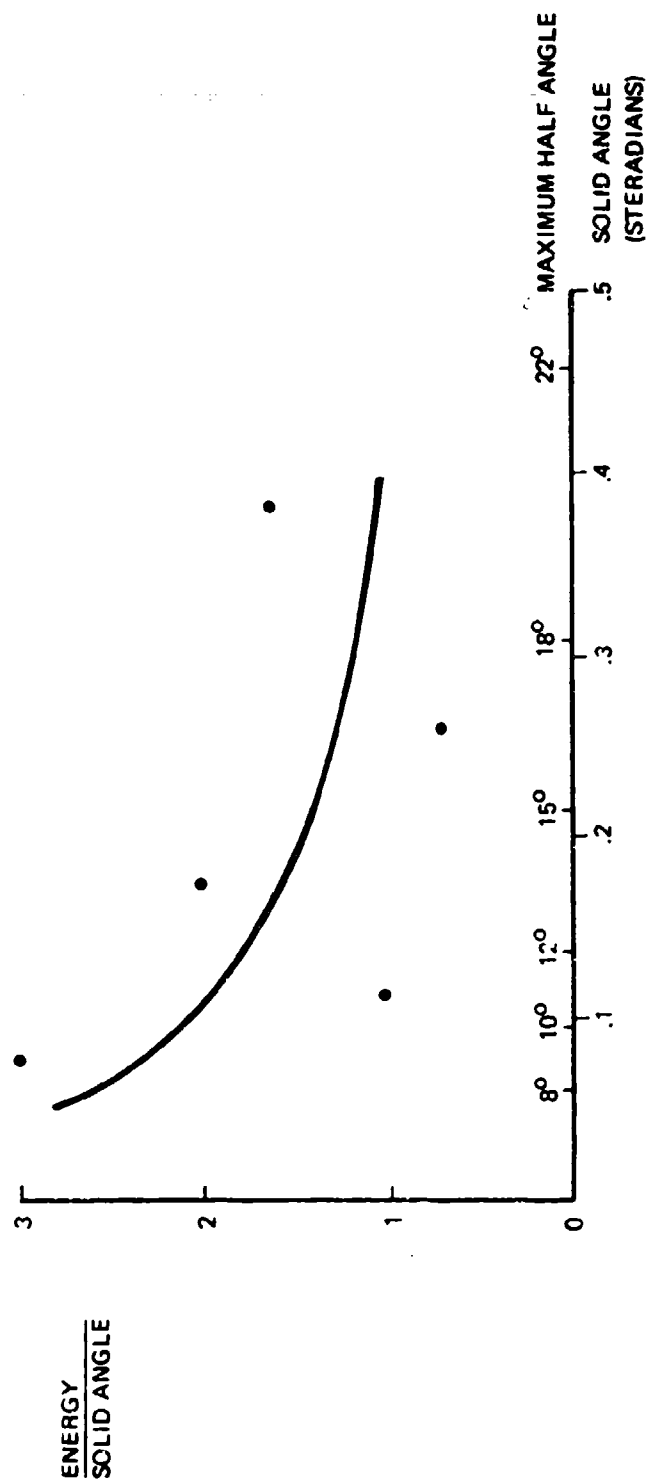
Figure 23: *10.6μ REFRACTED ENERGY/SOLID ANGLE FROM A LASER-SUPPORTED DETONATION WAVE.*

2.4 TRANSMITTED LASER ENERGY

The plasma induced by the laser-supported detonation wave was studied by an auxiliary laser beam from a CW CO_2 laser. A schematic diagram of the experimental arrangement is shown in figure 24. The CO_2 probe laser (Sylvania Model 648 with a power output of 2 watts) was operated in a single mode and had an output beam approximately 1 mm in diameter. Since the probe laser had some temporal fluctuation it was necessary to continuously monitor its output. This was done by placing a chopper (B) in the probe laser path and chopping at a frequency of approximately 1 kc.

The Marx Bank Laser is then fired only when the gold-doped germanium detector indicates maximum probe power. Thus, one oscillo-scope monitors the relatively slow chopped time dependence of the probe laser and also sends a delayed trigger to the Marx Bank Laser. The high-speed transmitted probe intensity is then monitored with a separate oscilloscope.

Since the LSD wave plasma is cylindrical and is about 3 mm in diameter, it acts like a diverging lens spreading out the probe laser beam. The lens (C) was intended to direct the refracted beam to the detector. The narrow bandwidth filter (F) greatly reduced the amount of optical energy originating in the LSD wave itself which reached the detector. In addition, care was taken to reduce the scattered high-power laser energy from reaching the detector.

An example of the transmitted laser intensity is shown in figure 25. There is a small amount of scattered 10.6μ laser energy from the Marx Bank Laser. The time delay to the abrupt drop in transmitted signal is caused by the distance of the probe laser beam in front of the target plane, $z = .64$ cm. After the initial delay, one notes that the transmitted signal is essentially zero for a period of 35μsec or more. Comparing figures 25a and 25b, one notes a longer time delay before loss of transmission in the lower
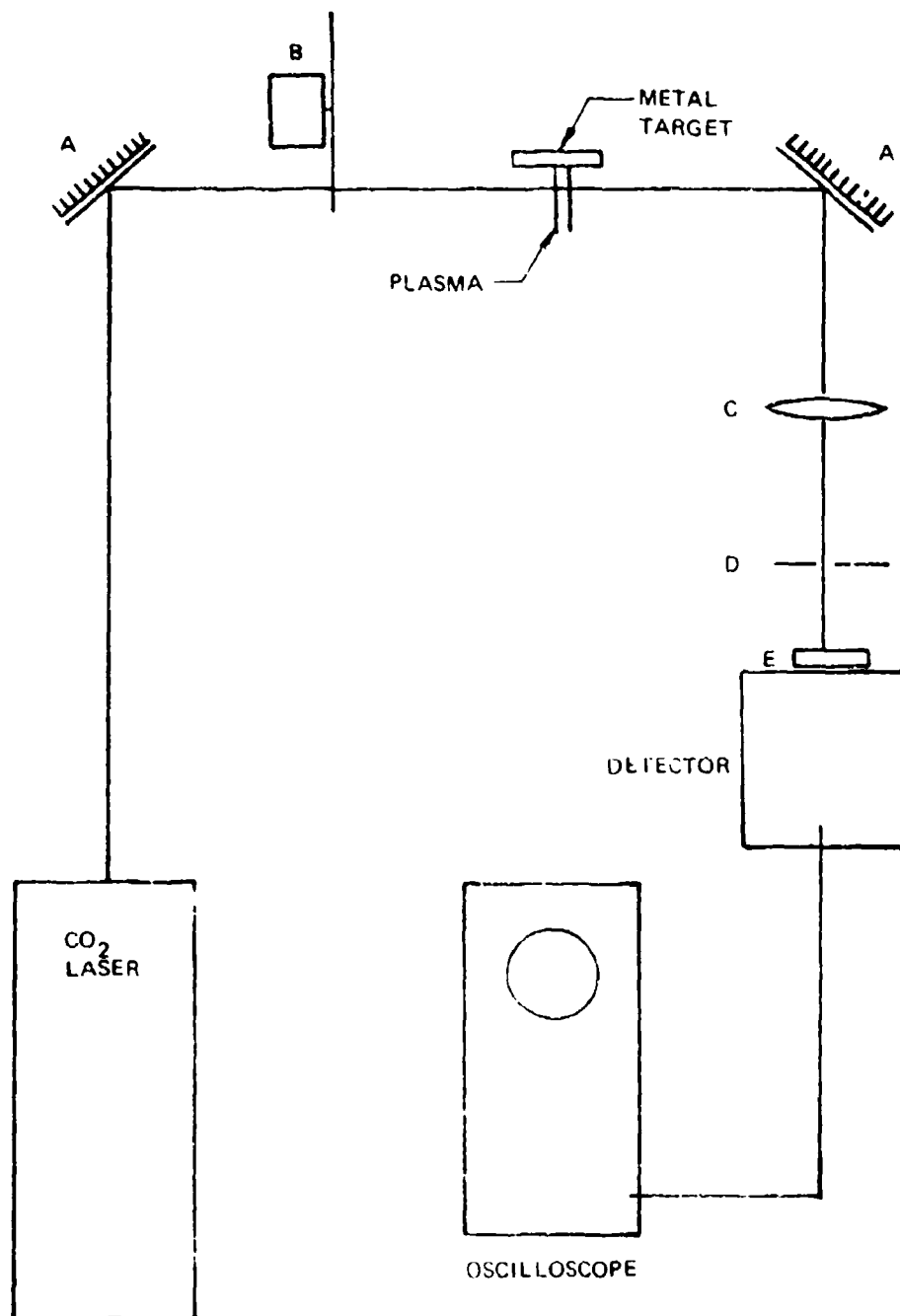
Figure 24: *EXPERIMENTAL ARRANGEMENT FOR MEASURING TRANSMISSION OF A CO_2 LASER BEAM THROUGH A LASER-SUPPORTED DETONATION WAVE. A IS A MIRROR, B IS A CHOPPER USED IN ORDER TO OBTAIN ZERO LEVEL IN THE PRESENCE OF A FLUCTUATING LASER OUTPUT. C IS A GERMANIUM FOCUSING LENS, D IS A 1 MM APERTURE, AND E IS A NARROW-BAND FILTER.*

33
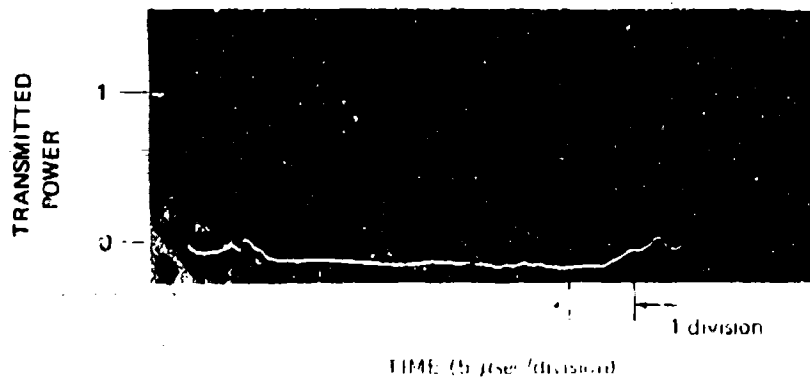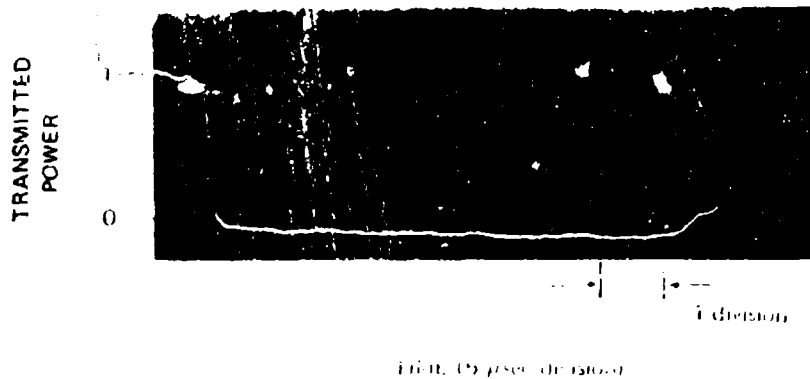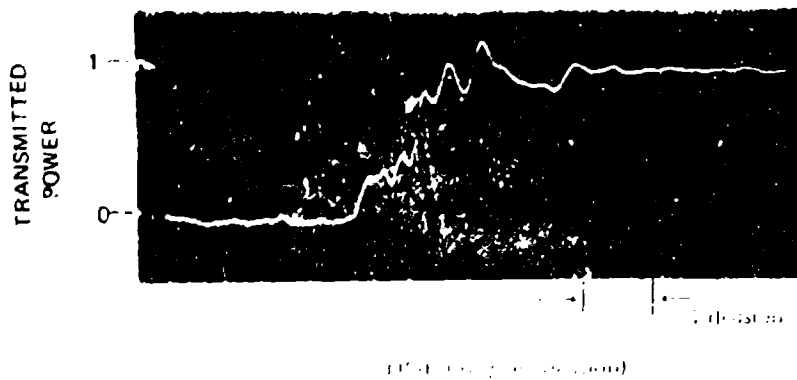
Figure 25   TRANSMISSION OF A CO_2 LASER PROBE BEAM THROUGH A
LASER SUPPORTED DETONATION WAVE FOR TWO MARX BANK
LASER BEAM ENERGIES.

energy LSD wave. Figure 25c shows that the transmitted signal remains essentially unattenuated (or unrefracted) for times greater than 50μsec.

From the time delay till probe signal cutoff, as observed in figures 25a and b, one can determine the intensity variation of LSD wave velocity. (This was done with a more appropriate sweep speed of 1μsec/division.) These data indicates that the LSD wave velocity V is

$$V \doteq E^{.32} \tag{5}$$

where E is the laser energy (or intensity). This result is consistent with theoretical expectations of LSD wave theory indicated by equation 1.

The interpretation of the data of figure 25 is not completely understood since refractive effects are not ruled out. As seen from the data of Hora[7], an electron density of $n_e \doteq 10^{18}$ at a temperature of 1 eV(11,600°K) leads to an absorption coefficient k

$$k \doteq 10 \text{ cm}^{-1} \tag{6}$$

This means the transmitted laser intensity through the 3-mm diameter LSD plasma would be about 5 percent. This is consistent with throughput observations given in figure 25. On the other hand, the "plasma lens" would cause a probe laser beam angular divergence θ of approximately

$$\theta \doteq \frac{\omega_p^2}{\omega^2} \doteq \frac{n_e}{10^{19}} \text{ radians} \tag{7}$$

35

For $n_e = 10^{18}$ one would obtain a probe beam divergence of

$$\theta = 0.1 \text{ radian} \tag{8}$$

It is necessary, in our experimental arrangement, to place the lens (C) at a distance of about 65 cm from the plasma in order to reduce scattered Marx Bank Laser energy and to reduce intense optical radiation from reaching the detector. In this case, as seen from equation 8, one expects that the probe CO_2 beam (even without absorption) would be completely refracted away from the aperture of the lens (C). For this reason, one cannot claim nearly 100 percent attenuation of the probe laser in the LSD plasma. A more careful experiment at higher frequency appears necessary in order to accurately determine absorption.

SECTION III

INTERFEROMETRIC PHOTOGRAPHY

An event with a nonuniform index of refraction will refract and change the phase of light which passes through it. Laser-supported absorption waves are composed of plasma, compression waves, and rarefaction waves accompanied by vapor evolved from the target surface. Each of these alone will modify the initial index of refraction distribution, and all taken together produce complex changes.

Interferometry compares the phase of an unaffected reference beam with the phase of a second beam which passes through the event. In the limit of small changes and essentially no refraction, the intereference pattern produced and recorded in a film plane can be analyzed to reconstruct the index of refraction distribution. An additional limitation to analysis is the possibility of two competing contributions to the refractive index since neutral species retard the phase while excess electron densities advance it. The summed refractive index can be determined in many cases where the individual components of it cannot. For electrons, the index of refraction, n, is[18]

$$n = \sqrt{1 - \frac{\omega_p^2}{\omega^2}}$$

where ω_p is the plasma frequency. For neutral species, on the other hand, (n-1) is proportional to the species density.

In a single-pass interferometer, the phase change is seen as fringe shifts, with one dark (or light) fringe for each 2π of phase change between beams or for each differential change in path length of one wavelength. For a single-species neutral disturbance, one finds

$$\frac{\rho - \rho_o}{\rho_o} = \frac{\lambda \Delta F}{L \ (n_o - 1)} \tag{9}$$

where equation 9 is strictly valid for a uniform plane slab of gas
of density ρ and an initial density ρ_o. In equation 9, λ is the
vacuum wavelength, L is the slab thickness, and n_o is the index of
refraction of a gas of density ρ_o. (For air, at standard pressure,
$(n_c - 1) = 2.9 \times 10^{-4}$.) For a fully ionized disturbance, on the other
hand, one finds

$$\frac{\omega_p{}^2}{2\omega^2} = -\frac{\lambda}{L} \ \Delta F - (n_o - 1) \tag{10}$$

where we have assumed that $\omega_p{}^2/\omega^2 \ll 1$. Equation 10 shows that the
addition of electrons to the perturbing media has qualitatively the
same effect as removing the neutral species. Equations 9 and 10
are approximations based on uniform density plane slabs. More
detailed calculations[20,21,22,23,24,25] of realistic geometries
and allowing density gradients have been previously considered
and these results have been used in the following analysis.

3.1 RUBY LASER INTERFEROGRAMS

A ruby interferometer was used to study laser-supported absorp-
tion waves and vapor jet interaction with air and a schematic
diagram of the experiment is shown in figure 26. This is a double-
pass Michelson interferometer which doubles the fringe shift but
which also reduces the spatial resolution since during only one of
the two passes through the event is it focused on the film. A
Pockels cell was used to Q-switch the ruby laser at a preselected
time during the LSA wave. A narrow-band filter and complete light
baffle shielded the film from the intense light of the LSA wave.

38
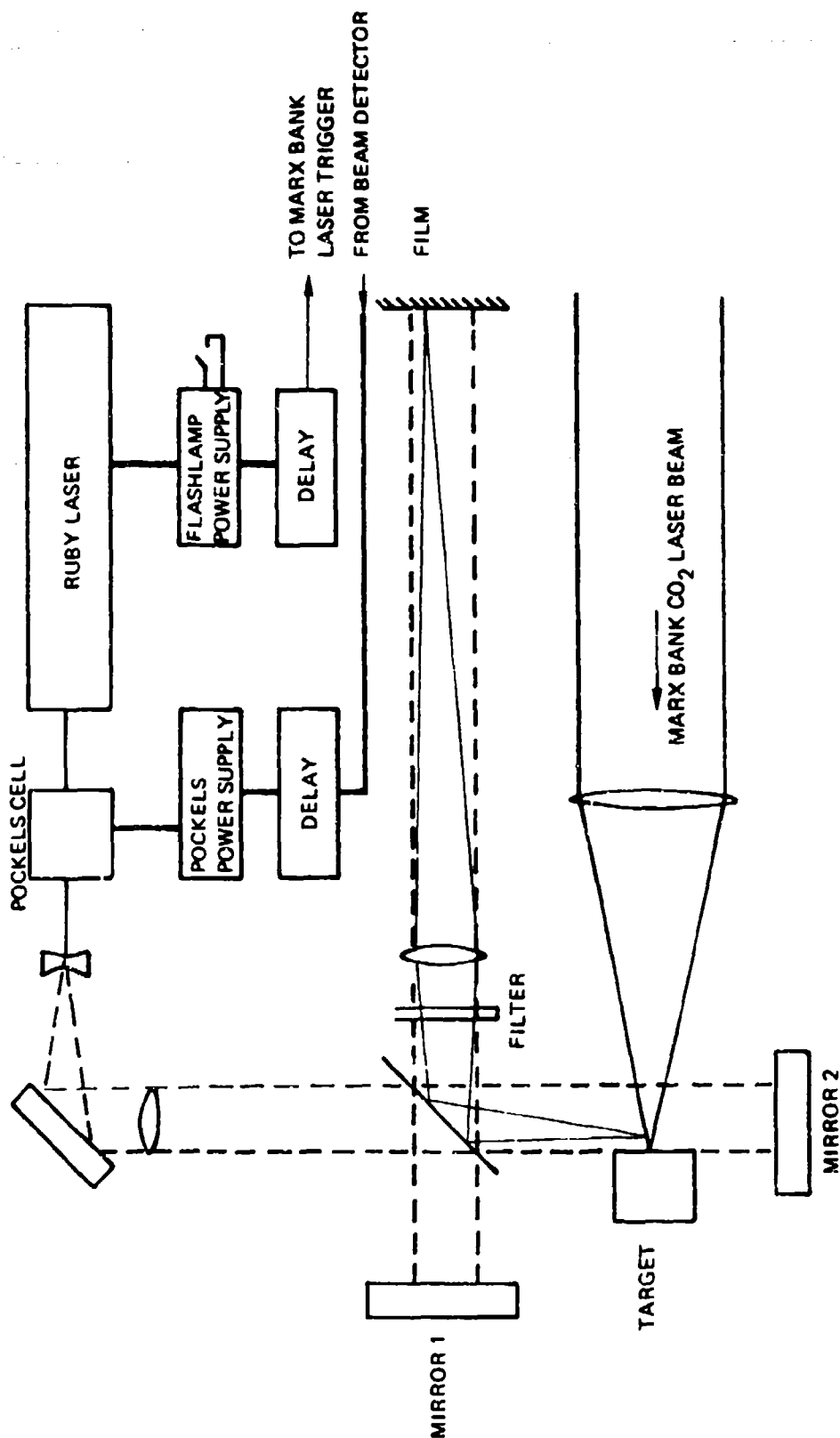
Figure 26 : RUBY LASER MICHELSON INTERFEROMETER USED TO VIEW LASER-SUPPORTED ABSORPTION WAVE

A modification of this setup produced a single-pass Mach-Zehnder interferometer arrangement as shown in figure 27. Mirrors 1 and 2 were replaced by corner cube reflectors which separated the beam in the target vicinity into one element traveling in each direction. The nature of the ambient interference pattern of the film changed from an adjustable fringe spacing to a pattern with only one fringe which occurs when the reference and sample beams are collimated.

In all the data discussed below, the beam area followed the indications given in equation 4 with a minimum focal diameter of 2.4 mm and with the target at that position. By use of appropriate lenses and spacings, the interferometer was arranged to give a magnification of 3.17 on the interferograms. Figure 28 is an example of a strong LSD wave propagating away from the inclined target surface and up the laser beam. The appearance of these interferograms is significantly different from ordinary photographs which show only the luminous regions. There is clearly a conical shape which shows the radial propagation of the shock wave created by the LSD wave. This travels outward to the region beyond the luminous core. Near the target, some indication of vapor coming from the surface is seen. Most of the fringe shift occurs near the shock wavefront, however, resolution is lost at the propagation front of the LSD wave itself, and significant darkening appears as seen in figure 28.

Additional features of the propagation of the LSD wave and absorption of the ruby laser wavelength (.694μ) are shown in the shadowgram (figure 28) which was obtained by blocking the reference arm of the interferometer. Further features of the growth of the LSD wave first shown in figure 28 are given in figures 29, 31, and 32. These interferograms were obtained on successive Marx Bank Laser shots by varying the time delay to the Pockels cell shown in figure 26. This process is useful here due to the high-reliability of the laser.
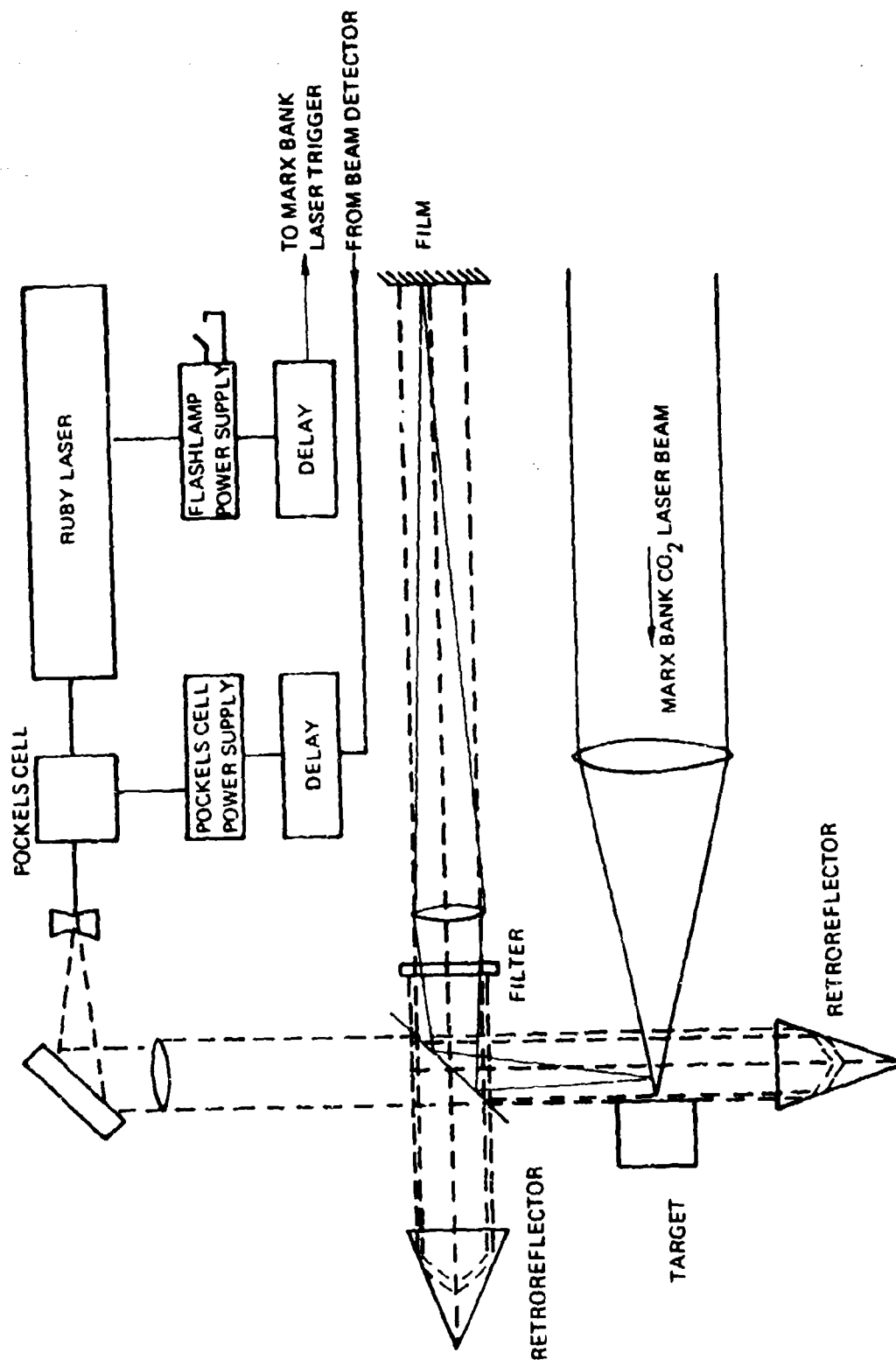
Figure 27: RUBY LASER MACH-ZEHNDER INTERFEROMETER USED TO VIEW LASER-SUPPORTED ABSORPTION WAVE.

5.5 μsec
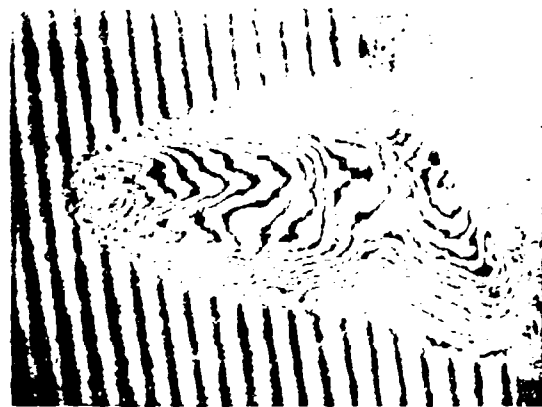
5.5 μsec

Figure 28.: COMPARISON OF A DOUBLE-PASS INTERFEROGRAM WITH A
SHADOWGRAM FOR LASER-SUPPORTED DETONATION WAVES
WHICH ARE IGNITED AT A 30° ALUMINUM TARGET BY 15J
LASER BEAMS.

42
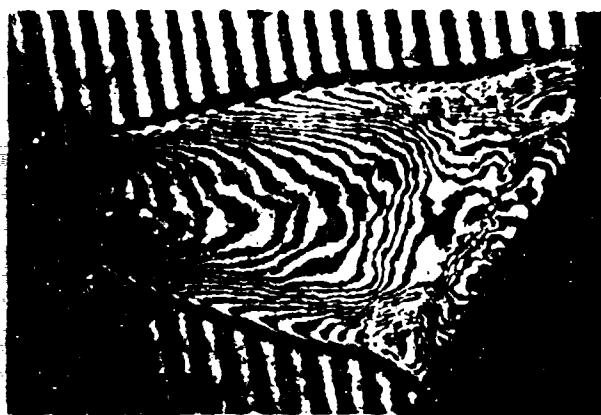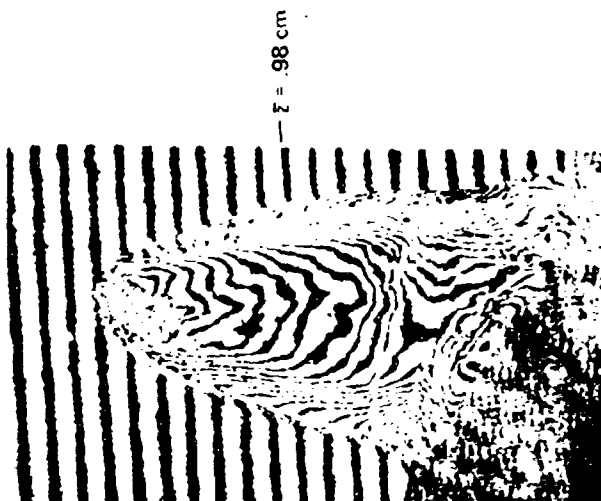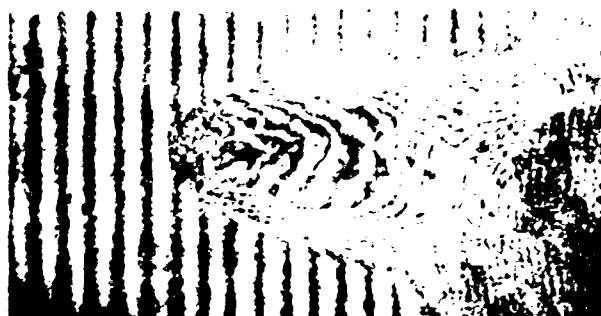
Figure 29: GROWTH OF A LASER-SUPPORTED DETONATION WAVE. DOUBLE-PASS INTERFEROGRAMS
SHOW THREE TIMES AFTER ITS IGNITION AT A 30° ALUMINUM TARGET BY A 15J LASER BEAM.
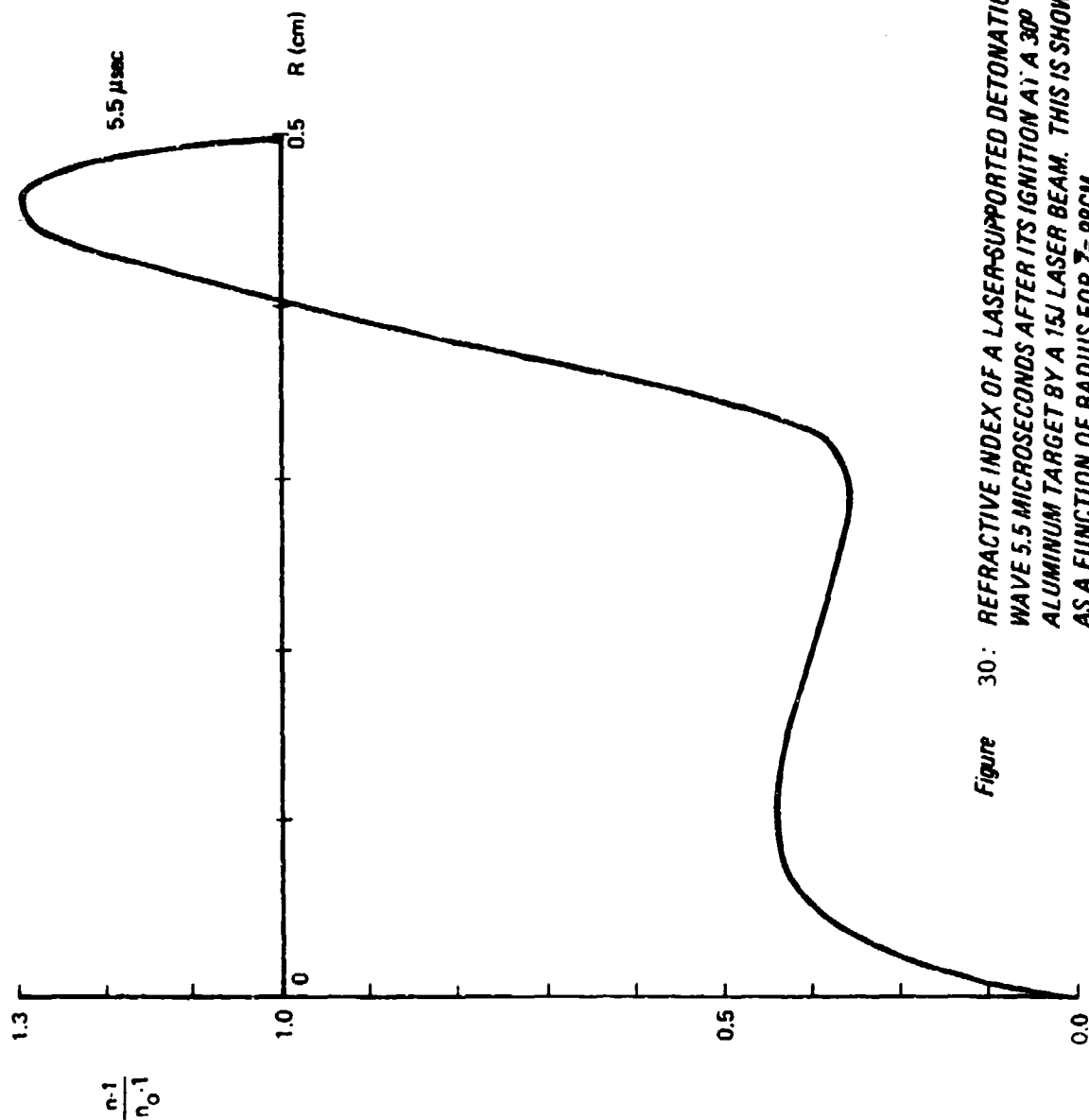
Figure 30: *REFRACTIVE INDEX OF A LASER-SUPPORTED DETONATION WAVE 5.5 MICROSECONDS AFTER ITS IGNITION AT A 30°*
ALUMINUM TARGET BY A 15J LASER BEAM. THIS IS SHOWN
AS A FUNCTION OF RADIUS FOR Z=.98CM.
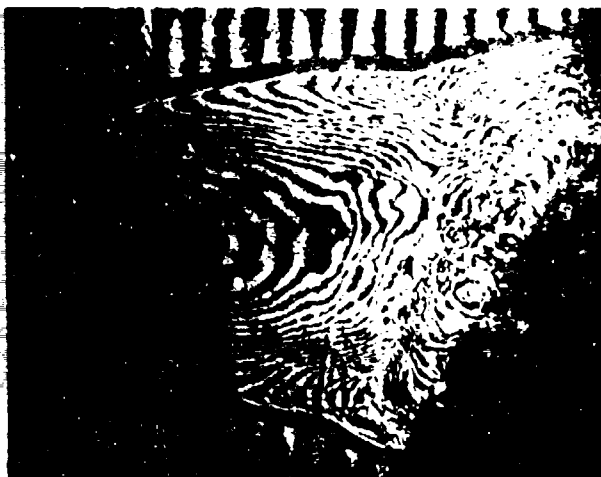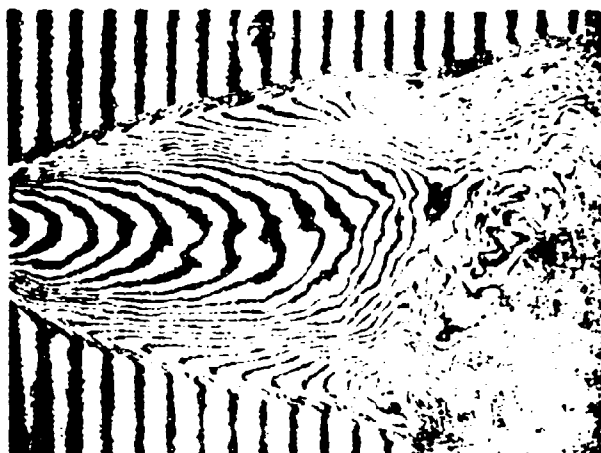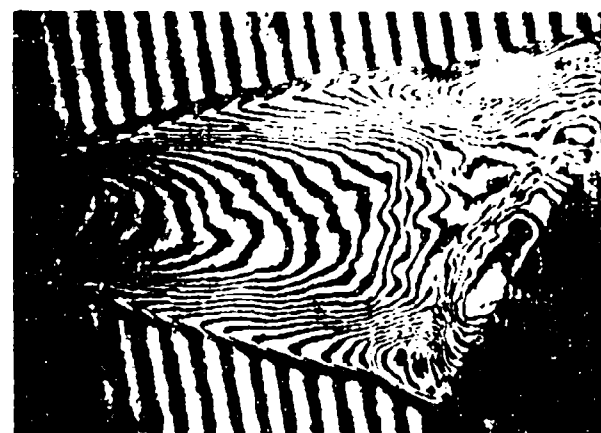
Figure 31: GROWTH OF A LASER-SUPPORTED ABSORPTION WAVE WHICH CONTINUES AFTER LASER-SUPPORTED DETONATION WAVE CONDITIONS NO LONGER EXIST. DOUBLE-PASS INTERFEROGRAMS SHOW THREE TIMES AFTER THE LASER-SUPPORTED DETONATION WAVE IGNITION AT A 30° ALUMINUM TARGET BY A 15J LASER BEAM.

z = 1.68 cm
z = 1.40 cm
z = 1.14 cm
z = 0.87 cm

1 cm

11 μsec
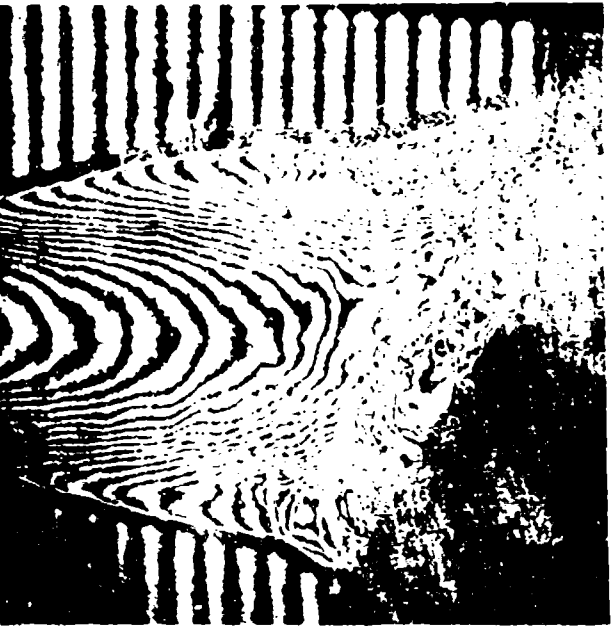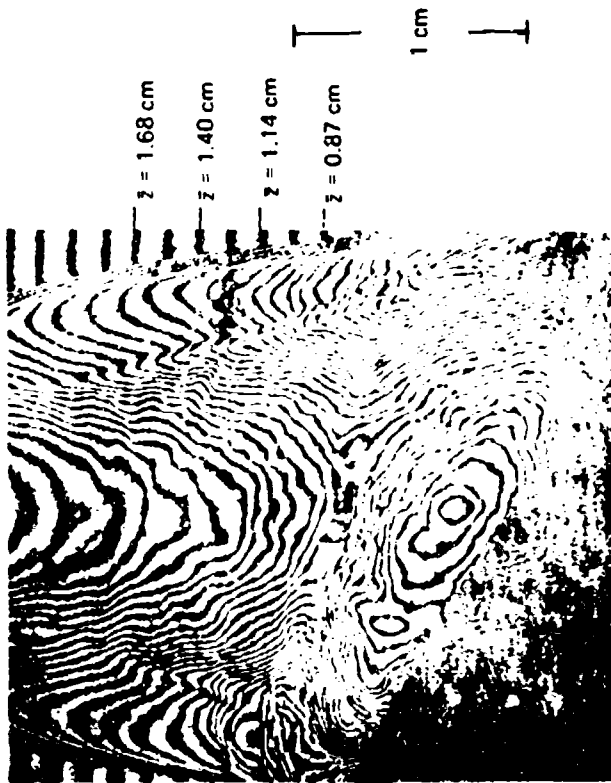
16 μsec

Figure 32: *CONTINUED GROWTH OF A LASER-SUPPORTED ABSORPTION WAVE AFTER LASER-SUPPORTED DETONATION WAVE CONDITIONS NO LONGER EXIST. DOUBLE-PASS INTERFEROGRAMS SHOW TWO TIMES AFTER THE LASER-SUPPORTED DETONATION WAVE IGNITION AT A 30° ALUMINUM TARGET BY A 15J LASER BEAM.*

The method for converting fringe-shift data obtained from the interferograms to plots of density versus radius is given in Section 3.3, however, a result of this analysis is given in figure 30. The ratio $(n-1)/(n_o-1)$ is equal to gas density ratio (ρ/ρ_o) when the electronic contribution to the refractive index is negligible. The data presented in figure 30 were obtained by counting fringes on the interferogram taken at 5.5μsec after ignition given in figure 29, and at the axial position of $\bar{z}$ = .98 cm, where $\bar{z}$ is the average height above the inclined target surface. The sharp dip at the origin may be an artifact of the analysis procedure, but the picture is clearly one of a radial compression wave followed by a rarefaction. The quantity $(n-1)/(n_o-1)$ is directly proportional to density in the absence of competing electronic refractive index changes.

The total mass within the 0.5-cm radius disk does not seem to be conserved if we look at this curve and consider only neutral species contributions. Radial integration over this volume would require the peak in $(n-1)/(n_o-1)$ to reach about 4 for mass conservation. Otherwise, there is a 30-percent error in mass conservation. This contradiction and the necessary resolution of the problem in terms of electron densities and longitudinal mass flow is discussed below.

A series of radial plots for different values of the average longitudinal distance from the target is shown in figure 33. These correspond to the four cuts across the 11μsec interferogram in figure 32 at $\bar{z}$ = .87, 1.14, 1.4 and 1.7 cm. These all are very similar and again show the compression and rarefaction regions.

When the Mach-Zehnder configuration of the interferometer as shown in figure 27 is used, one obtains high resolution data since the event is focused on the film and refractive edge effects are thereby minimized. The overall appearance of LSD waves studied by both the single-pass and double-pass interferograms is unchanged
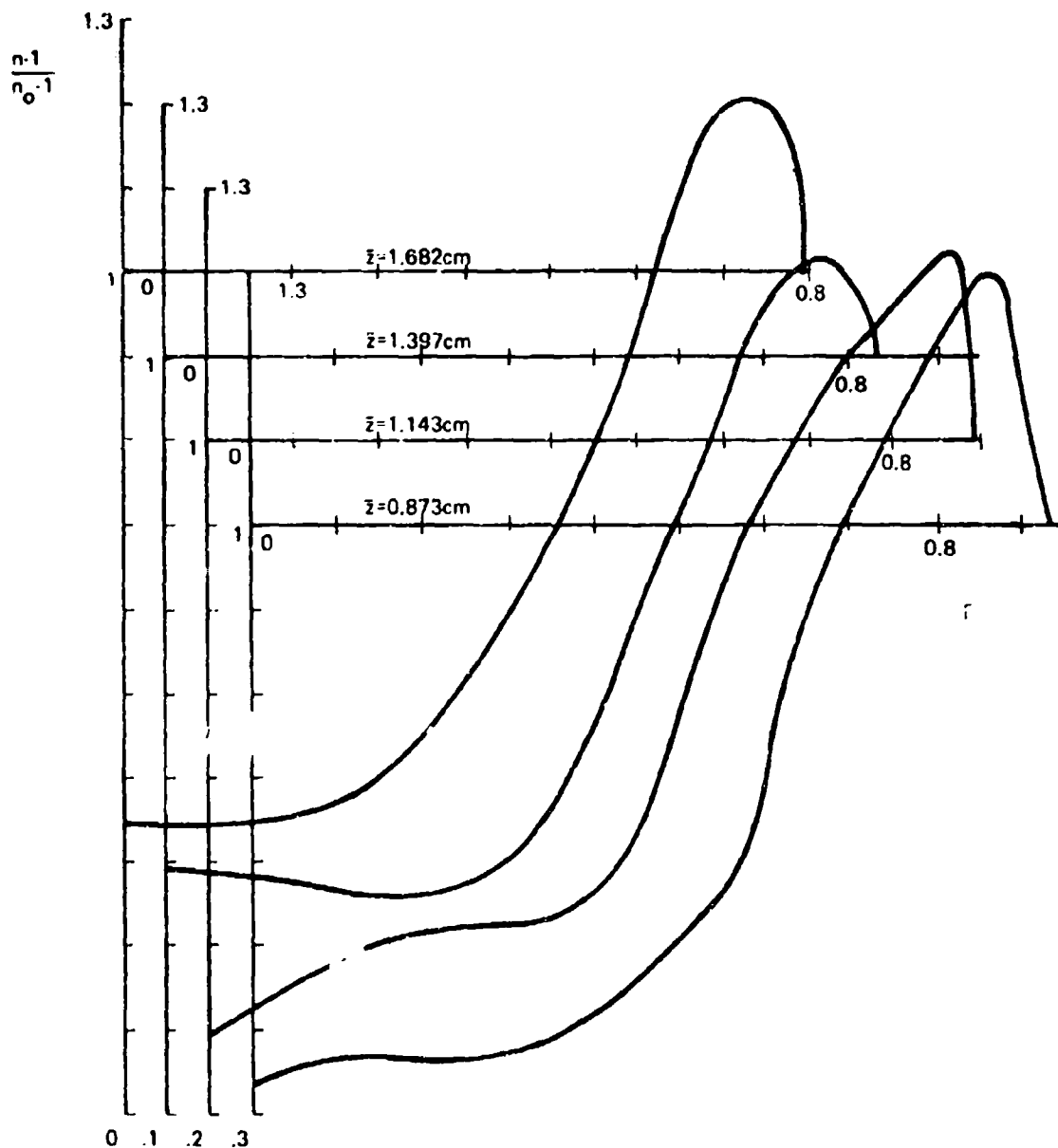
Figure   33: REFRACTIVE INDEX OF A LASER-SUPPORTED ABSORPTION
              WAVE 11 MICROSECONDS AFTER THE IGNITION OF A LASER-
              SUPPORTED DETONATION WAVE AT A 30° ALUMINUM TARGET
              BY A 15J LASER BEAM. THIS IS SHOWN AS A FUNCTION
              OF RADIUS FOR FOUR $\bar{z}$

except that the number of fringe shifts is halved as shown by the comparison presented in figure 34. The three lines 60° apart are the prism edges of the two retroreflectors. The improved resolution in the single pass picture allows the propagating end of the LSD wave to be seen, indicating the complicated fine-grained absorption and refraction processes which occur. Radial plots of mass density or $(n-1)/(r_o-1)$ are shown for these photographs in figures 35 and 36.

As the incident laser intensity is reduced on an aluminum target, the sharp features of the LSD wave are lost and one obtains a long luminous plasma column in the vicinity of the beam. An example of this laser-supported blast wave is shown in figure 37 at an intensity level approximately .9 that needed to support a strong LSD wave. This shock wave is clearly spherical and not conical in shape and travels at relatively high velocity. On the interferogram, the shock-wavefront is seen to be much wider than the compression wave for a LSD wave. Assuming spherical symmetry of this shock wave, one can analyze the density profile at any chord of the sphere. Such an analysis has been performed for the cut at $Z = .51$ cm and the results are shown in figure 38 as a plot of $(n-1)/(n_o-1)$ versus the radial coordinate perpendicular to the laser beam axis. It is interesting to note that a numerical integration of the mass density profile shown in figure 38 yields a total mass constant to within 5 percent of that gas mass originally lying within the .77-cm radius disk. At the present, no self-consistent interpretation of this empirical observation is offered.

The LSA waves ignited from absorbing targets can also be studied with interferometry and one clearly observes evaporated material leaving the surface with its momentum nearly normal to the surface. This can be seen in figure 39 which indicates that at times of 10 and 20 microseconds, the evaporated silica material flows closely behind the air shock-wavefront and has well defined boundaries. The overall event has a spheroidal shape rather than a spherical one, and the location of maximum negative fringe shift is found to
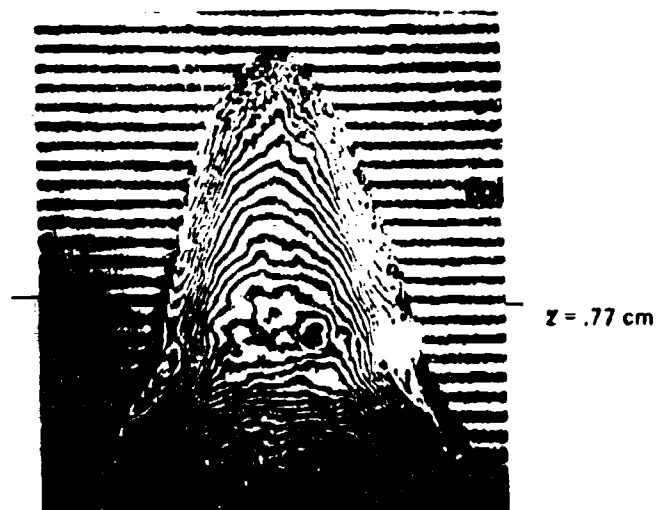
Figure 34 a: DOUBLE-PASS INTERFEROGRAM OF A LASER-SUPPORTED DETONATION WAVE
5.5 MICROSECONDS AFTER ITS IGNITION AT AN ALUMINUM TARGET BY A 15J
LASER BEAM.
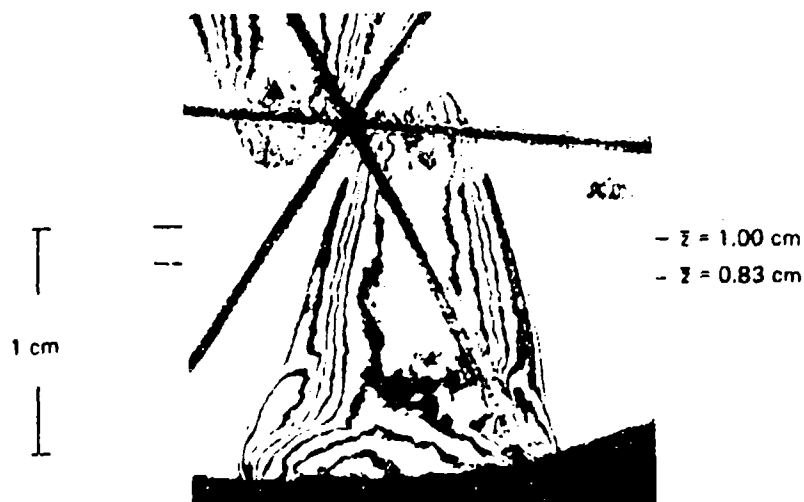
Figure 34b: INTERFEROGRAM OF A LASER-SUPPORTED DETONATION WAVE 5 MICROSECONDS
AFTER ITS IGNITION AT AN ALUMINUM TARGET BY A 15J LASER BEAM.
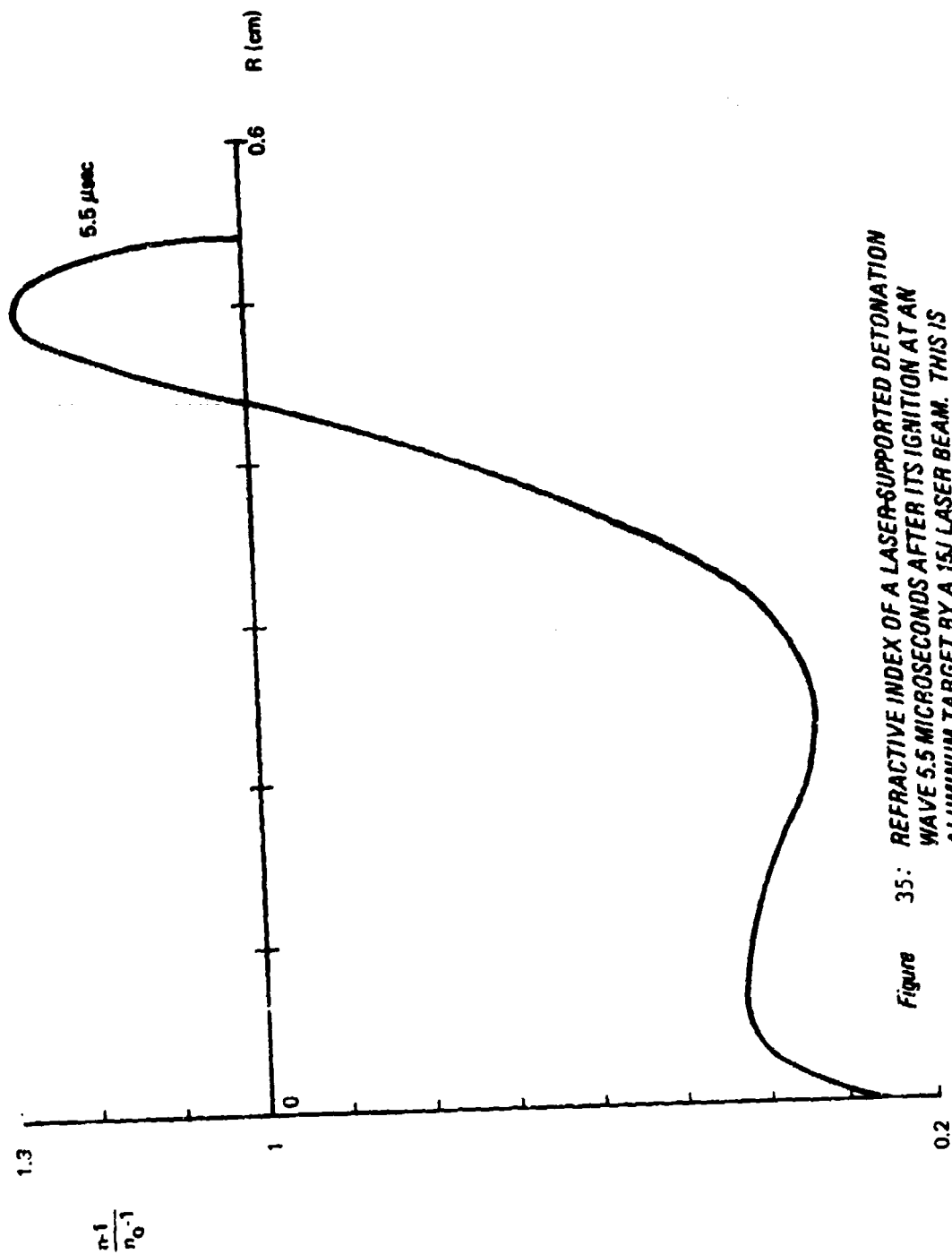
Figure 35.: REFRACTIVE INDEX OF A LASER-SUPPORTED DETONATION WAVE 5.5 MICROSECONDS AFTER ITS IGNITION AT AN ALUMINUM TARGET BY A 15J LASER BEAM. THIS IS SHOWN AS A FUNCTION OF RADIUS FOR $\bar{Z}=.77CM$.
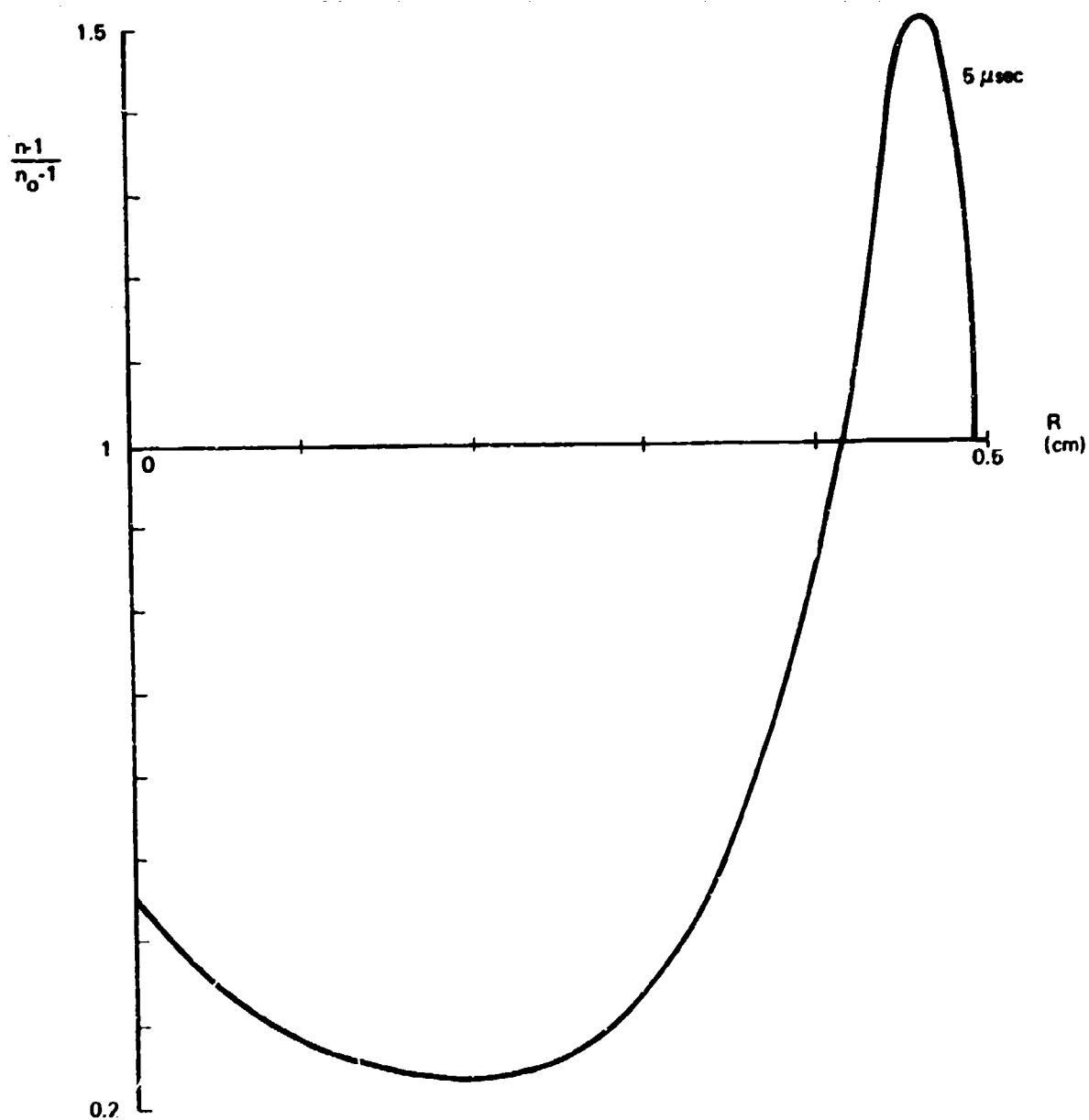
Figure   36: REFRACTIVE INDEX OF A LASER-SUPPORTED DETONATION
                WAVE 5 MICROSECONDS AFTER ITS IGNITION AT AN
                ALUMINUM TARGET BY A 15J LASER BEAM. THIS IS SHOWN
                AS A FUNCTION OF RADIUS FOR Z=.83CM.

1 cm

z = .51 cm

Figure 37: DOUBLE-PASS INTERFEROGRAM OF A LASER-INDUCED SHOCK WAVE WITH POSSIBLE TARGET VAPOR 10 MICROSECONDS AFTER ITS INITIATION AT A 30° ALUMINUM TARGET. THE INCIDENT LASER BEAM HAD 6.1J WHICH WAS SLIGHTLY SMALLER THAN THE LASER-SUPPORTED DETONATION WAVE IGNITION THRESHOLD.
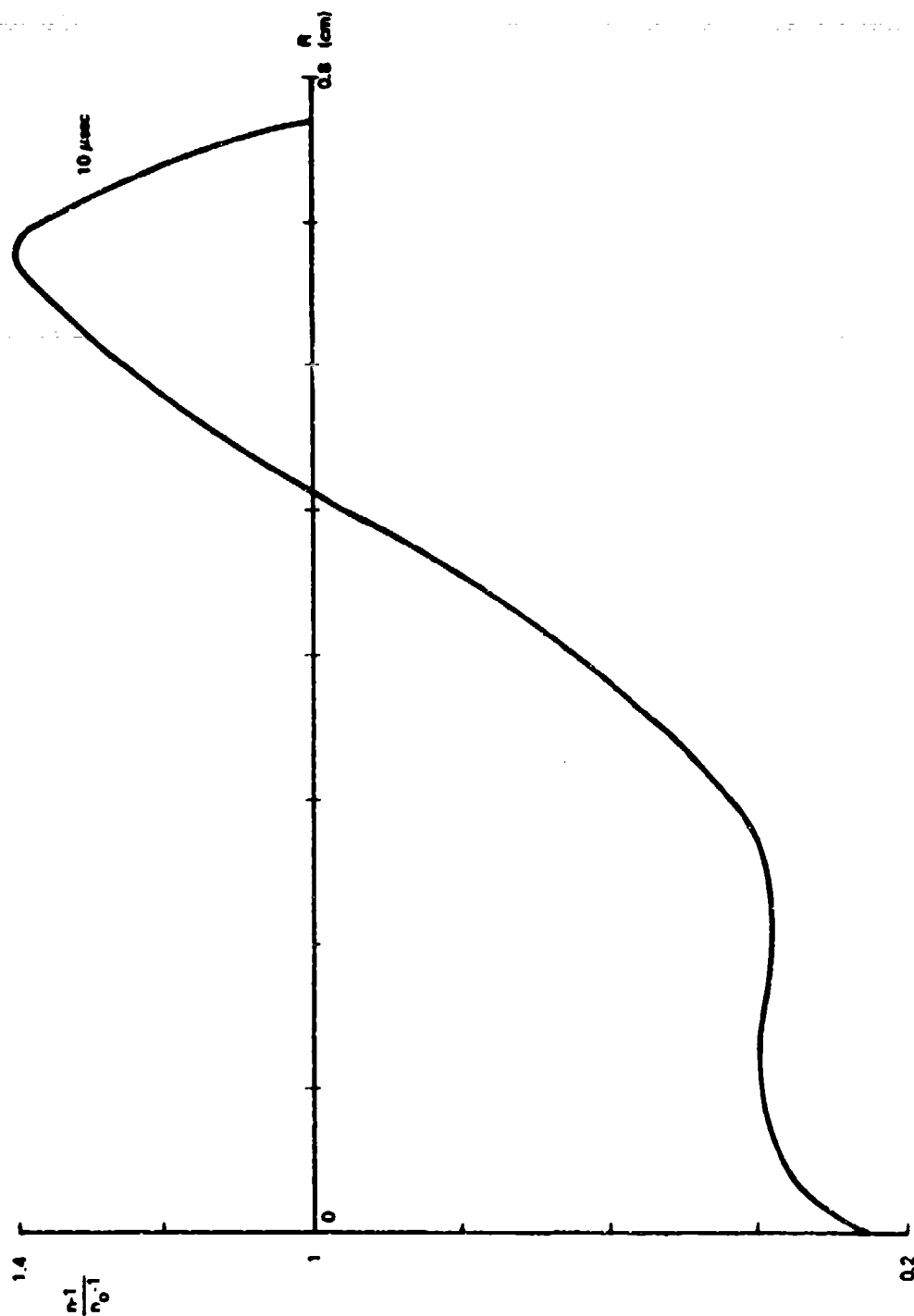
Figure 38: REFRACTIVE INDEX OF A LASER-INDUCED SHOCK WAVE WITH POSSIBLE TARGET VAPOR 10 MICROSECONDS AFTER ITS INITIATION AT A 30° ALUMINUM TARGET BY A 6.1J LASER BEAM. THIS IS SHOWN AS A FUNCTION OF RADIUS FOR $\bar{Z}$=.51CM.

54

10 μsec

1 cm

z̄ = 1.10 cm

20 μsec

Figure 39: DOUBLE-PASS INTERFEROGRAMS SHOW A COMBINATION OF LASER-INDUCED
TARGET VAPOR AND A LASER-INDUCED SHOCK WAVE AT 10 AND 20 MICROSECONDS
AFTER THEIR INITIATION AT A SILICA TARGET BY A 15J LASER BEAM.

lie closer to the wave front than to the target. An analysis of the lower picture at $\bar{z} = 1.1$ cm in figure 39 leads to the radial plot of $(n-1)/(n_o-1)$ in figure 40 where, once again, one sees a large uniform rarefaction region following the compression wave.

Additional interferograms and a shadowgram of the target-vaporized material and blast wave produced at a silica target are shown in figure 41. This sequence of data were taken with a total delivered energy of approximately 7.5 joules and indicates that the maximum fringe shift region lies closer to the target surface than the data figure 39 with a laser energy of 15 joules. The lower interferogram, taken at 20μsec and near the end of the laser pulse, is analyzed at an axial position of $\bar{z} = .68$ cm and the results shown in figure 42.

In addition to silica, Lucite is another material which can absorb very large laser intensities at 10.6μ without igniting laser-supported detonation waves. This is strictly true only after the target is "cleaned" by a preliminary laser pulse. A series of ruby interferograms showing the ejection of vaporized target material from a Lucite target with a total delivered energy of 15 joules is shown in figure 43. With this energy, the peak laser intensity at the target surface is approximately 4.8×10^7 watts/cm^2. It appears, as expected, that the amount of vaporized Lucite target material is considerably larger than similar interferograms made for a silica target and shown previously in figures 39 and 41.

In contrast to the silica interferograms, the vaporized Lucite material appears to come off at greater angles, and the region of maximum negative phase change lies closer to the target than to the wavefront, however, the overall spheroidal shapes are very similar in the two cases. An Abel inversion of the lower interferogram taken at 8μsec and shown in figure 43, has been analyzed and the results at $\bar{z} = .54$ cm are shown in figure 44. This radial plot of $(n-1)/(n_o-1)$
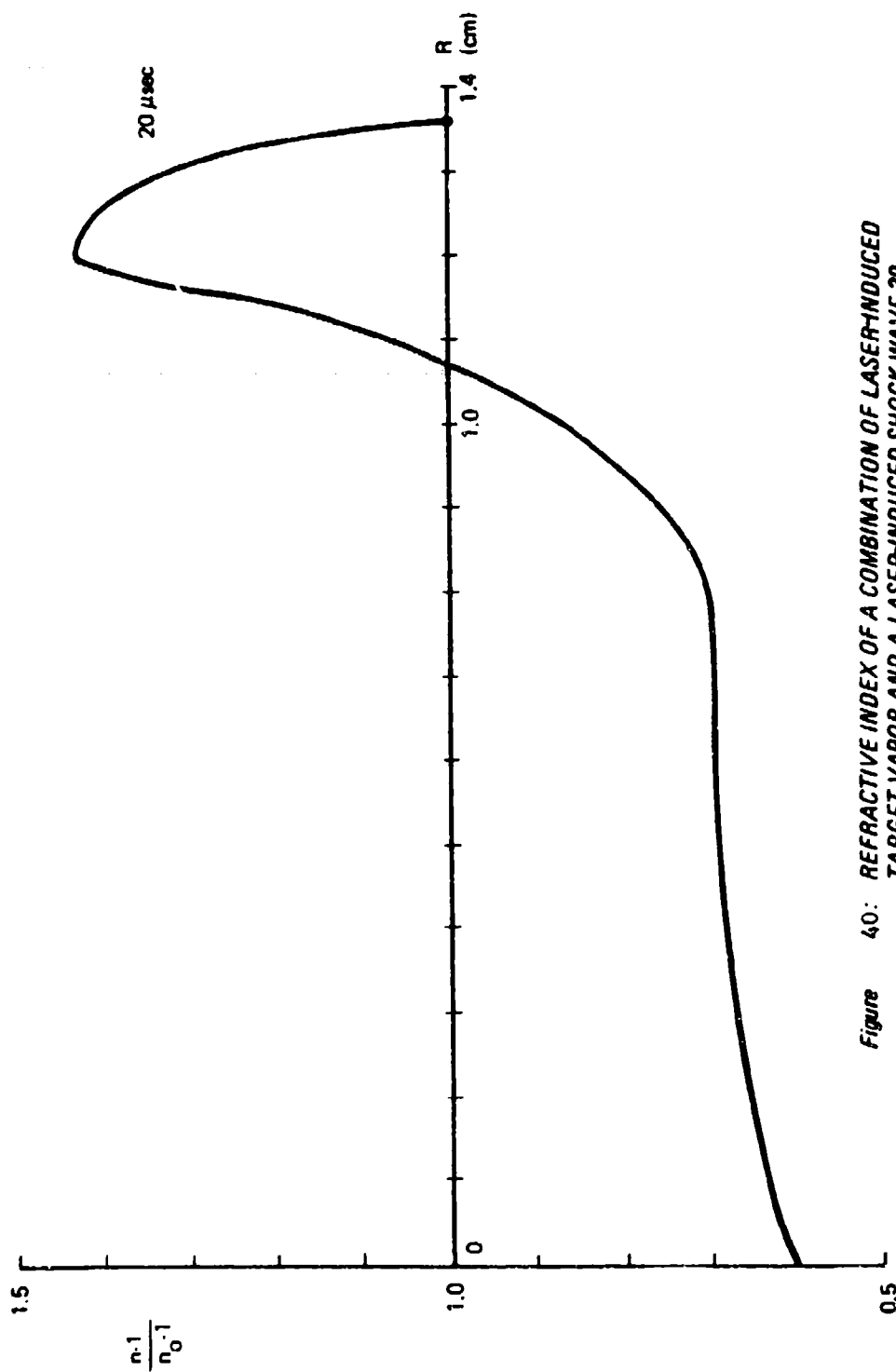
Figure 40: REFRACTIVE INDEX OF A COMBINATION OF LASER-INDUCED TARGET VAPOR AND A LASER-INDUCED SHOCK WAVE 20 MICROSECONDS AFTER ITS INITIATION AT A SILICA TARGET BY A 15J LASER BEAM. THIS IS SHOWN AS A FUNCTION OF RADIUS FOR $\bar{Z} = 1.10CH$.
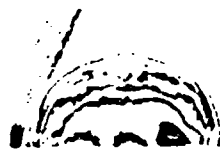
INTERFEROGRAM 4 μsec

INTERFEROGRAM 10 μsec   SHADOWGRAM 10 μsec

— z = .68 cm

1 cm
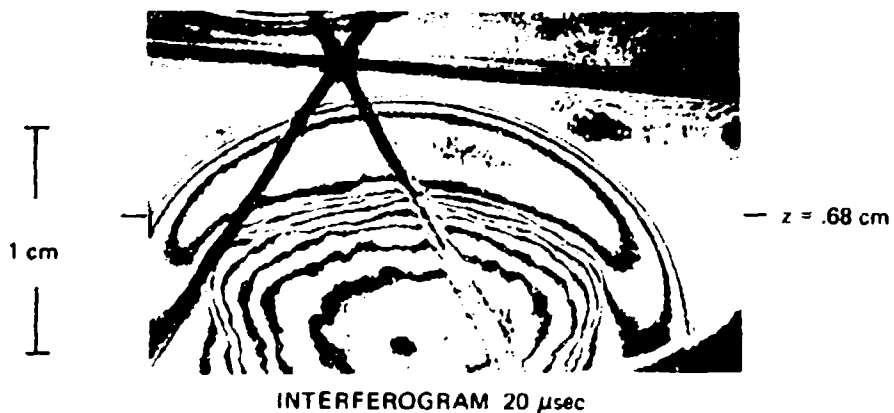
INTERFEROGRAM 20 μsec

Figure 41: INTERFEROGRAMS AND A SHADOWGRAM SHOW THE GROWTH OF LASER-INDUCED TARGET VAPOR AND A SHOCK WAVE DEVELOPED FROM A SILICA TARGET BY A 7.5J LASER BEAM.
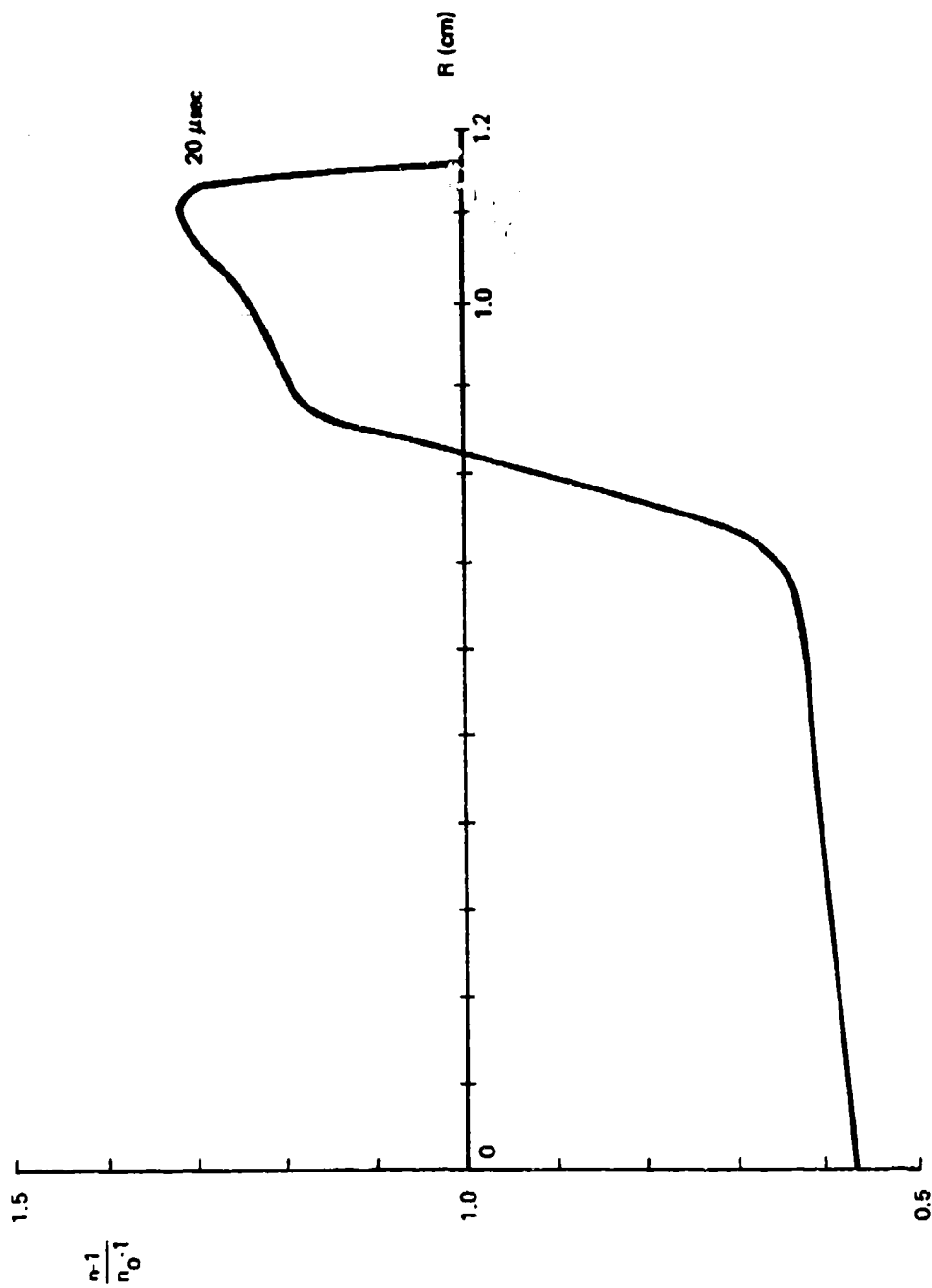
Figure 42: REFRACTIVE INDEX OF LASER-INDUCED TARGET VAPOR AND A SHOCK WAVE 20 MICROSECONDS AFTER ITS INITIATION AT A SILICA TARGET BY A 7.5J LASER BEAM. THIS IS SHOWN AS A FUNCTION OF RADIUS FOR $\bar{Z}$=.68CM.

2 μsec

5 μsec

1 cm

z = .54 cm
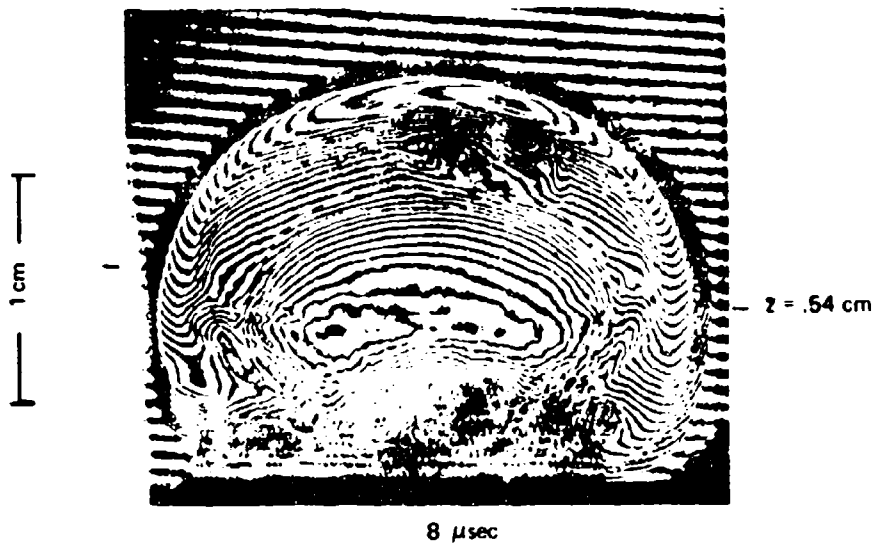
8 μsec

Figure 43: *DOUBLE-PASS INTERFEROGRAMS SHOW THE GROWTH OF LASER-INDUCED TARGET VAPOR AND A SHOCK WAVE DEVELOPED FROM A LUCITE TARGET BY A 15J LASER BEAM.*

60
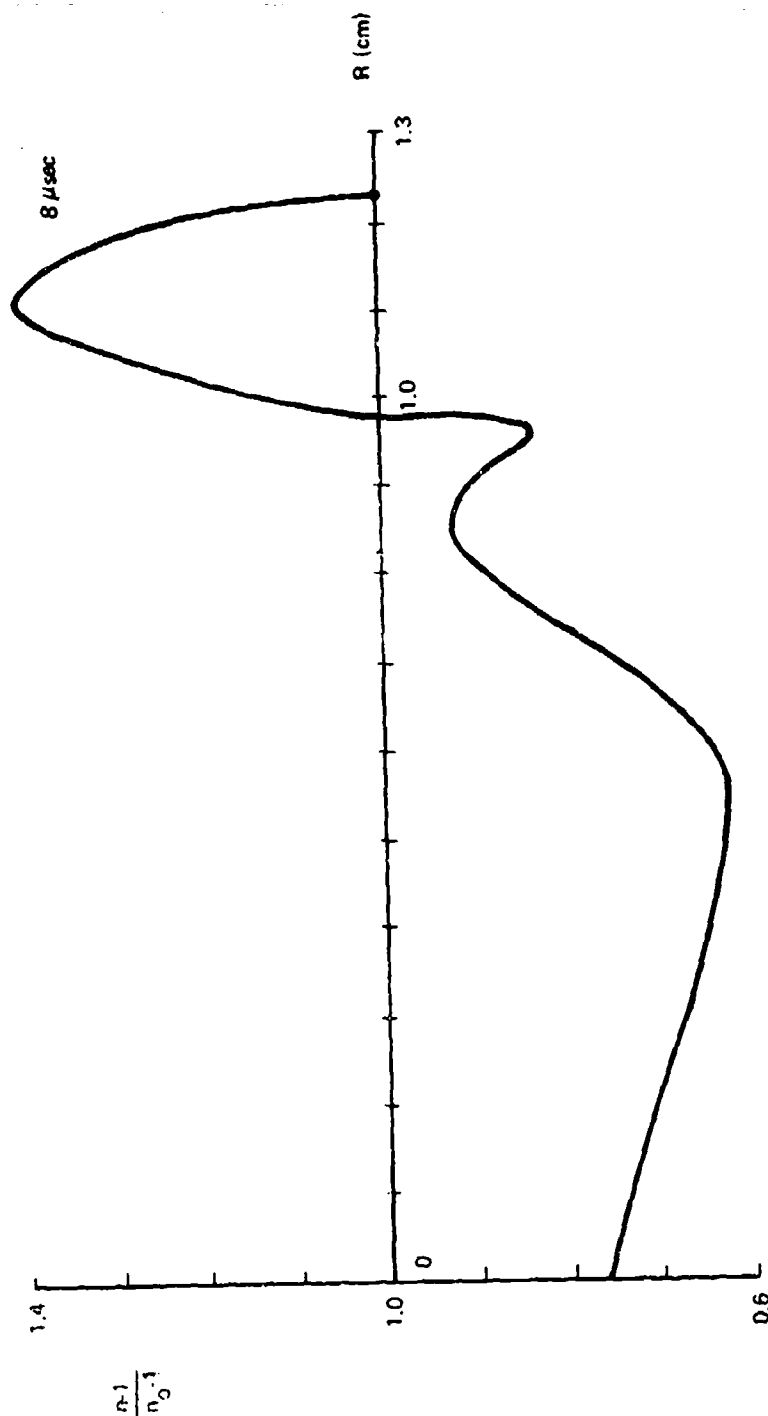
Figure 44.: REFRACTIVE INDEX OF LASER-INDUCED TARGET VAPOR AND A SHOCK WAVE 8 MICROSECONDS AFTER ITS INITIATION AT A LUCITE TARGET BY A 15J LASER BEAM. THIS IS SHOWN AS A FUNCTION OF RADIUS FOR $\bar{Z}$=.54CM.

shows two separate wavefronts, indicating that the inner one is
evaporated material. It is coincident with the apparent evaporated
material front in the interferogram. Strong absorption occurs near
the target; however, absorption is weaker near the evaporated
material front.

Reducing the laser energy by a factor of two causes a reduced
vaporization rate as shown by the sequence of interferograms of
figure 45. This data for a delivered energy of 7.5 joules should
be compared with the 15 joule data previously given in figure 43.

Little absorption is seen near the target, but the absorption
near the evaporated material front remains high. Figure 46 shows
shadowgraphs which clearly display absorption and refraction regions.
The lower shadowgram was taken just before the lower interferogram
in figure 45. The upper shadowgram was taken earlier on a different
sample which has been exposed to enough shots to develop a noticeable
crater. A definite jet blow-off effect is seen in the upper shadowgram
which is only suggested in the lower shadowgram. The lower interfero-
gram in figure 45 was analyzed along the cut at $\bar{z}$ = .57 cm, and the
corresponding radial plot of $(n-1)/(n_0-1)$ is shown in figure 47 which
shows a dip in density just inside the compressed region. Such
behavior may occur in figure 44, but be masked by the evaporated
material since there is a downward trend for increasing radius
beginning at the center. It should be noted that the plots of
$(n-1)/(n_0-1)$ are proportional to gas density only when the electron
contribution to the refractive index is negligible and, in addition,
the refractive index of the gaseous vaporized material is the same
as that of air. At this point, these assumptions are not verified
and further work is required to obtain more useful information.
This additional work involves identification of species in the
vaporized material and use of two-wavelength interferometry.

2 μsec
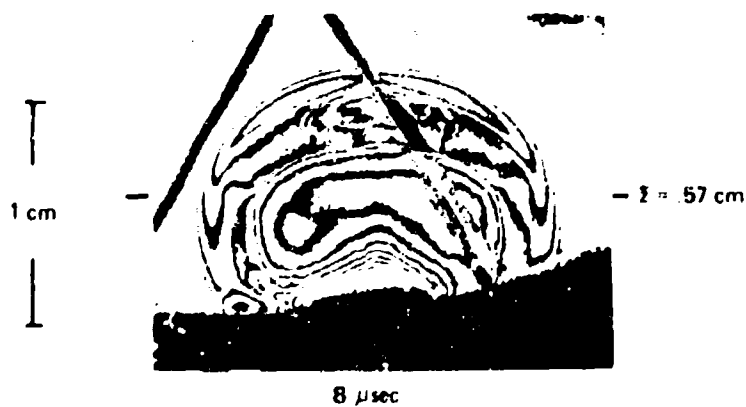
4 μsec

1 cm

Σ = .57 cm

8 μsec

Figure 45: INTERFEROGRAMS SHOW THE GROWTH OF LASER-INDUCED TARGET VAPOR AND
A SHOCK WAVE DEVELOPED FROM A LUCITE TARGET BY A 7.5J LASER BEAM.

7 usec

1 cm

8 μsec

Figure 46: *SHADOWGRAMS OF LASER-INDUCED TARGET VAPOR AND A SHOCK WAVE DEVELOPED FROM A LUCITE TARGET BY A 7.5J LASER BEAM SHOW PROMINENT ABSORPTION BY THE LASER-INDUCED TARGET VAPOR.*

64

$\dfrac{n^{-1}}{n_0^{-1}}$

8 μsec

R (cm)
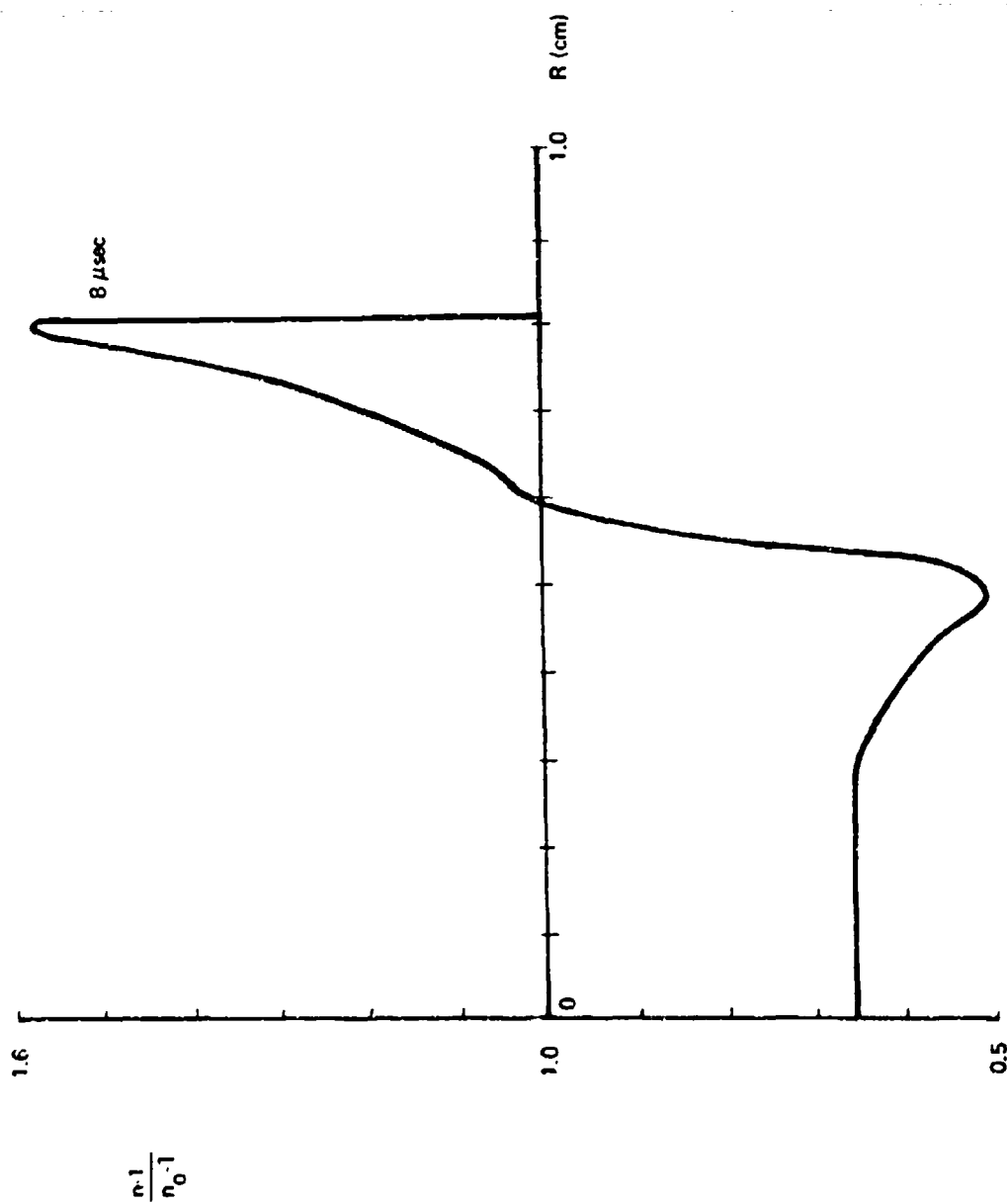
Figure 4.7: REFRACTIVE INDEX OF LASER-INDUCED TARGET VAPOR AND A SHOCK WAVE 8 MICROSECONDS AFTER ITS INITIATION AT A LUCITE TARGET BY A 7.5J LASER BEAM. THIS IS SHOWN AS A FUNCTION OF RADIUS FOR $\bar{Z}=.57CM$.

65

The above comments concerning the interpretation of interferometric data apply, as well, to the data on laser-supported detonation waves. In this case, however, the species are known to consist of singly ionized nitrogen, oxygen, and electrons since LSD wave properties are not dependent on the target material which originally ignited the wave. This can be seen by comparing the Mach-Zehnder interferograms of LSD waves ignited from a titanium target (figure 48) to those of figure 29 which show LSD waves ignited from an aluminum target. This series of interferograms is analyzed at a fixed distance of $\overline{z}$ = .32 cm, and the data is shown for the several instants of time in figure 49. The radial plots of $(n-1)/(n_o-1)$ seem to vary with time in a somewhat irregular manner. It is interesting to note the negative value of $(n-1)/(n_o-1)$ for the one microsecond curve which indicates an electronic contribution to the index of refraction. After this time, the inner region shows a low density similar to the previous aluminum data. This 1 microsecond data occurs, of course, near the peak power of the Marx Bank Laser intensity.

A comparison of the radial density profile of LSD waves ignited from both aluminum and titanium targets is shown in figure 50. These data are both taken at nearly equal distances behind the LSD front itself; however, the data are actually taken at different times and distances from the target. The aluminum data is taken from figure 34 at a distance $\overline{z}$ = 1.0 cm and at a time of 5μsec while the titanium data is from figure 48 at $\overline{z}$ = .73 cm and at a time of 4μsec. It is apparent from figure 50 that the target itself plays little role in the actual propagation of LSD waves. The target is important, however, in the ignition of the LSD wave where such properties as reflectivity and thermal conductivity play a large role.

All of the analyzed interferograms which have been previously presented show rather small compressions compared with what one would expect based solely on predictions of the shock conservation equations[26]. These radial shock wave velocities, V_R, as measured

66
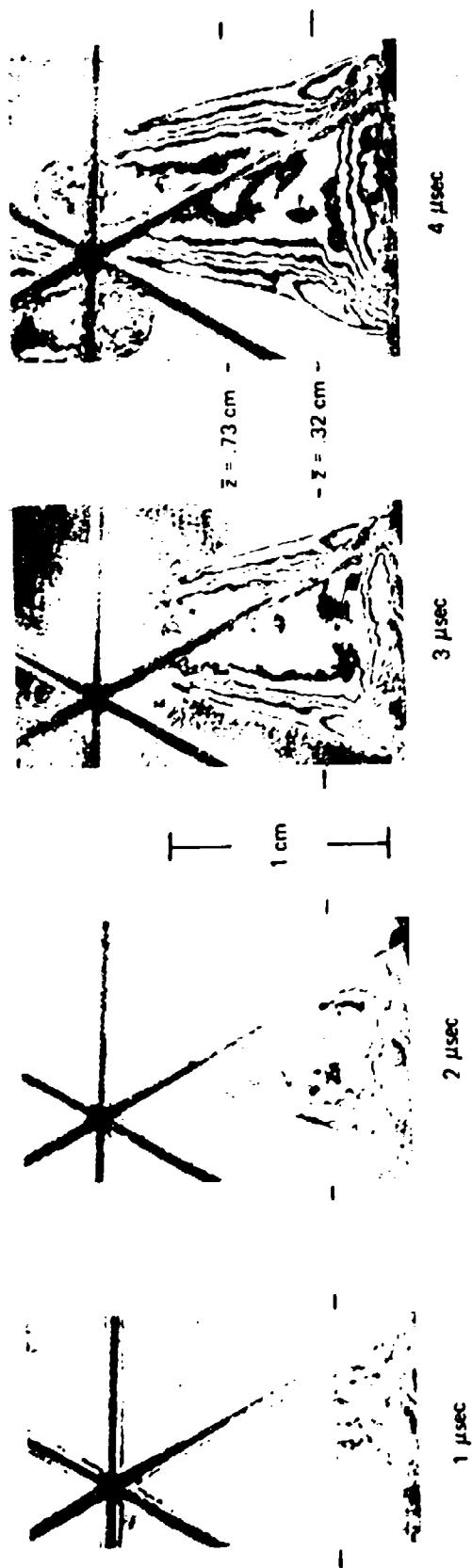
Figure 48: INTERFEROGRAMS SHOW THE GROWTH OF A LASER-SUPPORTED DETONATION WAVE IGNITED FROM A TITANIUM TARGET BY A 15J LASER BEAM.
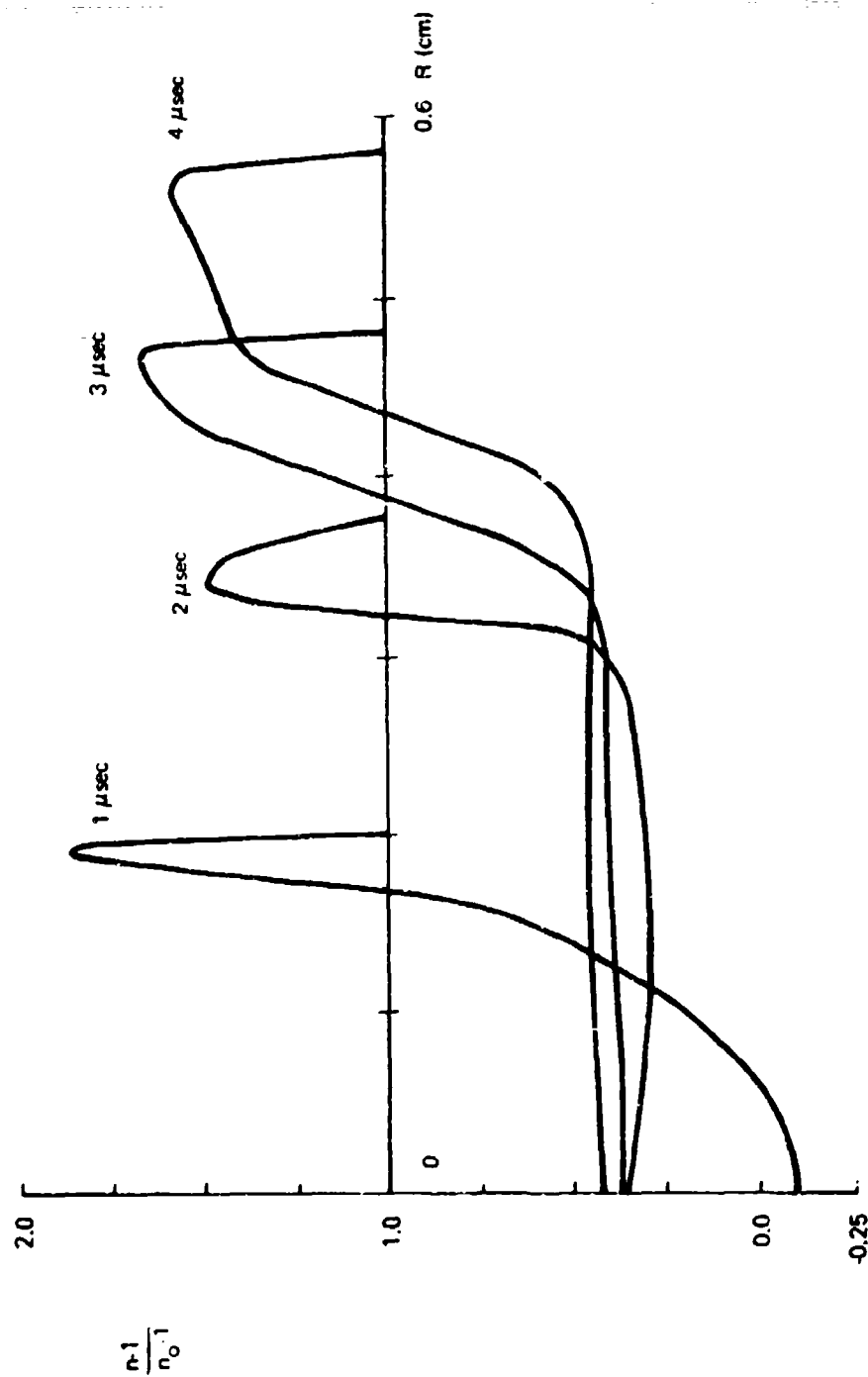
Figure 49: REFRACTIVE INDEX OF LASER-SUPPORTED DETONATION WAVES AT FOUR TIMES AFTER IGNITION AT A TITANIUM TARGET BY A 15J LASER BEAM. THESE ARE SHOWN AS FUNCTIONS OF RADIUS FOR $\bar{Z}=.32CM$.
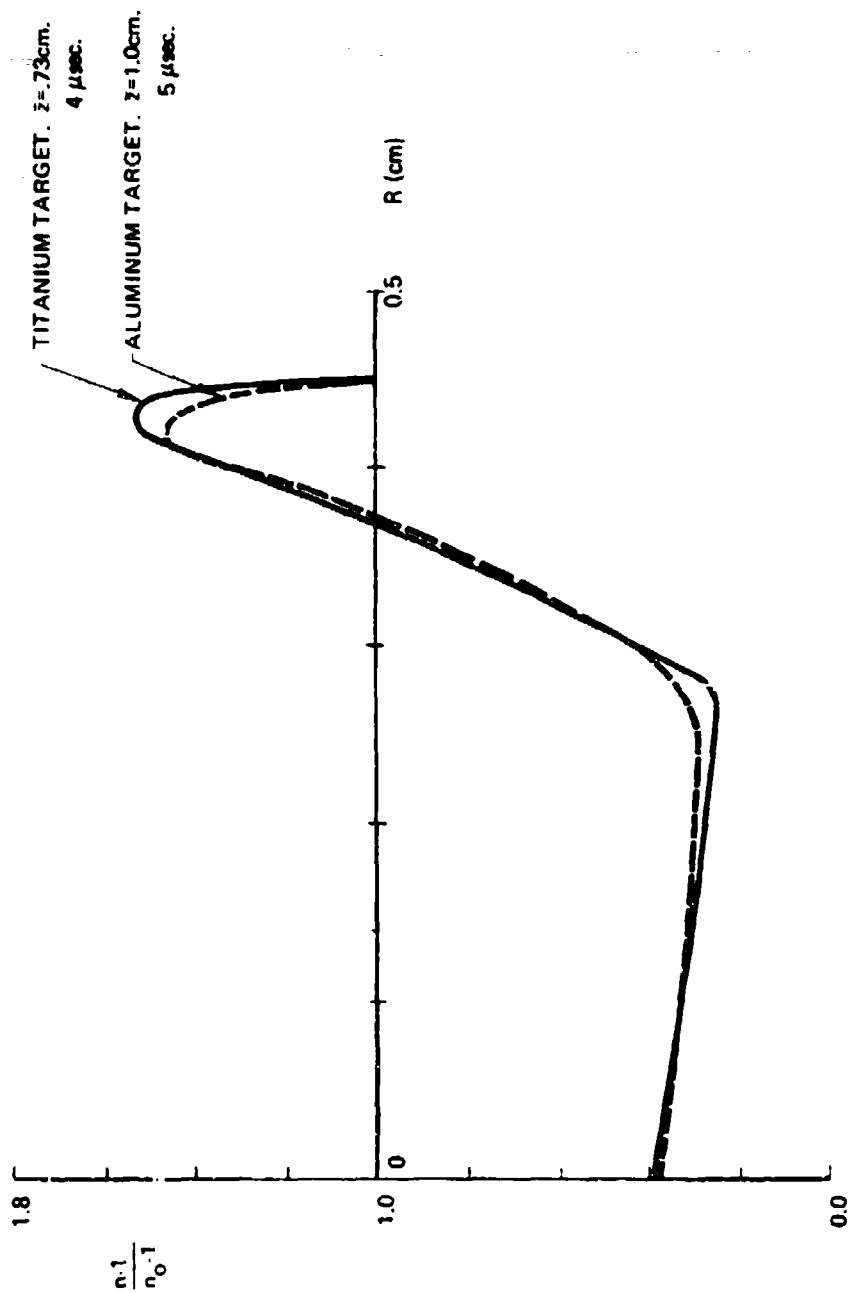
Figure 50: COMPARISON OF THE REFRACTIVE INDICES OF LASER-SUPPORTED DETONATION WAVES IGNITED AT TITANIUM AND ALUMINUM TARGETS BY A 15J LASER BEAM.

from the interferograms are related to the normal shock velocity
by $V_n = V_R \cos \theta$, where θ is the conical shock wave angle. One
can then compare theoretical mass densities based on the shock
conservation equation with the interferometric data. This is done
using the interferograms of figures 29, 31, and 32 where data is
analyzed at $\bar{z} = 1.0$ cm. The peak compression at the radial shock
waves are thus computed from measured radial expansion velocities.
Typically, the radial Mach number is $M \approx 3$ at a time of 5.5μsec.
In this way, the peak compression (ρ/ρ_o) is plotted versus time after
LSD wave ignition from an aluminum target. Figure 51 shows this
computation for $\gamma = 1.4$ and for $\gamma = 1.17$. It is evident that the
expected compressions of at least 4 are considerably greater than
those previously deduced from the Abel inversions of interferograms.
One possible explanation of this discrepancy is to assume that
there is an important electronic contribution to the refractive
index in the shock wavefront. An estimate of the electron density
required to cause this effect may be deduced from equations 9 and
10, which indicate the opposite contribution to the sign of the
refractive index. Thus, the measured fringe shift ΔF is actually
proportional to

$$\Delta F \approx n_o - 1 - \frac{\omega_p^2}{2\omega^2} \qquad (11)$$

while the reduced data has tacitly assumed a negligible electron
density. Assuming $\gamma = 1.4$ and using the data of figure 51, one
obtains

$$\rho/\rho_o = 3.5$$

at $t = 5.5$μsec. The maximum "compression" as measured in figure 41
is 1.35. The discrepancy between these two results can be resolved
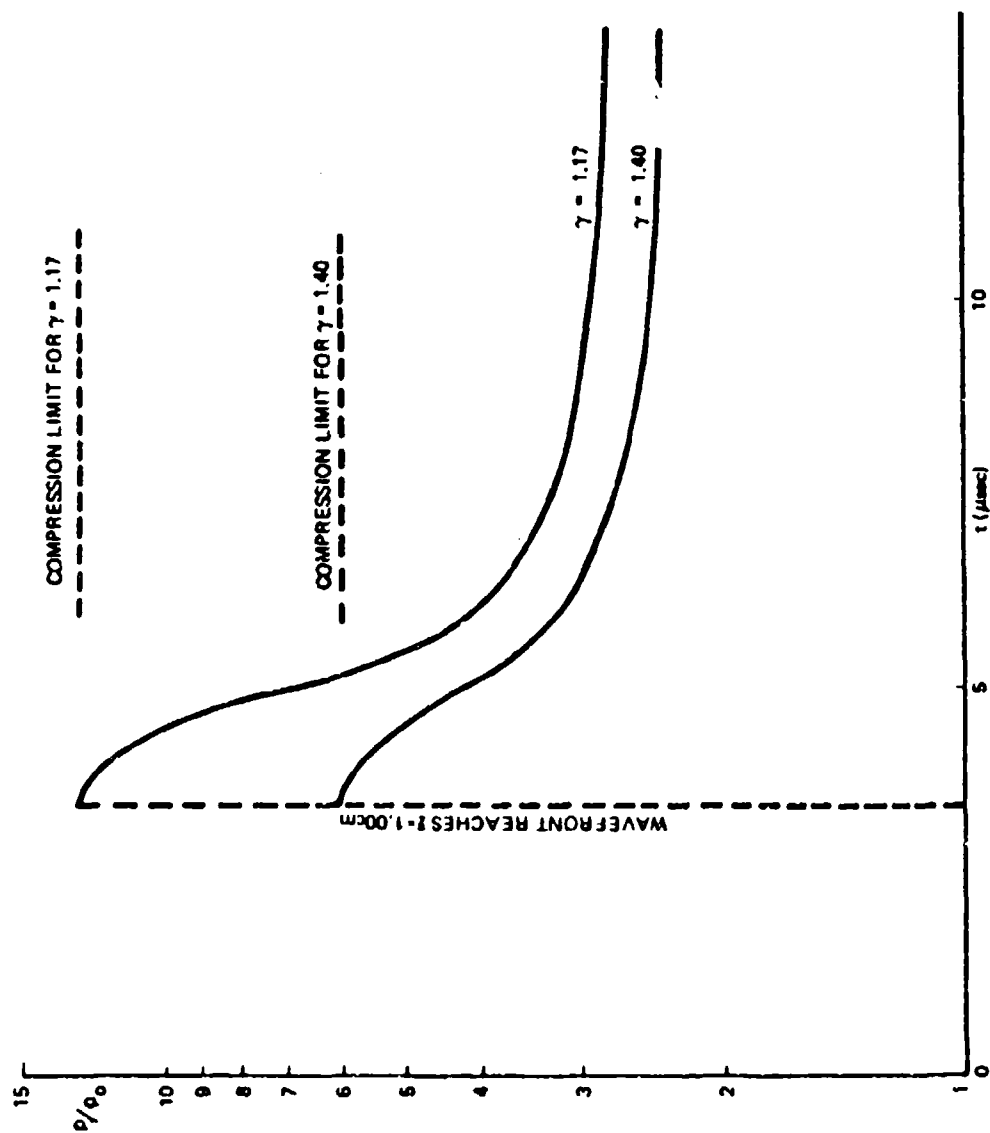
Figure 51: PEAK COMPRESSION CALCULATED FROM THE RADIAL VELOCITY AT $\bar{Z}=1.00CM$ OF A LASER-SUPPORTED DETONATION WAVE IGNITED AT AN ALUMINUM TARGET BY A 15J LASER BEAM. CURVES FOR TWO VALUES OF γ ARE SHOWN.

by assuming an electron density of $n_e = 2.8 \times 10^{18} cm^{-3}$. The
ionization under these conditions is approximately 2.8 percent.

At the later time of 11μsec and again referring to the results
of figure 51, one finds a calculated peak compression of 2.4 This
compression should be compared with the estimated data of figure 45
which indicates a compression of only 1.25. The apparent discrepancy
can again be resolved by assuming an ionization of 2.2 percent.
In this case, the electron density is $1.6 \times 10^{18} cm^{-3}$ and $(\omega_p^2/\omega^2) =$
6.9×10^{-4}.

3.2 TIME-RESOLVED INTERFEROMETRY

In addition to the interferograms previously discussed, which
have an overall view of the "event" at selected times, a Mach-Zehnder
interferometer was set up using a CW argon laser at a wavelength
of .488μ. The interference fringes along a line coaxial with the
high power CO_2 laser beam were followed to yield time-resolved
interferometry as first demonstrated by Basov[27]. When the fringe
shift can be followed across the shock front, (in some cases, there
are too many fringes and the photographic resolution is not good enough
to allow the   required counting) this fringe-profile or contour
map of the events' history can be analyzed in space and time to
determine the index of refraction.

A diagram of this interferometer is shown in figure 52. The
4880 Å beam from the argon laser has only about 0.1 watt, so careful
arrangements were needed to produce usable interferograms. After
initial "beam cleaning", a cylindrical mirror focused the beam to a
line focus in the region in front of the target. Slits near the
target and at several points in the following optical train reduced
extraneous light. Two prisms split and recombined the beams. The
event focus was in one arm where the CO_2 beam was incident on a
target. These prism elements and turning mirrors were adjusted to
product straight fringes which were perpendicular to the line focus.
After recombination, a narrow-band 4880 Å filter eliminated the unwanted
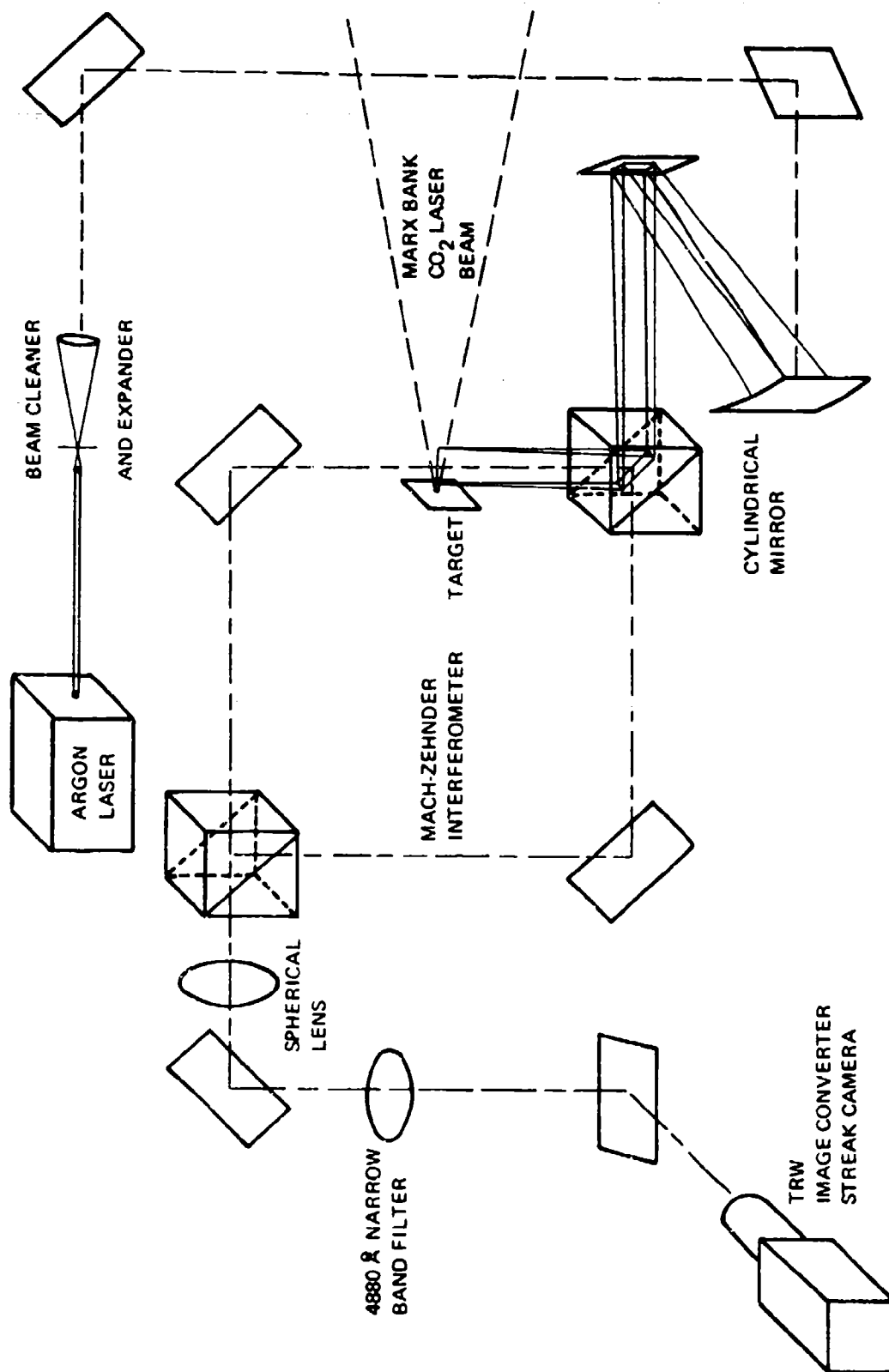
Figure 52: TIME-RESOLVED INTERFEROMETER FOR INVESTIGATIONS OF LASER-PRODUCED BLAST WAVES AND LASER-SUPPORTED DETONATION WAVES.

73

LSD light from the event. A spherical lens focused the interference pattern into a line on the image converter tube face. The TRW camera operated in its normal streak mode to sweep the interference pattern over a time interval of 10μsec. An approximate estimate of the fractional density change can be obtained from the interferograms by using equation 9 to obtain $\Delta\rho/\rho_0 \cong .8\Delta F$.

Even with great care, the fringe shift at the LSD wavefront was sufficiently large that we could not count the fringe shift. As a minimum, however, we found at least +2 fringes (and probably much greater). Part of this problem is caused by both refraction and absorption of the 4880 Å laser beam by the high-density gas at the LSD wavefront. This effect can be seen by observations made by blocking one arm of the interferometer which leads to a form of shadowgram. Following the large positive fringe shift occurring at the front of the LSD wave, one observes a negative fringe shift observable in figure 53 for a laser energy of 6 joules. At later times, slower waves traveling near Mach 1 can be seen, which probably result from target material vaporization or gas desorption from the target.

By making a series of interferograms which cover 40 microseconds, one can observe a third wavefront which is very slow (Mach number .5) and initially appears about 25 microseconds after ignition of the LSD wave (figure 54). In addition to LSD wave ignition, these targets show interesting effects at laser intensities below LSD wave threshold. When laser intensity is high, (7.5 joules) LSD waves ignited from alumina look the same as those ignited from aluminum or other metallic targets as seen in figure 55. The transition $B \rightarrow X/0>0$ of aluminum oxide (AlO)[28] at 4842 Å is sufficiently near the 4880 Å wavelength of the argon laser to be a good absorber of the interferometer beam. Below intensities for LSD wave ignition, the vapor comes off with a velocity which increases as laser intensity increases up to about Mach 1. In this range of velocities, absorption

LASER BEAM →

TIME
(μsec)

DISTANCE (cm)
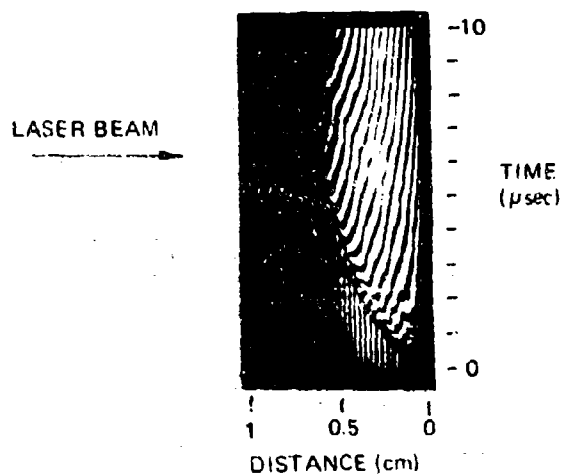
Figure 53: **TYPICAL TIME-RESOLVED INTERFEROGRAM OF THE LONGITUDINAL AXIS OF A LASER-SUPPORTED DETONATION WAVE IGNITED AT AN ALUMINUM TARGET.**

LASER BEAM →

TIME
(μsec)

-10

1	0.5	0

DISTANCE (cm)
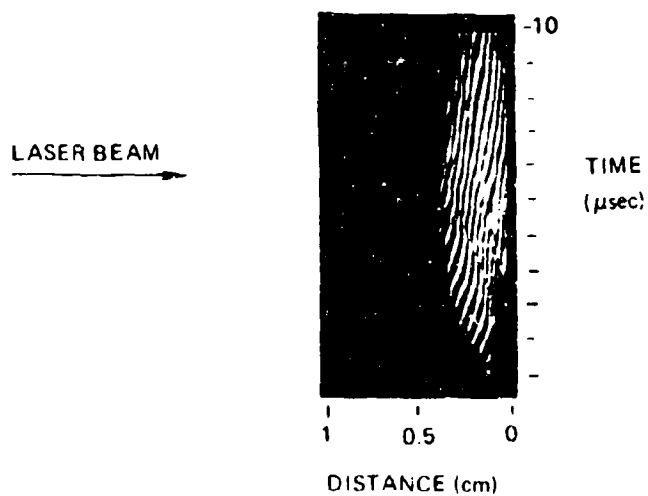
Figure 55: *TIME-RESOLVED INTERFEROGRAM OF THE LONGITUDINAL AXIS OF A LASER-SUPPORTED DETONATION WAVE IGNITED AT AN ALUMINA TARGET BY A 7.5J LASER BEAM.*

77

of the 4880 Å wavelength becomes progressively stronger, however, above Mach 1 the air shock wave and vapor front begin to separate with the vapor velocity now just under Mach 1 when the air shock speed reaches Mach 1.3. Under these conditions, the fringe pattern indicates first a positive density increase at the front of $\Delta\rho/\rho$ = +1.3 followed a short time later by a negative fringe shift of $\Delta\rho/\rho$ = -1.7. This behavior is seen in figure 56a which also indicates that velocity of the vaporized material slows down as it moves farther and farther from the target surface.

When the CO_2 laser intensity is increased so that the vapor front velocity reaches Mach 2, a maximum volume of vapor appears to be produced. This vapor reaches out to about 4 mm from the target surface and then recedes as shown in figure 56b. As the shock velocity reaches Mach 3, the vapor appears only out to 1 mm and lasts for only 2 microseconds. At full intensity, a shock velocity of Mach 10 is reached and no vapor effect is seen. The data from a series of such time-resolved interferograms taken with increasing energy is shown in figure 57. Each curve is taken at a different laser energy normalized such that q_o represents 17 joules of delivered energy and also the highest available laser intensity. As mentioned above, at this peak intensity of approximately 5.3×10^7 watts/cm^2, LSD waves are always ignited and no target vapor is observed. All the curves shown in figure 57 are at lower intensities where significant vaporization occurs and show the outer boundary of the absorbing AlO vapor. The density of the vapor must be high since the boundary is very distinct and the absorption over the 2-3 mm path is as much as 90 percent. It appears that the vapor boundary begins to recede when a LSD wave is ignited and this LSD wave then shields the target surface from the CO_2 beam energy and the target surface then cools.

As the LSD wave moves away from the target surface, it sees lower laser beam intensity because of the focused condition of the beam and because the CO_2 laser power decreases after the initial peak

LASER BEAM →

TIME
(μsec)

— 10
—
—
—
—
—
—
—
—
— 0

| | | |
1   0.5   0
DISTANCE (cm)
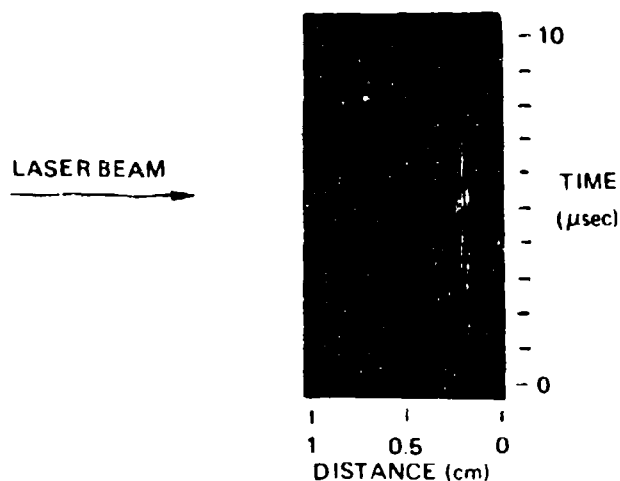
Figure 56a: *TIME-RESOLVED INTERFEROGRAM OF THE LONGITUDINAL AXIS OF LASER-INDUCED TARGET VAPOR AND A PRESSURE WAVE DEVELOPED AT AN ALUMINA TARGET BY A 1.5J LASER BEAM. A IO ABSORPTION IS SEEN AFTER THE WAVEFRONT PASSES.*

LASER BEAM →

TIME
(μsec)

— 10
—
—
—
—
—
—
—
—
— 0

| | | |
1   0.5   0
DISTANCE (cm)
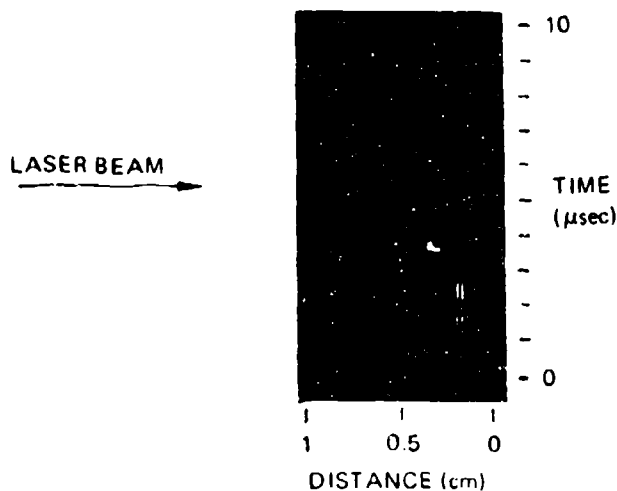
Figure 56b: *TIME-RESOLVED INTERFEROGRAM OF THE LONGITUDINAL AXIS OF A LASER SUPPORTED ABSORPTION WAVE NEAR ITS IGNITION THRESHOLD WHICH WAS IGNITED AT AN ALUMINA TARGET BY A 3.75J LASER BEAM. A IO ABSORPTION IS SEEN AFTER THE WAVEFRONT WITH A BOUNDARY WHICH SHOWS THE MAXIMUM EXTENT OF A IO AS A FUNCTION OF TIME.*
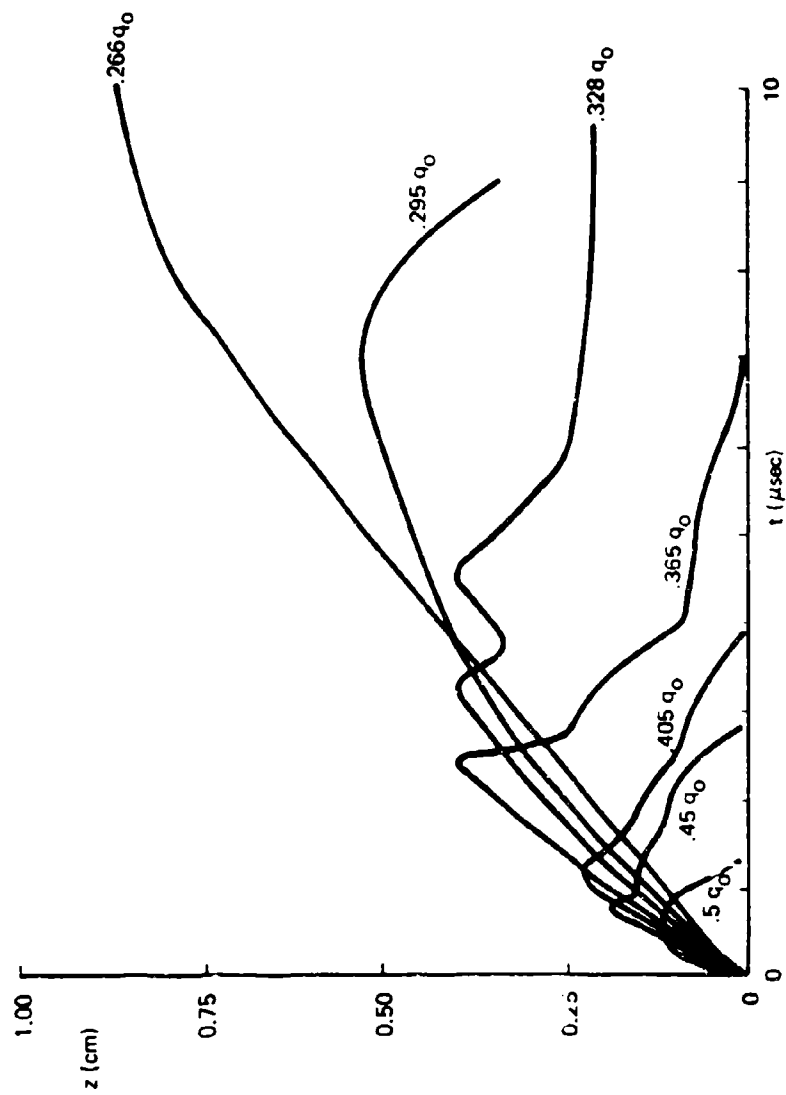
Figure 57: *ALUMINA TARGET ABSORBING VAPOR BOUNDARY*

at 0.5μsec and again after the second peak at 3.1μsec. As a
consequence, the LSD wavefront is initially very narrow but widens
as intensity drops. When the absorption boundary slows down appreciably,
the LSD absorption length becomes increasingly greater and appears
from optical data as a wave traveling toward the target surface.
(See Section II and IV for additional details.) At the front of this
wave, AlO is dissociated and can no longer absorb at 4880 $\overset{o}{A}$. At late
times when the AlO recombines, its density is low because of diffusion
away from the target and little absorption occurs.

Silica is another absorbing target whose vapor, however, does
not absorb at 4880 $\overset{o}{A}$. For a full laser intensity of 17 joules,
fractional density changes of $|\Delta\rho/\rho| \approx 4$ occur with vapor induced
shock velocities of Mach 5. From data such as given in figure 58,
it can be seen that for the shock wave (or wavefront) velocities
greater than Mach 1, an additional slower wavefront also exists
which is probably the target vapor. At very low incident laser
energies of approximately 1 joule, it is relatively easy and
unambiguous to follow these fringe paths.

3.3 ABEL INVERSION AND DETERMINATION OF THE RADIAL VARIATION OF THE INDEX OF REFRACTION

The fringe patterns discussed previously require mathematical
processing[29] in order to obtain the actual variation with radial
position. This occurs because the optical path through the laser-
supported detonation waves samples a continuum of radial positions
on its path through the plasma.

The observed fringe shift as dependent on the linear observed
distance x is dependent on an integral of the form

$$N(x) = 2 \int_{x}^{r_o} \frac{n(r)r\ dr}{\sqrt{r^2 - x^2}} \tag{12}$$

0.84J

1.23J

1.37J

1.52J
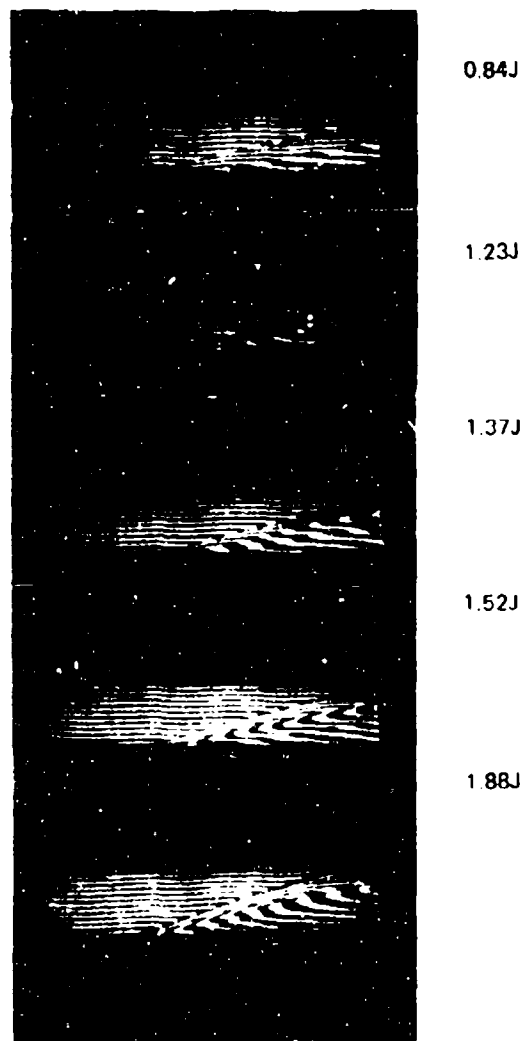
1.88J

Figure 58: TIME-RESOLVED INTERFEROGRAMS SHOWING THE CHANGES IN THE LASER INDUCED TARGET VAPOR AND IN THE PRESSURE WAVES DEVELOPED AT A SILICA TARGET BY LASER BEAMS WHOSE ENERGIES VARIED FROM 0.84J TO 1.88J.

which has the inversion

$$n(r) = -\frac{1}{\pi}\int_r^{r_o} \frac{N^1(x)\, dx}{\sqrt{x^2-r^2}} \qquad (13)$$

In equation 12, $N(x)$ is the phase shift of the interferometer beam at a distance x from the origin of a cylindrically symmetric disturbance of maximum radius r_o. The radial dependence of the index of refraction is $n(r)$ and the derivative of the measured fringe shift in the x direction is $N^1(x)$.

Our data have been analyzed by a numerical technique derived in reference 29 which requires evenly spaced input data. This is necessary since tables of coefficients are used which minimize error. The actual data derived from the interferograms is not evenly spaced, however, and we have obtained such data by fitting piece-wise, cubic curves to the data points and the interpolating to the required evenly spaced data points. These data points were then utilized in the numerical inversion routine along with estimated data points at maxima.

A test case was devised in order to test the computer program in which the gas in a cylinder of radius .5 cm was originally uniform and at atmospheric pressure. This gas was then redistributed to the following density profile

$$\left. \begin{array}{l} \rho/\rho_o = .19 \text{ for } o<r<.4 \text{ cm} \\[2em] \rho/\rho_o = 1.85 \text{ for } .4<r<.5 \text{ cm} \end{array} \right\} \qquad (14)$$

This step function was then used to calculate the fringe shift ΔF as a function of the viewing coordinate x.

$$\Delta F = \left[\frac{3.4}{\lambda} \sqrt{.25-x^2} - \frac{6.64}{\lambda} \sqrt{.16-x^2}\right] (n_o-1) \qquad 0<x<.4cm$$

$$\Delta F = \frac{3.4}{\lambda} \sqrt{.25-x^2} \quad (n_o-1) \qquad\qquad\qquad .4<x<.5cm \qquad (15)$$

$$\Delta F = 0 \qquad\qquad\qquad\qquad\qquad\qquad\qquad x>.5cm$$

This exact fringe shift variation is shown in figure 59 as a function of x for $(n_o-1) = 2.9 \times 10^{-4}$ (corresponding to air). This fringe shift variation was then numerically re-inverted using the computer program to obtain $\Delta\rho/\rho$, the fractional density change as a function of radius which is shown in figure 60. The agreement with the assumed densities is very good, except near the density step. Twice as many points per division are used for the outer one-quarter of the radius and this procedure was followed for all the inversions.
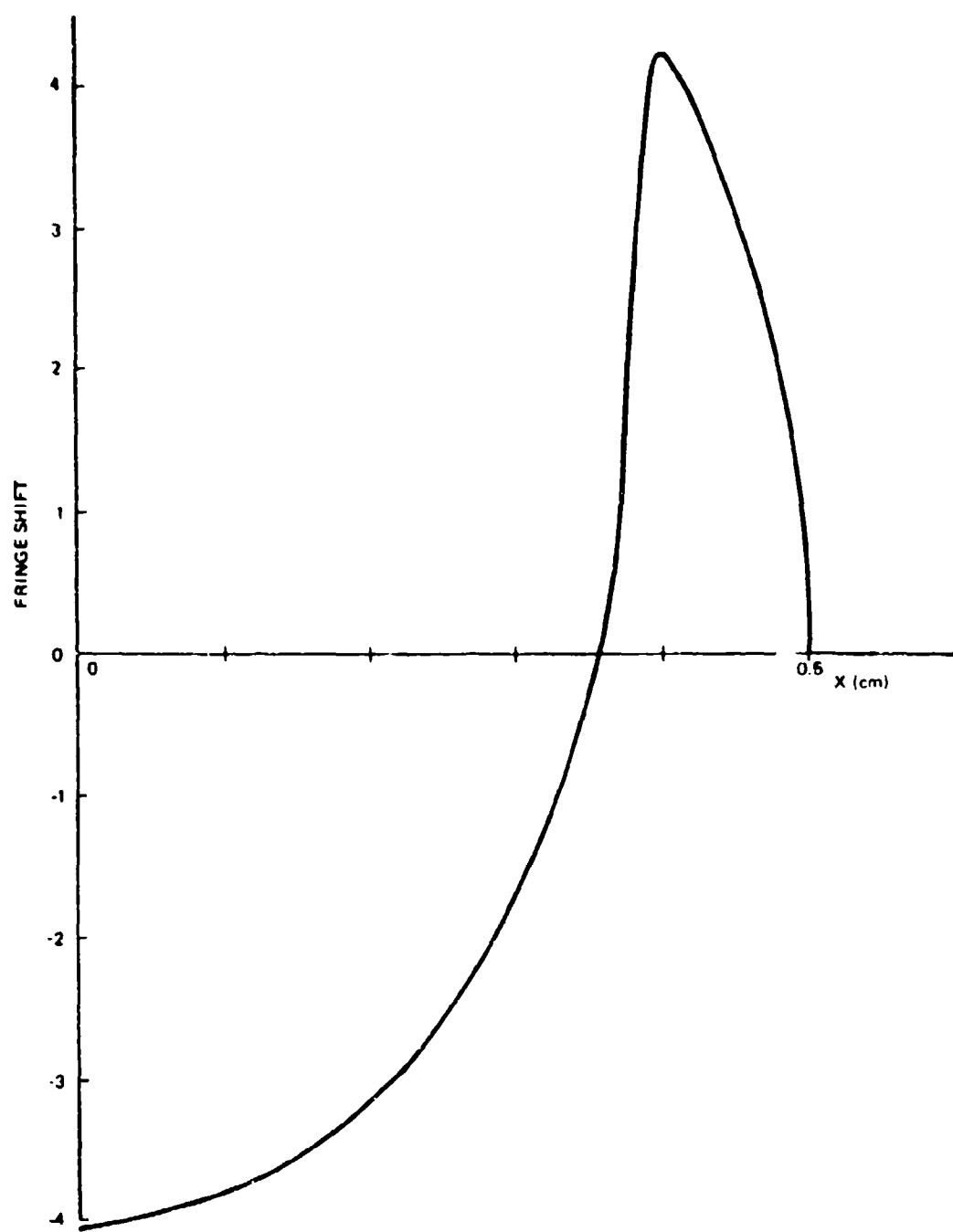
Figure   59: *CALCULATED FRINGE SHIFT ABEL INVERSION TEST CASE*
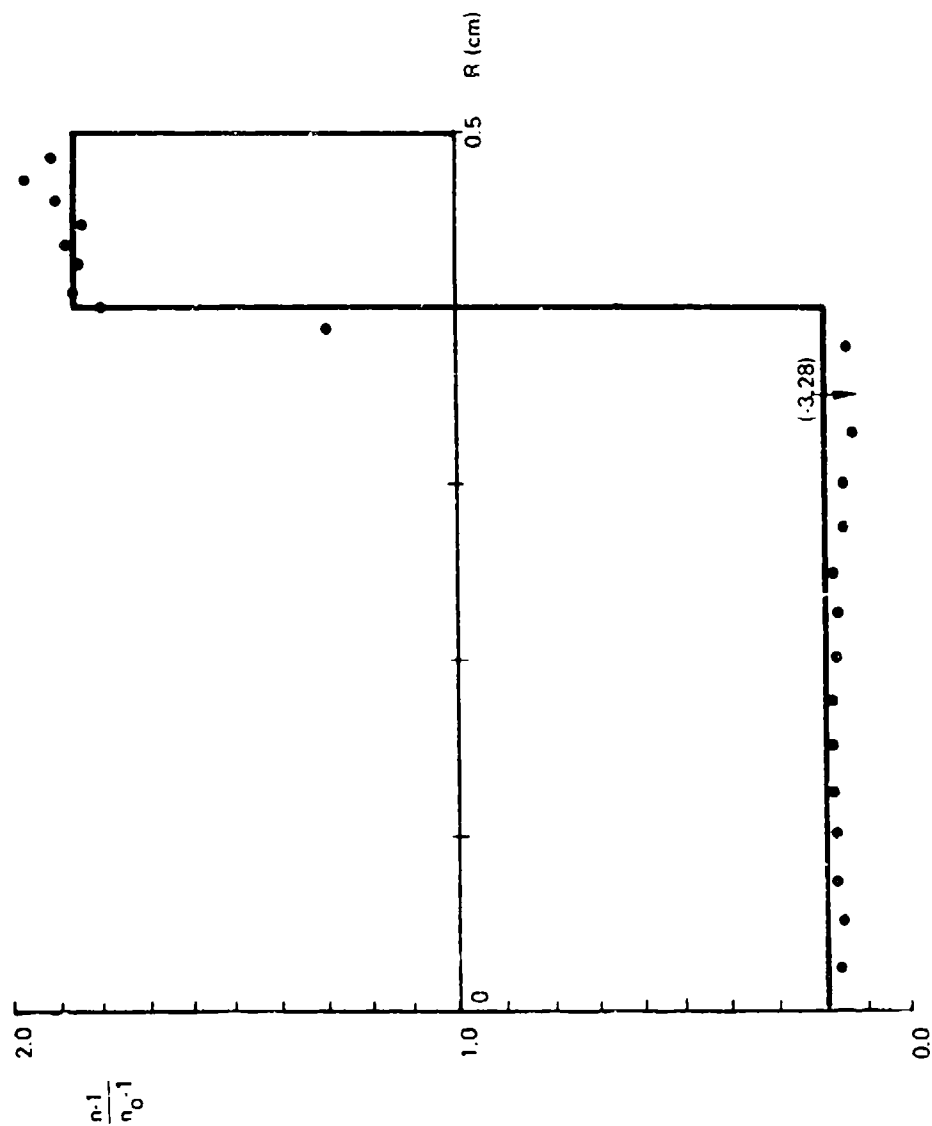
Figure 60: COMPARISON OF ABEL INVERSION WITH ASSUMED REFRACTIVE INDEX FOR TEST CASE

SECTION IV

SPECTROSCOPIC STUDIES OF LASER-SUPPORTED ABSORPTION WAVES

Light emissions from laser-supported absorption waves ignited by the 10.6 micron CO_2 laser pulse at several kinds of solid surfaces have been studied by both time-integrated and time-resolved spectroscopic techniques. The time-integrated emission spectra are taken with a quartz prism spectrograph (Hilger-Watts) which is of good resolution in the near ultraviolet. Identification of species is done with the help of standard reference books[30,31,32]. The time-resolved spectra of low resolution in the visible are taken with a transmission spectrograph (TRW 42A) and an image converter camera (TRW ID). A correlation with the time-integrated spectrum yields information concerning the time variation of the strong emission lines.

A schematic for the time-resolved experiments is shown in figure 61. A moveable mercury lamp is used for both distance and spectral calibrations. For the time-integrated experiments, the quartz spectrograph is used instead of the transmission spectrograph. The wavelength scales of the spectra are calibrated with reference lights of hydrogen, helium as well as mercury. The dispersions found for the two spectrographs are summarized in Table 1.

Table 1

Dispersion of Spectroscopic Instruments

Wavelength ($\overset{o}{A}$)	Dispersions ($\overset{o}{A}$/mm)	
	Hilger-Watts	TRW 42A
2000	4.1	---
2500	8.5	---
3000	15	---
3500	24	---
4000	35	129
5000	65	144
6000	105	157
7000	155	---
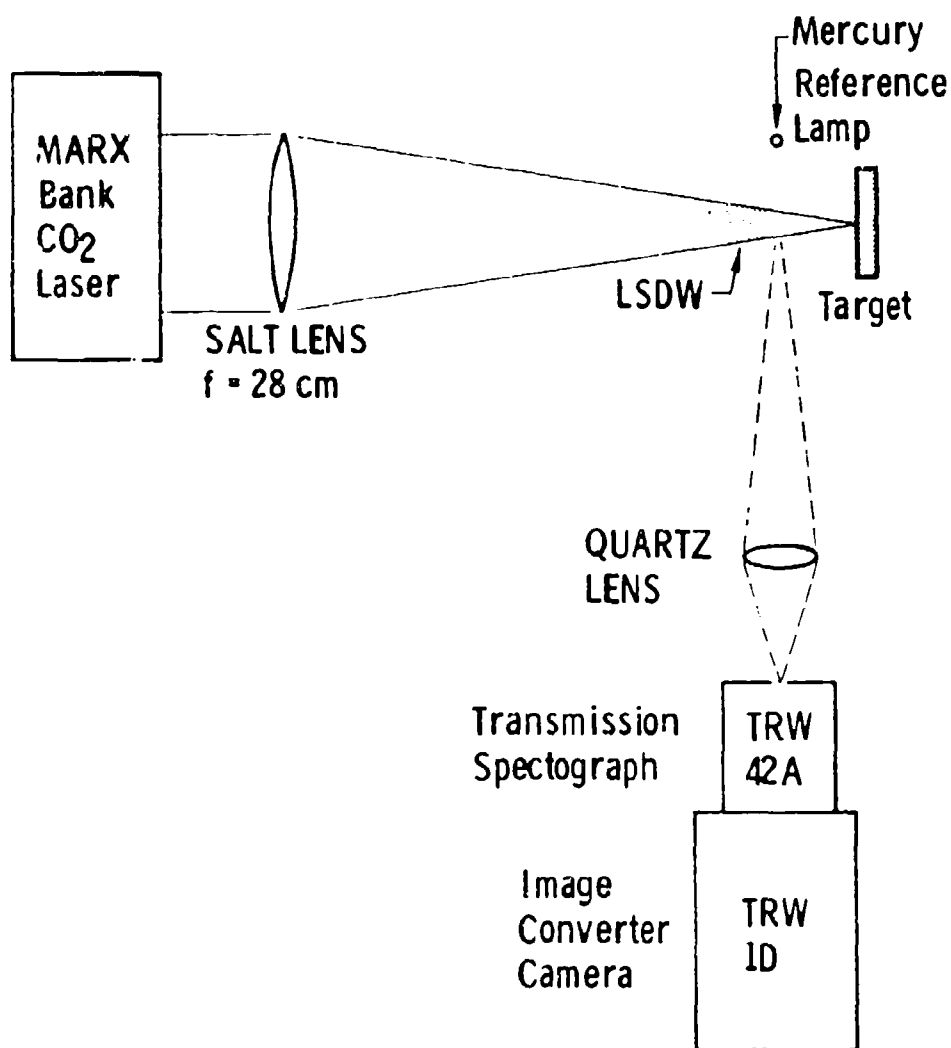
Figure 61   Schematic   for the time-resolved spectroscopic study of laser supported absorption waves.

Two types of absorption waves have been studied so far. They are:

(a) The laser-supported detonation wave which travels towards the laser light source at a supersonic speed and consists mainly of N^+, O^+ and a small fraction of N^{++} and O^{++}; and

(b) The laser-supported blast wave which travels along the outward surface normal of the target at a slower speed and consists mainly of molecular and atomic species derived from the target materials.

In addition to the experimental studies, a theoretical calculation of the equilibrium composition of air has been carried out. The temperature and the electron density in the LSD waves are estimated to be greater than $25,000°K$ and 1.5×10^{17} per cm^3, respectively. Details of the results and analyses are presented below.

4.1 TIME INTEGRATED SPECTRA

Emission spectra of laser supported absorption waves generated from targets of aluminum, copper, nickel, tungsten, soda glass, Teflon, masking tape, boron nitride, alumina and others are recorded with spectroscopic plates (Kodak type 1-F and 1-O). The intensity versus wavelength trace is obtained by using a microdensitometer. Some preliminary results have been described in an earlier paper[33]. We note that the preliminary experiments have been performed with the axis of the spectrograph arbitrarily located at $30°$ from the axis of the laser beam. The spectra obtained at $30°$ (the next five figures) are of a greater light intensity but otherwise not much different from those obtained at $90°$ (the remaining figures in this section).

Figure 62 shows a section of the spectrum in the range from 2280 to 2620 $\overset{o}{A}$ obtained from an aluminum target with a 7-joule pulse. The carbon lines at 2296.9 and 2478.6 $\overset{o}{A}$ establish the wavelength
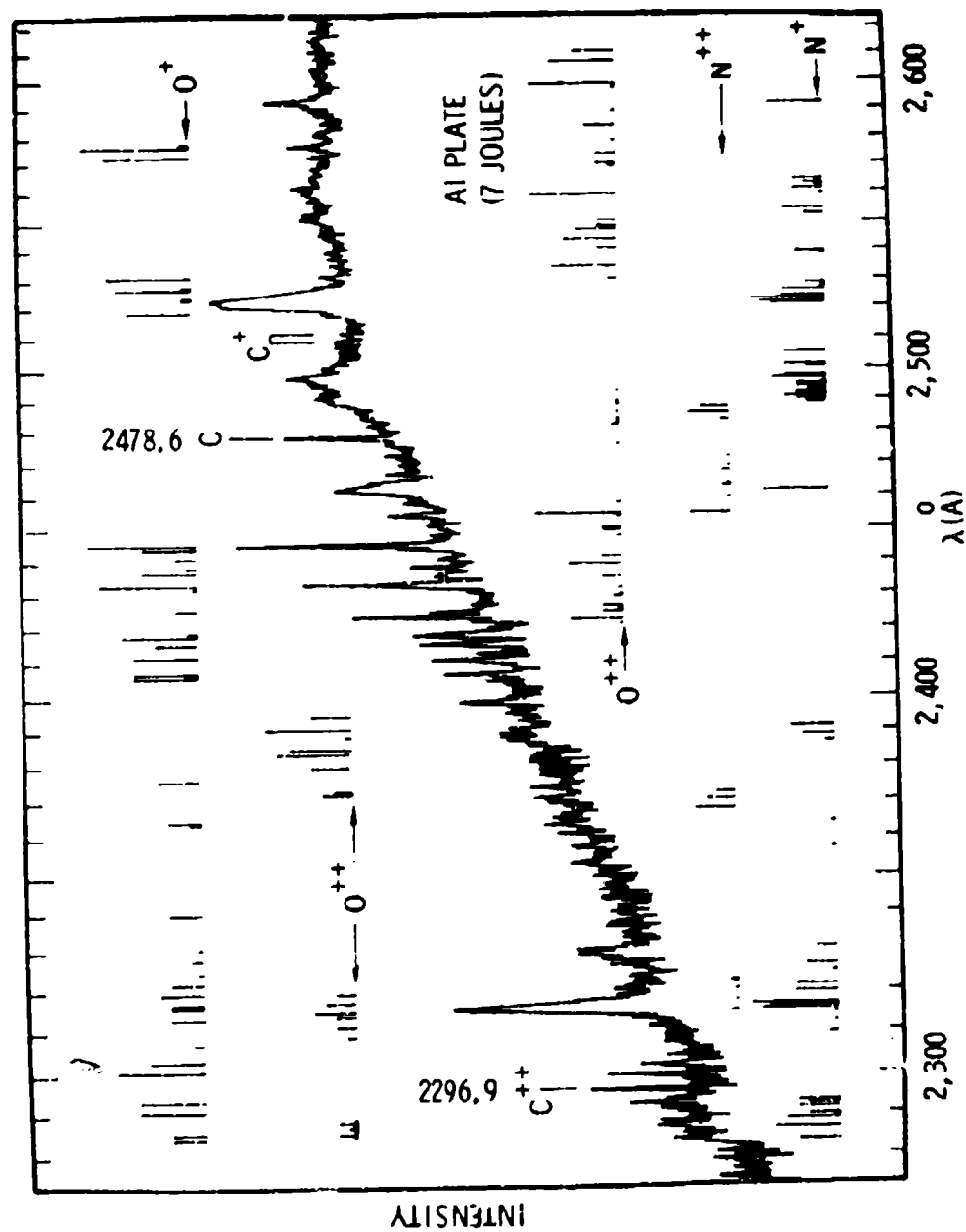
Figure 62   A section of the emission spectrum of an LSD wave generated from an aluminum plate.

scale. The vertical lines in the figure designate the wavelength and intensity of all possible emission lines of N^+, O^+, N^{++} and O^{++} (obtained from a condensed electric spark through air) as listed in Striganov[30]. It is apparent that a large part of the spectrum can be identified as due to N^+ and O^+, while a small part can be attributed to N^{++} and O^{++}. We have searched for neutral atomic and diatomic species of air but have failed to find them. The small amount of carbon present in the spectrum may be either due to evaporation of the absorbed layer on the surface or due to some carbon-containing materials in air.

Figure 63 shows a section of the spectrum obtained from a masking tape target in which a hole is burned through the tape for each shot. Comparing with figure 62, we see that the carbon lines are more prominent whereas the N^+ and O^+ lines are slightly weaker in figure 63. Other features in the spectrum include emission lines of Mg (2852.1 $\overset{o}{A}$), Mg^+ (2795.5 and 2802.7 $\overset{o}{A}$), the CN violet band system (B→A, with 0, 0 at 3883.4 $\overset{o}{A}$), etc. We note that the spectrograph is aligned such that light emission from species derived from target materials illuminates the entire slit. In contrast, the N^+, O^+, C^+ and C^{++} lines illuminate only a fraction of the slit. It appears that some carbon evaporated from the surface during the initial stage of laser irradiation is heated by the LSD wave.

Figure 64 shows a section of the emission spectrum in the range from 2400 to 2700 $\overset{o}{A}$ obtained from a soda glass target. In addition to the N^+ and O^+ lines from the LSD wave, emission lines from the target materials such as Na and Si are very prominent. (The sodium D-lines at 5890 and 5896 $\overset{o}{A}$ are observed to a distance as far as 1.5 cm from the target.) Of special interest is the Si^{++} line at 2541.8 $\overset{o}{A}$ which illuminates only a fraction of the slit similar to the behavior of C^+ and C^{++} discussed above. It is likely that some silicon evaporated from the surface during the initial stage of
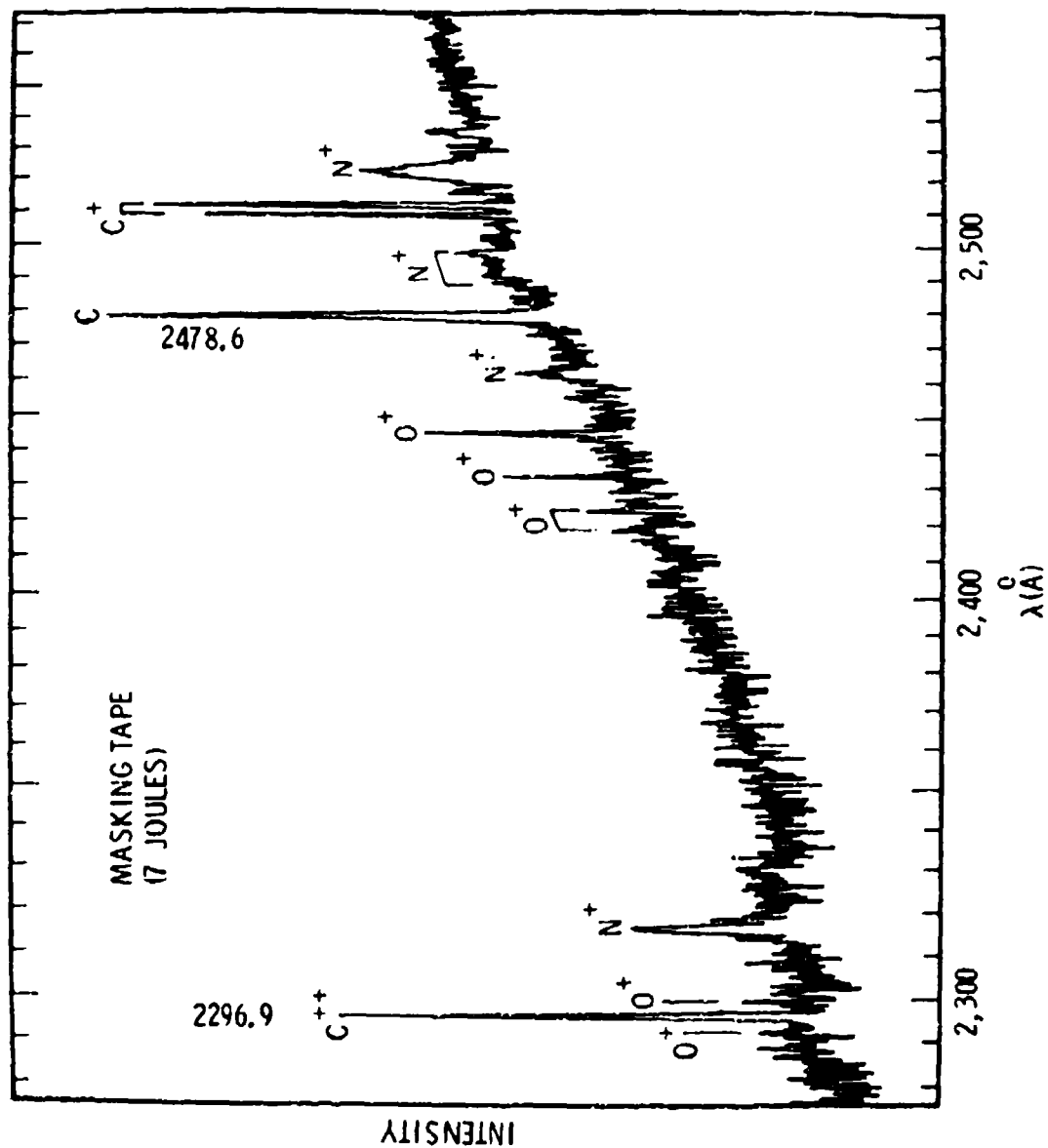
Figure 63   A section of the emission spectrum of an LSD wave generated from a masking tape target.
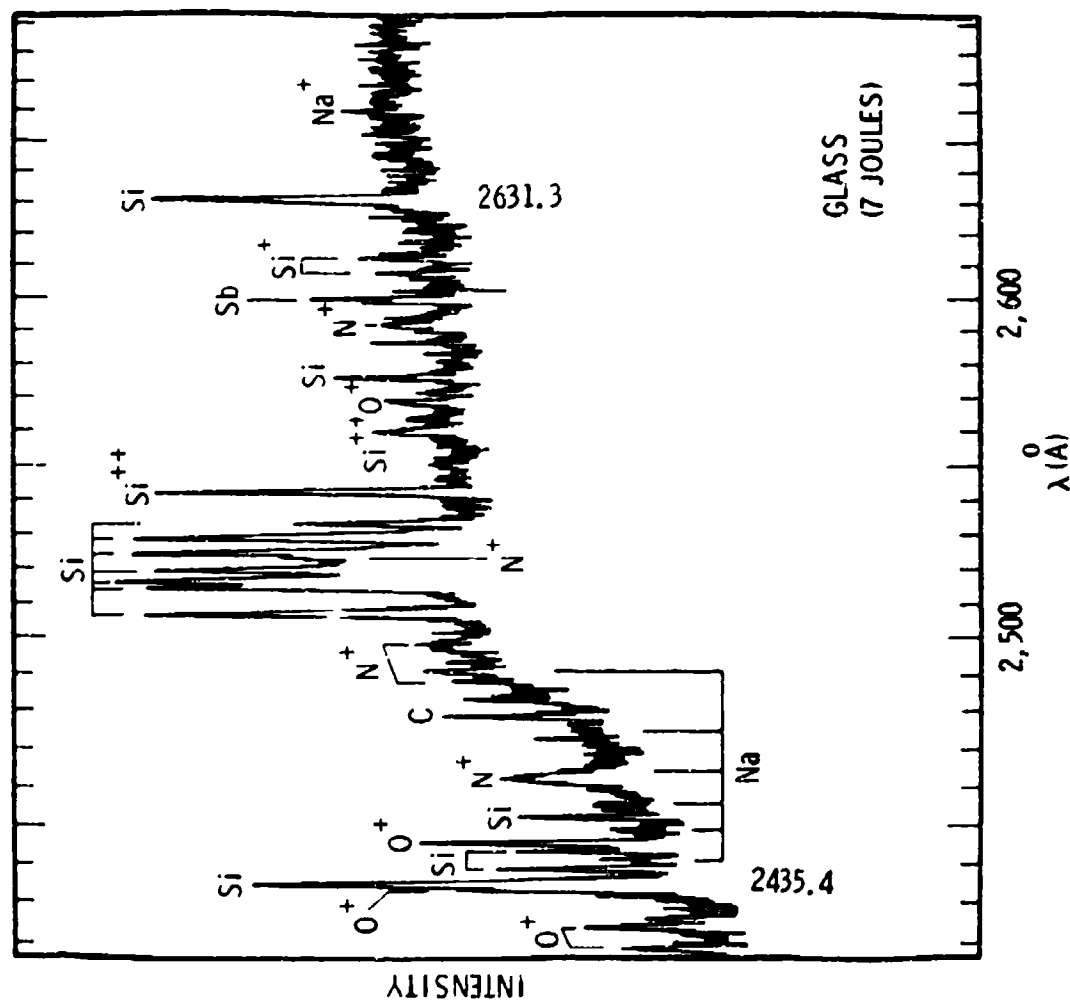
Figure 64   A section of the emission spectrum of an LSD wave generated
from a soda glass target.
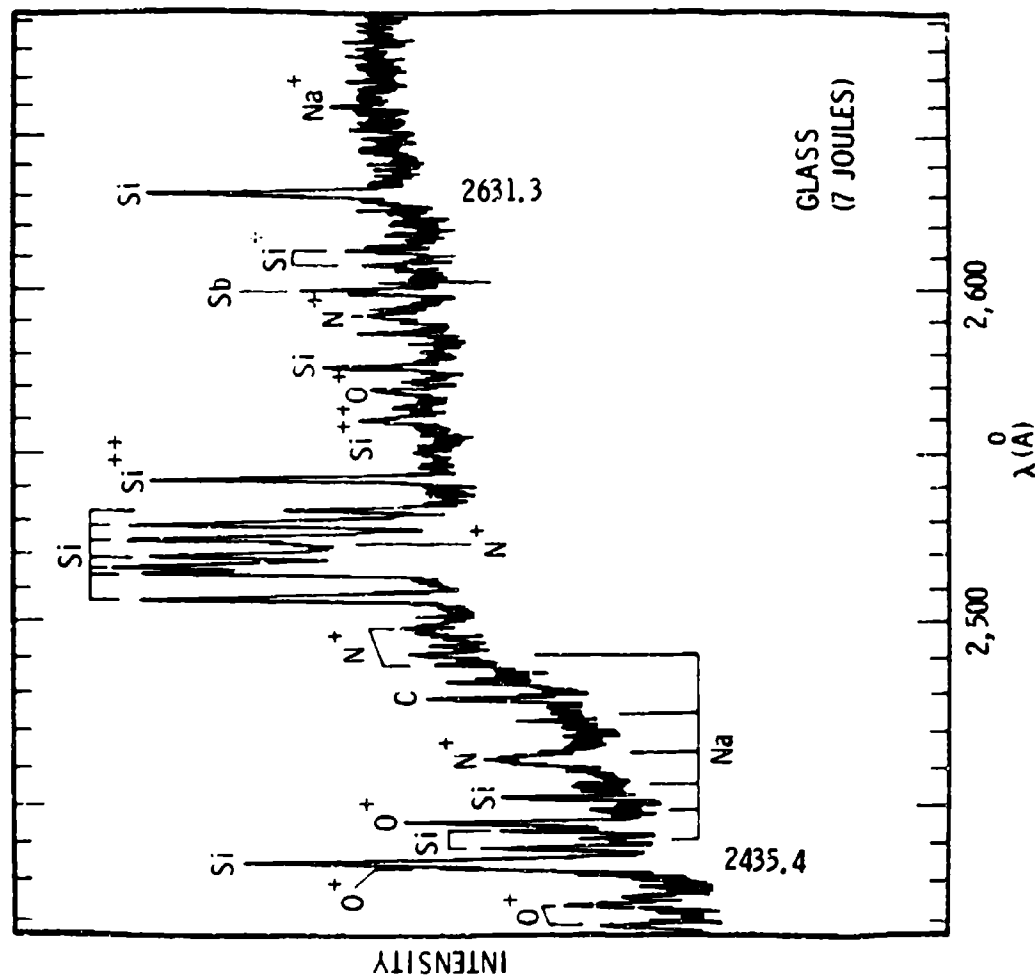
Figure 64   A section of the emission spectrum of an LSD wave generated from a soda glass target.

laser irradiation is heated by the LSD wave.

Under certain conditions, the laser irradiation on a target
surface does not generate a detonation wave but a blast wave. The
emission spectrum in the latter case consists mainly of bands from
molecules at a much lower temperature (probably in the range from
3000° to $4000^{\circ}K$ as observed in a flame).

Figure 65 shows the spectrum from an aluminum-black target
(which is very heavily anodized aluminum). The atomic lines
of Al and Na served to establish the wavelength scale. A well
developed band system is attributed to the AlO (B→X) transition.[32]
The Kodak 1-F plate is sensitive for wavelength shorter than 7000 $\overset{o}{A}$.

Figure 66 shows the emission spectrum from a boron nitride
target. Calcium is found to be a major impurity in the target.
A series of waves of bands with maxima designated by arrows can be
identified as the triatomic molecule BO_2[32]. Note the LSD waves
have been generated with these strongly absorbing targets at high
laser energies.

Emission spectra have also been taken with the spectrograph
located at $90^{\cup}$ from the laser beam. Figures 67, 68 and 69 show
three sections of the spectrum of an LSD wave generated with a 15-
joule pulse and looking at 7 mm in front of an aluminum target plate.
All possible lines of N^+, O^+, N^{++} and O^{++} from the reference book
by Striganov and Sventitskii[30] are designated. The arrows at the
bottom of figures 68 and 69 indicate the strong lines which show
up in the time-resolved spectrum. The four sections of the LSD
wave spectrum presented in figures 62, 67, 68 and 69 are typical for
all metallic targets which reflect the 10.6μ light. Even for an
absorbing target, the same spectrum persists provided the laser pulse
energy is much above the threshold for the generation of an LSD
wave.
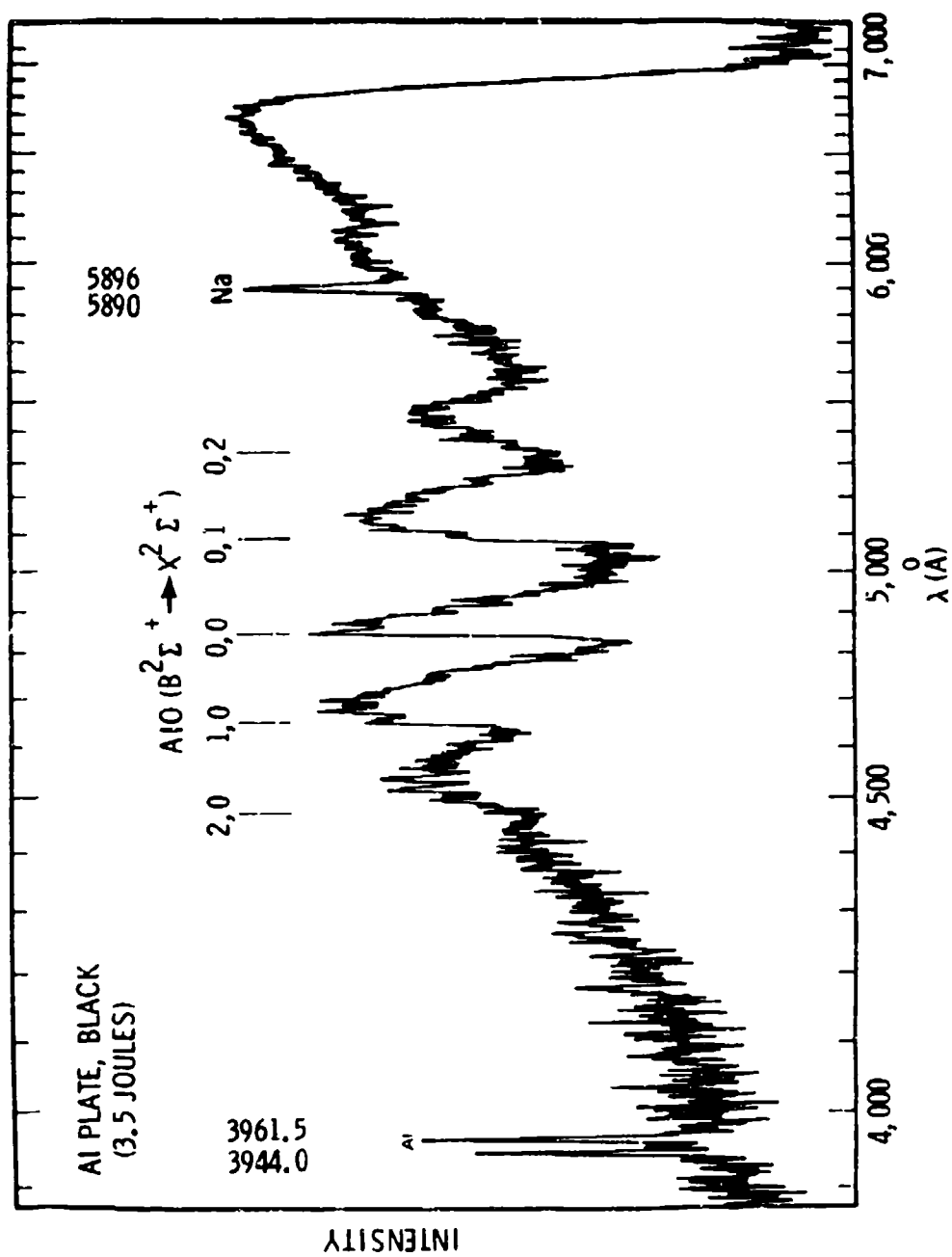
Figure 65   Emission spectrum of an LSB wave generated from an aluminum-black target.
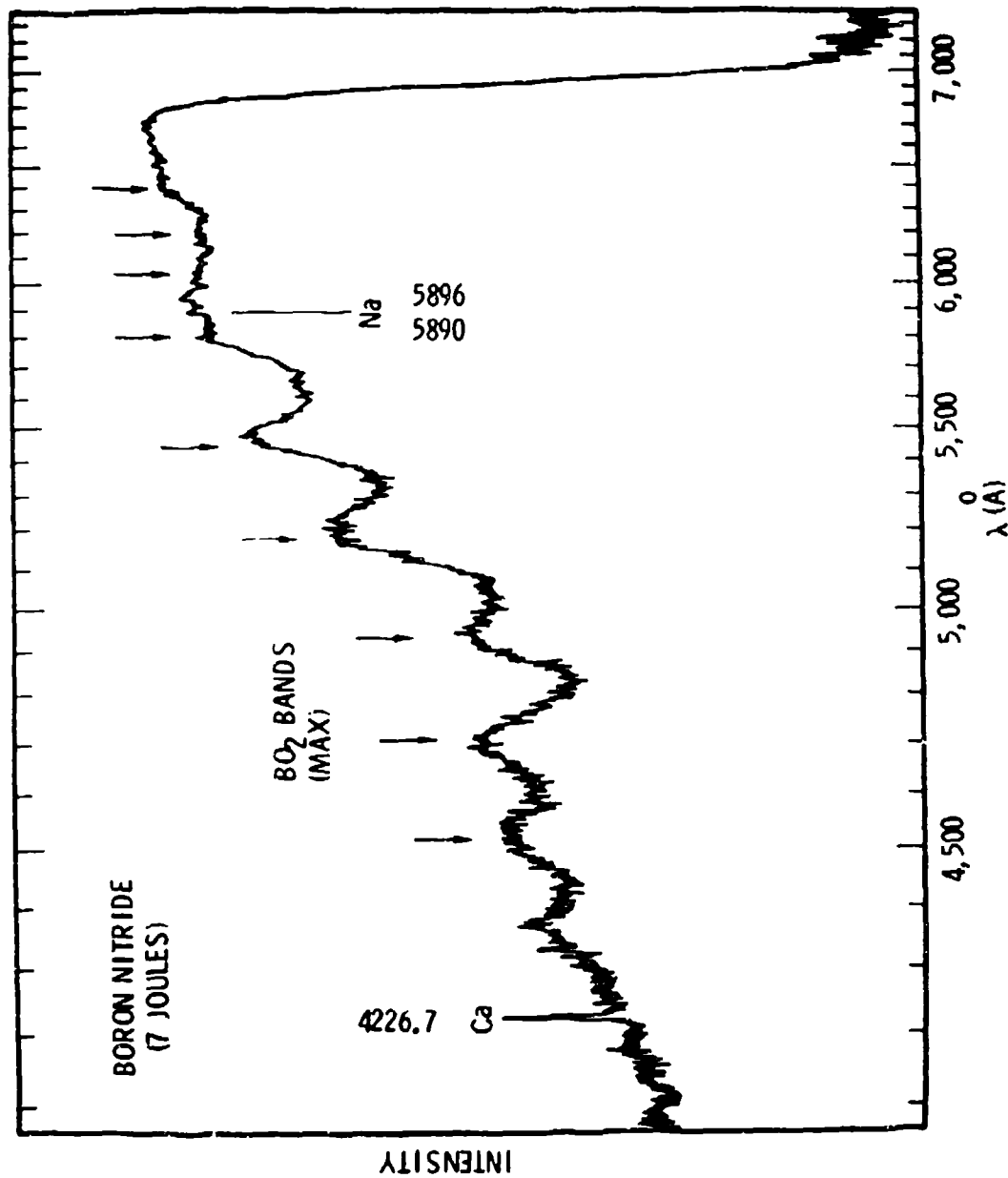
Figure 66   Emission spectrum of an LSB wave generated from a boron nitride target.

96
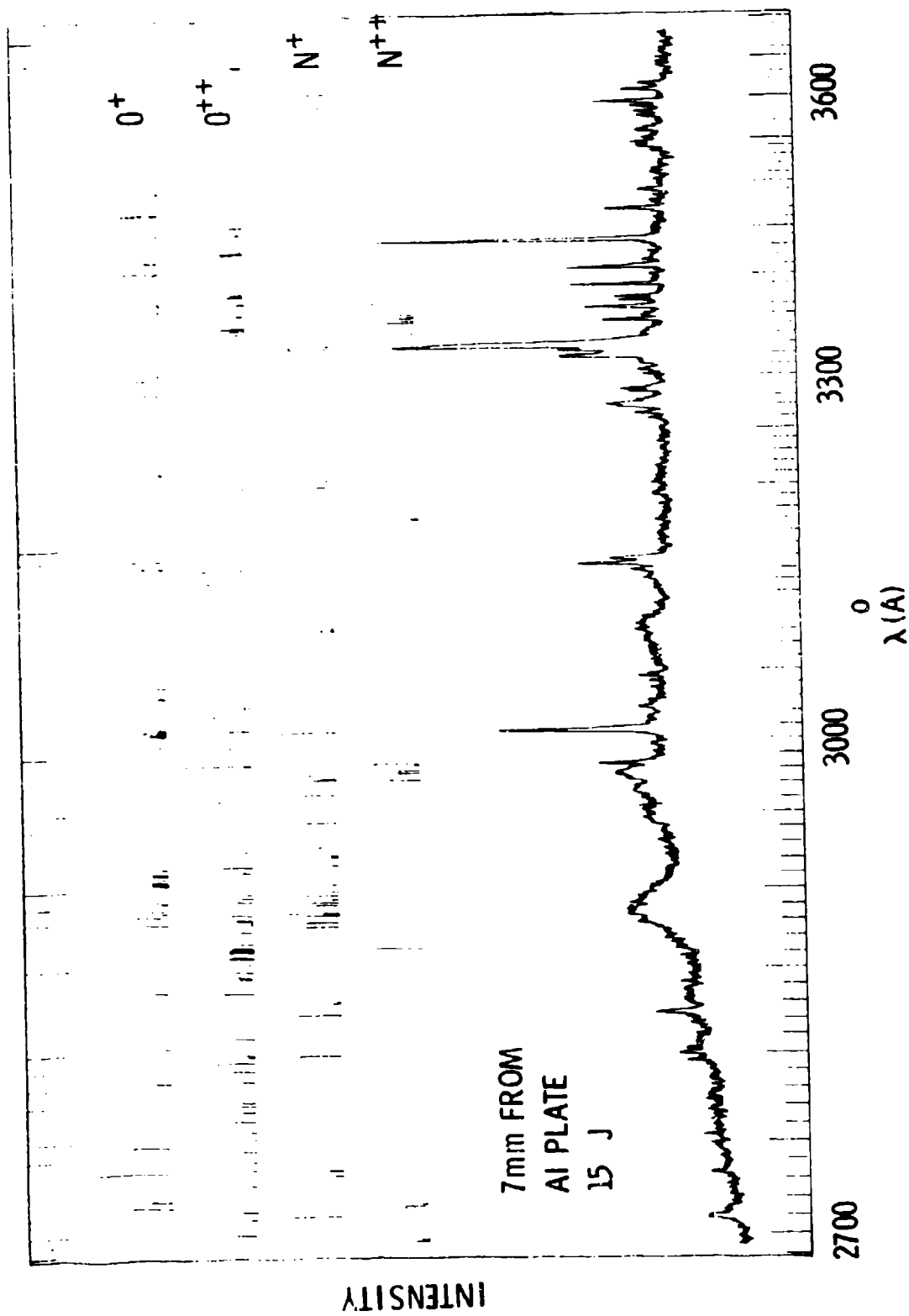
Figure 67   A section of the emission spectrum of an LSD wave generated from an aluminum plate.
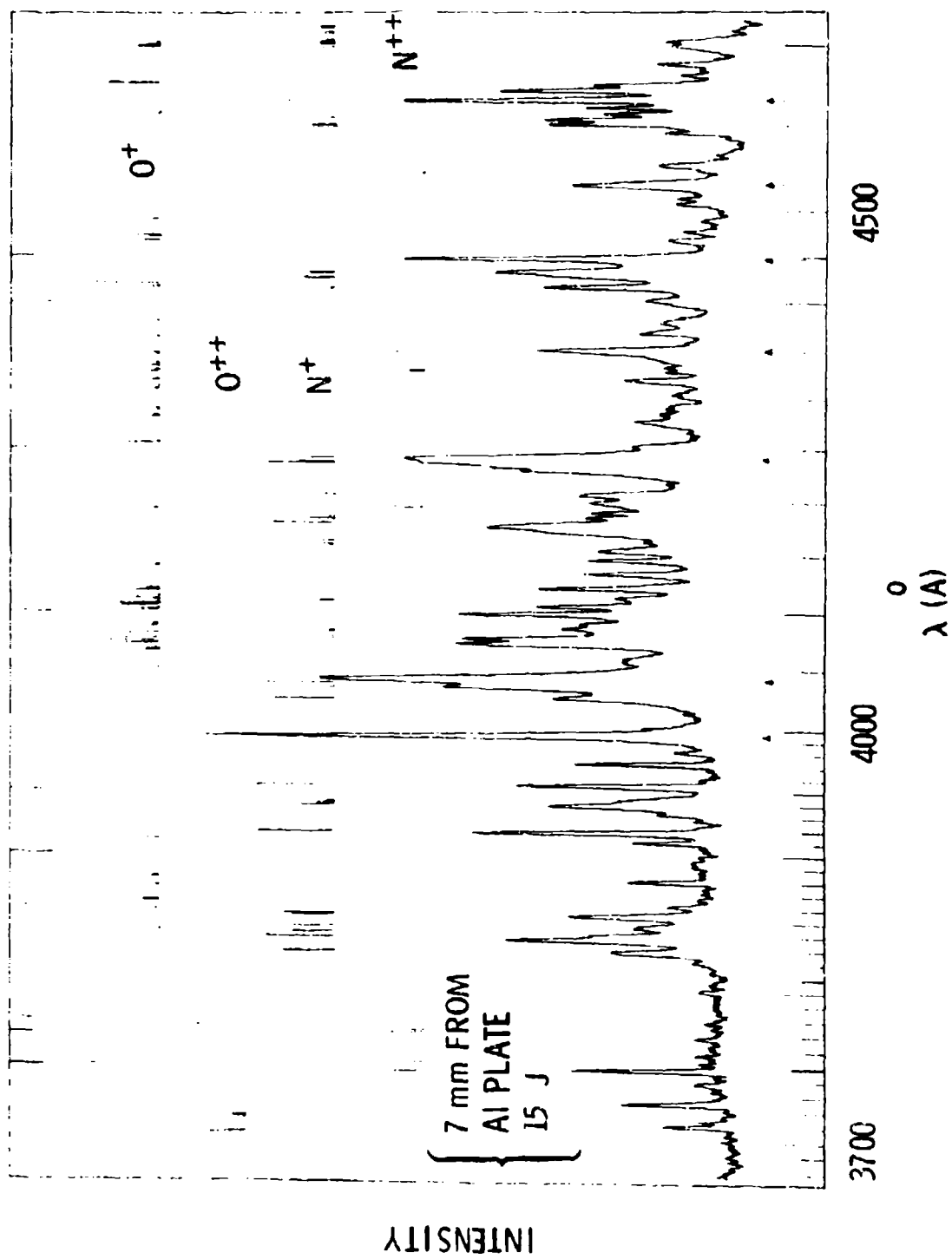
Figure 68   A section of the emission spectrum of an LSD wave generated from an aluminum plate.

98
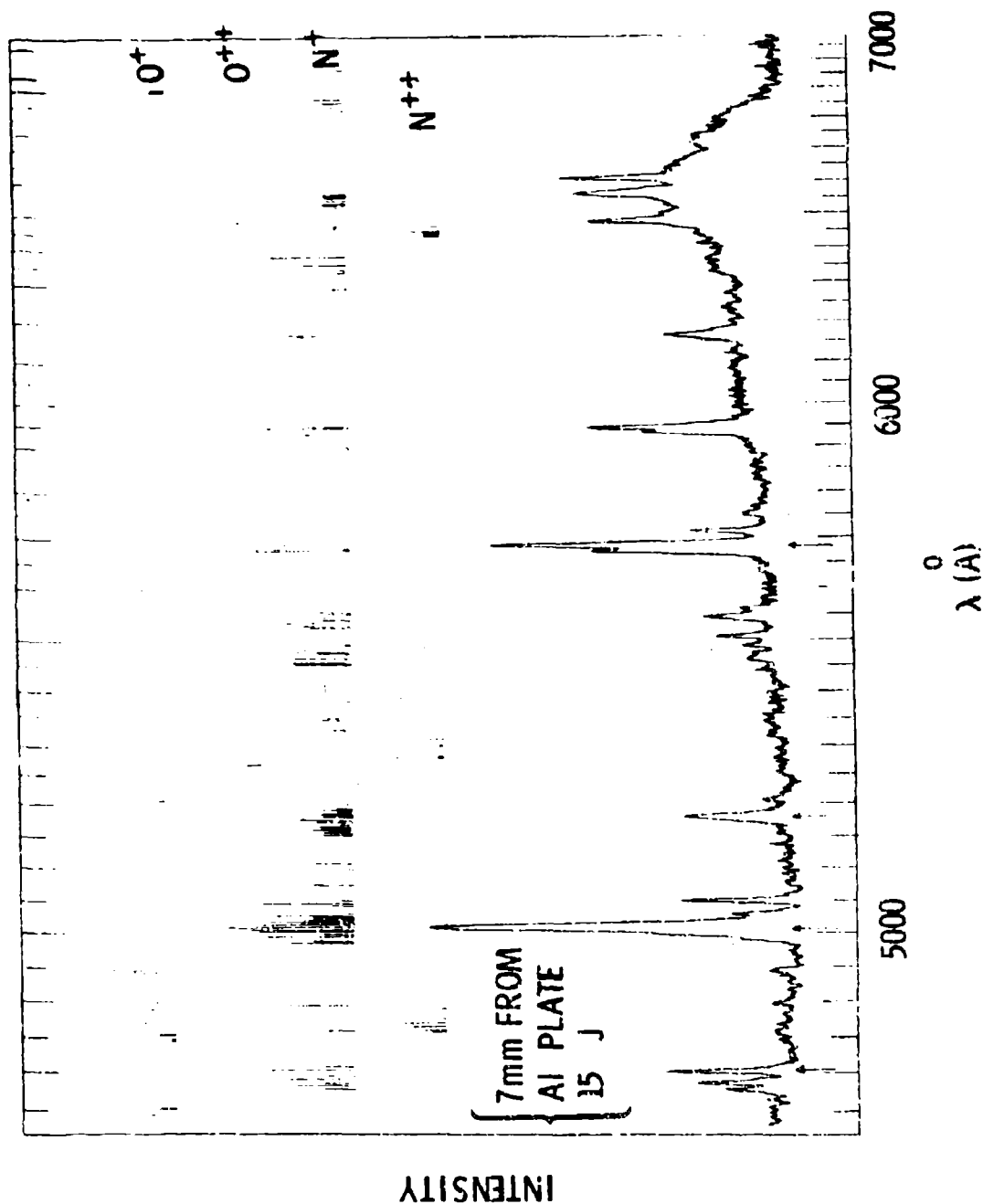
Figure 69 A section of the emission spectrum of an LSD wave generated from an aluminum plate.

4.2 EQUILIBRIUM COMPOSITION OF AIR AND TEMPERATURE ESTIMATES

In order to estimate the temperature and the electron density in the LSD waves, a theoretical computer calculation (previously developed) of the equilibrium composition of air has been carried out. The basic assumptions are ideal gas behavior and instant equilibrium. For each possible species, neutral or charged, the total partition function is written in terms of atomic or molecular constants available from optical spectroscopy[34]. Thermodynamic functions such as entropy and free energy are related to the partition function by the standard formulae derived from statistical mechanics[35]. At a given temperature and pressure, the equilibrium composition is found by an iteration procedure which minimizes the free energy of the system subject to the conditions of conservation of charge and mass[36]. Earlier work and other methods for the calculation of equilibrium composition can be found in a review paper[37].

Starting from a combination of 79% nitrogen and 21% oxygen, the equilibrium composition of air has been calculated for pressures from 0.01 to 100 atm and for temperatures from 10^3 to 10^{5o}K. Figure 70 shows the calculated air composition at 1 atm for temperatures below 20,000°K. The number density n (per cm^3) for a given species can be calculated by

$$n = 7.35 \times 10^{21} \ F \ P/T \tag{16}$$

where F is the mole fraction, P is the pressure (in atm) and T is the temperature (in °K). We see that as the temperature increases, the molecules dissociate into atoms which subsequently ionize. For the convenience of discussion, a cross-over temperature, T_c, can be defined. At 1 atm, the T_c for (N_2, N) and (N, N^+) are found at 6600 and 14,700°K, respectively. On the other hand, the O_2 molecule is not so strongly bound so that the T_c for (O_2, O) occurs at 3400°K (see figure 70).
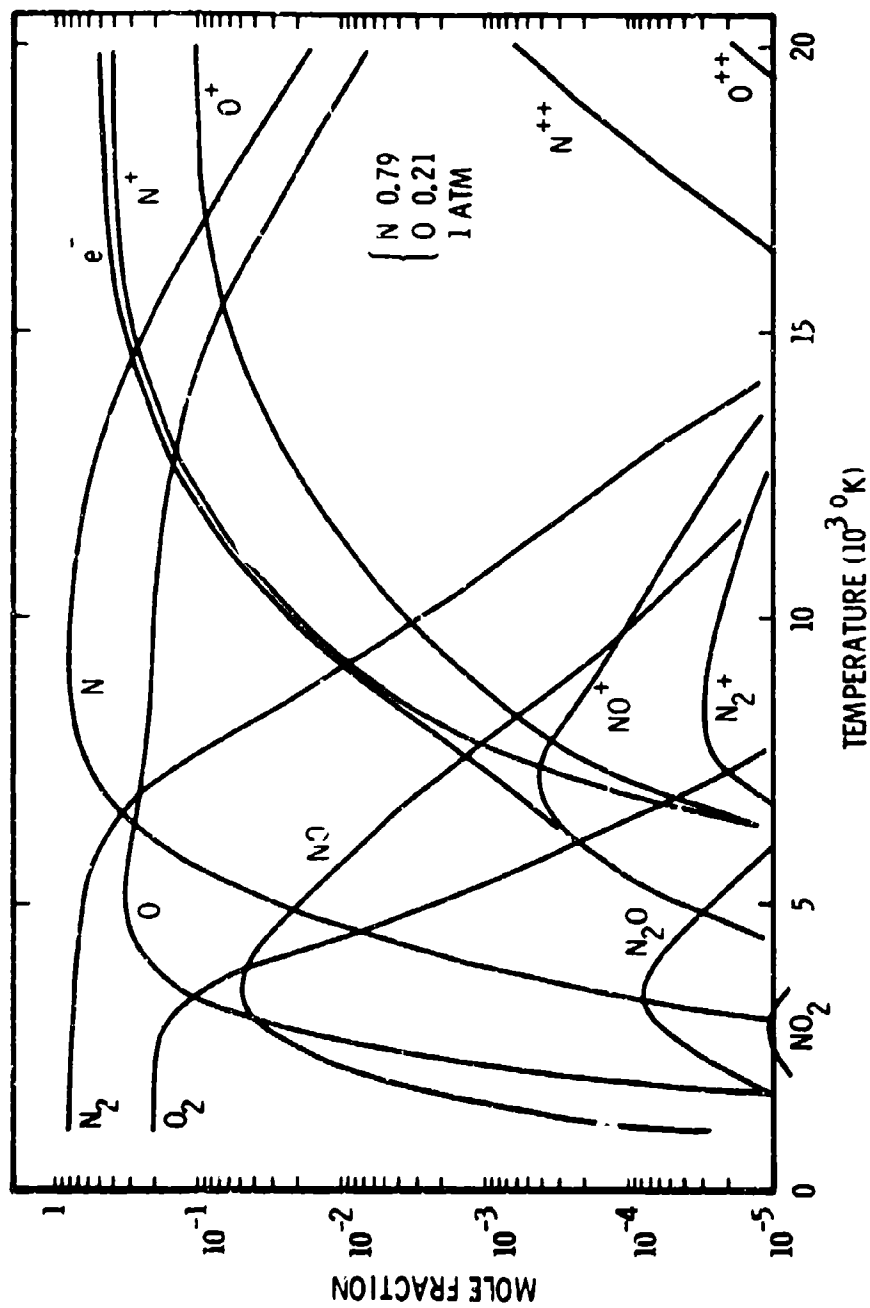
Figure 70   Calculated equilibrium composition of air at 1 atm.

Figure 71 shows the calculated air composition at a pressure of 100 atm for temperatures below 20,000°K. Comparison with the previous figure shows a qualitative similarity except all the cross-overs tend to occur at a high temperature for the high pressure case. A summary of the T_c for species in air is shown in figure 72. Our results are in good agreement with earlier calculations on the composition of air[38,39].

As mentioned previously, the emission spectrum of the LSD waves consist mainly of N^+ and O^+ with a small contribution from N^{++} and O^{++} (figures 62, 67, 68 and 69). If local thermodynamic equilibrium is assumed, then the temperature in the LSD waves is estimated to be slightly lower than the T_c for (N^+, N^{++}) and (O^+, O^{++}). For LSD waves at 1 atm, the estimated temperature is about 25,000°K and the electron density is 1.5×10^{17} per cm^3. If the pressure in the LSD wave is 100 atm, the temperature and electron density are estimated as 40,000°K and 1.0×10^{19} per cm^3, respectively

According to Griem[40], a measurement of the relative line intensities of subsequent ionization stages of the same element yields information concerning the temperature of the species. We find in figure 63 that the intensity ratio of the lines C^{++} (2296.9 Å) and C^+ (2509 to 2512 Å) is 0.67 after correcting for the continuum background. This yields temperatures from 23,000 to 37,000°K for electron densities from 1.5×10^{17} to 1.0×10^{19} per cm^3, respectively. The line intensity can be measured quite accurately by weighing the cutout of a spectral line from a chart paper. For example, the intensity ratio of the C^+ (2509.1 Å) to C^+ (2511.7 and 2512.0 Å) is found to agree with the ratio of their transition probabilities[31] to within .03. However, the temperature is not very sensitive to the intensity ratio[40].

Another estimate of the temperature is obtained from the intensity distribution of the continuum emission. For a perfect black body[41],
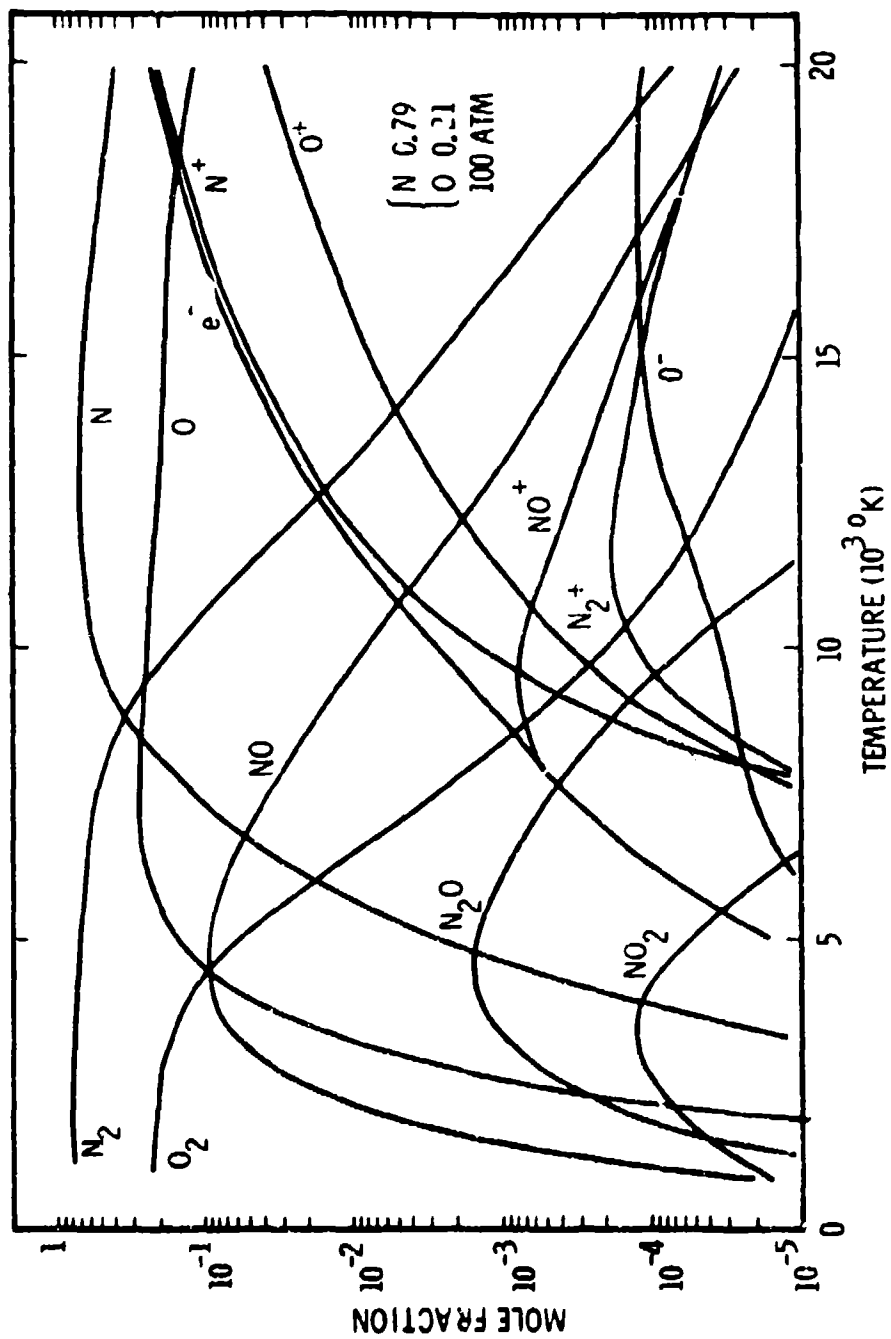
Figure 71   Calculated equilibrium composition of air at 100 atm.
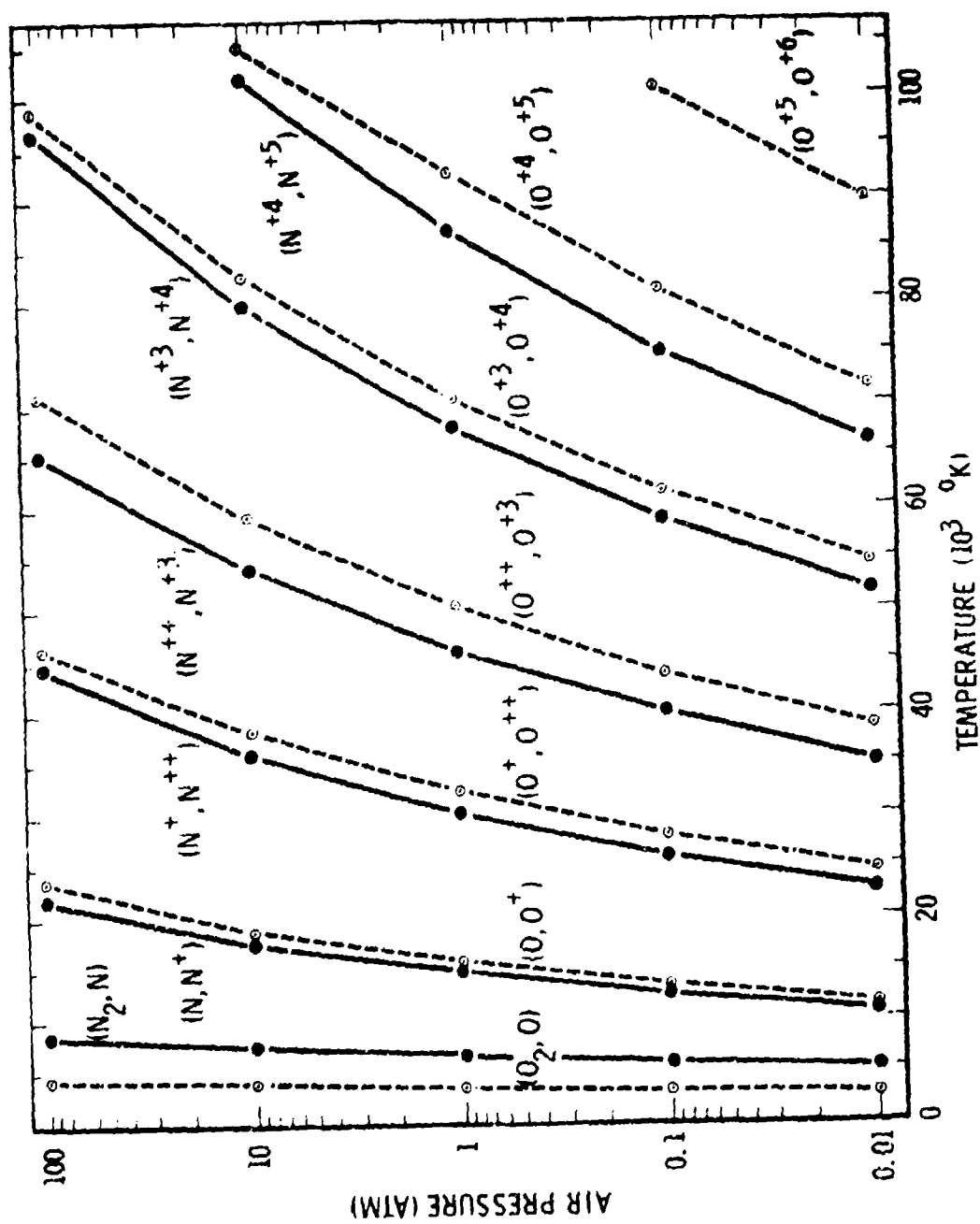
Figure 72   Cross-over temperatures for species in air.

104

the spectral energy density function exhibits a maximum at $h\nu = 2.822kT$.
The continuum spectral emission recorded from strong LSD waves
(at intensities well above threshold) exhibit two broad maxima
as a function of wavelength, however. The first one, between 4500
and 2600 Å would correspond to a black-body temperature in the range
between $12,000°$ and $20,000°K$. The second one, located at a wavelength
shorter than 2000 Å would correspond to a temperature higher than
$30,000°K$ (which could be the LSD wavefront temperature during the
early stage of the laser pulse).

For a target which absorbs light appreciably at 10.6μ , a blast
wave is observed. The emission spectrum in this case consists
mainly of bands from molecules at a much lower temperature (probably
around $4000°K$ as occurs in flames). The results shown in figures
65 and 66 tend to confirm the theoretical work by Chang, Drummond,
and Hall[42] that the molecular species evaporated from an opaque
target may become transparent to the laser radiation when the vapor
is heated to around $4500°K$, provided the laser power density is
below the threshold for breakdown.

4.3 TIME-RESOLVED SPECTRA

Time-resolved emission spectra of LSD waves have been obtained
from several types of targets (soda glass, carbon, sapphire, boron
nitride, aluminum plate, etc.) as a function of laser pulse energy,
distance from the target and delay time. A schematic of the
experimental arrangement is shown in figure 61. The transmission
spectrograph yields a spectrum in the wavelength range from 3800
to 6200 Å . Typical time-resolved spectra of LSD waves obtained at
7 mm in front of an aluminum plate during the first 10μsec of the
laser pulse with energies of 15 and 7.5 joules are shown in Figure 73.
Mercury reference lines superimposed on the spectra are also shown.
Each figure is a single exposure picture taken with Polaroid type
41C films of speed ASA 10,000. We see in these figures that the
velocity of the wavefront, as expected, depends on the laser energy.
In figure 73a, the light emission exhibits a break in time, which

Hg calibration
lines

4047 Å
4358
5461
5770
5790
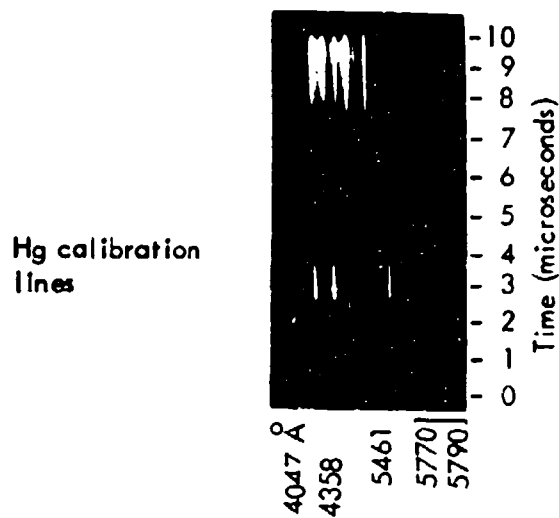
(a)   TIME-RESOLVED SPECTRUM OF A LSD-WAVE IGNITED
       FROM AN ALUMINUM PLATE WITH A 15 JOULE LASER
       PULSE AND LOOKING AT 7 mm IN FRONT OF THE TARGET.

Hg calibration
lines
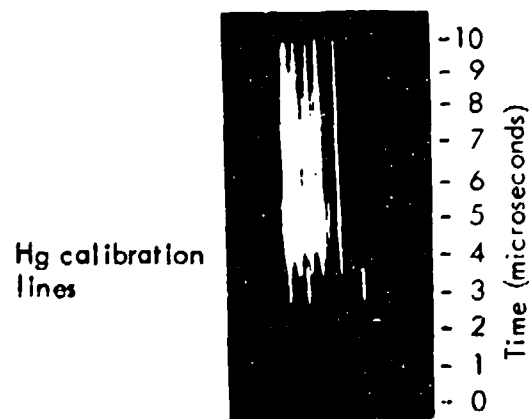
(b)   SIMILAR TO ABOVE EXCEPT WITH A 7.5 JOULE PULSE.

Figure 73   Pictures of time-resolved spectra of LSD waves.

occurs for a higher energy pulse and at a distance close to the target. The spectrum is characterized by about a dozen emission lines superimposed on a continuum. The LSD wave, once generated, yields a spectrum which seems to be insensitive to the type of target, distance, laser power and delay time, except for intensity variations. For absorbing targets, emissions from target materials are observed following the LSD wavefront which contains air species only.

Time-resolved spectra of LSD waves have also been taken with Kodak Royal Pan film of speed ASA 400 for micro-densitometric analysis. The results of 10 superimposed exposures at two-time larger f-stop yields a spectrum of almost identical appearance compared with the single exposure picture. Figure 74 shows the spectra at 3, 7 and 9μsec after the start of the 15-joule pulse and looking at 7 mm in front of the aluminum target plate (same conditions as for figure 73a). Full width at half maximum of spectral lines as small as 24 $\overset{o}{A}$ has been observed in a helium reference spectrum. (The inherent line width is 15 $\overset{o}{A}$.) However, the line widths in an LSD wave spectrum are typically broader than 50 $\overset{o}{A}$ due to the necessary intensity-resolution trade-off and unresolved features in the spectrum.

We see in figure 74 that the emission spectrum at each instant seems to be the same except that the intensity changes with time. Identification of peaks in the time-resolved spectrum is accomplished with the help of the time-integrated spectrum (see the arrows at the bottom of figures 68 and 69). Due to the response threshold of the image convertor camera, the weaker features do not show up in the time-resolved spectrum. Thus, all peaks in figure 74 have been assigned to N^+ except the small peak at 4350 $\overset{o}{A}$ which is attributed to O^+. The LSD wave spectrum (N^+ and O^+) lasts for about 25μsec, which is the duration of the laser pulse.

107
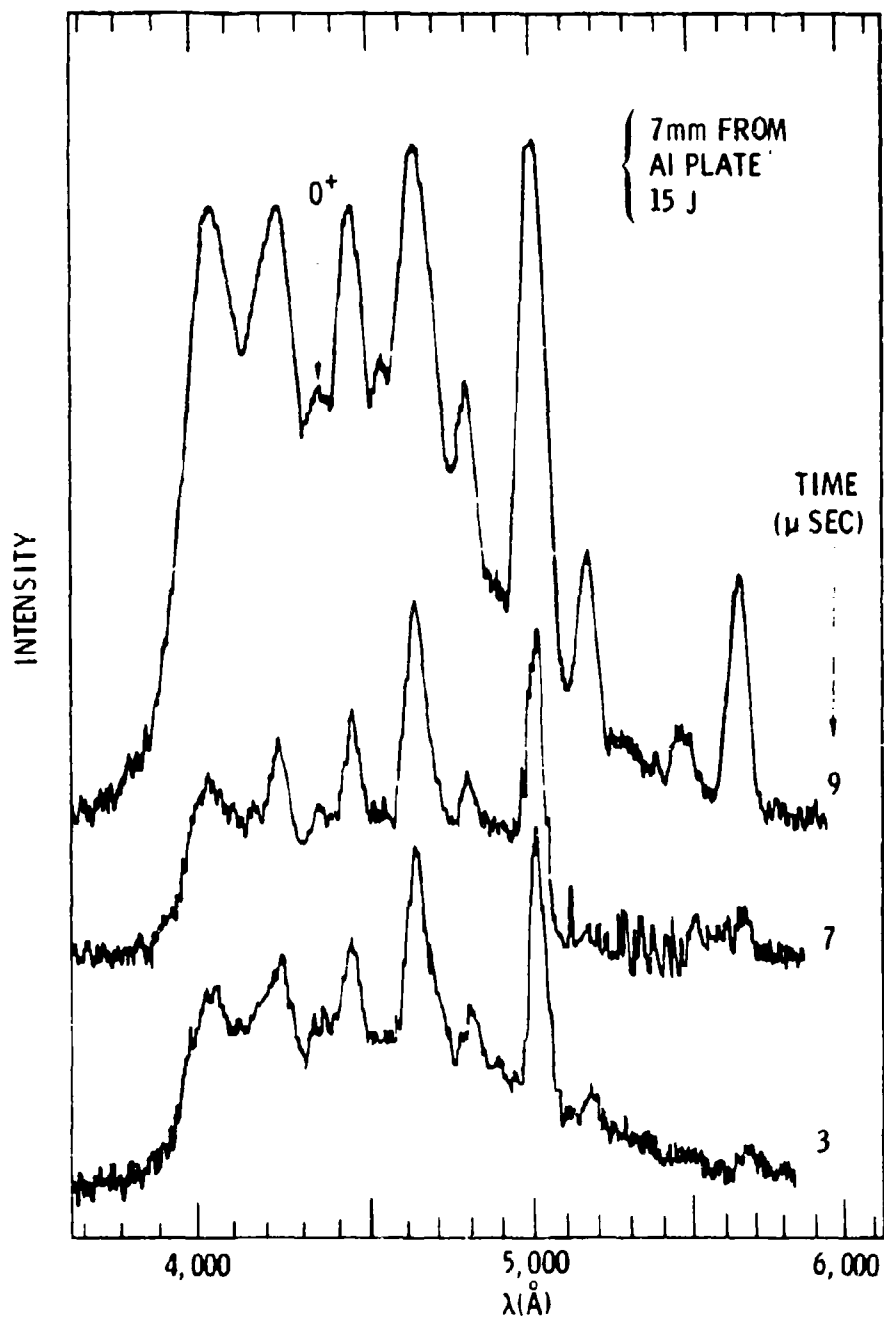
Figure 74   Densitometer traces of time-resolved spectra of LSD waves at several instants of time.

In order to demonstrate the temporal development of the LSD
waves, we have chosen the N^+ 5005 $\overset{o}{A}$ line (actually many unresolved
lines plus the continuum background). Figure 75 shows the intensity
variation of this line obtained with 15 joule pulses from an
aluminum plate target at distances from 1 to 20 mm. From the onset
of the wavefront (arrows pointed downwards) an average forward speed
is estimated to be about 4×10^5 cm/sec. A striking feature of this
figure is that the light emission is not continuous in time. At
distances of 7 mm and smaller, there exists an interval within
which the intensity is essentially zero. The onsets of the second
luminous part (arrows pointed upwards) seem to indicate a wave
traveling back to the target. The average backward speeds are
estimated as 10^6 and 7×10^5 cm/sec between 7→4 mm and 4→1 mm,
respectively. These waves have previously been observed by image
converter photographs as indicated in Section II and in the interfero-
metric data of Section III. These backward waves are the result
of the increased laser absorption length as the laser intensity
decreases at the front of the LSD wave.

Figure 76 shows the temporal variations of the LSD waves as
represented by the N^+ 5005 $\overset{o}{A}$ line at several energies by looking
at a fixed distance of 7 mm in front of an aluminum plate. The
results shown in figures 75 and 76 suggest that the break in emission
intensity is related to the high electron density of the LSD wavefront.
After an air breakdown has been triggered at the solid surface, the
plasma absorbs radiation by inverse Bremstrahlung and travels towards
the laser light source as a detonation wave.

From a time-resolved spectrum, one can measure the time it takes
for an LSD wave to travel a given distance. Results on five different
targets at three pulse energies and four distances are summarized in
figure 77. For targets which absorb the 10.6 micron energy, the
ignition of LSD waves is often delayed and the scattering of data
points in the figure indicates the difficult nature of the experiments.
The target samples were chemically cleaned but are typical of those
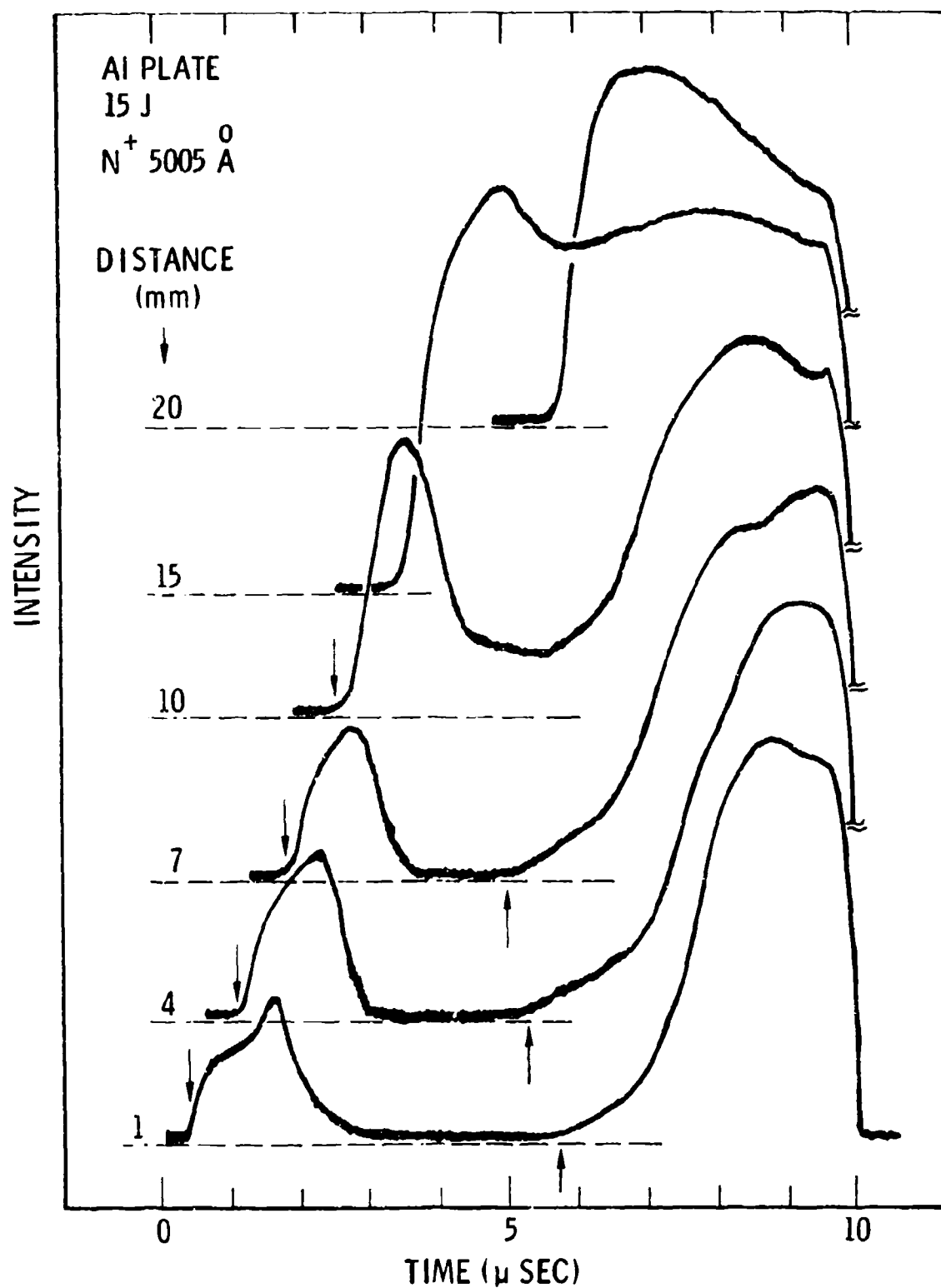
Figure 75   Intensity variation of the LSD wave spectrum as represented
by the N^+ 5005 $\overset{o}{A}$ line at several distances.

110
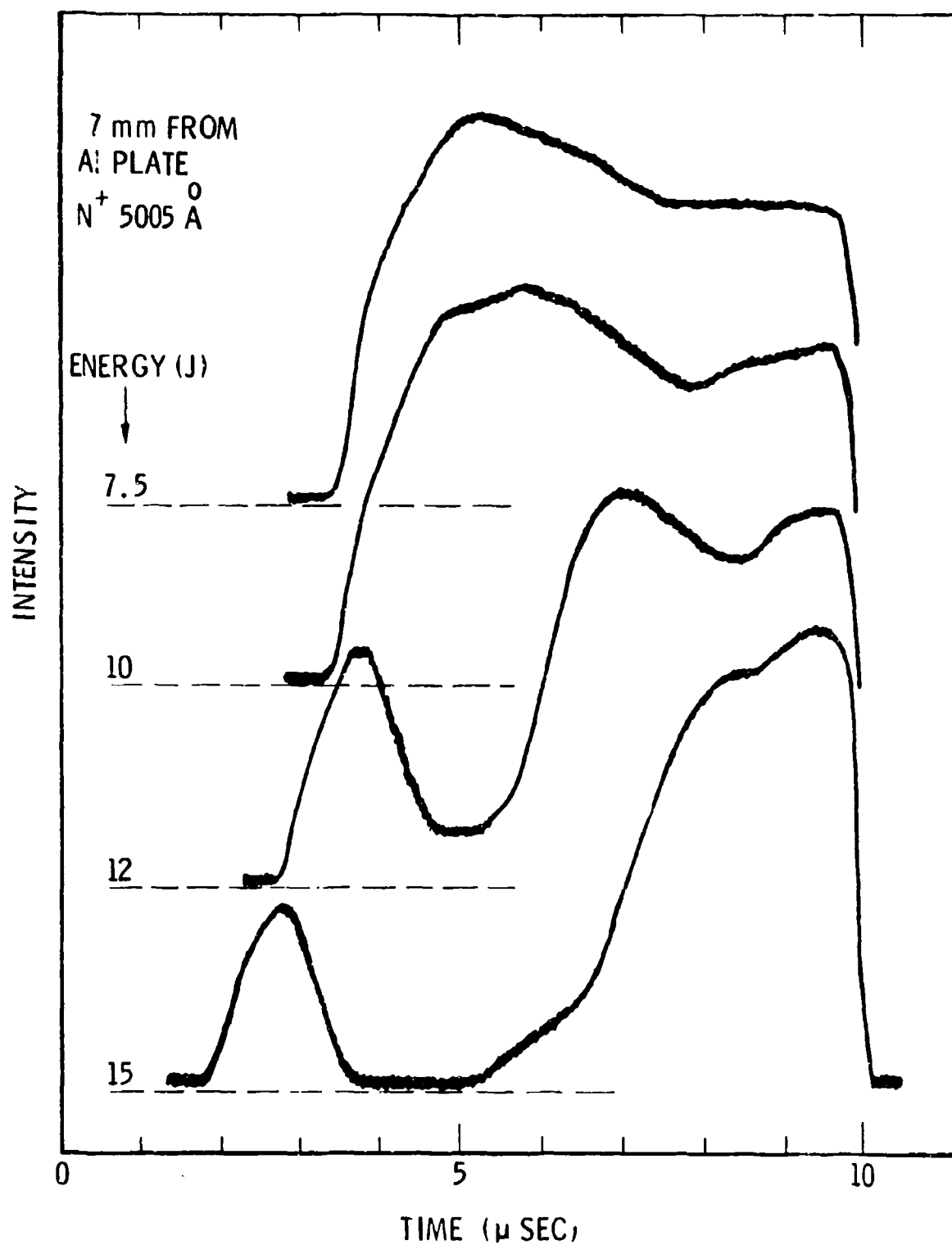
Figure 76   Intensity variation of the LSD wave spectrum as represented by the N^+ 5005 Å line at several energies.

111
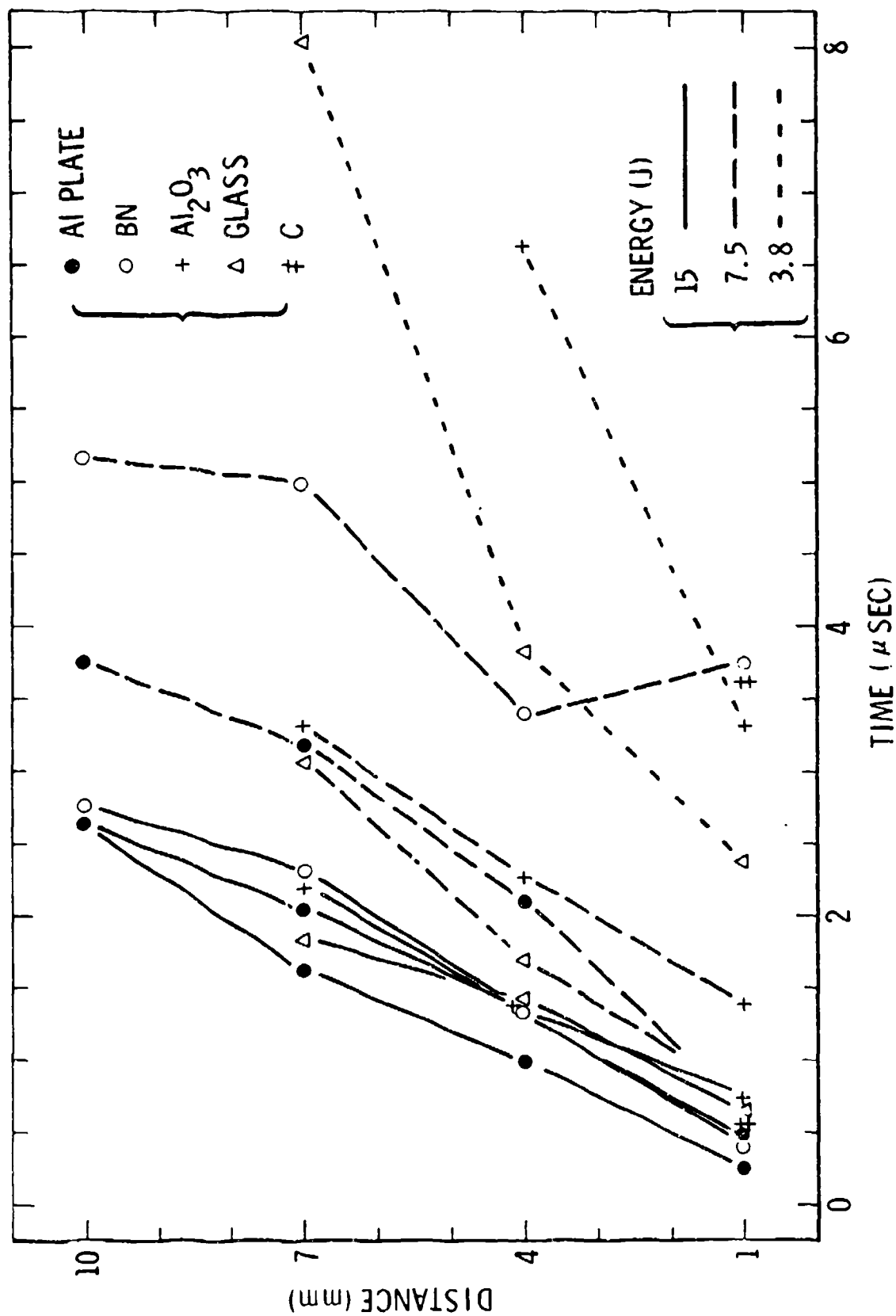
Figure 77   Summary of the time elapsed for the LSD wavefront to travel a given distance for several samples.

found in a laboratory with unspecified surfaces in which contaminations on the surface may be important.

Figure 78 shows the average forward speed of an LSD wave which traveled between 1 and 4 mm plotted against the cube root of the laser pulse energy for several targets. For an ideal detonation wave[4], the speed is expected to be proportional to the cube root of the power density. In the present experiments, the 10.6μ laser pulse exhibits two peaks at 0.5 and $3\mu sec$ after the start of the pulse (with maximum power densities of 5.0×10^7 and 3.0×10^7 W/cm^2, respectively); it then decays to zero at the end of about $25\mu sec$. Since the surface condition and ignition delay may vary from one experiment to another, the laser power responsible for each LSD wave also varies. In view of this, the qualitative agreement with the one-third power dependence should be regarded as satisfactory.

It is perhaps evident from the results in Figure 78 that the average speed of LSD waves generated from soda glass and alumina are somewhat higher than that from the other two targets. One possible reason for this may be because soda glass and alumina targets yield metal vapors of sodium and aluminum which are easily ionized. We note also that the threshold for ignition of LSD waves are also lower for soda glass and alumina (see Section V).

For a sample which absorbs the 10.6μ laser light appreciably, a blast wave propagating normal to the target is generated. The emission spectrum in such a case consists of target materials which, in contrast to the air species, travel a shorter distance at a slower speed and emit light longer, e.g., Ca (4226.7 Å) and Ca^+ (3933.7 and 3968.5 Å) from boron nitride or glass; Al (3944.0 and 3961.5 Å) and AlO (B→X, with zero-zero at 4842.1 Å) from alumina, etc. Thus, with the laser beam perpendicular to the sample surface, one first observes the LSD wave with a characteristic air spectrum followed by evaporated materials from the target.

found in a laboratory with unspecified surfaces in which contaminations on the surface may be important.

Figure 78 shows the average forward speed of an LSD wave which traveled between 1 and 4 mm plotted against the cube root of the laser pulse energy for several targets. For an ideal detonation wave[4], the speed is expected to be proportional to the cube root of the power density. In the present experiments, the 10.6μ laser pulse exhibits two peaks at 0.5 and 3μsec after the start of the pulse (with maximum power densities of 5.0×10^7 and 3.0×10^7 W/cm^2, respectively); it then decays to zero at the end of about 25μsec. Since the surface condition and ignition delay may vary from one experiment to another, the laser power responsible for each LSD wave also varies. In view of this, the qualitative agreement with the one-third power dependence should be regarded as satisfactory.

It is perhaps evident from the results in Figure 78 that the average speed of LSD waves generated from soda glass and alumina are somewhat higher than that from the other two targets. One possible reason for this may be because soda glass and alumina targets yield metal vapors of sodium and aluminum which are easily ionized. We note also that the threshold for ignition of LSD waves are also lower for soda glass and alumina (see Section V).

For a sample which absorbs the 10.6μ laser light appreciably, a blast wave propagating normal to the target is generated. The emission spectrum in such a case consists of target materials which, in contrast to the air species, travel a shorter distance at a slower speed and emit light longer, e.g., Ca (4226.7 Å) and Ca$^+$ (3933.7 and 3968.5 Å) from boron nitride or glass; Al (3944.0 and 3961.5 Å) and AlO (B→X, with zero-zero at 4842.1 Å) from alumina, etc. Thus, with the laser beam perpendicular to the sample surface, one first observes the LSD wave with a characteristic air spectrum followed by evaporated materials from the target.

Figure 78   Energy dependence of the average forward speed of the LSD
wave traveled between 1 and 4 mm.

Figure 79 shows the emission spectra of laser-supported absorption waves excited by a 7.5-joule pulse from an alumina sample and looking at 4 mm in front of it. At 2μsec, the spectrum is very similar to the air spectrum (N^+ and O^+) shown in figure 74. The emission intensity decreases to a minimum after 4μsec and increases again after about 5μsec (similar to the general behavior shown in figures 75 and 76). At 15μsec after the start of the pulse, the spectrum exhibits emission features of Al and AlO superimposed on the "air" spectrum.

The emission spectrum of the B→X transition in AlO is of particular interest because the separations of the vibrational energy levels in the $B^2\Sigma^+$ state are slightly smaller than the laser photon energy. Figure 80 shows the spectra obtained 1 mm in front of an alumina sample with several different energy pulses. For the 15 and 7.5-joule cases, strong emission from N^+ and O^+ is excited during the earlier part of the laser pulse. At 16μsec, however, the spectrum consists mainly of Al and AlO and a weak N^+ 5005 $\overset{o}{A}$ line. On the other hand, the 3.8-joule pulse excites a weak emission from the air species but the AlO features are quite strong. It is surprising to find that the emission bands of $\Delta v = 2$ and 1 are much stronger than the other bands of $\Delta v = 0$, -1, and -2 during the time of the laser pulse. (Compare the time-integrated spectrum of the B→X transition in AlO observed in an LSB wave as shown in figure 65.) Furthermore, the $\Delta v = 2$ band is more intense than the $\Delta v = 1$ band for lower energy pulses. Presumably, this is due to less shielding of the laser radiation by the LSD waves generated at low energy. The preference for simultaneous electronic and vibrational relaxations in the presence of an intense laser radiation may be regarded as an evidence of a kind of stimulated emission. However, further work on this subject is needed.
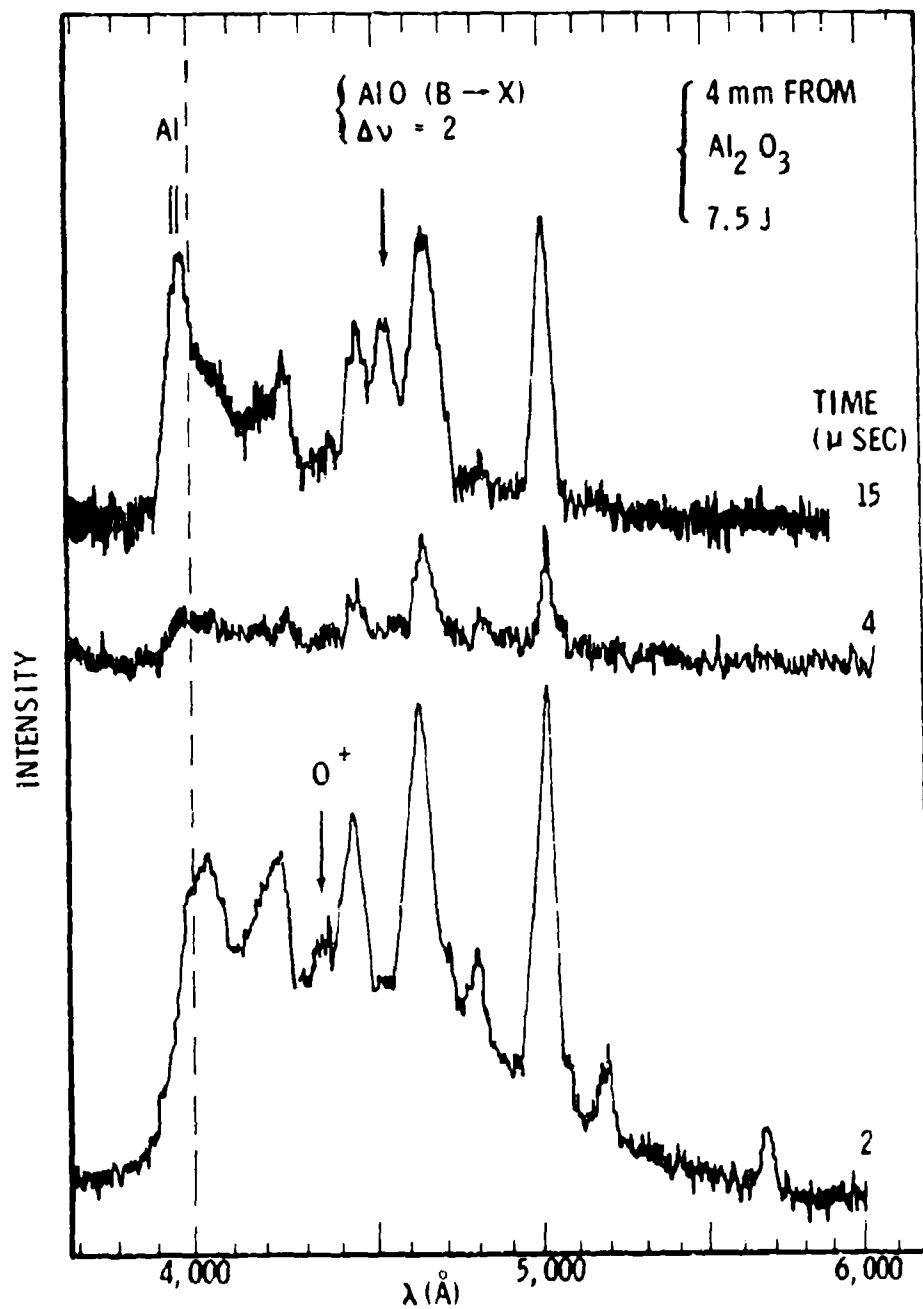
Figure 79   Time-resolved spectra of LSD waves observed at 4 mm from an alumina sample at several instants.
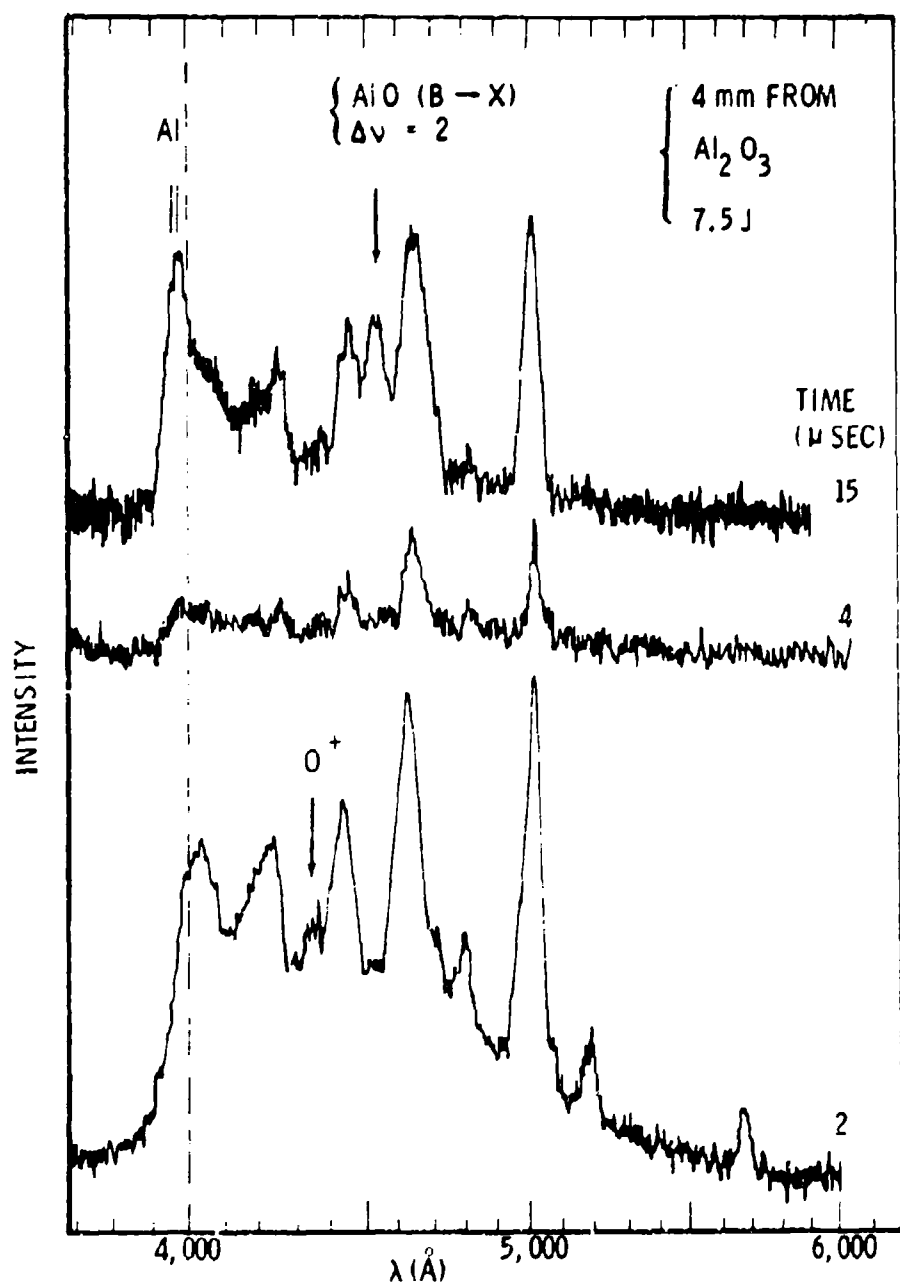
Figure 80   Time-resolved spectra of LSB waves observed at 1 mm
from an alumina sample at several energies.

4.4 DISCUSSION

The emission spectra of sparks produced at the focus of a giant-pulse ruby laser ($h\nu = 1.78$ eV) have been studied by several authors[43-47]. Typically, the plasma consists of singly charged atomic species from air. Gas breakdown with pulsed CO_2 laser radiation ($h\nu = 0.117$ eV) has been studied by Smith[1,48] and the breakdown threshold in cold air was found to be about 2×10^9 W/cm^2, depending on the focused spot size. With external sources of electrons to initiate the cascade process, however, the threshold could be lowered by a factor of five. This is similar to the theoretical considerations[15] and the present observations that the laser intensity needed to maintain a laser-supported detonation (LSD) wave is lower than that needed to ignite it. As noted in the first paper on this subject[49] breakdown effects were observed to occur at sample surfaces much more readily than in a gas.

Our present studies described above show that air breakdown and laser-supported detonation waves can be triggered by a solid surface at a laser intensity much below the cold air breakdown threshold. The gaseous plasma of N^+ and C^+ is probably a general phenomenon related to laser-supported detonation waves, regardless of the ignition process.

It is of interest to consider the role of a solid surface in lowering the threshold of air breakdown induced by a giant-pulse laser. The two-step mechanism for gas breakdown is believed[48] to be: (a) to obtain the first several electrons by multiphoton ionization and (b) to multiply the number of electrons in a cascade process. In the present experiments, electron emission from a hot surface layer at the beginning of the pulse may have produced the equivalent of mechanism (a), provided the surface layer absorbs appreciably at the laser wavelength. Other possibilities which may have contributed to the threshold lowering include: (1) metal vapor of a low ionization potential from the surface, (2) evaporated

materials of lower electron affinity than air, and (3) enhanced
electric field due to reflection of the surface and surface
irregularities.

SECTION V

IGNITION THRESHOLDS OF LASER-SUPPORTED ABSORPTION WAVES

The determination of thresholds for ignition of laser-supported detonation waves involves some degree of arbitrariness. The reason for this difficulty is that there are a fairly large number of types of waves that can be generated at solid target surfaces. Some of these waves have been discussed in Section II and include: (1) vaporized jets and their interaction with the air background, (2) laser-supported combustion waves moving at very low velocity and exhibiting a luminous plasma column extending to the target surface, and (3) laser-supported detonation waves with a very narrow absorption zone traveling up the laser beam. A partial listing of various other laser effects is given by DeMichelis[50].

At the present time, there is no unified ignition theory for laser-supported absorption waves ignited at solid surfaces. The results given here show that absorption waves are generated with pulse lengths of approximately 10μsec and peak incident intensities of 5×10^7 watts/cm^2 or lower. It is difficult to understand under these conditions how vaporization can occur in such short times for highly reflective aluminum surfaces[51]. Experimentally, however, one obtains such waves on all tested reflective surfaces. Other mechanisms leading to ignition from solid target surfaces include surface defects, desorption of gases on the surface, gas breakdown induced by high intensities produced at reflective surfaces, and highly absorbing surface defects.

The actual surface reflectivity is extremely important in leading to vaporization. Both the initial cold reflectivity and the temperature dependence of the absorptivity are needed in order to compare a vaporization induced ignition theory with experiment. Unfortunately these properties are not well known. Chun and Rose[52] and Bonch-Bruevich[53] have considered some aspects of the variation of surface reflectivity and material properties with temperature. Basov[54] has also considered the reduction of surface reflectivity

with laser intensity. Additional theoretical considerations of the metal reflectivity by Uhihara[55] and non-linear effects in the surface[56] have been discussed. It appears, however, despite these works, that the determination of ignition thresholds for most common materials remains as largely an empirical study.

5.1 MATERIAL DEPENDENCE

One way of determining ignition thresholds is to use the TRW image converter camera. At each laser energy and for each target material, the plasma in front of the target is photographed. An absorption wave traveling up the laser beam can then be distinguished from vaporized material by mounting the target at an angle to the beam. In our case, the target normal was at an angle of 30° to the incident beam. We have performed such a sequence of measurements involving many laser shots and many materials and a listing of these tested materials and certain of their characteristics is given in Table 2.

It is evident from this table that merely taking a given laser target and repeatedly hitting the same focal sp- with a high power laser and searching for absorption waves leads to erroneous results. This occurs because the surface is either cleaned or "dirtied" by the hot plasma from previously ignited absorption waves. In the case of silica, for example, the surface is cleaned and subsequent ignition of laser-supported detonation waves is impossible. In the case of tantalum, on the other hand, the surface is tarnished after a single shot and the ignition thresholds are reduced.

It has been observed with certain metallic targets (aluminum alloy, tantalum, copper and tungsten) that threshold determination can lead to a hysteresis effect when using the same target (and focal spot) and increasing (or decreasing) in steps the laser flux to reach LSD wave ignition. That is, as the threshold was reached by increasing the laser energy it was found that the ignition energy

TABLE 2

MATERIALS TESTED FOR LSD WAVE THRESHOLDS

MATERIAL	COMMENTS
Copper	Tested with 4 different cleaning techniques. Tends to become "cleaned" by the laser pulse.
Tantalum	Surface chemical reactions caused by high surface temperatures caused tarnishing and reduced reflectivity.
Aluminum alloy (7075)	No easily observed surface damage.
Oxidized Aluminum	Oxide layers 20 $\overset{o}{A}$, 200 $\overset{o}{A}$, and 2000 $\overset{o}{A}$ thick show no noticeable differences in thresholds.
Nickel	Doesn't tarnish easily.
Tungsten	Becomes discolored after several laser shots on the same spot.
Stainless Steel (Alloy 321)	Surface melting and tarnishing occurs
Silver	Multicolor surface discoloration occurs.
Titanium	Surface melting and tarnishing occurs.
Soda Glass	Ignites LSD waves with multiple shots on the same spot.
Polycarbonate	Ignited LSD waves with multiple shots on the same spot.
Lucite	First pulse makes LSD waves but subsequent pulses are absorbed at surface making a vapor jet.
Silica	First pulse makes LSD waves but subsequent pulses are absorbed at surface leading to vapor jets.
Teflon	First several pulses ignited LSD waves but eventually ignition is not achieved and vapor jets are produced.
Fiberglass epoxy	Each shot on same spot ignited LSD waves
Cork	Each shot on same spot ignites LSD waves.

122

TABLE 2 (Continued)

MATERIAL	COMMENTS
Alumina	Golden brown colored stain forms and LSD waves are ignited.
Painted aluminum	Three types of paint tested, absorption waves form readily.

was greater than that observed when the threshold was reached by
lowering the laser energy. A possible interpretation of this
effect is that the lower energies tend to clean the surface of the
target whereas the existence of the detonation wave tends to contaminate
the target. For both tantalum and aluminum, this effect is very
pronounced leading to factor of two differences in threshold levels.
It thus was imperative that new samples be used on each shot and
a standard cleaning procedure adopted for determining thresholds.

The exact process of cleaning target surfaces does
not appear to be too important. This is true at least for surfaces
which don't have obvious sources of contamination, such as finger-
prints. For example, several materials were tested with different
cleaning techniques and no important differences in LSD wave thresholds
were found. These tests were done for stainless steel (aloy #321)
where two surface preparation techniques were used which led to
visual differences in the two samples, but the thresholds for igniting
LSD waves were very close. For copper, four different cleaning
techniques were tested, and again little change in LSD wave thresholds
were found. For oxidized aluminum, with oxide layers approximately
$20 \overset{o}{A}$, $200 \overset{o}{A}$, and $2000 \overset{o}{A}$ thick again no important differences in
thresholds were obtained. There are more sophisticated sample
preparation techniques which were not used here. These include
vacuum heating at low pressure and electron and ion beam desorption
of gases. It was felt, however, that the most important threshold
determinations were for "practical" surfaces exposed to atmospheric
conditions. In all cases, however, chemically clean samples were
used for each laser shot in the determination of ignition of LSD
waves. These samples were typically squares approximately 1.2 cm
on a side and varying in thickness from .03 to .20 cm. In all cases,
the target was placed at the position of the minimum focal spot
area. Additionally, the laser operating conditions were kept constant
for all shots. Thus the gas mixture ratios, pressure, and voltage
of the Marx Bank Laser were fixed. Energy density changes at the

target were accomplished by the use of plastic attenuators (Handi-Wrap, Tedlar) near the laser output mirror. In this way the energy and power monitors of the laser beam indicated the true variations actually incident on the target. These attenuators are described in Appendix A where it is also shown that they don't significantly change the power density distribution at the target.

On the basis of monitoring only the image converter photographs of absorption waves ignited at targets, the thresholds indicated in Table 3 are obtained. These thresholds are based only on the visual appearance of image converter photographs of waves traveling up the laser beam. In many cases, their appearance is of a rather long luminous column extending to the target. Near threshold, however, these waves do not have the appearance of the narrow-absorption zone of laser-supported detonation waves. In many cases, one can observe weaker intensity sparks at the target surface at even lower laser intensities than given in Table 3. These have not been classified as igniting absorption waves, however, since there is no evidence that they travel up the laser beam and away from the target. The energy density thresholds, E_T, given in Table 3 were obtained by dividing the total laser energy incident on the target sample by the beam area. The energy incident on the sample up until time of ignition was not directly measured. Typically, however, the time of ignition was between .25 and .5μsec. The peak laser intensity, q_{max} (watts/cm^2), was obtained by a numerical integration of the laser power detected by the gold-doped germanium detector and comparison with the laser energy measured by the calorimeter. The intensity, q_{max}, corresponds to the first laser peak occurring at approximately .5μsec. (We have utilized both q and I as symbols designating laser intensity in this report.)

As mentioned above, the ignition thresholds for laser-supported detonation waves can be determined by an analysis of the TRW image converter photographs. Our attempts to use the former method alone

TABLE 3

THRESHOLDS FOR IGNITION OF LASER-SUPPORTED ABSORPTION WAVES USING A 28 CM FOCAL LENGTH LENS AND USING A NEW SPECIMEN FOR EACH TEST AT ONE ATMOSPHERE.   THRESHOLD DETERMINED BY IMAGE CONVERTER PHOTOGRAPHS OF LUMINOSITY

Material	E_T(joules/cm^2)	q_{max}(watts/cm^2)
Copper Foil	266	3.83×10^7
Lucite	258	3.72×10^7
Polished Tungsten	229	3.30×10^7
Copper Plate	192	2.8×10^7
Tungsten Plate (unpolished)	186	2.68×10^7
Aluminum (7075 alloy)	176	2.53×10^7
Aluminum Foil	160	2.30×10^7
Tantalum	128	1.84×10^7
Carbon	88	1.27×10^7
Aluminum Black (very heavily anodized aluminum)	87	1.25×10^7
Lead Foil (polished)	64	$.92 \times 10^7$
Lead Plate (unpolished)	43	$.62 \times 10^7$

have met with problems, however. This method cannot resolve the difference between a very short-lived LSD wave ignited near threshold and other plasma phenomena in front of the specimen. Sometimes a blast wave, vapor jet, or even a hot specimen surface will look the same as a LSD wave near threshold. In particular, measurements at pressures less than 1 atmosphere made this decision about ignition difficult. A monitor of the specularly reflected beam power from the target provided a much sharper indication of the ignition of laser-supported absorption waves by being able to discriminate between highly absorbing plasmas and only weaksurface sparks. Ir somewhat the same manner used for determination of air breakdown thresholds[1], a somewhat arbitrary definition of LSD wave threshold was selected as occurring when the actual reflected power drops to less than .1% of the expected unblocked reflected power as determined from the incident power temporal shape.

The materials to be examined were attached to an aluminum block set at 30° to the plane of laser beam. This provided an elliptical spot at the target of 4 mm major axis and 3 mm minor axis when the focusing mirror had a focal length of 40 cm. With a focal length of 28 cm, the elliptical focal spot on target had dimensions of 2.4 mm by 3 mm. The specularly reflected beam from the target was collected by another mirror, attenuated and focused on a gold-doped germanium detector. A narrow-band 10.6μ filter on the detector eliminated the intense light from the LSD wave. By comparing the incident power shape versus time, obtained with a second detector, with the reflected power one can determine the ignition of the laser-supported absorption wave.

The detector which measured the reflected light showed that for some metals, when the ignition threshold was approached, the detonation wave could occur near the end of the laser pulse. This effect is shown in figure 81, which indicates the time variation of both the incident laser power and the reflected laser power. In

127
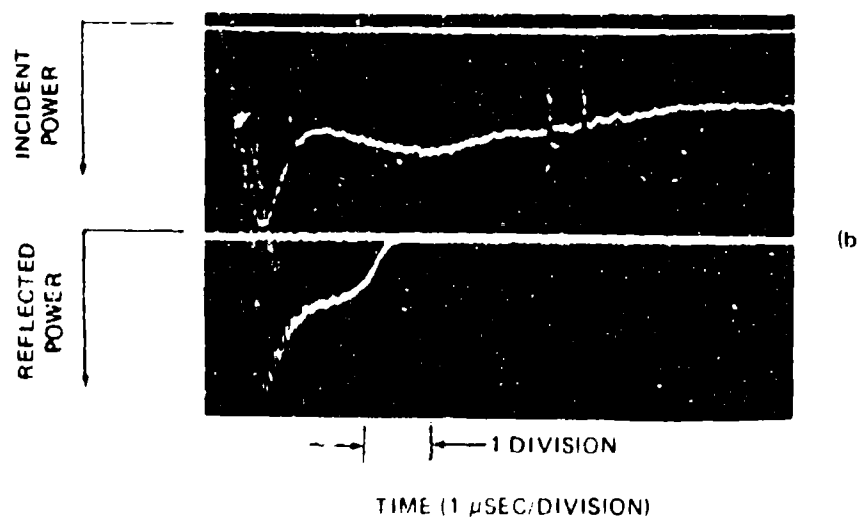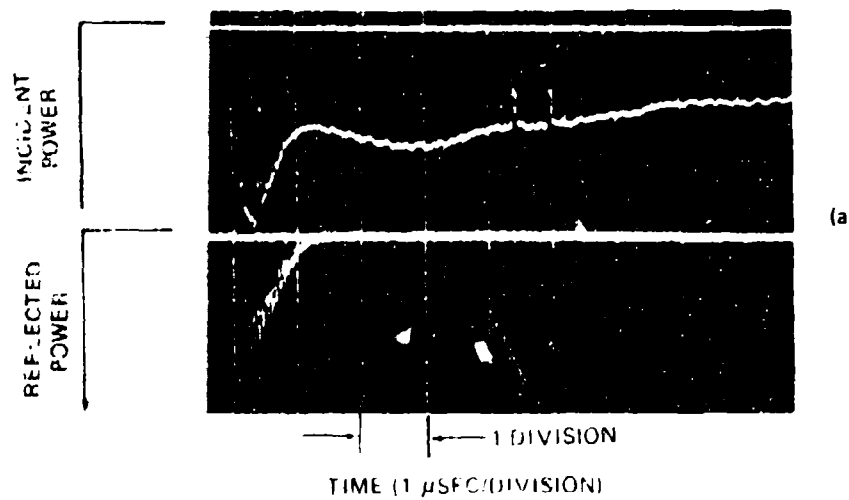
Figure 81: *TIME VARIATION OF BOTH INCIDENT AND REFLECTED POWER AT A COPPER TARGET. FIGURE 81a SHOWS IGNITION OF LASER-SUPPORTED DETONATION WAVES WITHIN ABOUT .5 μSEC. FIGURE 81b ON THE OTHER HAND SHOWS DELAYED IGNITION AT ABOUT 2.5 μSECS. THIS WAS CAUSED BY THE CLEANING EFFECT OF THE FIRST LASER PULSE.*

figure 81a, an LSD wave was ignited on a copper target early in the laser pulse as indicated by the rapid loss of reflected power for times greater than .5μsec. The small spikes on the oscillograph traces of the incident power were signals obtained from the image converter camera indicating when image converter pictures were taken. There are always a series of three such spikes and the first one indicates when sufficient light was present from the plasma to trigger the camera. In both figures 81a and 81b, the total laser energy was approximately 17 joules indicating an energy density at the target of approximately 380 joules/cm^2 and a peak intensity at the first laser spike of 5.6×10^7 watts/cm^2.

Figure 81b was obtained under essentially the same conditions as those of figure 81a except that the laser beam was incident on the same spot as hit previously. It is evident that ignition of laser-supported detonation waves is delayed by approximately 2μsec. This is evidently due to a "cleaning" effect caused by the hot plasma of the first shot on the target. Because of this "delayed ignition" effect near threshold, it is useful to also indicate threshold intensities in terms of energy density. This observed sudden decrease of reflected energy from the target (or a sudden increase in absorption) has been discussed by Vilenskaya[57] and Nemchinov[58] in terms of surface plasmas.

Further measurements of ignition of absorption waves were performed with a 28-cm focal length lens (and mirror). This produced a minimum beam diameter of 2.4 mm with an elliptical focal spot on the target normally inclined at 30° to the beam axis. (The major diameter on target was 3 mm.) The results of Table 4 were determined by analyzing both the image converter photographs and the reflected power. (The reflected power technique is not feasible for highly absorbing targets such as lucite, silica, and lexan.) The determination of absorption waves for highly absorbing targets is difficult since these materials can produce both blast waves induced by vapor jets

TABLE 4

THRESHOLDS FOR IGNITION OF LASER-SUPPORTED ABSORPTION WAVES USING
A 28-CM FOC/L LENGTH LENS AND USING A NEW SPECIMEN FOR EACH TEST
AT ONE ATMOSPHERE THRESHOLD DETERMINED BY MEASURING REFLECTED
SIGNAL

Material	$E_T(J/cm^2)$	$q_{max}(watts/cm^2)$
Fused Silica	310	4.5×10^7
Lucite	310	4.5×10^7
Lexan (polycarbonate)	280	4.0×10^7
H_2O	220	3.2×10^7
Teflon	195	2.8×10^7
Copper	191	2.75×10^7
Painted Aluminum (.001 cm gloss black lacquer)	173	2.5×10^7
Titanium	160	2.3×10^7
Fiberglass Epoxy	158	2.3×10^7
Cork	144	2.1×10^7
Nickel	137	1.97×10^7
Tungsten	124	1.79×10^7
Soda Glass	106	1.52×10^7
Painted Aluminum (.004 cm red enamel)	85	1.22×10^7
Aluminum Foil	84	1.2×10^7
Aluminum 7075 Plate	75	1.08×10^7
Lead	68	$.98 \times 10^7$
Alumina	59	$.85 \times 10^7$
Painted Aluminum (.004 cm flat black lacquer)	42	$.60 \times 10^7$

and absorption waves. Near threshold, it becomes difficult to distinguish between the two classes of waves and indeed the image converter photographs show that during a single laser pulse that both types of waves can exist at different times of the laser pulse. The laser intensities, q_{max}, and the laser energy density, E_T, are defined, as in Table 3, using the first peak of the laser power and the laser spot size on the target. It should be noted by comparing the data of Tables 3 and 4 that threshold determinations using only luminosity as a guide tend to indicate lower thresholds than when the reflected target signal is used.

5.2 PRESSURE DEPENDENCE OF IGNITION OF LASER-SUPPORTED DETONATION WAVES

A pressure chamber was constructed for these measurements and is shown in figure 3. It has two NaCl windows, one to admit the incident beam and one to allow a detector to monitor the reflected beam. This pressure chamber was used with a 10-cm diameter 28-cm focal length KCl lens. A measurement of the focal spot on lucite gave a diameter of 0.24 cm, in agreement with previous indications. The experimenter sights through a cathetometer and the transparent walls of the lucite chamber to position the specimen at the focal spot. The target is usually inclined with its normal 30° above the incident horizontal beam.

The theory of LSD wave propagation indicates a sustaining power intensity that decreases as the background pressure decreases[2,3]. In our experiments, which of course include effects of both ignition and propagation of absorption waves, no such decrease in intensity was observed. In fact, the most interesting fact to come from these measurements is the diversity of ignition threshold behavior with pressure change as shown in figure 82. The three metals do appear to follow the same negative pressure dependence and their LSD wave ignition thresholds are found to be roughly in the same proportion as their melting temperatures: Ti: 3.25, Al: 1.56, Pb: 1[59]. Nonmetals either show no variation with pressure or
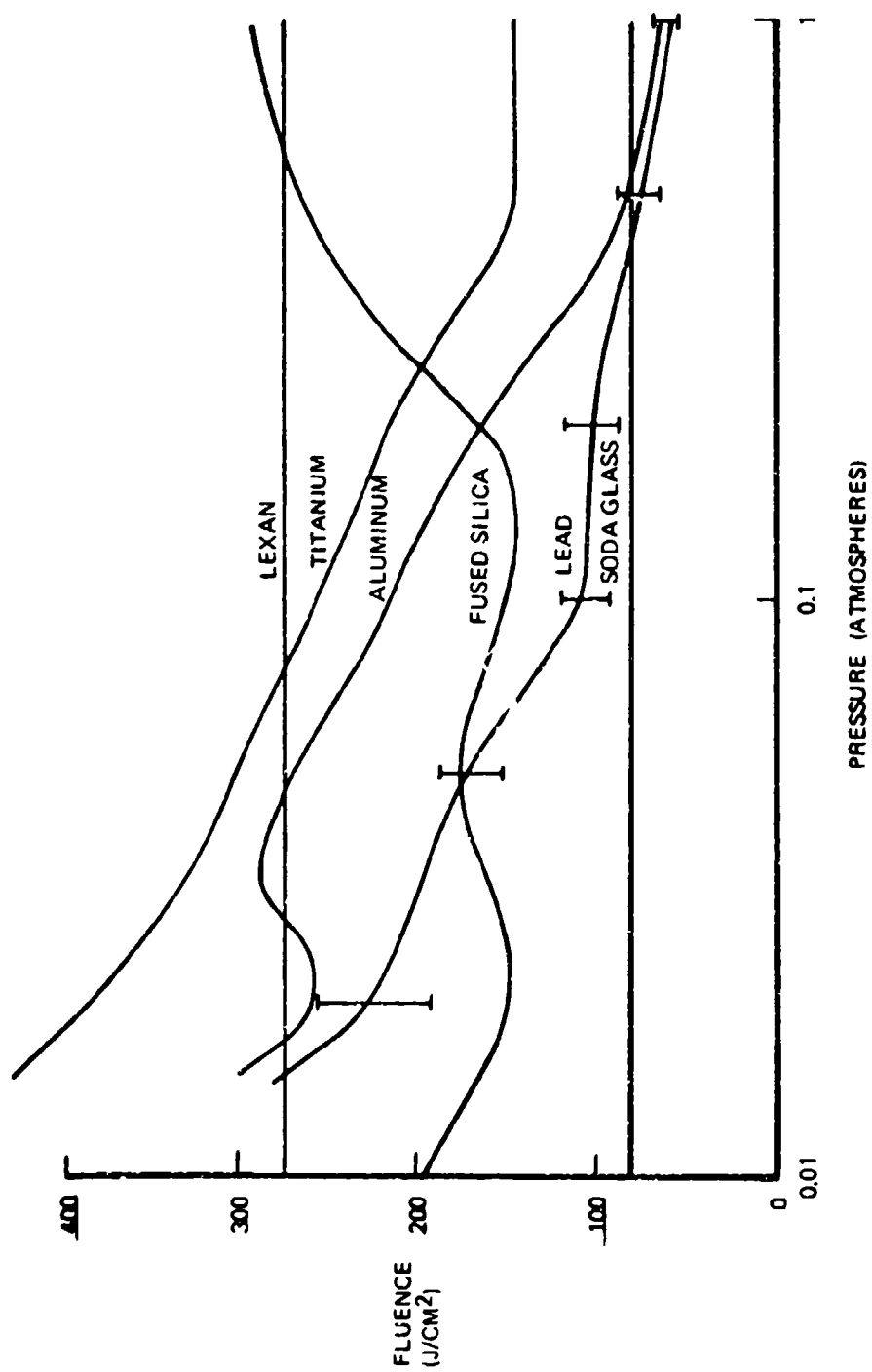
Figure 82: PRESSURE DEPENDENCE OF IGNITION THRESHOLDS OF LASER-SUPPORTED ABSORPTION WAVES FOR SIX SPECIMEN MATERIALS (ERROR BARS ARE SHOWN ONLY FOR LEAD)

132

else show an increased threshold as the pressure increases.

In figure 82, error bars are shown only for ignition thresholds for lead targets. These error bars arise because there is a statistical behavior of a given type of target material in igniting LSD waves. That is, repeating a given laser energy on two different samples of the same target material will not necessarily lead to the same ignition phenomena (especially near thresholds). In figure 82, the top of the error bar represents the energy density, above which LSD waves are always ignited. The bottom of the error bar represents the energy density level below which no LSD waves were ever ignited. The length of the error bar, at a given ambient pressure, then represents the statistical behavior of the given target material in igniting absorbing plasmas. These uncertainties were determined by analysis of the specularly reflected laser beam from the target, as discussed previously, and were approximately the same for all types of materials.

Another feature of LSD waves, as pressure is reduced, is the fading of any clear cut appearance in the photographs. Below 0.1 atmosphere, the framing camera record of LSD waves gradually begins to change to a more tenuous "blast wave" as shown in Section II. For this reason, the pressure dependence data in figure 82 should not be expected to tell the full story below 0.1 atmosphere even though it accurately reflects plasma blocking of the beam. It should also be stressed that this plasma blocking becomes a phenomenon with a shorter and shorter life as pressure is reduced.

SECTION VI
TARGET RESPONSE

This section discusses the response of several selected target materials to high-power laser beams. Target response includes such effects as melting, vaporization, and impulsive forces exerted on the target. All these damage mechanisms require coupling of laser energy either to the target surface or to the atmosphere surrounding the target. Coupling is dependent on an extremely large number of factors which can be divided into those effects that occur either in front of the target surface or at the target surface itself. In front of the target, laser-supported absorption waves occur which reduce the laser intensity reaching the surface. In addition, the vaporized blow-off material itself can interact both with the laser beam and with the ambient atmosphere to produce blast waves. Thus the gas-dynamic processes in front of the target are important in determining impulsive target loads generated either by direct reaction of the vaporized target or by the pressure disturbances produced by the absorption waves. All these plasma-related absorption effects also are crucial in determining the amount of laser energy reaching the target.

At the target surface, a complex sequence of effects occurs, including heating, vaporization and plasma generation. The energy coupled to the target surface by direct absorption at the surface depends on all the above factors as well as the surface reflectivity. We have accordingly performed several experiments whose goal is to determine target response as defined by impulsive forces, pressure distribution and material removal.

6.1 MATERIAL REMOVAL

A sequence of several hundred laser shots was used in order to determine energy requirements to remove target material at high power densities. The materials tested were Lucite and Lexan and were chosen because of their differences in forming LSD waves. As noted previously, both Lucite and silica ignite LSD waves from the first laser pulse incident on a chemically cleaned surface. Subsequent

134

pulses on the same spot do not ignite any absorption wave traveling
up the laser beam. This indicates a plasma surface cleaning ability.
On the other hand, a material such as Lexan (polycarbonate) is found
not to be cleaned by the plasma produced at the surface and LSD
waves are ignited with each subsequent laser pulse.

Data given in the appendix show the cross sectional area of
holes produced in Lucite and indicate the relatively smooth energy
density profile of the Marx Bank Laser. For Lucite, single shot
craters are shown in figure 83, where one sees an increasing crater
dimension with laser energy. It is interesting to note that for a
laser delivered energy of approximately 15 joules that we can obtain
two crater shapes, dependent on whether or not LSD waves were ignited.
The extreme right hand crater in figure 83 was produced when a LSD
wave was ignited. It should be noted that the shape tends to be
square (instead of circular). This phenomena is not related to
Lucite only but has been observed with several different materials.

Figure 84 shows the shapes of holes produced in Lexan at various
laser energies. The average energy density is found by dividing
the area of the laser spot (S $\approx$ .045 cm^2) and the peak intensity
(in watts/cm^2) is obtained by multiplying the laser energy by 3.2 x
10^6). One notes a qualitative change in the hole shape when LSD
waves are formed in Lexan. For Lucite, on the other hand, (see appen-
dix) no LSD waves were ignited even at the highest power density
(after the first "preliminary" pulse).

For both materials, Lexan and Lucite, we have measured the laser
energy required to remove material as a function of power density.
The basic data are shown in Tables 5 and 6. Crater volume was measured
with a microsyringe filled with methanol. The mass densities were
assumed to be 1.2 and 1.25 grams/cm^3, respectively for Lucite and
Lexan. The data given in Tables 5 and 6 are plotted in figure 85.
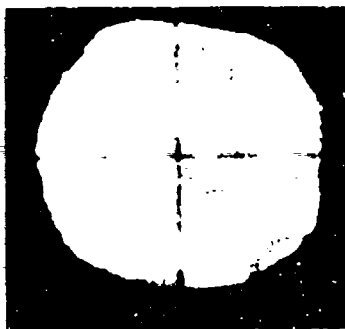
14 JOULES
(LASER-SUPPORTED
DETONATION WAVE)

14 JOULES

7 JOULES

1.8 JOULES

2 mm
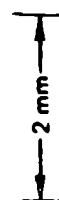
Figure 83: LASER-PRODUCED CRATERS IN LUCITE

136

Figure 84: *LASER-PRODUCED HOLES IN POLYCARBONATE (LEXAN) AS DEPENDENT ON POWER DENSITY*

TABLE 5

MATERIAL REMOVAL FROM LUCITE AS A FUNCTION OF POWER DENSITY

Joules Per Laser Shot	Joules/ cm^2	Maximum Intensity q (watts/ cm^2)	Number Of Shots	Maximum Penetration Depth (Total) (Milli-Meters)	Total Volume (Micro-liters)	Kilo-Joules Per Gram
1.1	24.4	3.5×10^6	17	.87	3.25	4.75
1.9	42.2	6.0×10^6	13	1.09	4.92	4.15
3.5	77.8	1.1×10^7	10	1.47	7.13	4.1
8.1	180	2.6×10^7	6	1.52	7.5	5.3
16	356	5.1×10^7	4	1.7	8.7	6.15

TABLE 6

MATERIAL REMOVAL FROM LEXAN (POLYCARBONATE) AS A FUNCTION OF POWER DENSITY

Joules Per Laser Shot	Joules/ cm^2	Maximum Intensity q (watts/ cm^2)	Number Of Shots	Maximum Penetration Depth (Total) (Milli-meters)	Total Volume (Micro-liters)	Kilo-Joules Per Gram
.31	6.87	$.99 \times 10^6$	27	.2	.5	13.5
1.1	24.3	3.48×10^6	17	.56	1.85	8.1
1.65	36.7	5.25×10^6	20	1.2	4.95	5.4
3.89	86.4	1.24×10^7	10	1.35	5.4	5.8
8.05	179	2.6×10^7	10	1.14	3.	21.4
8.2	182	2.61×10^7	10	1.03	6.2	10.7
15	333	4.8×10^7	12	.98	2.1	66
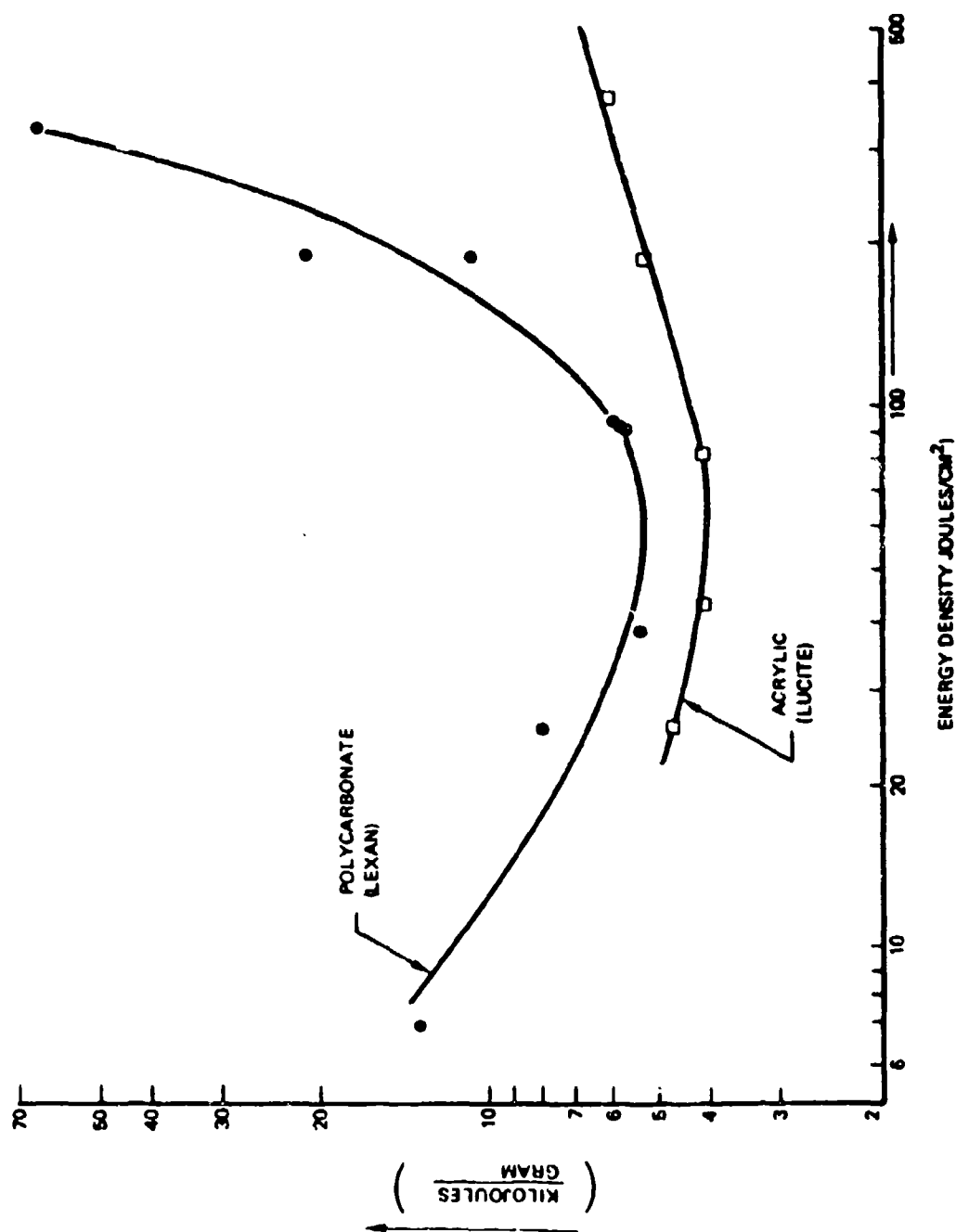
Figure 85: LASER ENERGY PER GRAM REQUIRED TO REMOVE MATERIAL FROM BOTH POLYCARBONATE AND LUCITE AS A FUNCTION OF ENERGY DENSITY. MULTIPLY ENERGY DENSITY ORDINATE BY 1.44 X 10^5 TO OBTAIN PEAK INTENSITY IN WATTS/CM^2.

The energy required to remove mass is much greater for Lexan (polycarbonate) than for Lucite (acrylic) for power densities greater than 2×10^7 watts/cm^2. This occurs, of course, because of the formation of LSD waves from Lexan. From figure 85 one finds, for $q > 1.4 \times 10^7$ watts/cm^2, that the joules per gram required to remove polycarbonate increases as nearly the 1.5 power of intensity due to the ignition of LSD waves. For Lucite, on the other hand, the joules per gram increases as only the one-third power of intensity which is due to plasma absorption in the blow-off target material. It is interesting to note that the peak intensity at which the energy removal rate decreases rapidly for Lexan (approximately $q = 1.4 \times 10^7$ watts/cm^2) is approximately one-third the intensity required for ignition of laser-supported absorption waves as indicated in Table 4.

6.2 IMPULSE

The laser-delivered impulse to several targets was measured with a linear velocity transducer (LVT) in the geometry shown schematically in figure 86. The LVT (Trans-Tek model 100,000) had a sensitivity of 48 millivolts per cm/sec. By measuring the peak voltage response of the LVT after pulsing the target with the laser beam, one determines the delivered impulse. This is done by measuring both the target and core mass and using the elementary relation

$$I = mV \tag{17}$$

where

I = delivered impulse (dyne-sec)

m = total target mass (grams)

V = target velocity (cm/sec)

(In equation 17, I represents impulse and not laser intensity).
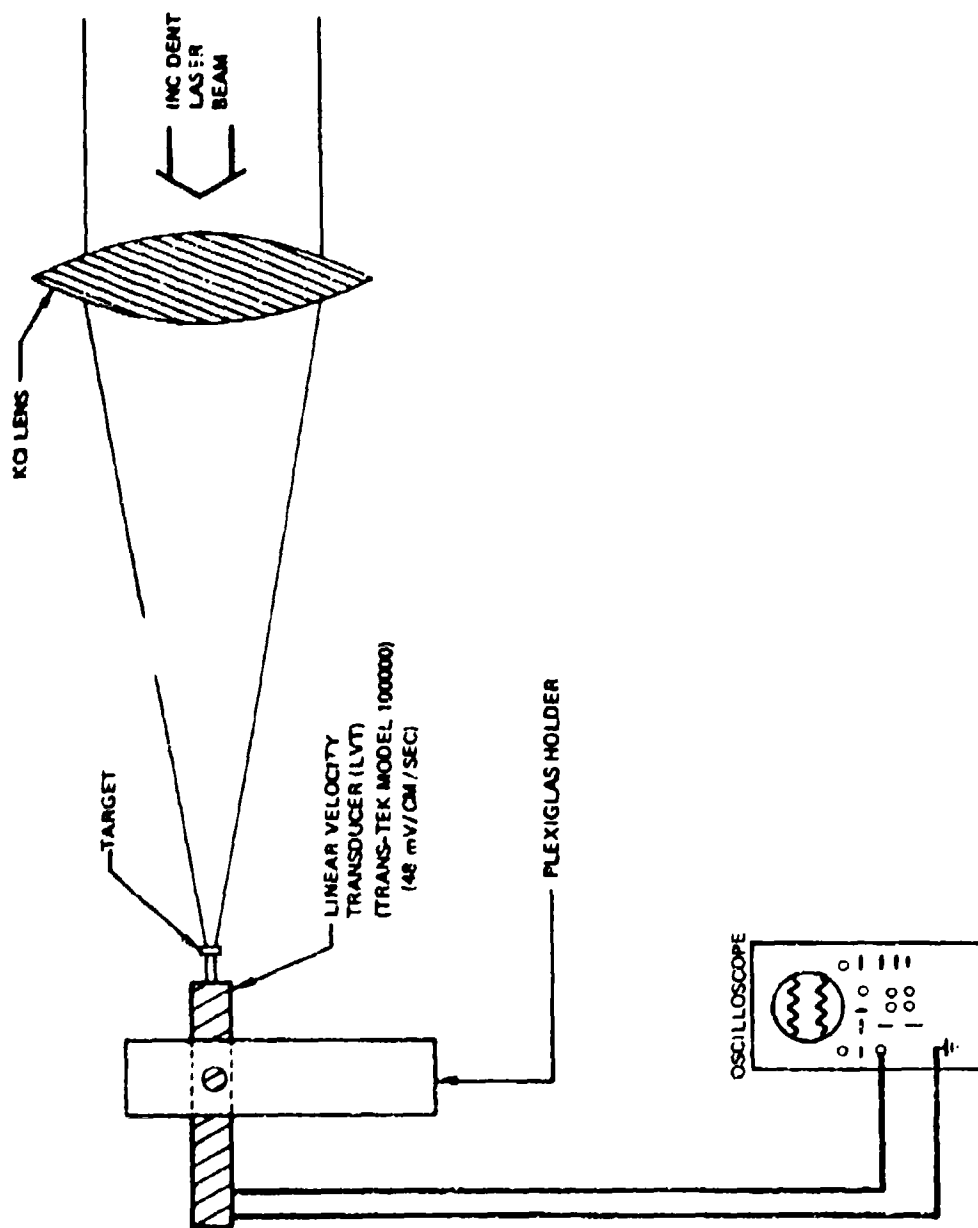
Figure 86: *SCHEMATIC DIAGRAM OF LINEAR VELOCITY TRANSDUCER (LVT) EXPERIMENT USED TO MEASURE SPECIFIC IMPULSE.*

142

Figure 87 shows the variation of impulse delivery with energy density to a Lucite target. The target had a square cross-sectional area (.64 cm on a side) and a mass of .19 gram. One notes an increase in impulse to a maximum $I/E \doteq 9$ dyne-sec/joule.

Assuming all the laser energy was delivered in an area of $S = .045$ cm^2 and an effective energy delivery time interval $t = 15$ microseconds, one finds an average pressure $\bar{p}$ of

$$\bar{p} = \frac{I}{tS} \doteq \frac{(14)(9)}{(15)(.045)} = 187 \text{ atmospheres} \tag{18}$$

The results of figure 87 should be compared with the results of Rudder[8] where LSD waves were ignited and obviously greatly reduced delivered impulse.

In the presence of LSD waves, the delivered impulse for a Lucite target is greatly reduced as seen by the single point on figure 87 at a delivered energy of 17.5 joules. This particular case was obtained as the first shot on a fresh Lucite sample which ignited a LSD wave. As noted previously, such a first pulse "cleans" the target surface and subsequent pulses do not ignite LSD waves.

Aluminum alloy targets, on the other hand, tend to ignite LSD waves even with many laser shots on the same focal spot. As a consequence, the delivered impulse is quite low as seen from figure 88. The data here consisted of two different kinds of targets. The smallest target was a circular disk of .42 cm diameter. The larger targets had a square cross-sectional area with dimensions of .64 and 1.27 cm. It is evident, as previously noted[7], that the delivered impulse does tend to increase as the area of the target increases. This effect is due to the existence of the radially
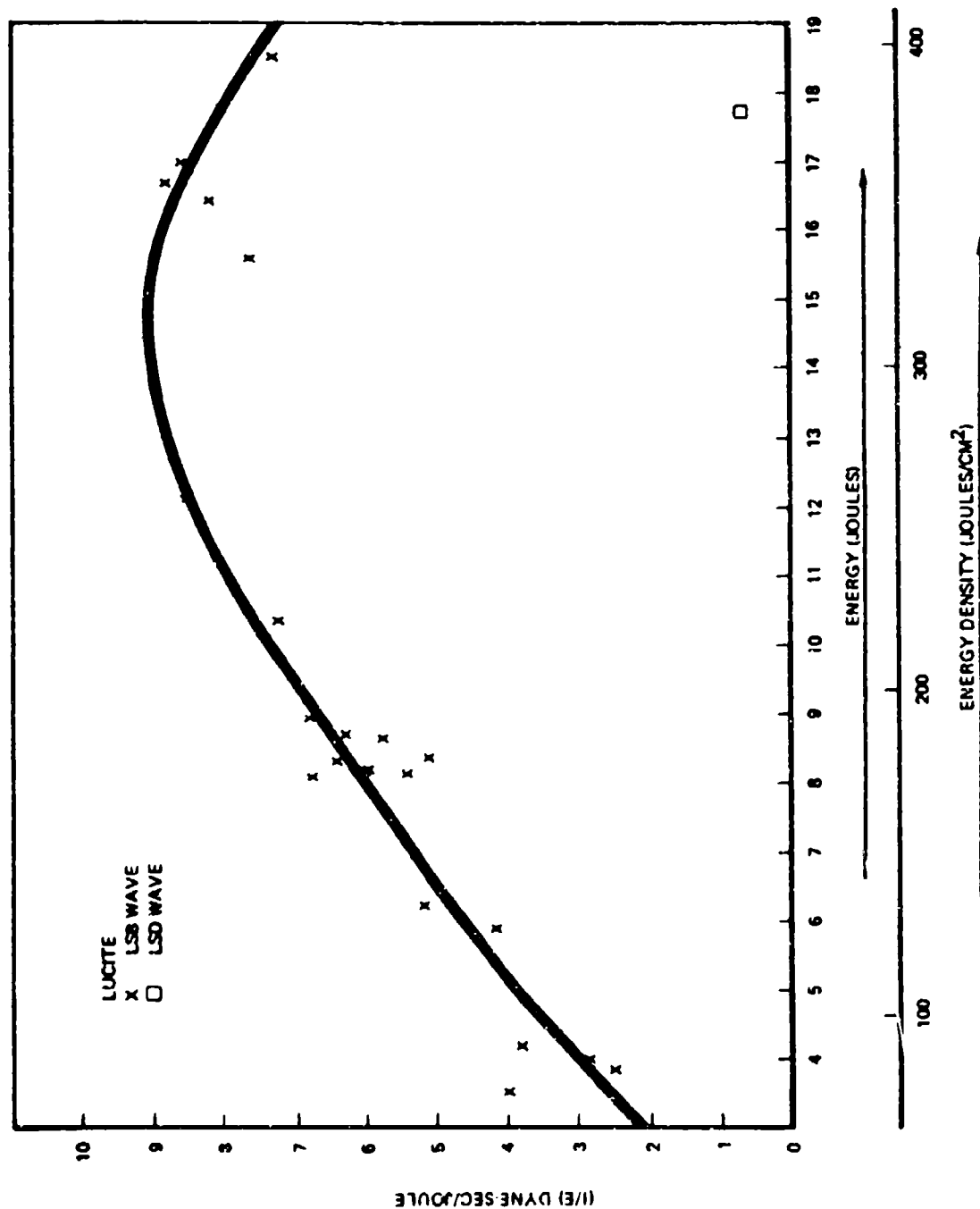
Figure 87: VARIATION OF SPECIFIC IMPULSE I/E FOR LUCITE AS A FUNCTION OF ENERGY DENSITY. MULTIPLY ENERGY DENSITY BY 1.44×10^5 TO OBTAIN PEAK INTENSITY IN WATTS/CM^2.
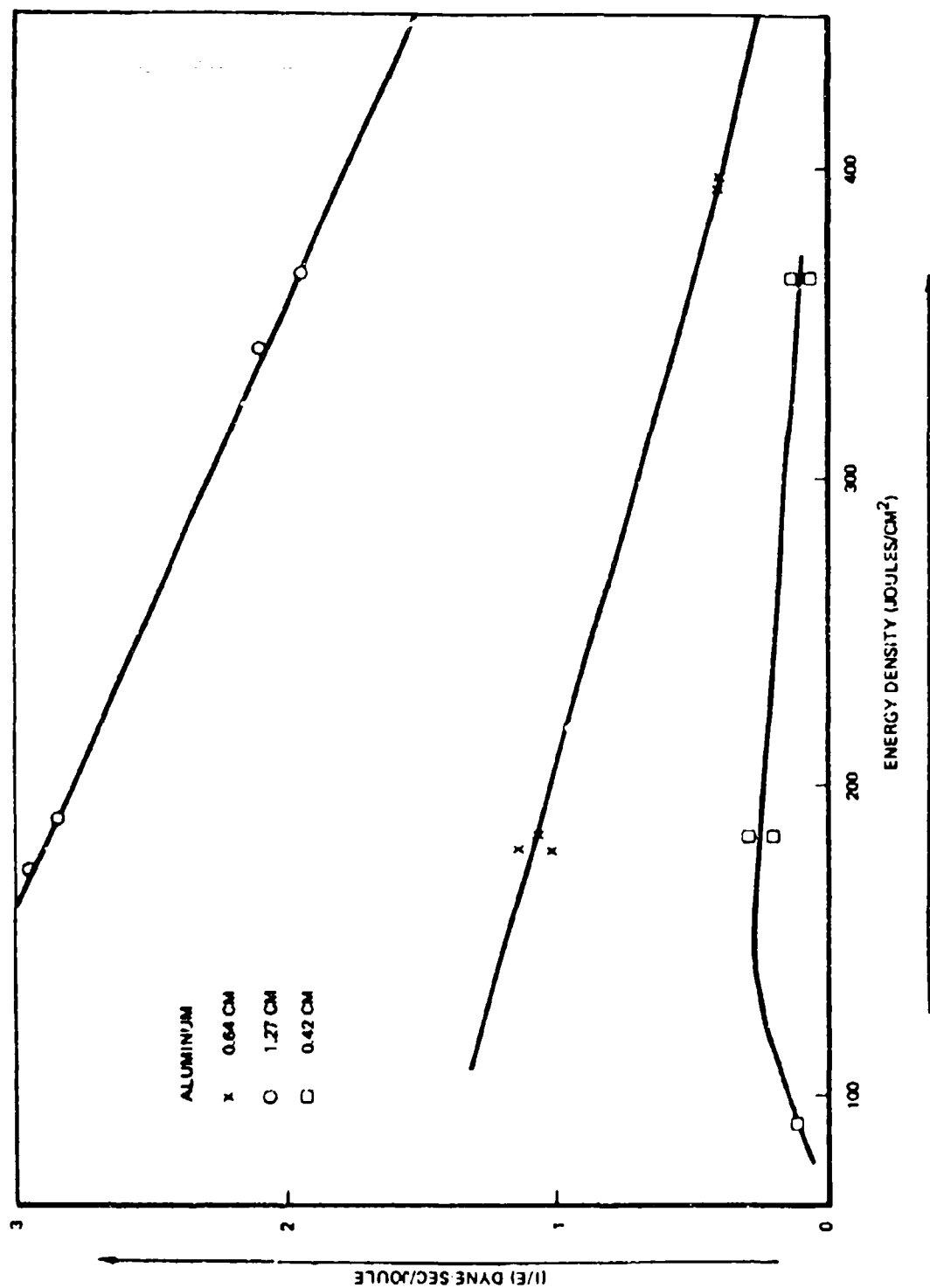
Figure 88: VARIATION OF I/E FOR ALUMINUM VERSUS INTENSITY WHEN LASER-SUPPORTED DETONATION WAVES ARE IGNITED. CURVES WITH TARGET AREAS OF .14, .41 AND 1.61 CM² ARE GIVEN.

145

driven shock wave sweeping across the target plane. This shock
wave is similar to a blast wave with its energy source the laser
energy transferred to the gas motion behind the front of the LSD
wave[9]. Our present amount of date doesn't permit an accurate
determination of a scaling law for the dependence of I/E on target
area. However, one can see from figure 88, that to a first
approximation that I/E is nearly linearly proportional to target
area.

It should be noted that the total impulse delivered to targets
when LSD waves are ignited is considerably less than that when the
primary impulse is due to target vapor blow-off. For this reason,
one expects less of a dependence of I/E on target dimensions for
Lucite targets than for aluminum (or other metal) targets.

6.3 PRESSURE MEASUREMENTS

An acousto-optical pressure transducer has been utilized to
make pressure measurements in the vicinity of laser-supported
detonation waves[60]. This transducer is based on the principle
of an air pressure wave (or shock wave) coupling to an acoustic
wave in a transparent glass rod. The pressure wave induces
birefringence in the rod through the stress-optic mechanism. The
induced birefringence is monitored optically by measuring the intensity
variation of one of the components of a circularly polarized light
beam passing through the diameter of the rod. A thin rod is used
in order to obtain good high-frequency response. (In our case, the
acoustic wave transmitted down the rod is nearly dispersionless
for frequency components less than one megacycle.)

Figure 89 shows an exploded view of the pressure transducer.
The laser (in our case, a He-Ne spectra-physics Model 119) emits
a linearly polarized beam of light which is changed into a circular
polarization by a quarter-wave plate. The beam is then focused
by a lens at the center of the glass rod. An acoustic wave (or
pressure pulse) incident on the end of the glass rod will be

146

ACOUSTO-OPTICAL PRESSURE TRANSDUCER FOR DETONATION WAVE DIAGNOSTICS

o STRESS WAVE DETECTED OPTICALLY

o MICROSECOND RESOLUTION

o PROVIDES ACOUSTICAL DELAY TO ELIMINATE
  ELECTRICAL NOISE INTERFERENCE
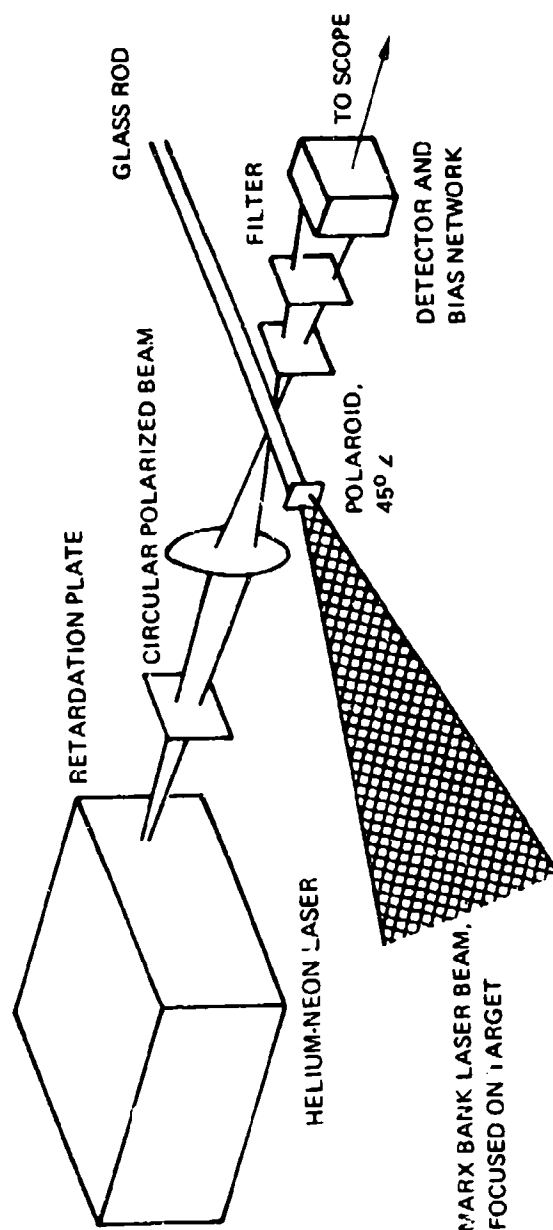
Figure 89:   EXPLODED VIEW OF ACOUSTO-OPTICAL PRESSURE PROBE FOR LASER-
              SUPPORTED DETONATION WAVE STUDIES.

transmitted down the glass rod as a one-dimensional acoustic wave.
(A one-dimensional wave is produced for low enough frequencies[61].)

In figure 89, the laser target is shown mounted directly to
the end of the glass rod, however, in most of our experiments this
was not done. The stresses generated in the glass rod by the
acoustic wave modify the state of polarization of the initially
circularly polarized beam. As a consequence, the beam exiting from
the glass rod is elliptically polarized. The change in polarization
of the beam can then be determined by mounting a polarizing filter
(Polaroid) with transmission inclined at 45° to the rod axis. For
small enough stresses, the variation of the detected signal at the
detector is then linearly proportional to the stress in the rod.
This device automatically provides a delay between the input
pressure pulse and the detector output and is useful in reducing
electrical interference (such as caused by the Marx Bank electrical
laser)

It is particularly of interest to determine the pressure
distribution excited in the plane of a target from which a laser-
supported detonation has been ignited. This is important since the
pressure waves induced by the LSD wave interact with the target
to produce additional impulse. To evaluate this mechanism, however,
one must also know the pressure time history at the surface.
Figure 90 shows a schematic diagram of the measurement scheme. The
pressure transducer is mounted on a moveable table constructed from
a milling table head and can be moved relative to the fixed ignition
position of the LSD wave. The transducer glass rod of diameter 2 mm
is moved in the slot (of width 2.5 mm). By changing the distance
r (from the rod to the center of the focal spot) and making a sequence
of laser shots, one can determine the pressure history in the target
plane. At this point, no estimate of the perturbing effect of the
slot on the measurement is available.
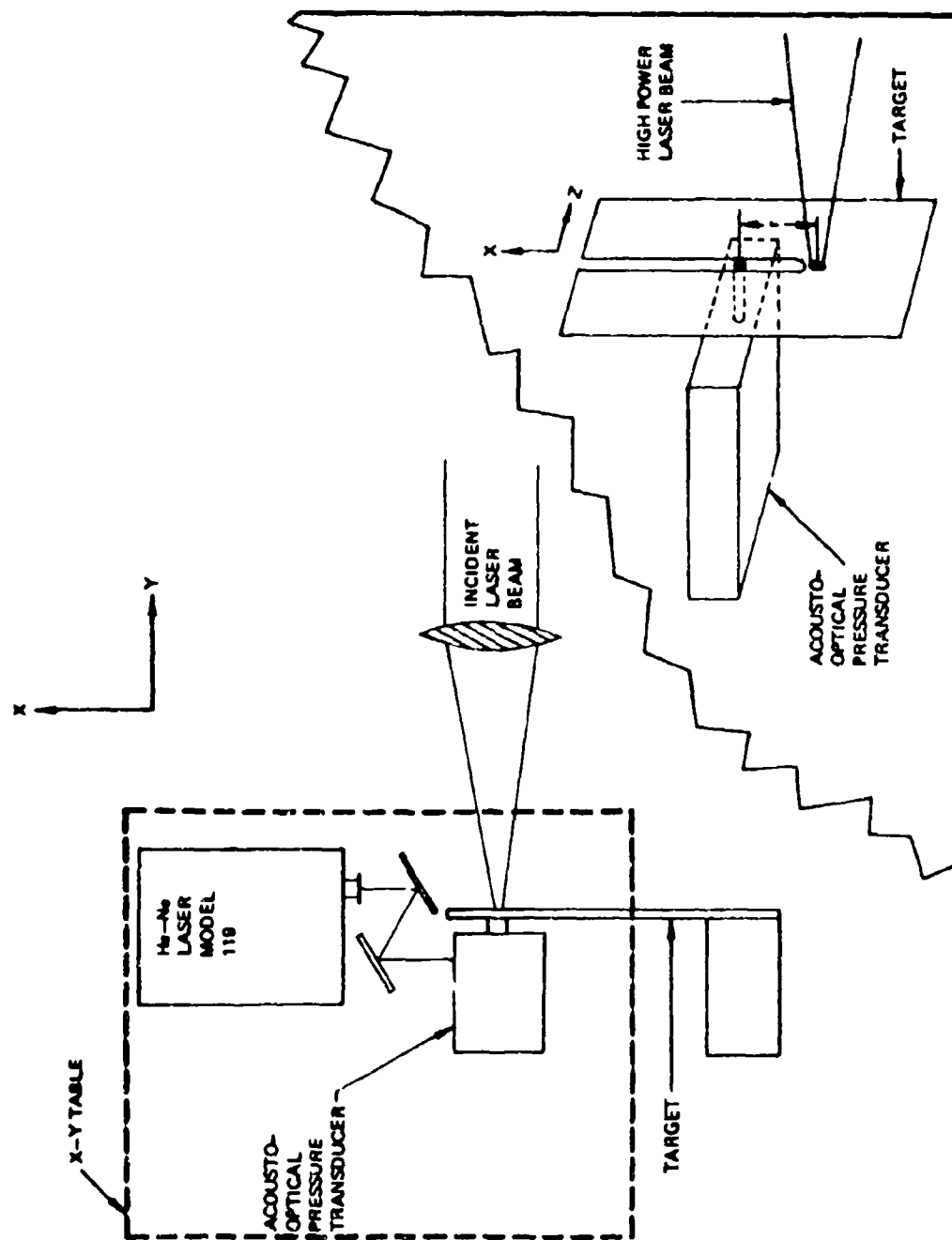
Figure 90: SCHEMATIC DIAGRAM OF PRESSURE MEASUREMENT EXPERIMENT IN THE TARGET PLANE.

An example of pressure histories taken at r = .51 and r = .89 cm is given in figure 91. The acoustic delay $t_A \simeq 7\mu sec$ is constant for each laser shot and caused by the acoustic delay time from the tip of transducer glass rod to the He-Ne laser beam. One can clearly determine the additional time delay caused by the finite shock speed across the target plane. This additional time delay is plotted versus position in figure 92. One determines that the radial position R of the front of shock wave is very closely approximated by the empirical relation

$$R = .26 \left(\frac{E}{17}\right)^{.16} \left(\frac{t}{10^{-6}}\right)^{.65} \text{ cm} \tag{19}$$

where E is the laser delivered energy (joules) and t is the time from ignition of the LSD wave.

The corresponding Mach number of the radial shock wave is

$$M = 5.1 \left(\frac{10^{-6}}{t}\right)^{.35} \left(\frac{E}{17}\right)^{.16} \tag{20}$$

As noted from figure 91, the peak pressure in the radial shock wave is also reduced in magnitude as the wave reaches larger distances from the laser beam axis. This dependence of maximum pressure in the radial wave is shown in figure 93. In this case, one finds

$$\text{maximum pressure} \simeq E^{.16} r^{-1.27} \tag{21}$$

where r is the distance to the center of the laser spot.

150
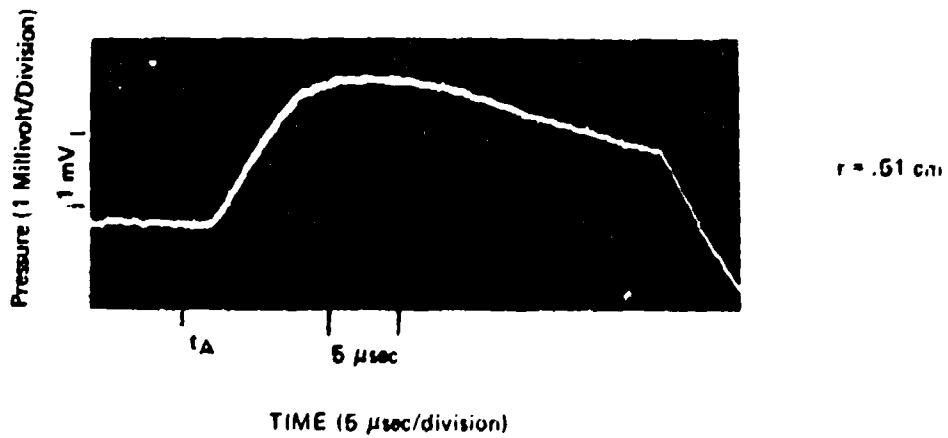
Figure 91: PRESSURE RESPONSE OF TRANSDUCER AT TWO RADIAL POSITIONS
(r = .51 and r = .89) IN THE PLANE OF TARGET. TO OBTAIN PRESSURE
IN ATMOSPHERES MULTIPLY THE ORDINATE BY 6.6.
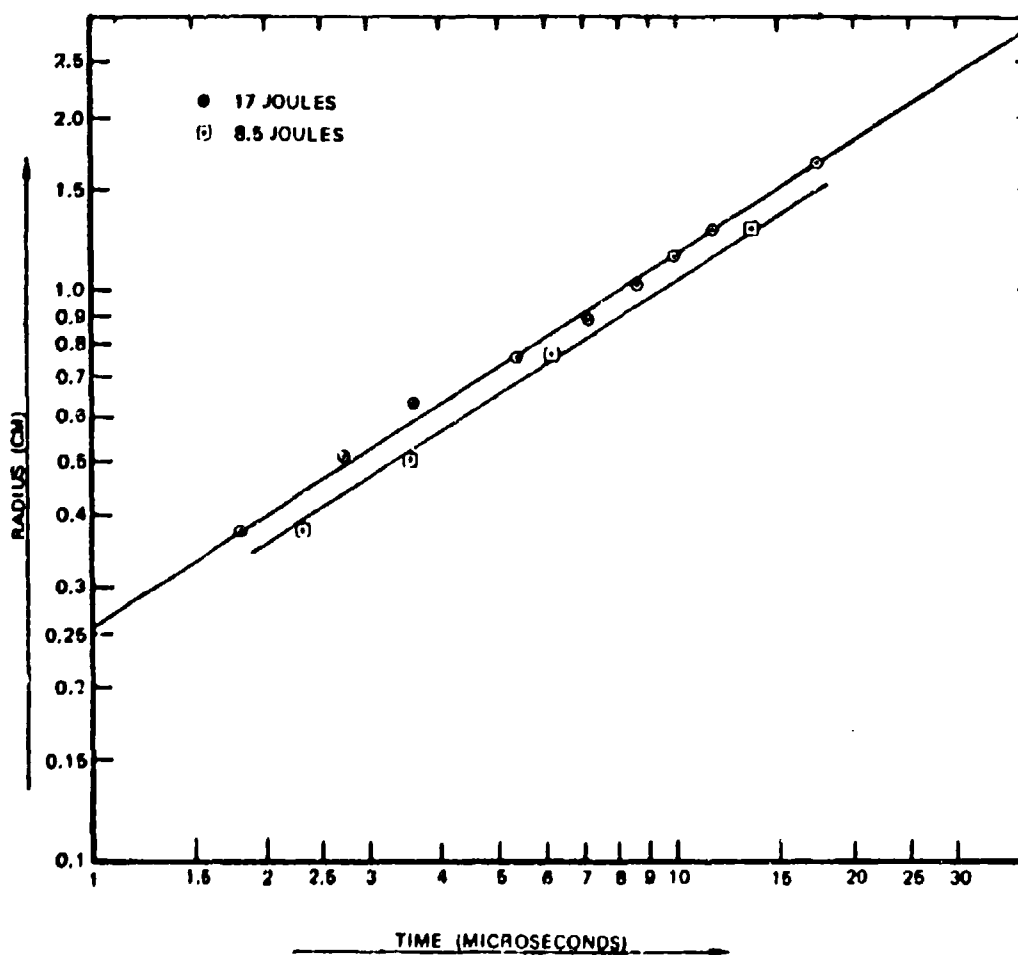
Figure 92: *RADIUS VERSUS TIME PLOTS FOR ENERGIES OF 17 AND 8.5 JOULES SHOWING THE EXPANSION OF THE RADIAL SHOCK WAVE AT THE TARGET SURFACE.*
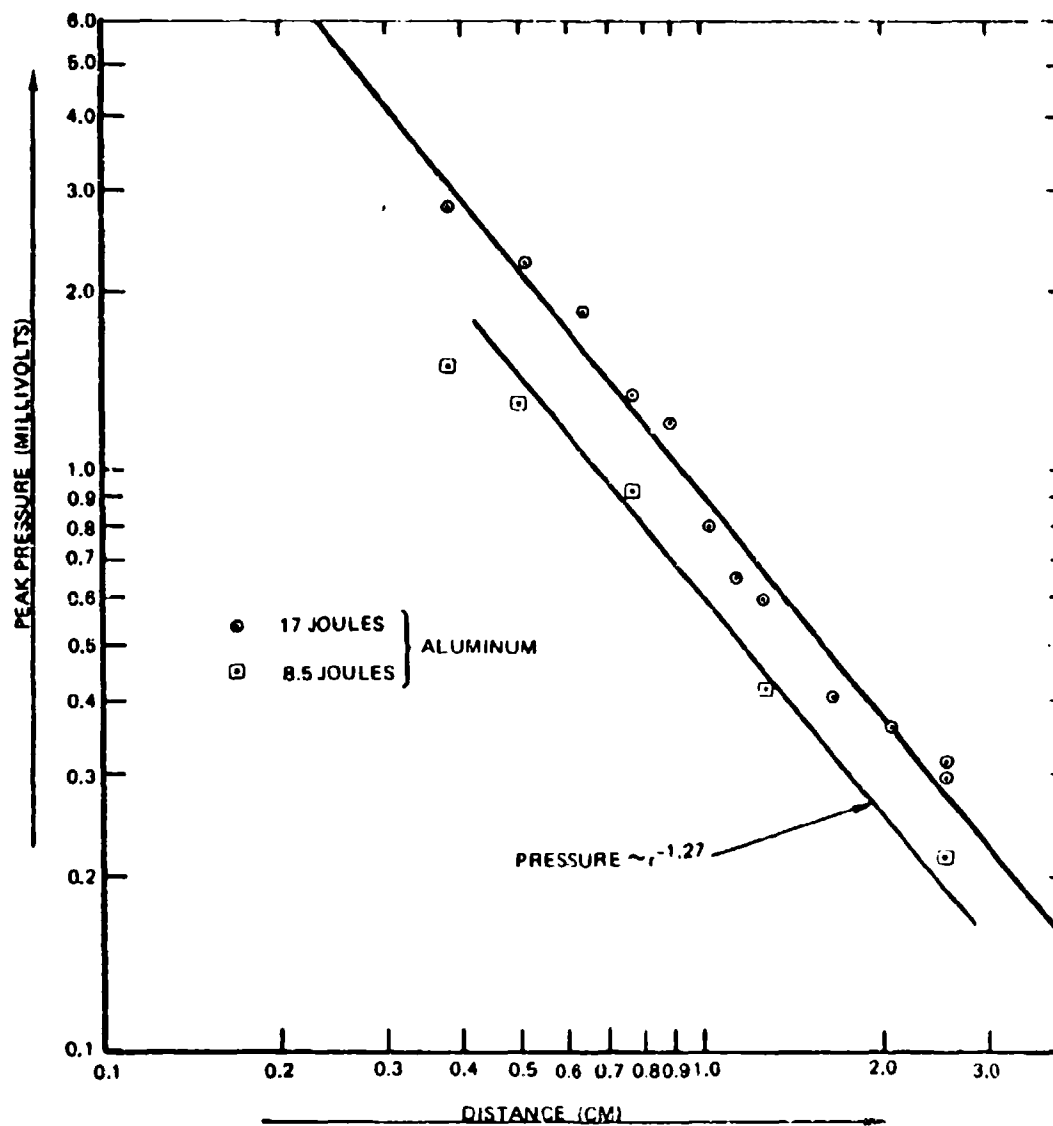
Figure 93: PEAK PRESSURE VERSUS DISTANCE OF THE RADIAL SHOCK WAVE FOR ENERGIES OF 17 AND 8.5 JOULES. MULTIPLY THE ORDINATE IN MILLIVOLTS BY 6.6 TO OBTAIN PRESSURE IN ATMOSPHERES.

The data given in figures 92 and 93 and in equations 19, 20, and 21 are for an aluminum alloy target.

The calibration of this pressure transducer was performed by comparing the pressure-time history of the transducer with the previously measured impulse. In particular, a .64-cm diameter Lucite target was attached to the glass rod transducer end. The 10.6μ high power laser was then focused on this target as shown in figure 89. The transducer response of this target for a CO_2 energy of 17 joules, reached a peak of 30 millivolts at a time 15μsec after firing the laser. The pressure decayed nearly linearly in time to essentially zero at a time of 44μsec after start of the laser pulse. Since Lucite relies only slightly on the air shock wave to produce impulse, one can assume that the pressure is distributed only over the laser spot of area $S = .045$ cm^2. From figure 87, the measured impulse in this situation is approximately

$$I = (17)(8) = (136) \text{ dyne-sec} \tag{22}$$

Since we know the pressure versus time, one finds the maximum P_o at the laser spot to be

$$P_o = \frac{2I}{St_2} \tag{23}$$

where $t_2 = 44$μsec is the maximum time the pressure existed. Evaluating equation 23, one finds

$$P_o = \frac{(2)(136)}{(.045)(44)} = 137 \text{ atmospheres} \tag{24}$$

The pressure given by equation 23 is delivered over the beam area of .045 cm^2, however, the transducer area is smaller which means the acoustic pressure in the rod is larger by the ratio of areas which is 1.44. This means that the calibration of transducer voltage (U millivolts) versus rod pressure P_r is given by

$$P_r = \frac{(137)(1.44)}{30} \ U = (6.6) \ U \ \text{atmospheres} \tag{25}$$

Thus, one needs to multiply the scale of figure 93 in millivolts by 6.6 to obtain shock pressure in atmospheres.

Another sequence of data was taken with the acousto-optic transducer mounted so that the radial shock wave hits head on toward the gauge. A schematic diagram of this setup is shown in figure 94. Data were taken for various values of axial and radial positions and an example of these pressure-time histories is shown in figure 95. One notes, by comparison with figure 91, that the transducer response has a much faster rise time. The data of figure 95 were taken at an axial position of $Z = .15$ cm in front of the aluminum target and with 17 joules of CO_2 laser energy delivered to the target and LSD waves were ignited in all cases.

The faster rise time shown in figure 95 is due, in part, to the finite diameter of the glass rod (D = 2 mm). One estimates from equation 19 that the radial shock wave at a position $r = .51$ cm takes approximately 1.7μsec to completely engulf the 2 mm glass rod tip. This delay time does not completely account for the slow rise time as shown in figure 91, however. This difference, perhaps, is caused by the dynamic effect of reflected pressure waves in the case shown in figure 94.

A sequence of data taken with an aluminum target at several axial positions is given in figure 96. One notes a somewhat faster
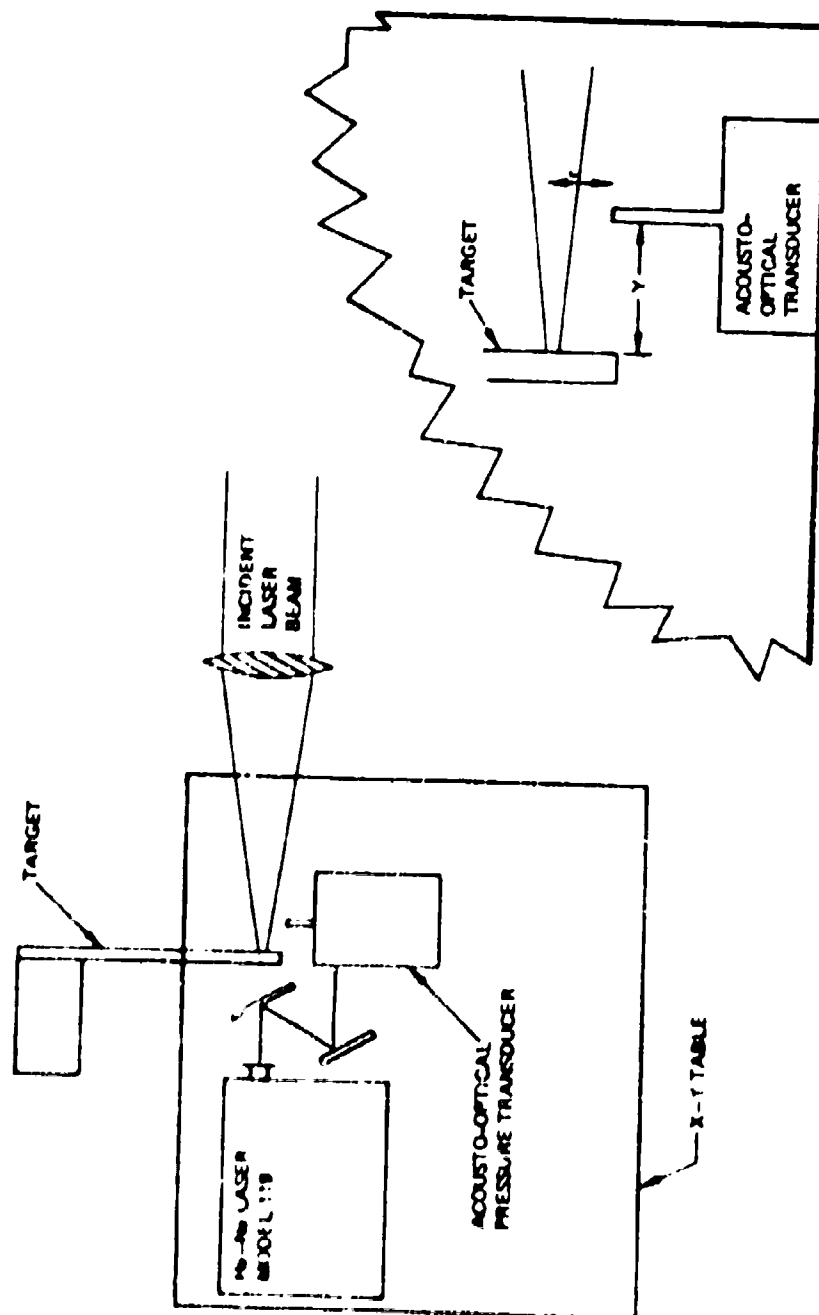
Figure 94: SCHEMATIC DIAGRAM OF PRESSURE MEASUREMENT EXPERIMENT TO DETERMINE RESPONSE IN FRONT OF THE TARGET.
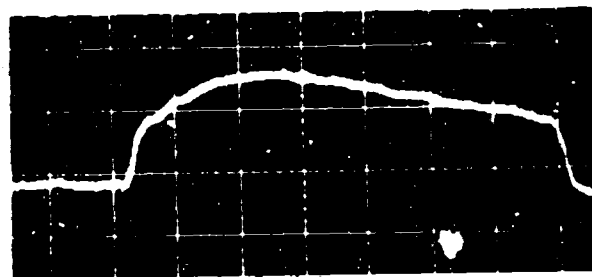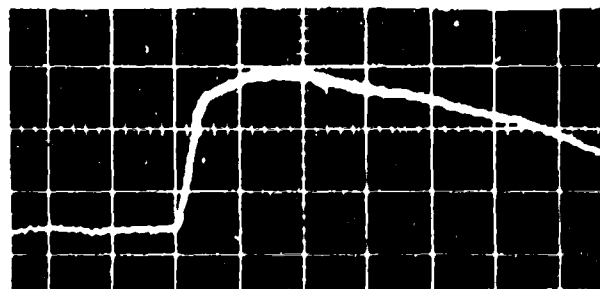
Figure 95: OSCILLOSCOPIC TRACES OF PRESSURE RESPONSE AT RADII OF .51 AND .89 CM. THE PRESSURE PROBE WAS NEARLY PERPENDICULAR TO THE RADIAL SHOCK WAVE. CONVERT TO PRESSURE IN ATMOSPHERES BY MULTIPLYING THE ORDINATE BY 6.6.
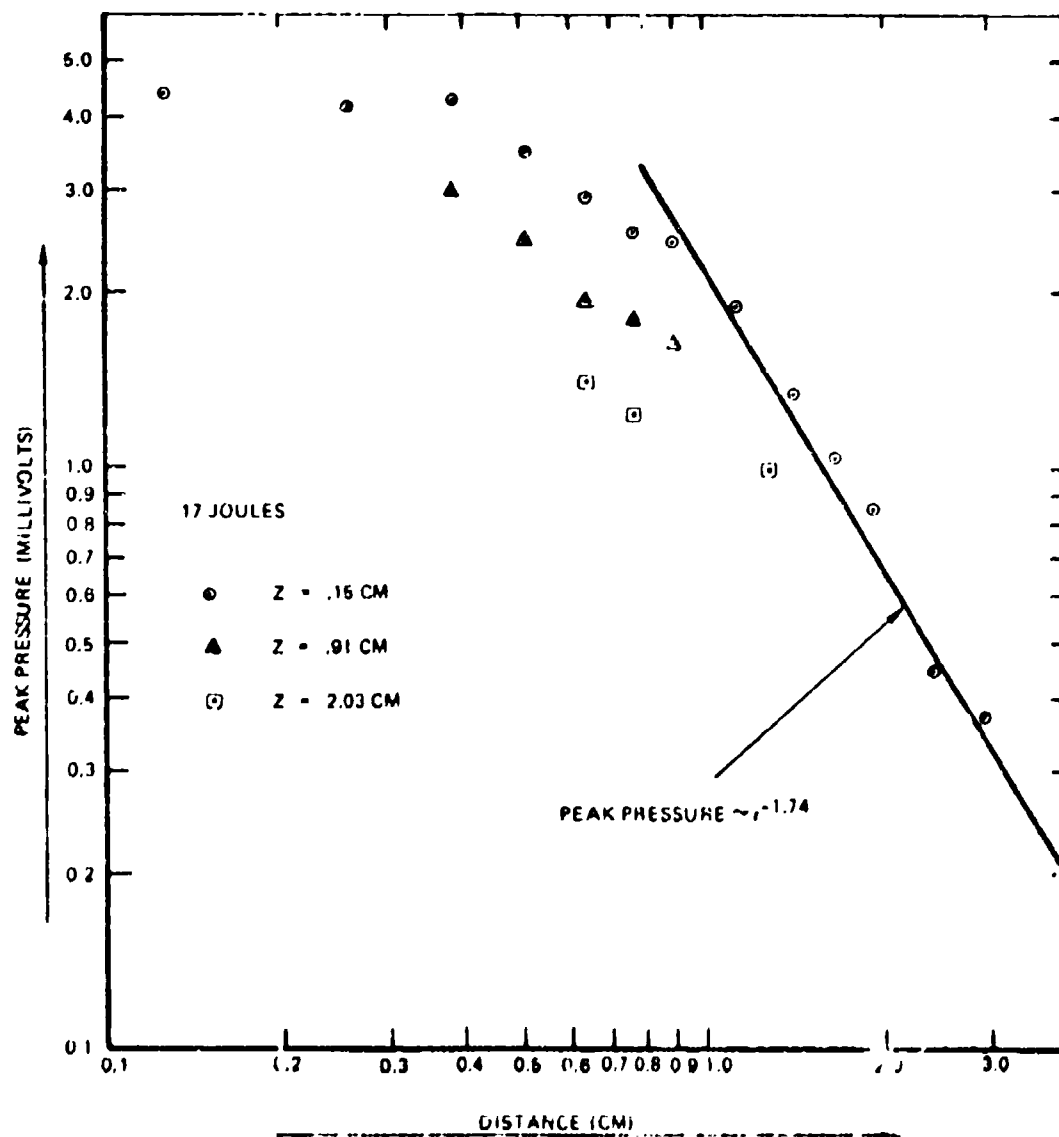
Figure 96: VARIATION OF THE RADIAL SHOCK WAVE STRENGTH AS A FUNCTION OF RADIUS FOR THREE AXIAL POSITIONS.

fall-off of peak pressure with radial distance in this geometry than with the transducer in the target plane. It is evident that the axial decrease in peak pressure is much less than that in the radial direction. This seems reasonable when one considers that the LSD wave ifself travels in the Z direction and as a consequence, should "drag along" its peak pressure. This is made somewhat more visible in figure 97 which shows a three-dimensional plot of the pressure variation given in figure 96.

Finally, a similar scan, shown in figure 98, of pressure versus radial position was taken with Lucite as the target. In this case, the CO_2 laser energy delivered to the target was 8.5 joules and the axial position was again Z = .15 cm. One notes by comparison with the data of figure 96 (aluminum target with 17 joules and ignition of LSD waves) that the peak air pressures associated with the Lucite target (where no LSD waves were ignited) are greater than those air pressures generated in the presence of LSD waves.

PRESSURE DISTRIBUTION
NEAR AN LSD WAVE
(ALUMINUM TARGET
17 JOULES)
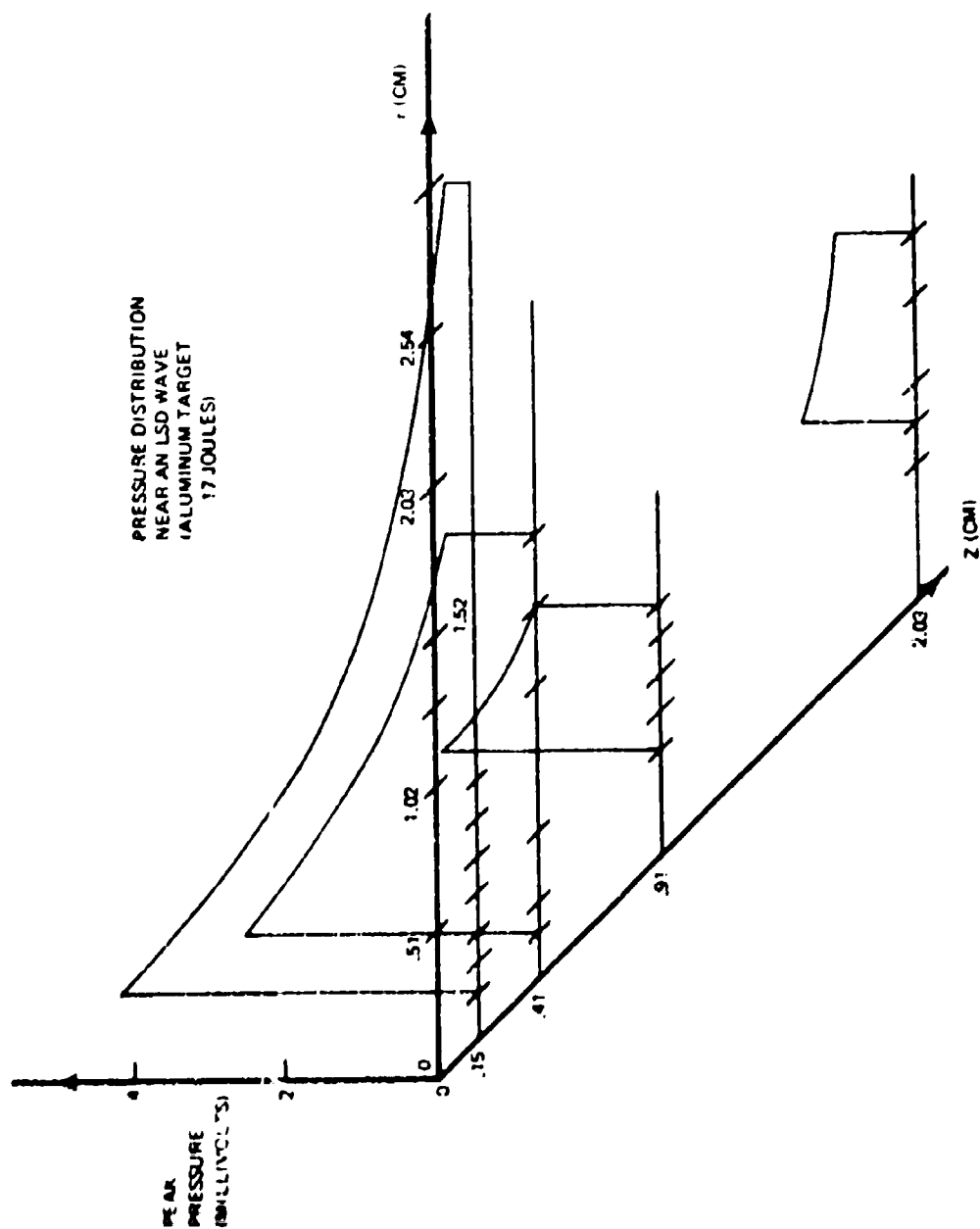
Figure 97. THREE DIMENSIONAL EXPERIMENTAL PLOT OF PEAK PRESSURE AS A FUNCTION OF Z AND r. MULTIPLY THE ORDINATE IN MILLIVOLTS BY 6.6 IN ORDER TO OBTAIN PRESSURE IN ATMOSPHERES.
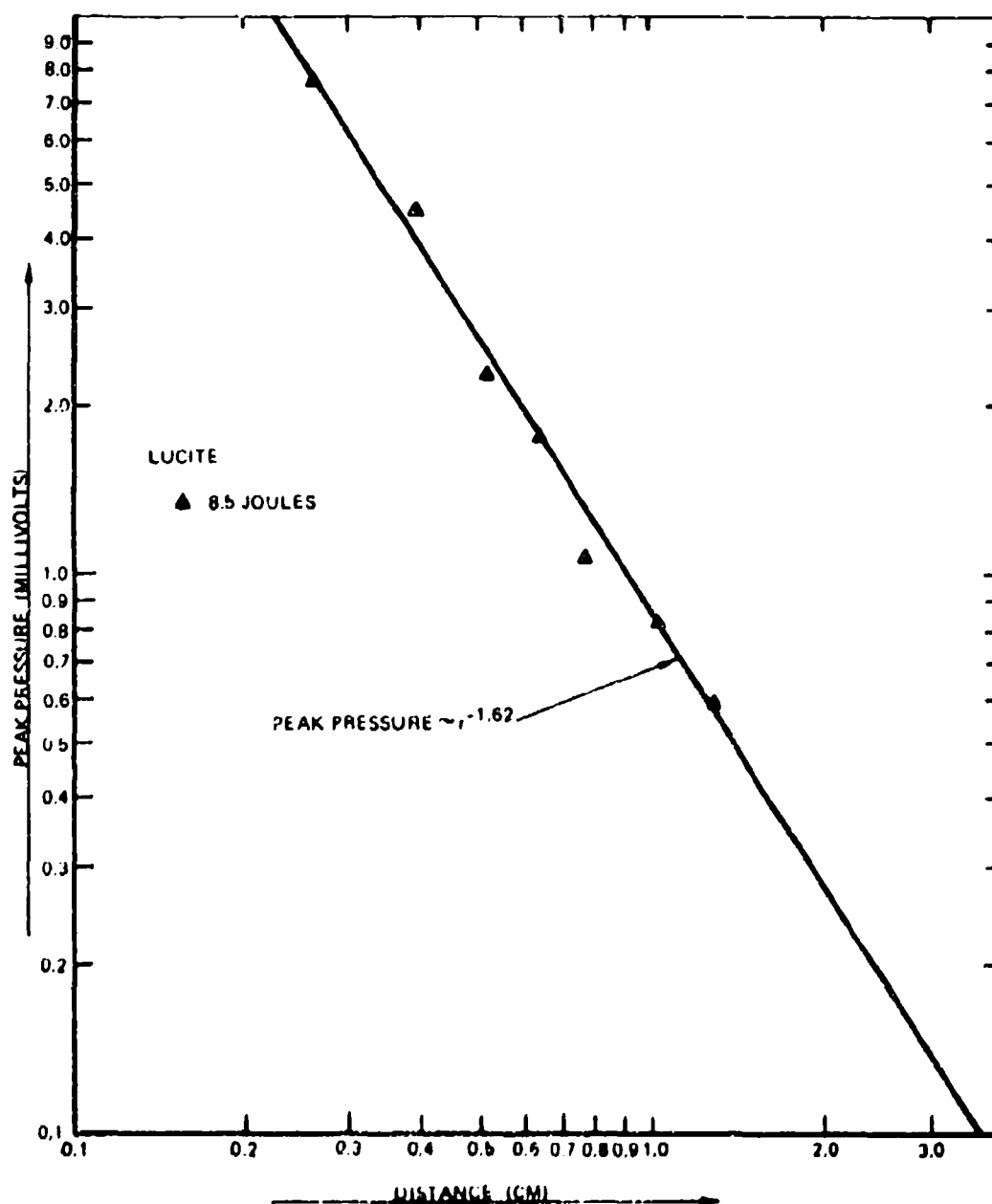
Figure 98: *PEAK PRESSURE AS A FUNCTION OF RADIUS FOR AN AXIAL POSITION OF Z = .15 cm.
THE TARGET WAS LUCITE AND THE LASER ENERGY WAS 8.5 JOULES. TO OBTAIN
THE PRESSURE IN ATMOSPHERES MULTIPLY BY 6.6.*

SECTION VII

A THEORETICAL INVESTIGATION OF LASER-SUPPORTED COMBUSTION WAVES

7.1 BACKGROUND AND INTRODUCTION

The existence of high-frequency and high-pressure electrodeless discharge is a well known phenomenon. These discharges include induction discharges where a high-frequency current is used to create a gas breakdown inside a solenoid[62]. In these cases, the frequency of the electromagnetic field is of the order of 1 to 100 megacycles, RF powers of the order of several kilowatts are used, and the gas temperature reaches approximately $10,000°K$. At microwave frequencies (3000 megacycles), self-shielding plasmas are generated in which the absorption front travels toward the power source[63]. This phenomenon is well known in the operation of high power wave guides.

It is natural to expect, at the very high powers at which lasers can operate, that similar discharges can be produced. Expecially with the development of extremely high-power CO_2 lasers these optical discharges have become observable. It is natural, however, to expect that power densities needed to create and maintain such optical discharges will increase as the frequency increases. This occurs because of the very rapid variation of absorption coefficient with wavelength. Raizer[6] made calculations on the power require-ments needed to maintain stationary optical discharges (plasmotrons) and showed that, at small beam diameters, the requirements are independent of radial dimensions. This occurs because thermal conduction losses balance laser input laser energy. For stationary optical discharges in air, power requirements are several kilowatts.

These stationary discharges can be regarded as occurring at the threshold intensity for maintenance of these classes of waves. As the laser intensity is raised, these waves propagate up the laser beam by a thermal conduction mechanism (or by some other mechanism involving radiative transfer). Such wave propagation has been studied theoretically both for high-pressure microwave discharges[64] and for laser-supported combustion waves[65]. In addition, various

aspects of laser energy transfer to plasmas leading to various related heating waves have also been studied[66,67]. Additional theoretical studies have been performed which predict the propagation and threshold maintenance conditions of laser-supported combustion (LSC) waves in the presence of transverse waves[68,69].

The experimental observation of laser-supported combustion waves (LSC waves) was first observed by Bunkin[3], who obtained propagating optical discharges with a neodymium laser beam in air. The first stationary optical plasmatron was obtained by Generalov[70], who used as low as 40 watts of CO_2 laser power focused to focal diameters of approximately .1 mm. Argon and xenon gases at high pressures (2-40 atmospheres) were used in order to reduce thermal conduction losses and increase laser absorption and hence reduce ignition thresholds. A similar experiment examining some aspects of the maintenance conditions of stationary combustion waves was performed by Franzen[71]. Striking high-speed motion pictures of propagating LSC waves were made by Conrad[72] using cw laser intensities of 10^5 watts/cm^2 and by Stegman, et al[73] using a CO_2 laser pulse of approximately 4 milliseconds duration. These photographs clearly show fast moving absorption fronts traveling up the laser beam. In this case, the laser intensity was approximately 10^6 watts/cm^2 and LSC wave velocities as high as 10^4 cm/sec were found.

The objective of this report is to perform analytical calculations which can be used to predict the behavior of laser-supported combustion waves obtained in experiments. Of particular interest is the dependence of LSC wave intensity thresholds on the geometrical parameters of the beam. In addition, propagation velocities as a function of laser intensity are important as well as determining the actual energy absorption in the wave zone.

The above objectives and goals are approached by making several analytical approximations to both the thermodynamic properties of

air and to the exact energy equation. These approximations allow
analytical calculations of this boundary value eigenvalue problem
which lead to LSC wave velocity, temperature, and energy absorption
from the laser beam.

In Section 7.2, the various approximations are discussed and
results obtained for radiation lossless one-dimensional LSC waves.
By adding a phenomenological radiation emission and reabsorption
effect as done in Section 7.3, one notes a possible LSC wave velocity
increase due to this increased effective radiation convection.
Following the analytical approximation of Raizer[65], the combustion
wave velocity as affected by radial losses is considered in Section
7.4. Here we are able to determine thresholds and the power
transmitted through the LSC wave.

Section 7.5 considers the one-dimensional LSC wave with optically
thin radiation losses. It is shown that these losses, restricted to
the expected magnitudes, affect only the small velocity low intensity
combustion waves.

The important effects of external boundaries is considered in
Section 7.6 where we determine that the LSC wave velocities observed
near boundaries should be much greater than those found in free
space.

Section 7.7 determines the shape of the front of large diameter
LSC waves as dependent on the radial intensity variation of the laser
beam.

7.2 ONE-DIMENSIONAL LSC WAVES NEGLECTING RADIATION LOSSES

We consider here the steady state propagation of subsonic laser-
supported combustion waves. These waves can propagate along high
intensity laser beams by the thermal conduction mechanism as discussed
by Raizer[65] and we utilize many features of this treatment. Since
the flow velocities V are subsonic, one can neglect terms proportional

164

to V^2 in the energy equation. The resulting coupled set of one-dimensional fluid mechanical equations becomes

$$P = \text{constant}$$
$$\rho_o v = \text{constant}$$
$$\frac{d}{dx} \left(\rho_o Vh - \lambda \frac{dT}{dx} + q \right) = 0$$

(27)

In equation 27, one defines

ρ_o = mass density of the ambient gas (1.29×10^{-3} gm/cm^3 under standard conditions for air)

V = LSC wave velocity (cm/sec) = constant

h = enthalpy (joules/gm)

λ = thermal conductivity (watts/cm $^\circ$K)

q = laser intensity (watts/cm^2)

T = gas temperature ($^\circ$K)

x = coordinate direction from the cold to hot gas (opposite to wave propagation direction) (cm)

P = ambient pressure = constant

In addition to the above fluid equations, it is necessary to define the laser beam coupling to the gas. This is defined by

$$\frac{dq}{dx} = -kq$$

(28)

where k is the temperature dependent absorption coefficient in air. This coefficient is shown in figure 99 where its dependence on temperature is shown for a constant pressure of one atmosphere.

The absorption coefficient k shown in figure 99 and the following curves of enthalpy and thermal conductivity are based on results obtained from a computer program designed to calculate high-
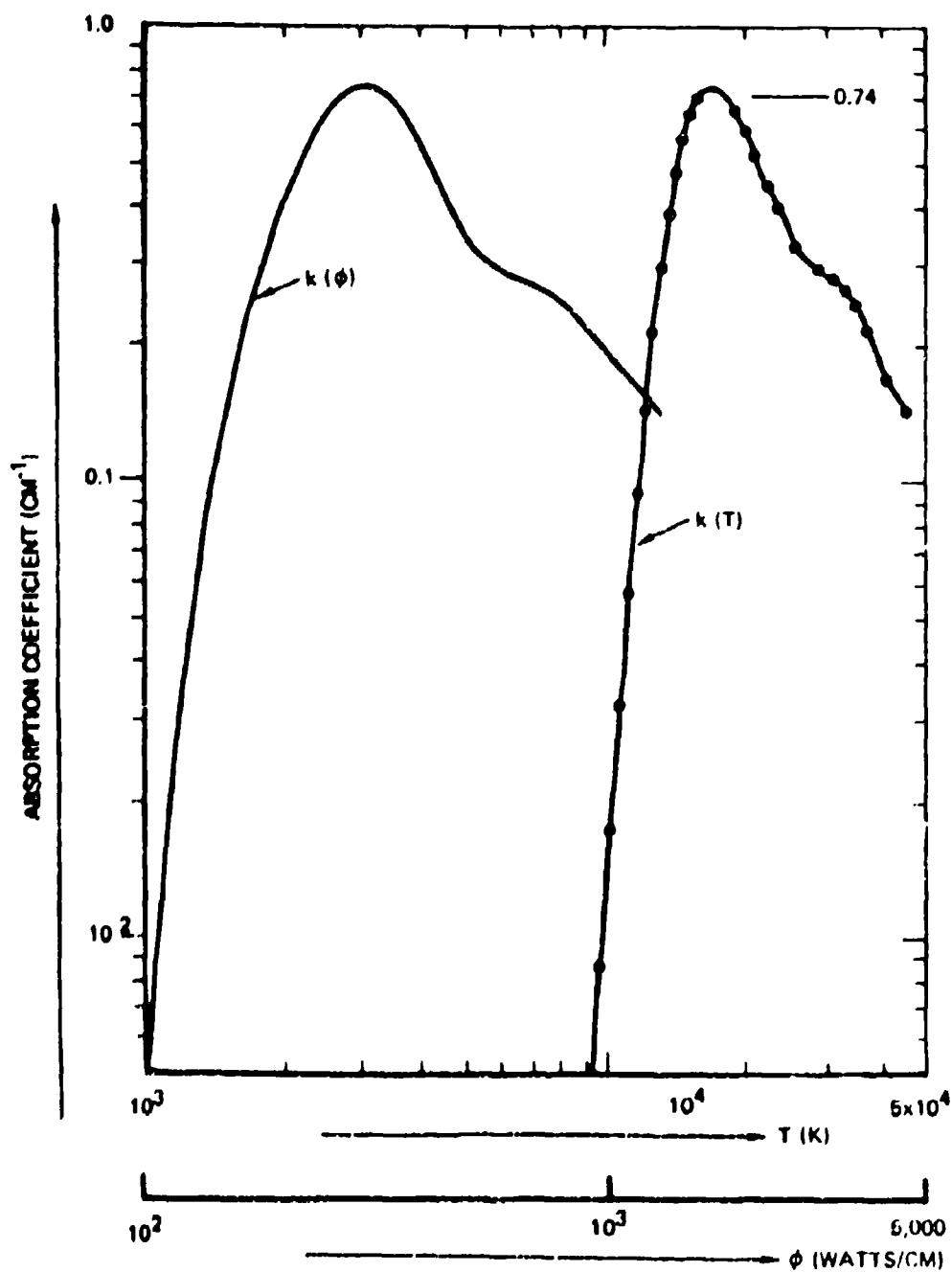
Figure 99 : ABSORPTION COEFFICIENT K FOR A CARBON DIOXIDE LASER IN AIR AS A FUNCTION OF THE TEMPERATURE T AND AS A FUNCTION OF THE INTEGRAL OF THE THERMAL CONDUCTIVITY WITH RESPECT TO THE TEMPERATURE

$$\phi = \int_0^T \lambda \, dT.$$

temperature properties of air[74]. Figure 99 also shows the variation
of the absorption coefficient as a function of the variable ϕ where

$$\phi = \int_0^T \lambda \, dT \text{ watts/cm} \tag{29}$$

as defined by Raizer[65] is sometimes a more useful variable. It
is interesting to note from figure 99 that the minimum absorption
length for 10.6μ radiation in atmospheric pressure air is approxi-
mately 1.4 cm.

The above coupled set of differential equations has a real
solution only for certain velocities of the LSC wave with respect
to the velocity of the cold gas. These eigenvalues are determined
only by solving the differential equations subject to boundary
conditions on both the hot and cold sides of the LSC wave and by
specifying the incident laser intensity q_o coming from the direction
of the cold gas.

In general, completely analytical solution of these equations
is impossible because of the temperature variation of the thermo-
dynamic properties of the hot air. This rapid variation of the
laser absorption coefficient k was indicated in figure 99, however,
both the enthalpy h, and the thermal conductivity λ also are
complicated functions of temperature as indicated in figures 100
and 101.

By making suitable analytical approximations to the actual
temperature variations shown in figures 99, 100 and 101, one can
arrive at a tractable set of coupled differential equation. First
of all, from figure 99, note the extremely rapid variation of the
absorption coefficient k with temperature. The magnitude of k
increases several orders of magnitude in just several thousand degrees
temperature rise. For this reason, it is felt that a valid first

167
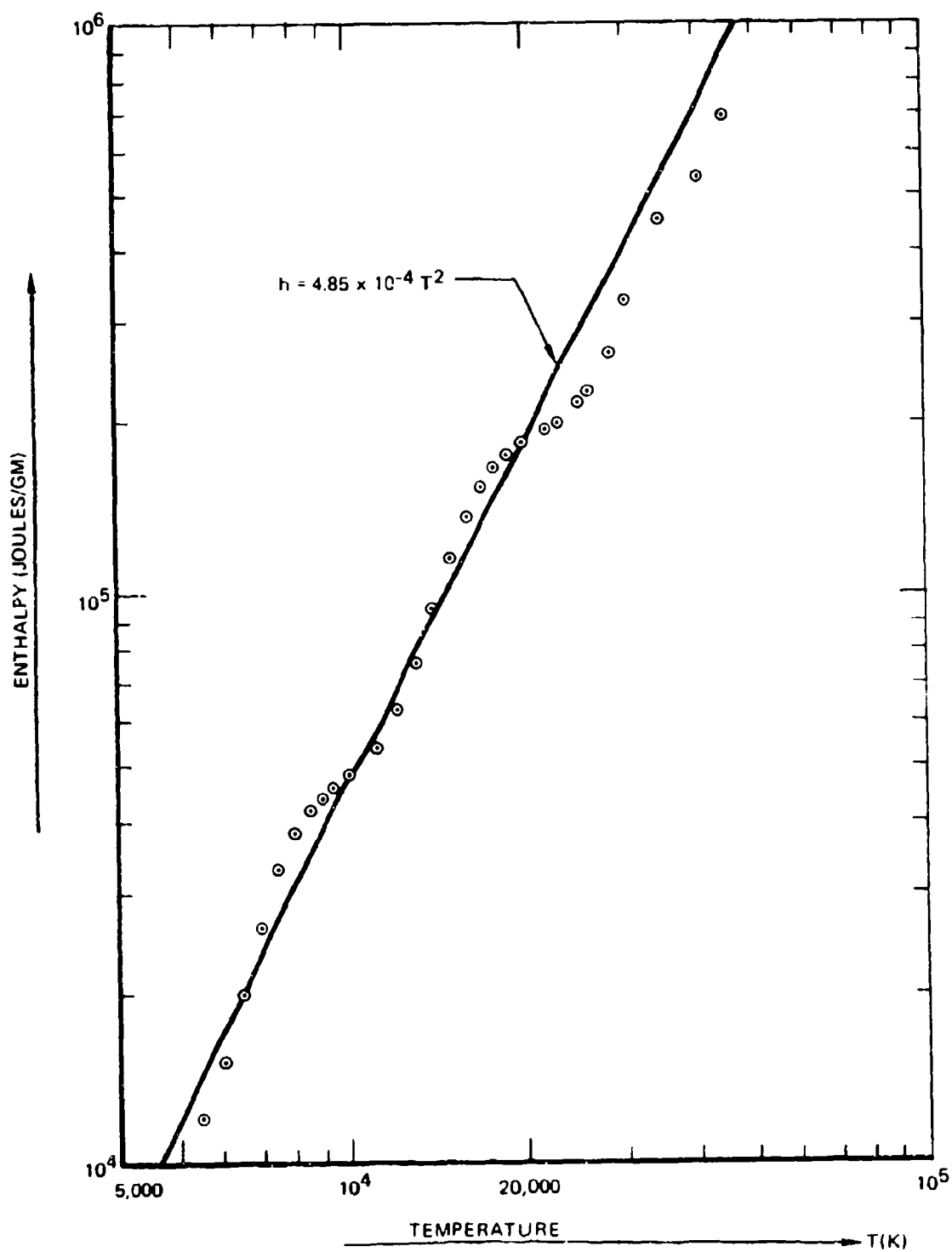
Figure 100 : *ENTHALPY h OF AIR AS A FUNCTION OF THE TEMPERATURE T.*

$\lambda = 2 \times 10^{-6} T$

THERMAL CONDUCTIVITY (WATTS/CM °K)

10^{-1}

10^{-2}

10^{-3}

2,000 10^4 50,000

T (K)
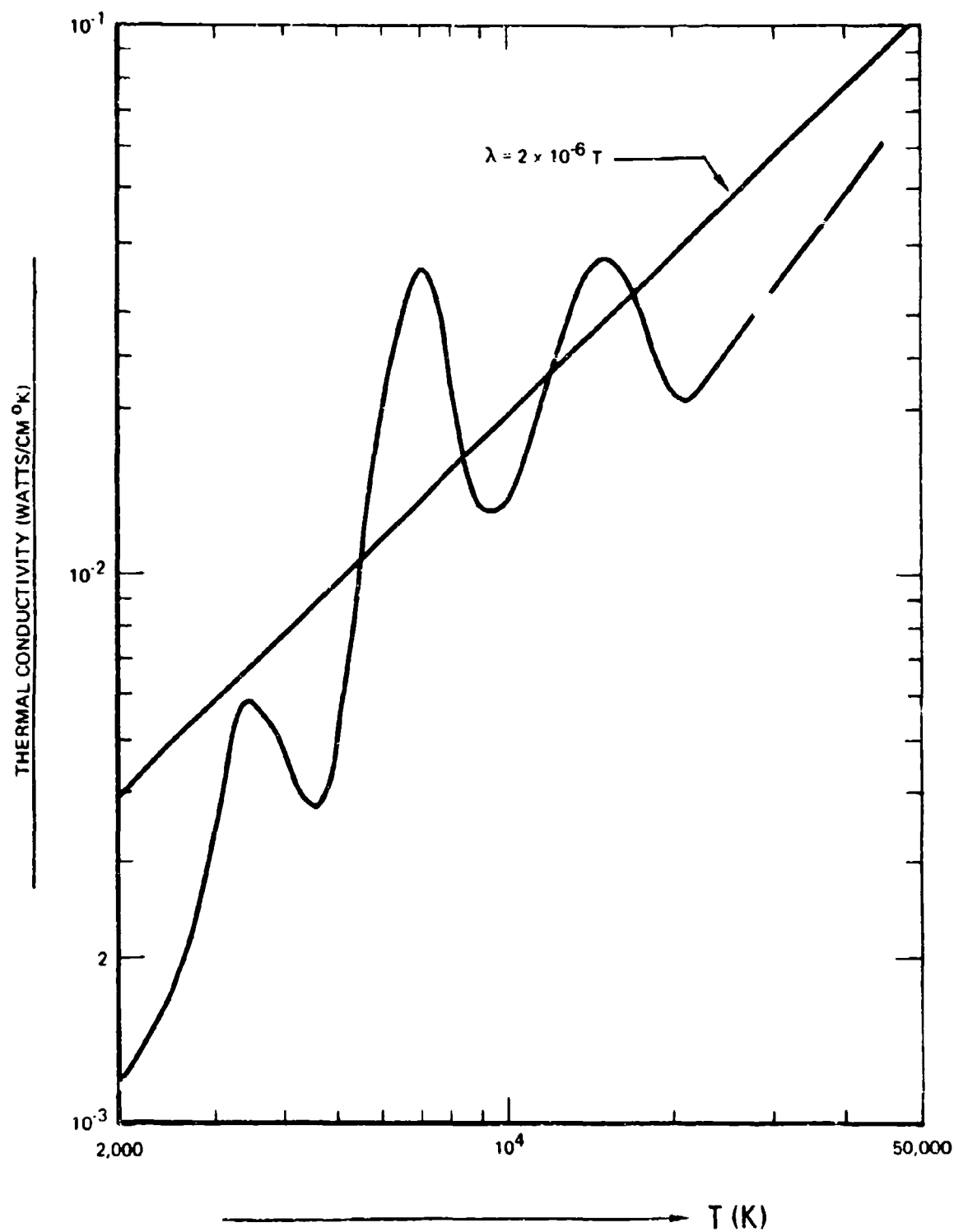
Figure 101   :   *THERMAL CONDUCTIVITY λ OF AIR AS A FUNCTION OF THE TEMPERATURE T.*

approximation to the absorption coefficient is given by a simple step function given by

$$k = 0 \text{ for } T < T_o$$

$$k = k_o \text{ cm}^{-1} \text{ for } T > T_o$$

$$\tag{30}$$

In equation 30, T_o can be considered an ignition temperature which is approximately 1.2×10^4 K. The peak absorption coefficient k_o is determined from figure 99 to be $k_o \approx .7 \text{ cm}^{-1}$. As seen from figures 100 and 101, both the enthalpy h and the thermal conductivity λ are complicated functions of temperature, but these shall be approximated by the simplest reasonable functions which will allow analytic solutions. From the basic data obtained from reference 72 shown in figures 100 and 101 for air, one sets

$$h = aT^2 \text{ joules/gm}$$

and

$$\tag{31}$$

$$\lambda = bT \text{ watts/cm K}$$

With the approximations of equations 30 and 31, one obtains a linear, coupled set of ordinary differential equations which can be analytically solved. It is most useful to define dimensionless variables and constraints in the basic energy equation (equation 27) and in the laser equation (equation 28) in order to make the problem solution universal. This is done by defining a dimensionless LSC wave velocity with respect to the cold gas.

$$\beta = \frac{2a\,\rho_o V}{bk_o} \tag{32}$$

170

This relationship to the cold gas velocity is important to recognize since, in experiments, the gas ahead of the LSC wave can be set in motion and affect considerably the apparent velocity. This cold gas motion can result either from winds or from the initial ignition process in which gas motion is perturbed. As seen later from Section 7.6, the presence of boundaries can also lead to a significant apparent LSC wave velocity increase.

The dimensionless laser intensity θ is the remaining independent parameter defined by

$$\theta = \frac{2q_o}{bT_o^2 k_o} \tag{33}$$

where q_o is the incident laser flux. The magnitude of θ indicates the importance of the laser absorption relative to power transfer by thermal conduction, while β is the ratio of enthalpy power flow to thermal conduction power flow over a laser absorption length. With these definitions and also defining the dimensionless distance z (distance measured in absorption lengths

$$z = k_o x \tag{34}$$

one obtains

$$\beta \frac{dY}{dz} - \frac{d^2Y}{dz^2} = 0$$

$$\left.\begin{array}{c} \\ \\ \end{array}\right\} \quad \text{for } z<0 \tag{35}$$

$$\frac{d\bar{q}}{dz} = 0$$

and

$$\beta \frac{dY}{dz} - \frac{d^2Y}{dz^2} - \theta\, \bar{q} = 0 \qquad\quad \text{for } z<0$$

$$\frac{d\bar{q}}{dz} = -\bar{q}$$

$$(36)$$

In equations 35 and 36, the dimensionless enthalpy Y is defined by

$$Y = T^2 \Big/ T_o^2 \tag{37}$$

and the variable laser intensity $\bar{q}$ is

$$\bar{q} = q/q_o \tag{38}$$

From the form of equations 35 and 36, it is evident that the origin of the coordinate system ($z = 0$) travels with the LSC wave and is located where the local temperature T is equal to the ignition temperature T_o. From $-\infty < z < 0$, the temperature of the cold gas (air) is brought up to the ignition temperature ($Y=1$) by the process of thermal conduction. For $0 < z < \infty$, laser energy is absorbed and the maximum temperature attained.

The solutions of equations 35 and 36, subject to the appropriate boundary conditions at $z = \pm\infty$ are

$$Y = \exp\,(\beta z) \text{ for } z<0$$

and

$$Y = 1 + \frac{\theta(1 - \exp\,(-z))}{1 + \beta} \text{ for } z>0$$

$$(39)$$

172

Since the slope of these two expressions is continuous at $z = 0$, one obtains the eigenvalue equation

$$\theta = \beta(1 + \beta) \qquad (40)$$

For large laser intensities $(\theta \gg 1)$, one obtains

$$\rho_o V = \sqrt{\frac{q_o k_o \lambda_o T_o}{2h_o^2}} \qquad (41)$$

in which

$$\left. \begin{array}{l} h_o = h\{T_o\} = a\, T_o^2 \\[2ex] \lambda_o = \lambda\{T_o\} = b\, T_o \end{array} \right\} \qquad (42)$$

The square-root dependence of LSC wave velocity was noted by Raizer[6], who used the approximations of constant specific heat and thermal conductivity and who obtained an LSC wave velocity greater by $\sqrt{2}$ than that given in equation 41. For relatively small laser intensities, however, $(\theta < 1)$, one finds the LSC wave velocity to be proportional to incident intensity

$$\rho_o V = \frac{q_o}{h_o} \qquad (43)$$

It is interesting to note from equation 39 that the maximum temperature $T(\infty)$ occurs at $z = \infty$ and is

$$T_\infty = T_o \sqrt{1 + \beta} \qquad (44)$$

173

The temperature indicated by equation 44 appears, in many cases, to predict excessive temperatures in LSC waves. It should be recalled, however, that the results of this section are valid for lossless one-dimensional waves.

The results obtained above are derived for the simplest possible approximation to the actual absorption coefficient given in figure 99. This approximation, given by equation 30, is a simple step function and it is reasonable to ask how model-dependent the results obtained are. One way of answering this question is to choose a more complex analytical model to the absorption curve of figure 99. Such a model is presented in figure 102-1.

This is a two-step absorption process for which

$$
\left. \begin{array}{l}
k = 0 \text{ for } T < T_o' \\[2ex]
k = k_o' \text{ for } T_o' < T < T_o \\[2ex]
k = k_o \text{ for } T > T_o
\end{array} \right\} \tag{45}
$$

Equation 45 is an attempt to model the initial rise of the absorption coefficient to its maximum value of k_o. The method of finding solutions of the combined energy equation and laser equation is very similar to that used previously. In this case, however, the origin of the coordinate system, $z = 0$, is defined to occur when the temperature equals T_o'. The coordinate z_1, on the other hand, is defined as occurring when the temperature equals T_o (defined as the ignition temperature previously used).

After algebraic manipulations and solving simple differential equations, one obtains the eigenvalue equation relating the dimensionless LSC velocity β and the dimensionless laser intensity θ.

Figure 102 : NORMALIZED LSC WAVE VELOCITIES β WITH RESPECT TO THE GAS AHEAD OF THE WAVE AS A FUNCTION OF THE NORMALIZED LASER INTENSITY θ FOR VARIOUS TWO-STEP ABSORPTION COEFFICIENTS k_o

175

$$\left\{ (1 + \beta) \left(\frac{1}{\beta} - \frac{1}{\theta} \right) \right\}^{\left(\frac{\beta}{r} \right)} (1-r)(\theta-\beta) = \beta(\beta+r)Y_1 - r\theta \qquad (46)$$

In equation 46,

$$r = \frac{k_o'}{k_o}$$

and

$$Y_1 = (T_o'/T_o)^2 \qquad\qquad\qquad (47)$$

It should be noted that in the limit $r = Y_1 = 1$, one obtains the previous result given by equation 40 for a simple one-step approximation to the absorption coefficient. The distance z_1 (distance measured in laser absorption lengths) between the positions of temperature T_o' and T_o is found to be

$$z_1 = \frac{-1}{r} \; \ln \left[(\beta+1) \left(\frac{1}{\beta} - \frac{1}{\theta} \right) \right] \qquad (48)$$

Equation 46 can be solved by a numerical iteration and the solutions are shown in figure 102 for $r = 0.5$ and T_o'/T_o equal to 0.5, 0.6, 0.7, 0.8, 0.9 and 1.0. (It should be noted that T_o'/T_o equal 1.0 is equivalent to the previous one-step absorption result.) The results given in figure 102 for a two-step model showing the increase of the absorption coefficient leads to only a slightly increased LSC wave velocity as compared to the one-step model. In both models, however, the maximum temperature reached is defined by

$$T_{max} = T_o \left(\frac{\theta}{\beta} \right)^{\frac{1}{2}} \qquad (49)$$

The actual absorption coefficient shown in figure 99 decreases with temperature for temperatures greater than approximately $16,000^{\circ}K$. This decrease in the magnitude of k is due to the plasma becoming nearly fully ionized. A similar two-step process in modeling this decrease in absorption coefficient with temperature is shown in figure 102-2 where one defines

$$\left.\begin{array}{l} k = 0 \text{ for } T < T_o \\[8pt] k = k_o \text{ for } T_o < T < T_o{}'' \\[8pt] k = k_o{}'' \text{ for } T > T_o{}'' \end{array}\right\} \tag{50}$$

Similar algebraic manipulations and equation solutions lead to eigenvalues relating LSC wave velocity and laser intensity for the step decrease in absorption coefficient.

$$\left\{(r + \beta)\left(\frac{1}{\beta} \cdot \frac{Y_1}{\beta} - \frac{1}{\theta}\right)\right\}^{\beta} (1-r) \ (\theta - \beta Y_1) = \theta - \beta \ (\beta+1) \tag{51}$$

In equation 51,

$$\left.\begin{array}{l} r = k_o{}''/k_o \\[14pt] Y_1 = (T_o{}''/T_o)^2 \end{array}\right\} \tag{52}$$

and

Equation 51 is solved (as before) by a numerical iteration and the solutions are again presented in figure 102 for $r = .5$ and values of $T_o{}''/T_o$ equal to ∞, 1.4, 1.2, and 1.0 It is evident that this decrease in the absorption coefficient at high temperatures leads to a slightly decreased LSC wave velocity when compared to the results found for the single step model. The distance between temperatures T_o and $T_o{}''$ is found to be

177

The actual absorption coefficient shown in figure 99 decreases with temperature for temperatures greater than approximately $16,000^\circ K$. This decrease in the magnitude of k is due to the plasma becoming nearly fully ionized. A similar two-step process in modeling this decrease in absorption coefficient with temperature is shown in figure 102-2 where one defines

$$\left. \begin{array}{l} k = 0 \text{ for } T < T_o \\[2ex] k = k_o \text{ for } T_o < T < T_o{}'' \\[2ex] k = k_o{}'' \text{ for } T > T_o{}'' \end{array} \right\} \tag{50}$$

Similar algebraic manipulations and equation solutions lead to eigenvalues relating LSC wave velocity and laser intensity for the step decrease in absorption coefficient.

$$\left\{ (r + \beta) \left(\frac{1}{\beta} \frac{Y_1}{\theta} - \frac{1}{\theta} \right) \right\}^\beta (1-r) (\theta - \beta Y_1) = \theta - \beta (\beta+1) \tag{51}$$

In equation 51,

$$\left. \begin{array}{l} r = k_o{}'' / k_o \\[2ex] Y_1 = (T_o{}'' / T_o)^2 \end{array} \right\} \tag{52}$$

and

Equation 51 is solved (as before) by a numerical iteration and the solutions are again presented in figure 102 for $r = .5$ and values of $T_o{}'' / T_o$ equal to ∞, 1.4, 1.2, and 1.0 It is evident that this decrease in the absorption coefficient at high temperatures leads to a slightly decreased LSC wave velocity when compared to the results found for the single step model. The distance between temperatures T_o and $T_o{}''$ is found to be

$$z_1 \approx -\ell n \left[(r + \beta) \left(\frac{1}{\beta} - \frac{Y_1}{\theta} \right) \right]$$ (53)

while equation 49 is again valid as the maximum temperature reached.

The results shown in figure 102 lead us to believe that the one-step model for variation of the absorption coefficient with temperature (equation 30) is fairly good since both T_0' and T_0'' cannot be greatly different from T_0.

7.3 ONE DIMENSIONAL LSC WAVES WITH EMISSION AND REABSORPTION OF RADIATION

This section discusses a phenomenological approach to considering the effect of radiation emission on the propagation of LSC waves. In one limit to this problem, the radiation transport of energy can be considered to be a diffusive process and one then obtains the previous results except that the correct radiation-conductivity should be used. On the other hand, if the transport process for high energy photons emitted from the hot LSC wave is not proportional to the temperature gradients, one obtains a different result. In general, the absorption coefficient, α, of ultraviolet radiation is both temperature and gas density dependent. We shall assume in the following, however, that α is a constant, representing an average absorption coefficient.

In addition, we assume that a certain given fraction f ($0 < f < 1$) of the incident laser radiation is re-emitted back into the cold gas where it is absorbed. This radiant energy, in this example, is considered to be absorbed with an exponential decay in the cold gas and represents short wavelength ultraviolet radiation whose only effect is to aid in the heating of the cold gas. In general, one expects f to be dependent on the final maximum temperature of the LSC wave and is a parameter to be determined from the results of this section. We assume a general dependence of

$$f = \left(\frac{q_{uv}}{q_o}\right) \quad \left(\frac{T_\infty}{T_o}\right)^m \tag{54}$$

where q_{uv} is radiant intensity emitted by the plasma at a temperature T_o and m is a coefficient defining how rapidly the ultraviolet radiation depends on temperature. (The parameter m is not explicitely evaluated in this report.)

Under the above assumptions, the energy equation (for z<0) becomes

$$\frac{d}{dx} (\rho_o Vh - \lambda \frac{dT}{dx}) = \alpha f q_o e^{\alpha x} \tag{55}$$

which in dimensionless form is

$$\beta \frac{dY}{dz} - \frac{d^2Y}{dz^2} = \alpha f \theta e^{\gamma z} \tag{56}$$

where $\gamma = \alpha/k$ is the dimensionaless ultraviolet absorption length. The solution of equation 56 with Y = 1 at z = 0 is

$$Y = (1 - \frac{f\theta}{(\beta-\gamma)} \exp (\beta z) + \frac{f\theta}{(\beta-\gamma)} \exp (\gamma z) \tag{57}$$

For z>0, the normalized energy equation is again equation 36 with $\bar{q}$ replaced by (1-f) $\bar{q}$ and which has the solution with Y = 1 at z = 0

$$Y = 1 + \frac{(1-f)\theta}{\beta + 1} - \frac{(1-f)\theta}{\beta + 1} \exp (-z) \tag{58}$$

Equating the slopes of equations 57 and 58 at $z = 0$ gives the eigenvalue equation

$$\theta = \frac{\beta(\beta + 1)}{1 + \beta f}.$$

(59)

which is displayed in figure 103 for certain values of f. In particular, the case $f = 0$ is identical to the results of Section 7.2. It should be noted that this radiation-aided heat addition to the cold gas can appreciably increase the propagation velocity of the LSC wave. This is evident for large velocities which are now found to be proportional to laser intensity (when f is a true constant). It is interesting to note that this mechanism for one-dimensional waves does not depend on the magnitude of the absorption coefficient α. The maximum temperature behind the combustion front is also found to be considerably reduced when compared to the radiationless case for large wave velocities. This maximum temperature is

$$T_\infty = T_0 \left(\frac{1 + \beta}{1 + f\beta} \right)^{\frac{1}{2}}$$

(60)

which approaches $T_0 / \sqrt{f}$ for large velocities.

For larger laser intensities (which implies large values of the dimensionless LSC wave velocity), one finds the explicit dependence of LSC wave velocity on the laser intensity. From equations 54, 59 and 60, one obtains

$$\hat{s} = \frac{\beta^{\left(\frac{2+m}{m}\right)}}{\theta_r^{(2/m)}}$$

and

$$(1/1+m)$$

(61)

$$T_\infty / T_0 = \left(\frac{\theta}{\theta_r} \right)^{(1/1+m)}$$

180
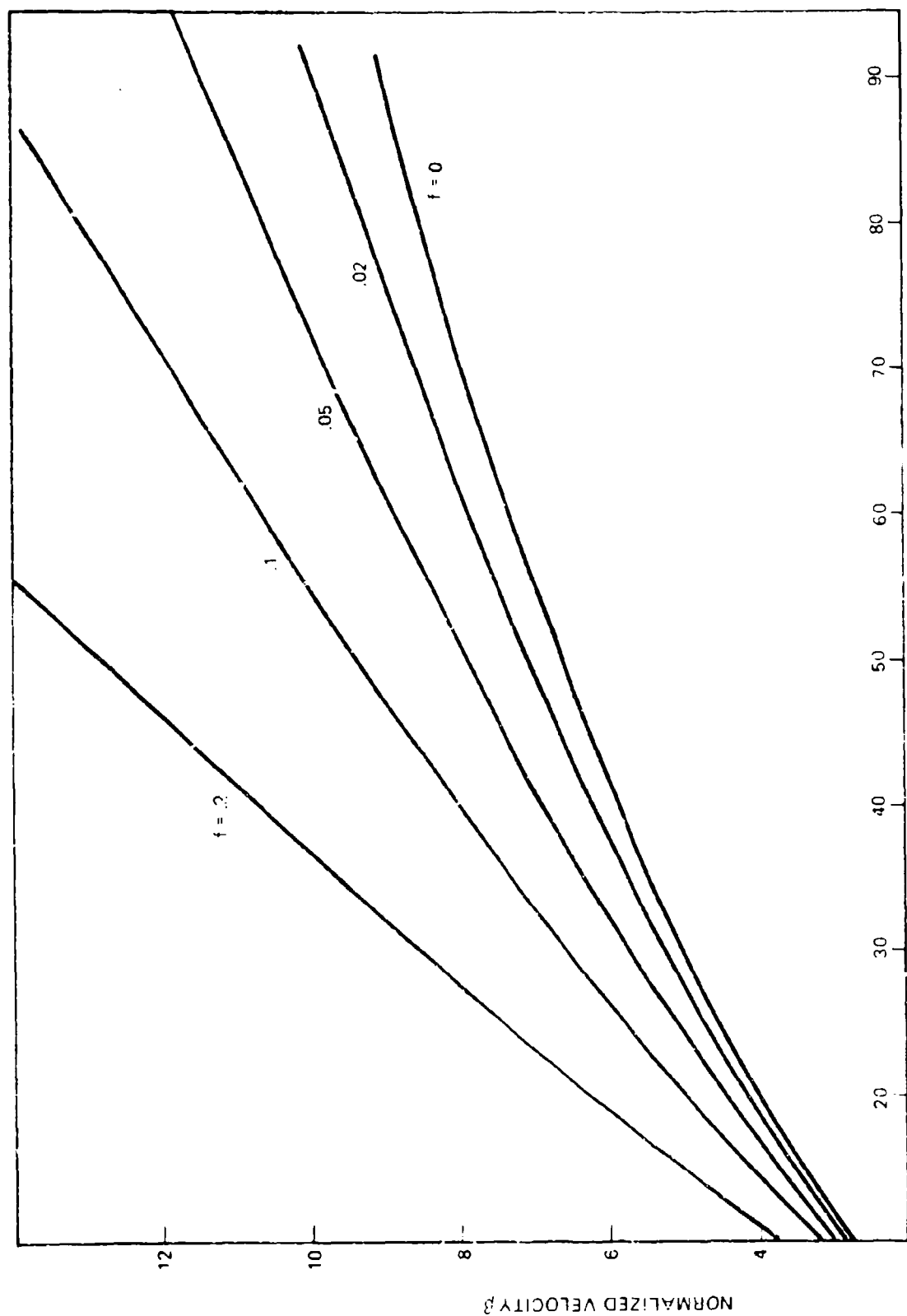
Figure 103. NORMALIZED VELOCITY β OF A LSC WAVE AS A FUNCTION OF THE NORMALIZED LASER
INTENSITY Θ WITH THE FRACTION f OF THE LOST RADIATION REABSORBED AS A PARAMETER.

181
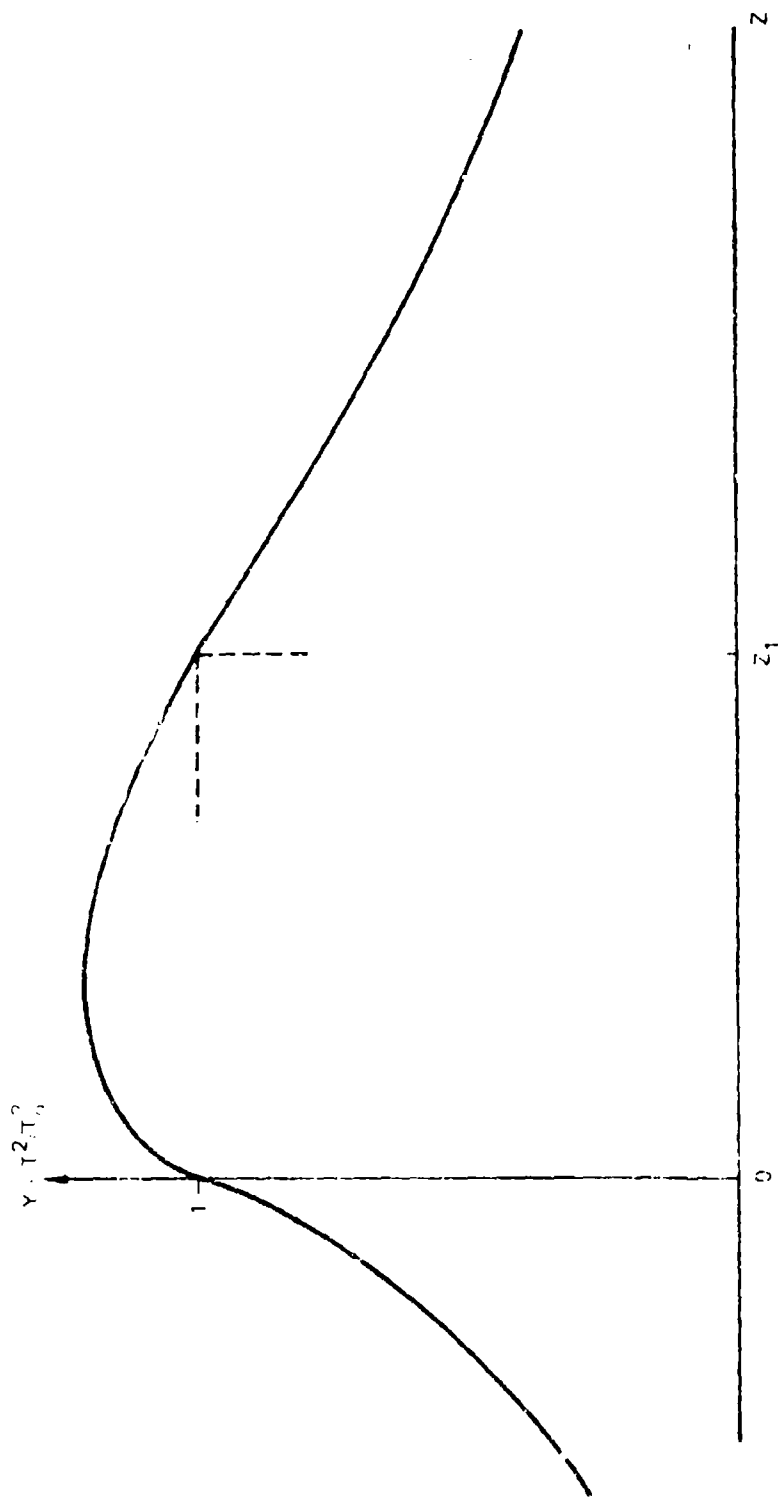
FOR $-\infty < Z < 0$, $Y = \exp(k_1 Z)$

FOR $0 < Z < Z_1$, $Y = C_1 \exp(k_1 Z) + C_2 \exp(k_2 Z) + C_3 \exp(-Z)$

FOR $Z > Z_1$, $Y = \exp(k_2 (Z - Z_1))$

Figure 104: NORMALIZED SQUARE OF THE TEMPERATURE Y OF AN LSC WAVE AS A FUNCTION OF THE NORMALIZED DISTANCE Z.

$$\theta_r = \frac{2\,q_{uv}}{bT_o^2 k_o} \tag{62}$$

Equation 61 indicates that only for a very rapid dependence of the ultraviolet emission on temperature (m large) is the LSC wave velocity nearly proportional to laser intensity.

7.4 QUASI ONE-DIMENSIONAL LSC WAVES WITH RADIAL HEAT CONDUCTION NEGLECTING RADIATION LOSSES

The effect of radial heat conduction losses can be approximately considered by appropriately modifying the one-dimensional energy equation as done by Raizer[6]. The dimensionless energy equation which is valid for $z>0$ then becomes

$$\beta\frac{dY}{dz} - \frac{d^2Y}{dz^2} - \theta\overline{q} + \frac{2A}{k_o^2 R^2}\, Y = 0 \tag{63}$$

where the radial thermal conduction effect is approximated by the last term on the left hand side of equation 63. In equation 63, R is the laser beam radius and A is a numerical factor ($0<A<2$). (As discussed by Raizer[65], we will use $A = 1.45$.).

The general physical behavior of the temperature is shown in figure 104. From $-\infty<z<0$, the temperature of the cold gas (air) is brought up to the ignition temperature ($Y = 1$) by the process of thermal conduction. For $0<z<z_1$, laser energy is absorbed and the maximum temperature is reached. For $z>z_1$, no further laser energy is absorbed and the temperature continually decreases due to radial heat conduction. Thus, one notes that $z = 0$ and $z = z_1$, define positions where the temperature falls below the ignition temperature.

183

For $z<0$ and $T<T_o$, the solution with $Y = 1$ and $z = 0$ is

$$Y = \exp \left\{ k_1 \, z \right\}$$

in which

$$k_1 = \frac{\beta}{2} \left(1 + (1 + 2A \left(\frac{b}{Ra \, \rho_o \, V} \right)^2)^{\frac{1}{2}} \right)$$

(64)

It is again necessary to match solutions on both the cold and hot sides of the LSC wave boundaries occurring at $z = 0$ and $z = z_1$. We include, in this analysis, the finite rate of laser absorption by including equation 36 for $0<z<z_1$. This was not done by Raizer in his original analysis[65].

For $0<z<z_1$ and $T>T_o$, the solution of equation 63 with $Y = 1$ and $\frac{dY}{dz} = k_1$ at $z = 0$ is

$$Y = \left(1 - \frac{\theta}{(2k_1 - \beta)(1+k_1)} \right) \exp \left\{ k_1 \, z \right\}$$

$$+ \frac{\theta\exp \left\{ (\beta-k_1) \, z \right\}}{(1+\beta-k_1)(2k_1-\beta)} - \frac{\theta\exp \left\{ -z \right\}}{(1+k_1)(1+\beta-k_1)}$$

(65)

Outside the "hot" region for $z>z_1$ and $T<T_o$, one obtains

$$Y = \exp \left\{ (\beta - k_1) (z - z_1) \right\}$$

and

$$\bar{q} = \exp \left\{ -z_1 \right\} = \text{constant}$$

(66)

By equating slopes of equations 65 and 66 at $z = z_1$, one finds

184

$$z_1 = \frac{-\ln(1-y)}{1 + k_1}$$

where   (67)

$$y = \frac{(1+k_1)(2k_1 - \beta)}{\theta}$$

It is evident from equation 67 that real solutions exist only
in the range $(0 < y < 1)$, which implies that required laser intensities
for a given LSC wave velocity are always greater as the beam
radius decreases.

One obtains the eigenvalue equation from equations 65 and 66
to be

$$-\frac{1}{1 + k_1} = \frac{\ln\left[\frac{dy}{(1-y)^{-d} - 1}\right]}{\ln(1-y)}$$ (68)

where

$$d = (1 + k_2)/(1 + k_1)$$

and   (69)

$$k_2 = \beta - k_1$$

For most physically interesting situations, the values of y found
from equation 68 will be very close to unity. For this reason,
the most useful technique for generating velocity-intensity curves
is by arbitrarily selecting values of y and d and then using
equation 68 to evaluate k_1. One is aided in this approach by
noting that $|k_2| < k_1$ which leads to

$$-1 < d < 1$$ (70)

We can thus generate a table of values of k_1 and k_2 as a function of y. To determine the physical parameters of the LSC wave, we then utilize the definitions of k_1 and k_2 to determine the corresponding velocity and radius. Similarly, the definition of y given by equation 67 determines the laser intensity. This procedure has been followed here yielding the results shown in figure 105 and 106 for the values

$$
\left.
\begin{aligned}
a &= 4.85 \times 10^{-4} \text{ joule/gm } (^{\circ}\text{K})^2 \\
b &= 2 \times 10^{-6} \text{ watt/cm } (^{\circ}\text{K})^2 \\
T_0 &= 1.3 \times 10^4 \, ^{\circ}\text{K and } 1.2 \times 10^4 \, ^{\circ}\text{K} \\
k_0 &= 0.5/\text{cm and } 0.74/\text{cm} \\
\lambda &= 1.45
\end{aligned}
\right\}
\tag{71}
$$

One should note that for each laser radius that an intensity threshold exists for zero wave velocity which, for small radii, is nearly a constant power condition. One should also note that each curve (for constant radius) assymptotically approaches the infinite radius case as laser intensity rises. Even though figures 105 and 106 are drawn on different scales, one can see that they are only slightly different, indicating that the exact numerical parameters used for T_0 and k_0 are not highly sensitive. There is only a slight change in the intensity thresholds and LSC wave velocity. Recalling that the analysis performed here allowed finite laser absorption as indicated by equation 36 and, since the resulting plasma is of finite length, one determines the amount of laser power q_T getting through the plasma of the LSC wave. This is done by use of equation 67 and noting that the transmitted power q_i is

$$
\frac{q_T}{q_0} = e^{-z_1} = (1 - y)^{\left(\frac{1}{1 + k_1} \right)}
\tag{72}
$$

186
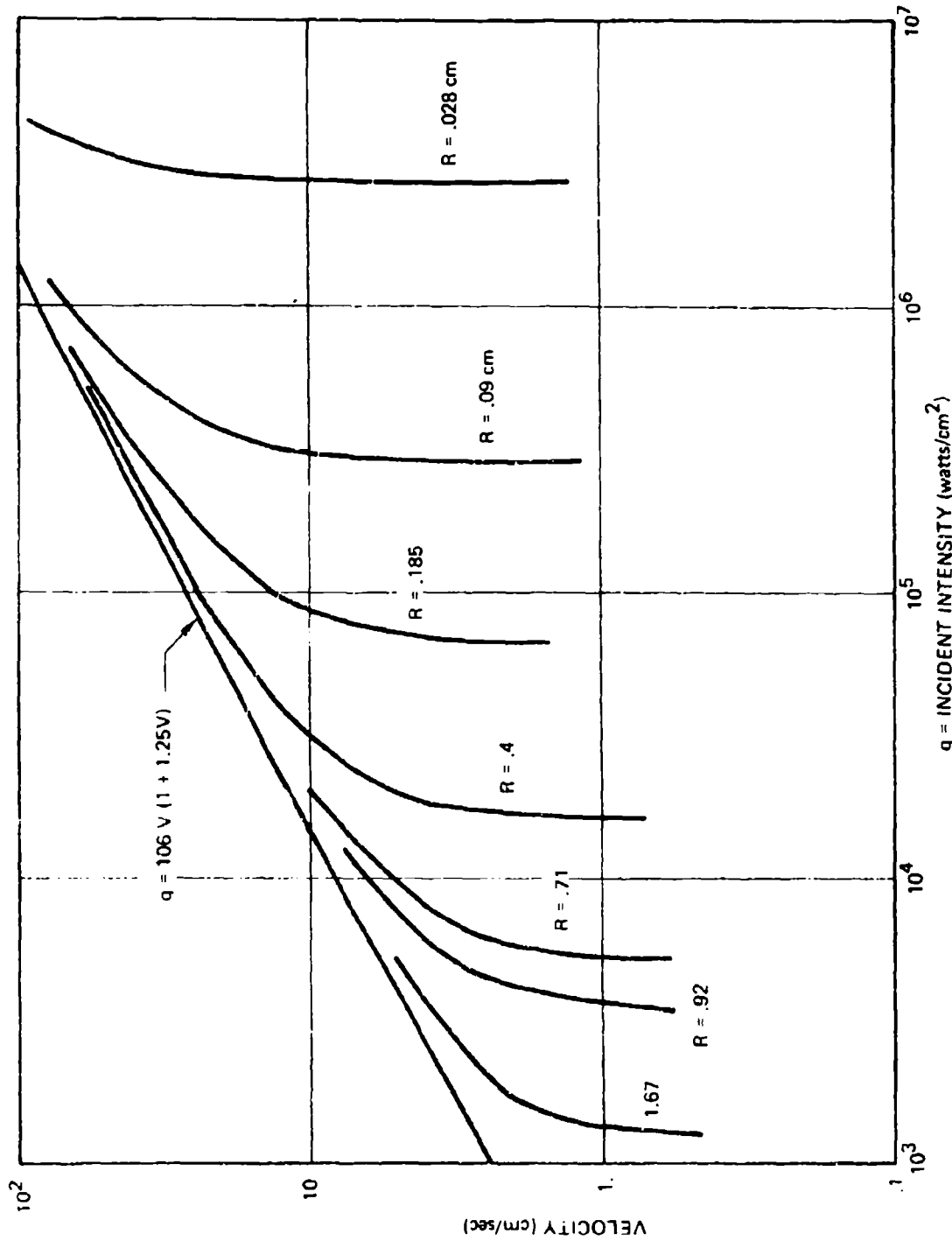
Figure 105 : VELOCITY V OF A SMALL DIAMETER LSC WAVE AS A FUNCTION OF THE LASER INTENSITY q_0 WITH THE RADIUS R AS A PARAMETER.
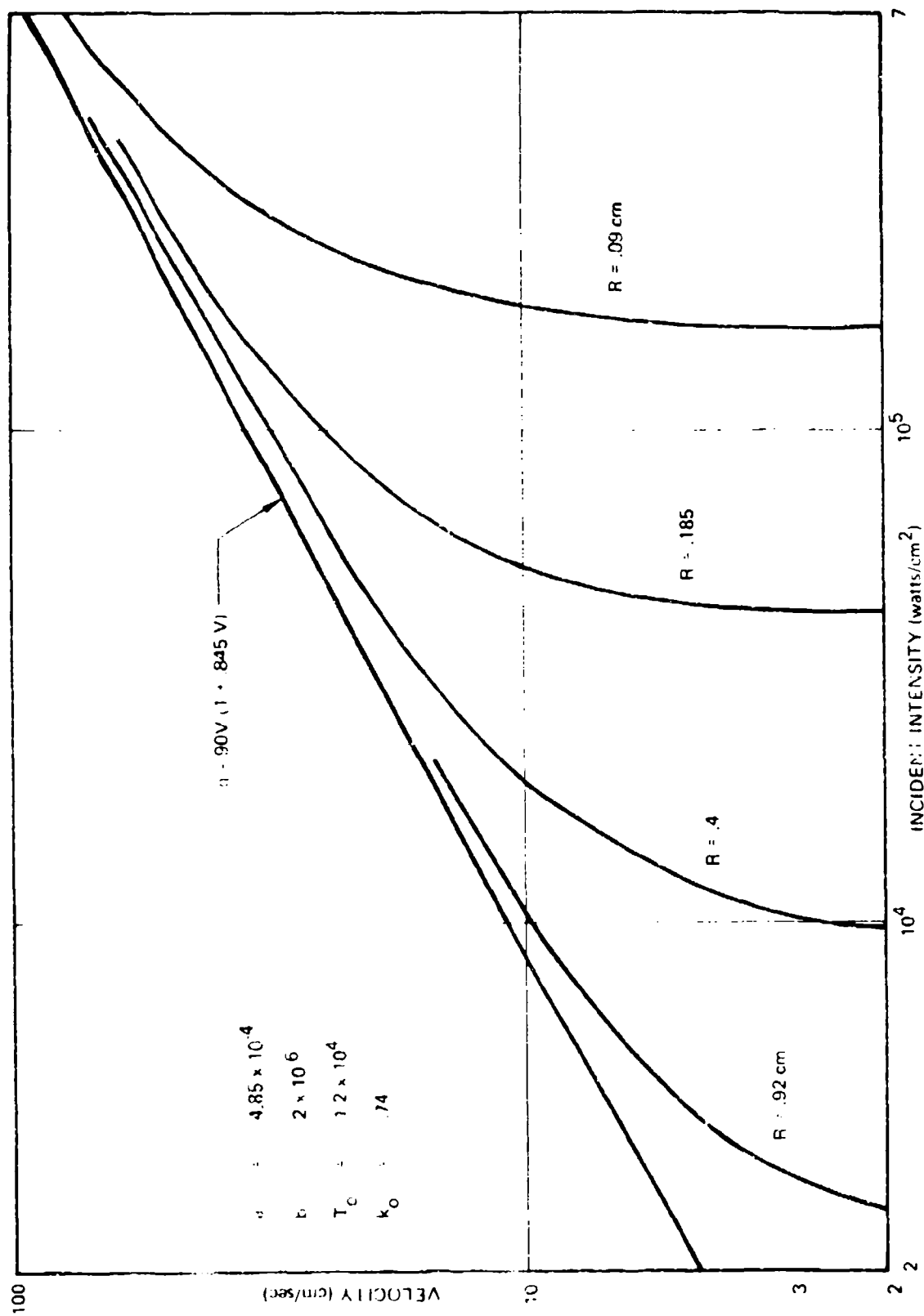
Figure 106: *VELOCITY V OF A LSC WAVE AS A FUNCTION OF THE LASER INTENSITY q_0 WITH THE RADIUS R AS A PARAMETER.*

The results of this calculation obtained by evaluating equation 68 is shown in figure 107. Here we plot transmitted power versus incident intensity q_o. For incident intensities less than threshold values one finds $q_T = q_o$. At the threshold, there is an abrupt drop in transmitted power which then continually decreases as q_o increases further. It is interesting to note that the threshold intensity (as $V \rightarrow 0$) is approximately determined by

$$q_o \, \pi R^2 = \frac{2^n \; A \; b \; T_o^2}{k_o}$$ (73)

which is the same as Raizer's[65] equation 16 and is equivalent to a total power requirement to maintain a stationary combustion wave. The results of figure 107 are somewhat similar to those found by Sziklas[75] using different approximations for high temperature air properties.

7.5 ONE-DIMENSIONAL LSC WAVES WITH RADIATION LOSSES

This section determines the approximate effect of radiation losses on the propagation of LSC waves. No radial heat losses are taken into account here and the radiation power loss is assumed to be completely lost to the LSC wave. This is equivalent to an optically thin process with volume radiation of a magnitude given in the data of John[76]. In the spirit of the Raizer model[65], one notes that optical radiation losses at one atmosphere pressure are nearly independent of temperature for $T > 1.2 \times 10^4 K$. (Raizer[65] actually assumes that these losses are proportional to temperature.) In this section we assume that the power losses are

$$\text{optical losses (watts/cm}^3) = \text{Rad. for } T > T_o$$ (74)

$$= 0 \text{ for } T < T_o$$

These power losses are expected to be approximately 8000 watts/cm^3.
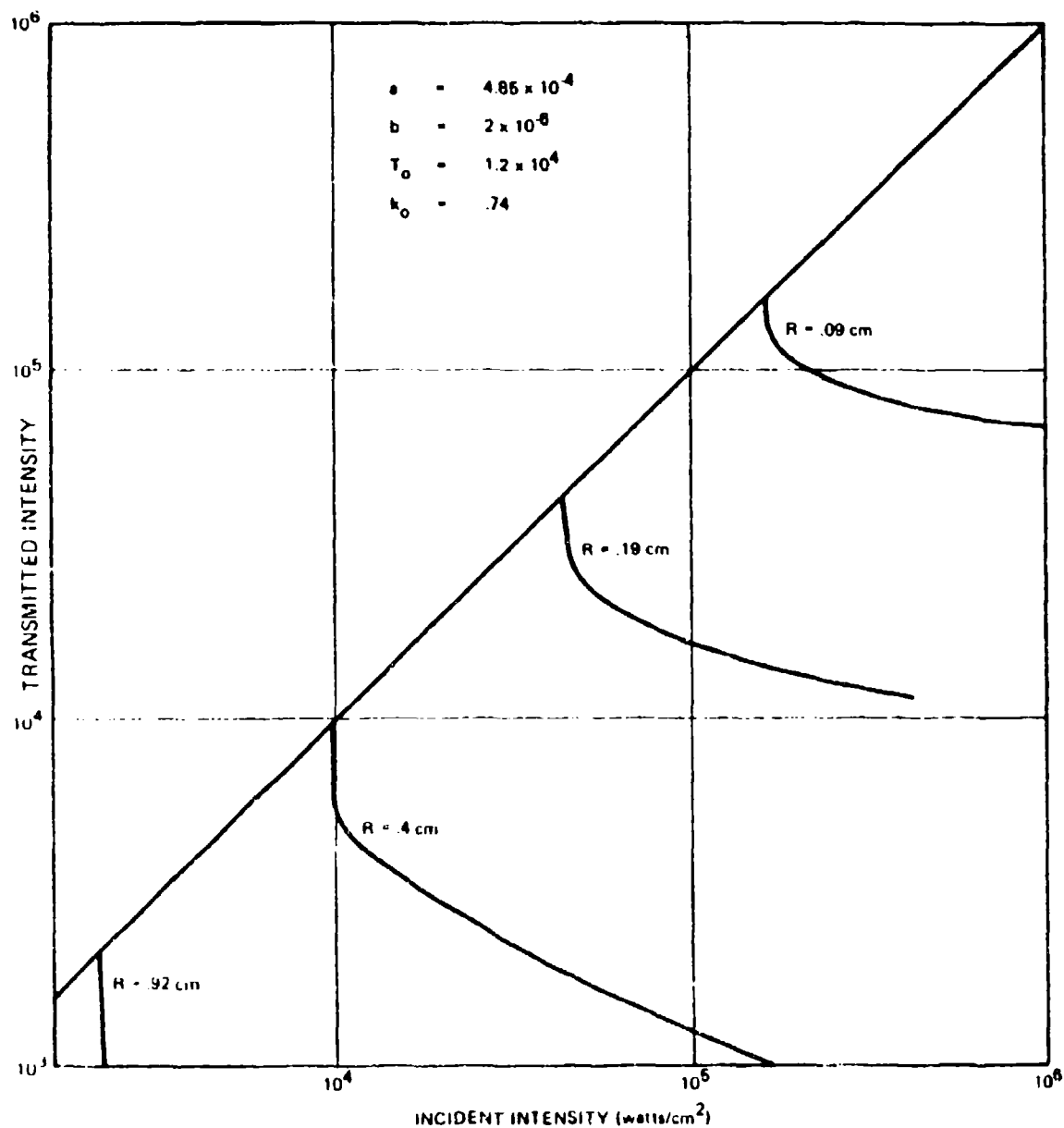
Figure 107 : TRANSMITTED INTENSITY q_T THROUGH A SMALL DIAMETER LSC
WAVE AS A FUNCTION OF THE INCIDENT INTENSITY q_0 WITH THE RADIUS R
AS A PARAMETER.

For z<0, in the cold gas, one obtains the same equations and solutions as previously found, however, for z>0 one finds

$$\beta \frac{dY}{dz} - \frac{d^2Y}{dz^2} - \theta\overline{q} + R = 0$$

where

$$R = \frac{2 \text{ Rad}}{b \, T_o^2 \, k_o^2}$$

(75)

Because of the radiation losses, the temperature will always have a maximum for z>0 and then decrease to $Y = 1$ at $z = z_1$. For $z>z_1$, neither laser absorption nor radiation losses occur. This determines the boundary condition at $z = z_1$ to be

$$Y = 1 \text{ and } \frac{dY}{dz} = 0$$

(76)

For $0<z<z_1$, the solution of equation 75 is

$$Y = B_1 \, e^{\beta z} - \left(\frac{R}{\beta} \right) z + B_2 - \frac{\theta e^{-z}}{\beta + 1}$$

(77)

where B_1 and B_2 are constants to be determined from the boundary conditions at both $z = 0$ and $z = z_1$. At $z = 0$, one obtains

$$1 = B_1 + B_2 - \frac{\theta}{\beta + 1}$$

$$B_1 = 1 + \frac{R}{\beta^2} - \frac{\theta}{\beta \, (\beta + 1)}$$

(78)

191

For $z<0$, in the cold gas, one obtains the same equations and solutions as previously found, however, for $z>0$ one finds

$$\beta \frac{dY}{dz} - \frac{d^2Y}{dz^2} - \theta\overline{q} + R = 0 \Bigg\}$$

where

$$R = \frac{2 \text{ Rad}}{b \; T_o^{\;2} \; k_o^{\;2}}$$

(75)

Because of the radiation losses, the temperature will always have a maximum for $z>0$ and then decrease to $Y = 1$ at $z = z_1$. For $z>z_1$, neither laser absorption nor radiation losses occur. This determines the boundary condition at $z = z_1$ to be

$$Y = 1 \text{ and } \frac{dY}{dz} = 0$$

(76)

For $0<z<z_1$, the solution of equation 75 is

$$Y = B_1 \; e^{\beta z} - \left(\frac{R}{\beta}\right) \; z + B_2 - \frac{\theta e^{-z}}{\beta + 1}$$

(77)

where B_1 and B_2 are constants to be determined from the boundary conditions at both $z = 0$ and $z = z_1$. At $z = 0$, one obtains

$$1 = B_1 + B_2 - \frac{\theta}{\beta + 1} \Bigg\}$$

$$B_1 = 1 + \frac{R}{\beta^2} - \frac{\theta}{\beta \; (\beta + 1)} \Bigg\}$$

(78)

191

which can be manipulated to yield

$$\frac{R}{\beta^2} + B_2 = \frac{\theta}{\beta} \tag{79}$$

at $z = z_1$, one obtains from equations 76 and 77

$$\left.\begin{array}{l} 1 = B_1 e^{\beta z_1} - \frac{\theta}{\beta} z_1 + B_2 - \frac{\theta e^{z_1}}{\beta + 1} \\[2em] \beta B_1 e^{\beta z_1} - \frac{R}{\beta} + \frac{\theta e^{-z_1}}{\beta + 1} = 0 \end{array}\right\} \tag{80}$$

The simultaneous solution of equations 78 and 80 determines B_1, B_2, z_1, and the relationship between θ and β. (LSC wave velocity versus laser intensity.) From equation 80 one finds

$$\theta = \frac{\beta + Rz_1}{1 - e^{-z_1}} \tag{81}$$

Substitution of equations 78, 79, and 81 into equation 80 yields the required eigen-solution of this radiation problem.

$$\frac{R}{\beta^2} = \frac{[(\beta+1)(1-e^{-z_1}) + e^{-z_1}(\beta+1) - 1]}{[(\beta+1)(e^{-z_1}-1)(1-e^{-\beta z_1}) + z_1 \beta(1-e^{-z_1(\beta+1)})]} \tag{82}$$

An arbitrary choice of z_1 and β in equation 82 defines a radiation loss term R and the subsequent use of equation 81 determines the laser intensity (through the dimensionless parameter θ).

Figure 10b shows one result of this calculation as a curve of
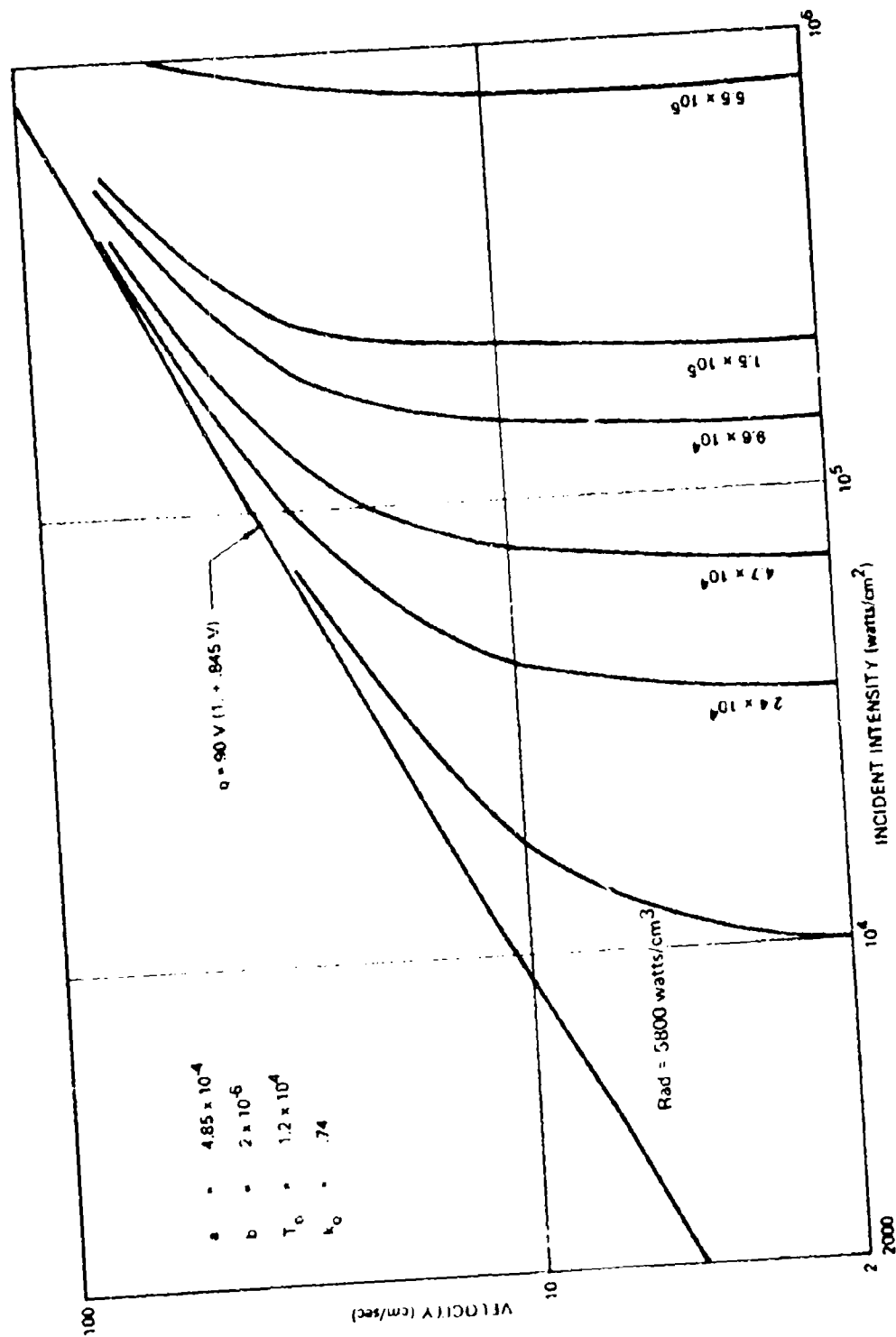
Figure 108: VELOCITY V OF A RADIATING LSC WAVE AS A FUNCTION OF THE LASER
INTENSITY q_0 WITH THE RADIATION LOSS RAD AS A PARAMETER.

193

LSC wave velocity as a function of laser intensity for fixed values of radiation loss. There is again a threshold intensity below which no LSC waves can propagate. (The resemblance to the case of radial heat conduction losses should be noted.) From John[75], $R_{ad} = 8000$ watts/cm^3 so that no LSC waves should ever propagate below a laser intensity of $q_o = 10^4$ watts/cm^2. Figure 109 shows the fraction of the laser power absorbed in the finite length LSC wave as a function of the "radiation effectiveness" R/β. For a fixed velocity of propagation (β = constant), the fraction of laser energy transmitted through the LSC wave is found to increase as the radiation losses increase. This occurs because the high temperature region of the LSC wave becomes shorter and shorter under conditions of high radiation loss. In addition, the laser intensity required to drive the LSC wave increases as the radiation loss increases. This effect is seen in figure 110, where the ratio q_o/q_* is plotted as a function of the radiation loss R, and where q_* is the laser intensity required in the absence of radiation losses. The peak temperature reached in the LSC wave is also found to decrease in a radiating LSC wave as shown in figure 111. For $R = 0$ (no radiation loss), the maximum temperature is given by equation 44 and in figure 111 we plot the ratio of maximum temperature in the LSC wave ($\theta_{max} = T_o\sqrt{Y_{max}}$) divided by T_w. It is seen that finite radiation loss always decreases the temperature of the wave. Actual variations of temperature in representative LSC waves versus distance are given in figure 112 and 113. These radiation curves are shown for the approximate thermodynamic properties for air

$$a = 4.85 \times 10^{-4} \text{ joule/gm } (^{\circ}K)^2$$

$$b = 2 \times 10^{-6} \text{ watt/cm } (^{\circ}K)^2$$

$$T_o = 1.2 \times 10^4 \; ^{\circ}K$$

$$k_o = .74/cm$$

(83)
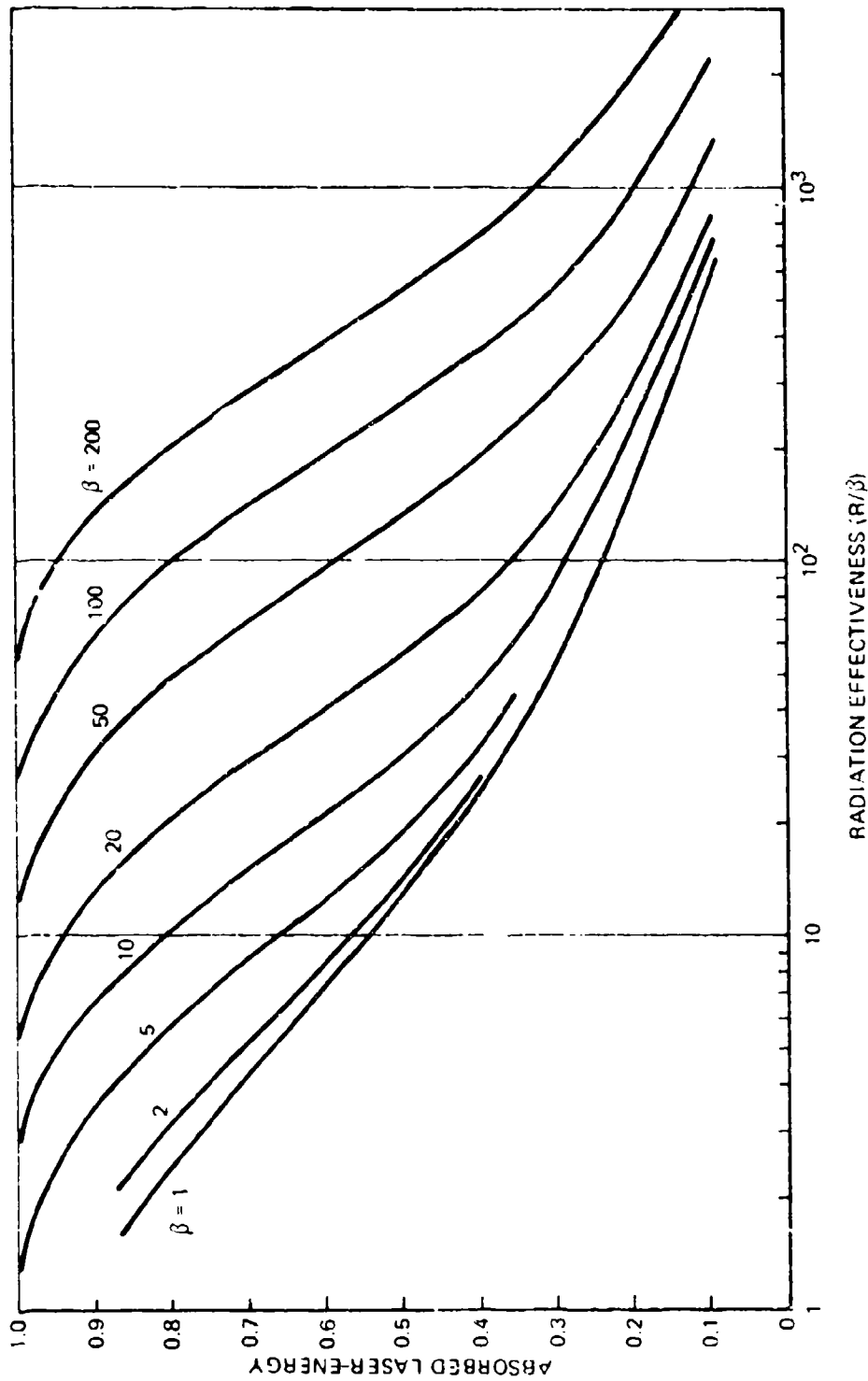
Figure 109: RATIO OF THE LASER INTENSITY ABSORBED $(q_0 - q_T)$ IN A LSC WAVE TO THE INCIDENT LASER INTENSITY q_0 AS A FUNCTION OF THE RADIATION EFFECTIVENESS R/β WITH THE NORMALIZED VELOCITY AS A PARAMETER.

195
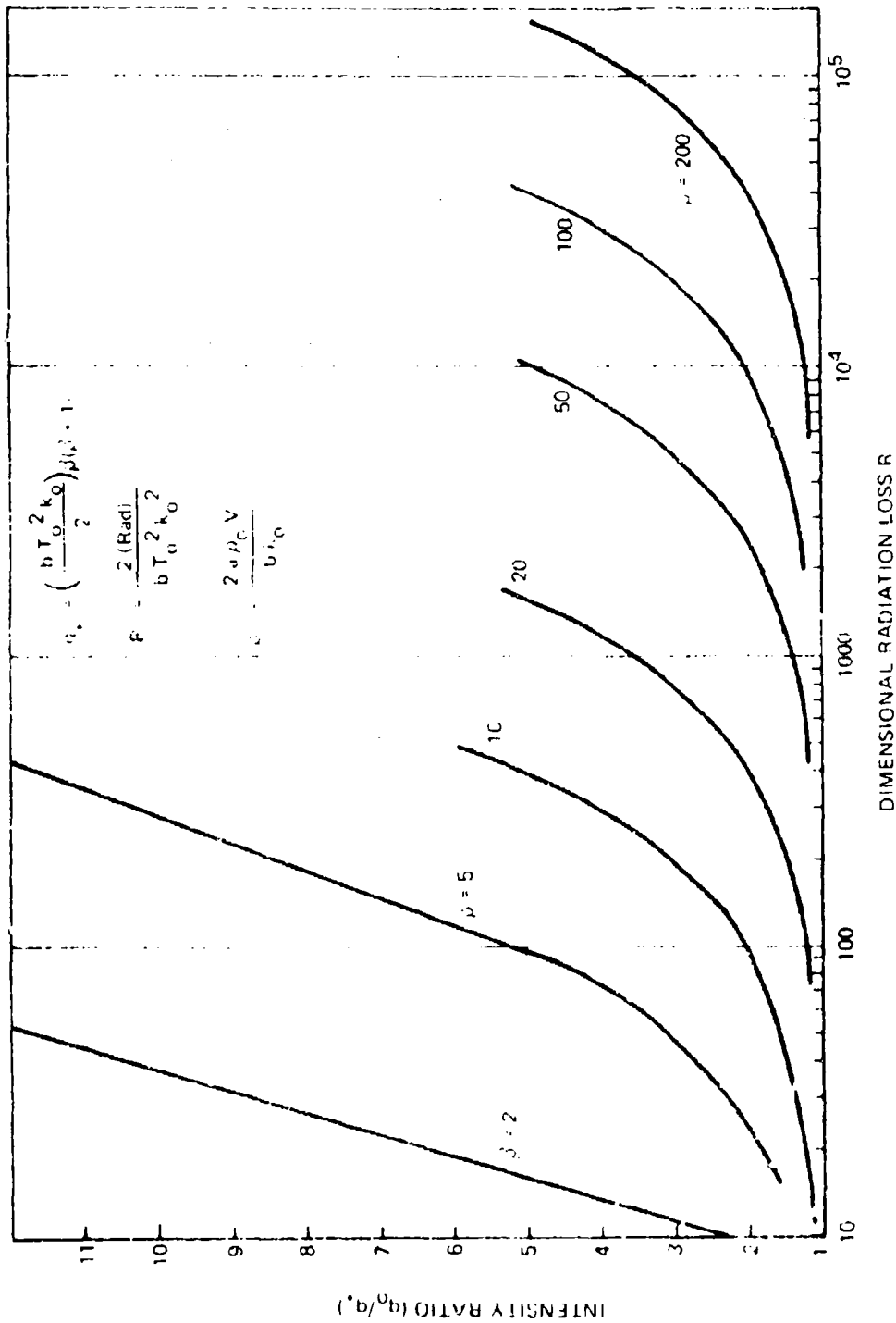
Figure 110. RATIO OF THE LASER INTENSITY WITH RADIATION LOSS q_0 TO THE LASER INTENSITY WITHOUT RADIATION LOSS q, AS A FUNCTION OF THE DIMENSIONLESS RADIATION LOSS R WITH THE NORMALIZED VELOCITY OF A LSC WAVE AS A PARAMETER.
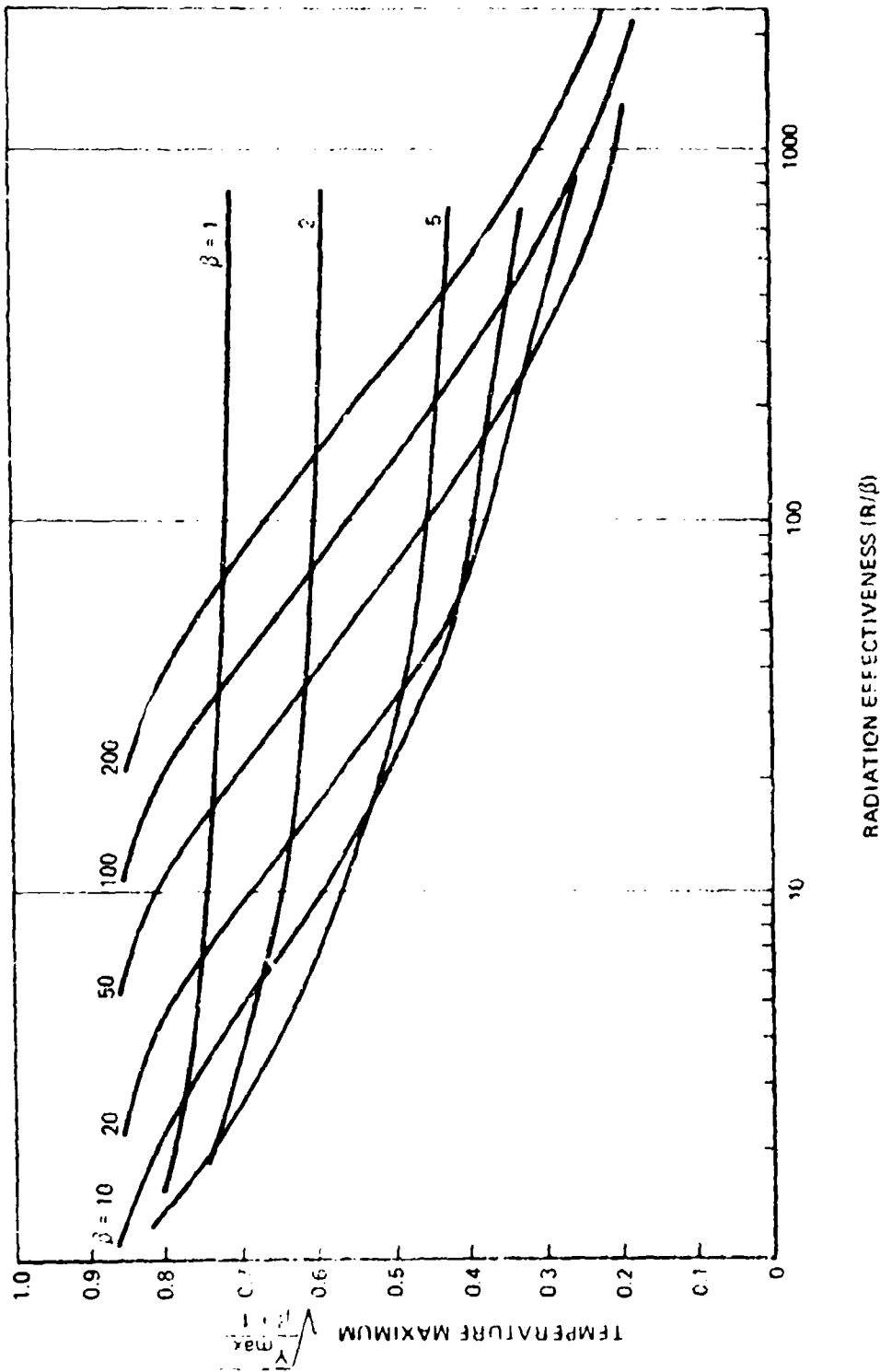
Figure 111 : RATIO OF THE MAXIMUM TEMPERATURE OF A LSC WAVE WITH RADIATION LOSS $(Y_{max})^{1/2}$ TO THE MAXIMUM TEMPERATURE WITHOUT RADIATION LOSS $(\beta + 1)^{1/2}$ AS A FUNCTION OF THE RADIATION EFFECTIVENESS R/β WITH THE NORMALIZED VELOCITY β AS A PARAMETER.

197

Figure 112 : DIMENSIONLESS SQUARE OF THE TEMPERATURE Y THROUGH A LSC WAVE AS A FUNCTION OF THE DIMENSIONLESS DISTANCE Z WITH THE RADIATION LOSS Rad AS A PARAMETER AND FOR V = 8 cm/sec.
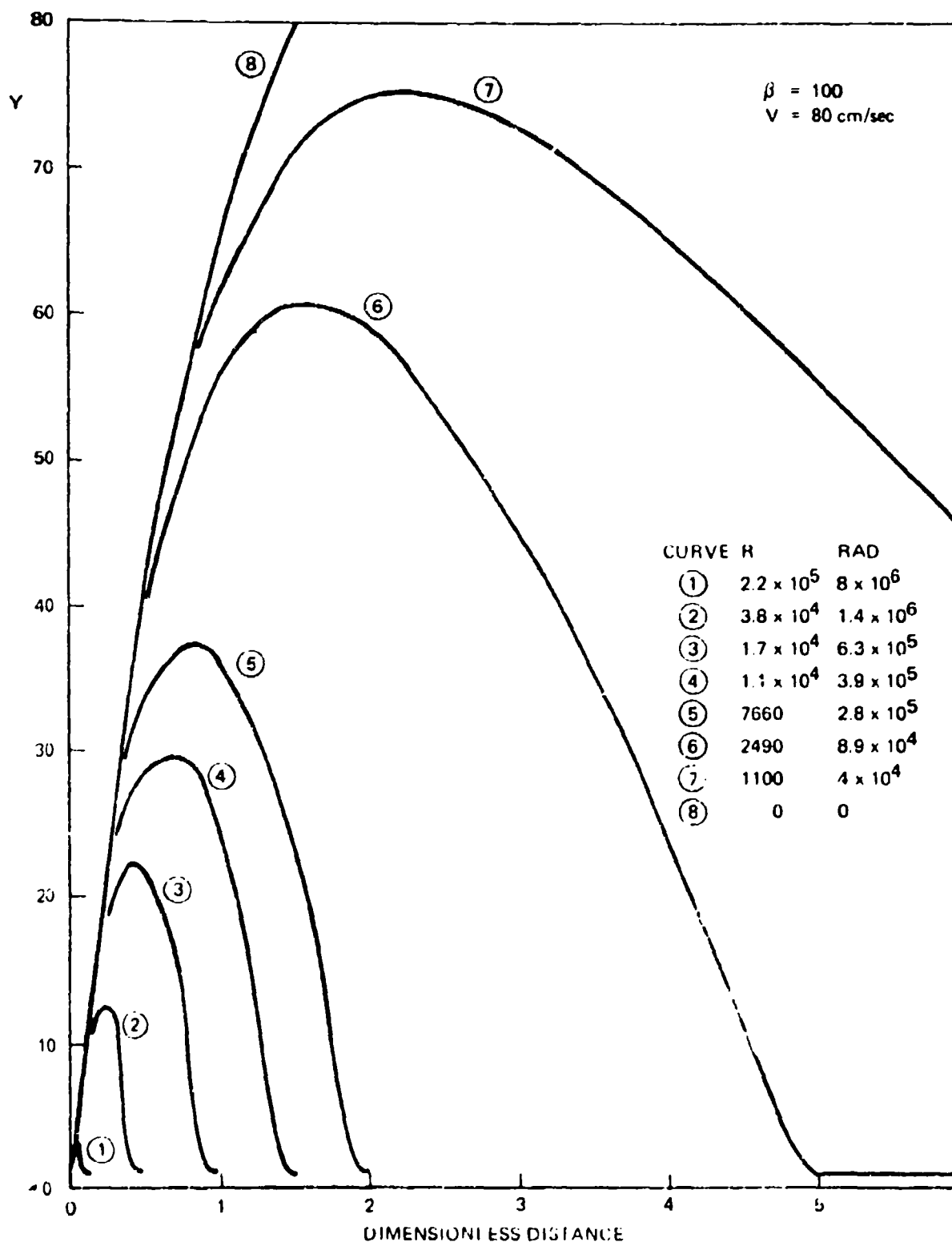
Figure 113. DIMENSIONLESS SQUARE OF THE TEMPERATURE Y THROUGH A LSC WAVE AS A FUNCTION OF THE DIMENSIONLESS DISTANCE Z WITH THE RADIATION LOSS RAD AS A PARAMETER AND FOR V = 80 cm/se.

Figure 112, for $V = 8$ cm/sec, shows a strong clamping of the temperature to values near ignition temperature T_0. For example, curve 3 corresponding to a radiation loss of 7020 watts/cm^3, indicates that the maximum temperature in the LSC wave is approximately 20,000°k and the hot plasma core to have a length of approximately 1 cm. On the other hand, for $V = 80$ cm/sec (as shown in figure 113) one finds that radiation loss effects, for "realistic" conditions are small. Thus, unless these losses are larger than expected they can be ignored when $\beta = 100$ or greater.

7.6 BOUNDARY RESTRAINTS ON LSC WAVES

This section discusses one consequence of igniting LSC waves near a solid boundary. For one-dimensional LSC waves with the laser beam incident perpendicular to the wall, one requires as a boundary condition that the fluid velocity be zero at the wall. In order to meet this requirement, additional pressure waves or shock waves must be emitted into the cold gas ahead of the LSC wavefront. In this way, the cold gas is set into motion in the direction of the LSC wave, causing the observed propagation velocity to be increased. An illustration of the situation is figure 114 which shows schematically the fluid properties of density, velocity, temperature, and laser intensity as a function of distance. Because of the solid boundary, one can assume that the fluid velocity vanishes, in laboratory coordinates, behind the combustion wave. This requires that a shock wave be generated that travels ahead of the "slow" combustion wave in order to satisfy all boundary conditions (if the LSC wave velocity is sufficiently large). The regions of space shown in figure 114 are divided into three parts. In region 0, the gas is unperturbed and of ambient temperature, pressure, and density. The shock wave, of velocity D, separates regions 0 and 1. The gas in region 1 is compressed and heated dependent on the shock mach number. The combustion zone, shown as the cross hatched area, separates regions 1 and 2. The analysis presented here is expected to be valid within a few laser beam

200
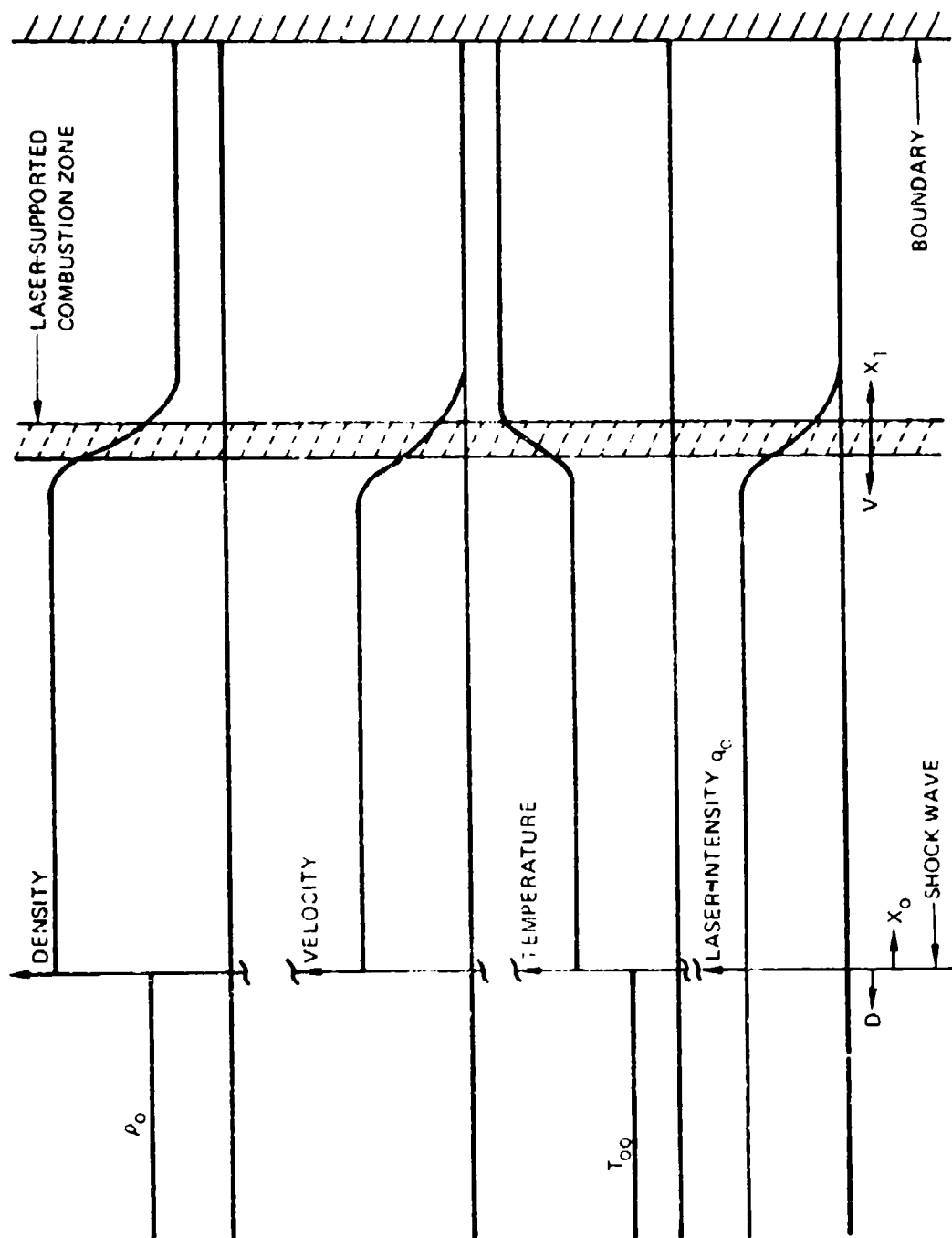
Figure 134 : SCHEMATIC OF THE DENSITY ρ, VELOCITY V, TEMPERATURE T, AND LASER INTENSITY q THROUGH A SHOCK WAVE AND A LSC WAVE AS A FUNCTION OF THE DISTANCE x.

diameters of the target. For larger distances from the target, radial spreading of the flow can be expected to reduce the flow velocities (and hence the observed LSC wave velocities would decrease).

We assume that the gas in region 1, behind the shock wave, remains an ideal gas which implies that the shock mach number is not too large. Under this restraint, one obtains[26]

$$\frac{\rho_1}{\rho_o} = \frac{(\gamma+1)\ M^2}{(2+ (\gamma-1)\ M^2)} \quad\quad (84)$$

where

$$\left.\begin{array}{l} \rho_o = \text{ambient gas density} \\[4pt] \rho_1 = \text{compressed gas density in region 1} \\[4pt] \gamma = \text{ratio of specific heats} \\[4pt] M = \text{shock mach number} = D/c_o \\[4pt] c_o = \text{ambient sound velocity} \end{array}\right\} \quad\quad (85)$$

The pressure behind the shock front P_1 is given by

$$\frac{P_1}{P_o} = \frac{2}{(\gamma + 1)}\ M^2 - \left(\frac{\gamma - 1}{\gamma + 1}\right) \quad\quad (86)$$

where P_o is the ambient pressure. The shocked temperature T_1 is

$$\frac{T_1}{T_{oo}} = \frac{\{2\ \gamma M^2 - (\gamma-1)\}\ \{(\gamma-1)\ M^2 + 2\}}{(\gamma + 1)^2\ M^2} \quad\quad (87)$$

202

where T_{oo} is ambient temperature. In the shock coordinate system, the gas velocity V_{1s} is given by

$$\rho_o D = \rho_1 V_{1s} \qquad (88)$$

while in laboratory coordinates the gas velocity V_{1L} (in region 1) is

$$V_{1L} = D - V_{1s} = D \left(1 - \frac{\rho_o}{\rho_1}\right) \qquad (89)$$

Since the LSC wave zone moves with a laboratory speed of V_L, the cold gas in the coordinate system x_1 moves at a speed V

$$V = V_L - V_{1L} = V_L - D \left(1 - \frac{\rho_o}{\rho_1}\right) \qquad (90)$$

Because of the conservation of mass one obtains

$$\rho_1 \left[V_L - D \left(1 - \frac{\rho_o}{\rho_1}\right) \right] = \rho_2 V_L \qquad (91)$$

where ρ_2 is the mass density in region 2. One notes that $\rho_1 > \rho_o$ and $\rho_2 < \rho_1$ making the gas in region 1 the most dense.

If one assumes that the ambient molecular gas is completely dissociated in region 2 and partially ionized, one obtains

$$\frac{\rho_2}{\rho_1} = \left(\frac{T_1}{T_2}\right) / g \qquad (92)$$

203

where

$$g = 2 (1 + x_e)$$

for a molecular gas and

$$g = 1 + x_e$$

for a monatomic gas where the fractional ionization is given by x_e.

The one-dimensional combustion wave heat equation is

$$\beta_s (1 - Y_1) - \frac{dY}{dz} + \theta (\bar{q} - 1) = 0$$

where

$$\beta_s = \frac{2 \rho_1 \left[V_L - D \left(1 - \frac{\rho_0}{\rho_1} \right) \right] a}{b k_1}$$

$$Y_1 = \frac{T_1^2}{T_0^2} \quad ,$$

and

$$k_1 = k_0 (p_1/p_0)^a$$

In equation 94, k_1 is the laser absorption coefficient in the compressed and shocked gas where typically one expects $\alpha \approx 2$[65]. The previously used laser attenuation equation is again used as defined by equation 36.

For $z < 0$

$$Y = Y_1 + (1 - Y_1) \exp \{ \beta_s z \}$$

$$\bar{q} = 1$$

204

For z>0, the solution of 94 is

$$Y = Y_1 + \frac{\theta}{\beta_s} - \frac{\theta\, e^{-z}}{\beta_s + 1} \tag{96}$$

Since $Y = 1$ at $Z = 0$, one obtains the condition

$$\frac{\theta}{\beta_s\,(\beta_s + 1)} = 1 - Y_1 \tag{97}$$

which along with the boundary condition at $z = \infty$ leads to the final temperature T_f as determined by

$$\frac{T_f^2}{T_o^2} = Y_f = Y_1 + \frac{\theta}{\beta_s} = Y_1 + (1 - Y_1)(1 + \beta_s) \tag{98}$$

By combining equations 90, 91, 92, 94 and 98, a cubic equation in β_s is obtained

$$\left. \beta_s^3 + \frac{g^2 \cdot Y_1}{g^2(1-Y_1)}\, \beta_s^2 - \frac{2\,Y_1\,K}{g^2(1-Y_1)}\, \beta_s - \frac{Y_1\,K^2}{g^2(1-Y_1)} = 0 \right\}$$

in which

$$\left. K = \frac{2ab(\rho_1 - \rho_o)}{bk_1} - \frac{4ac_o\rho_o M(M^2-1)(\gamma+1)^\alpha}{bk_o(2+(\gamma-1)M^2)(2\gamma M^2-(\gamma-1))^\alpha} \right\} \tag{99}$$

For a given Mach number, the above cubic equation can be solved for β_s explicitly by numerical iteration and then equation 97 can be solved for θ.

For z>0, the solution of 94 is

$$Y = Y_1 + \frac{\theta}{\beta_s} - \frac{\theta \, e^{-z}}{\beta_s + 1} \tag{96}$$

Since $Y = 1$ at $Z = 0$, one obtains the condition

$$\frac{\theta}{\beta_s \, (\beta_s + 1)} = 1 - Y_1 \tag{97}$$

which along with the boundary condition at $z \to \infty$ leads to the final temperature T_f as determined by

$$\frac{T_f^2}{T_o^2} = Y_1 = Y_1 + \frac{\theta}{\beta_s} = Y_1 + (1 - Y_1)(1 + \beta_s) \tag{98}$$

By combining equations 90, 91, 92, 94 and 98, a cubic equation in β_s is obtained

$$\left. \beta_s^3 + \frac{g^2 \cdot Y_1}{g^2(1-Y_1)} \, \beta_s^2 - \frac{2\,Y_1\,K}{g^2(1-Y_1)} \, \beta_s - \frac{Y_1\,K^2}{g^2(1-Y_1)} = 0 \right\} \tag{99}$$

in which

$$K = \frac{2ab(\rho_1 - \rho_o)}{bk_1} - \frac{4ac_o\rho_o M(M^2-1)(\gamma+1)^\alpha}{bk_o(1+(\gamma-1)M^2)(2\gamma M^2-(\gamma-1))^\alpha}$$

For a given Mach number, the above cubic equation can be solved for β_s explicitly by numerical iteration and then equation 97 can be solved for θ.

The solutions of equation 99 are shown in figure 115 for the velocity V_L of the LSC waves in the laboratory reference frame and in figure 116 for the velocity V of the LSC waves in the reference frame in which the shocked but relatively cool gas ahead of the absorption zone is stationary. V is equivalent to the velovity calculated in the previous sections while V_L is more than two orders of magnitude larger. The parameters used in figures 115 and 116 are those previously indicated by equation 83 except curves are shown for three different values of the absorption coefficient, k_o, in order to indicate the sensitivity of the results to exact numerical values. In addition, the further gas properties needed are

$$\left.\begin{array}{l} T_{co} = 300^{o}K \\[4pt] \gamma = 1.4 \\[4pt] \rho_o = 1.2 \text{ gm/cm}^3 \\[4pt] c_o = 3.47 \times 10^4 \text{ cm/sec} \\[4pt] g = 4 \end{array}\right\} \qquad (100)$$

The value of g = 4 assumes the gas is nearly fully ionized.

It is evident from the results shown in figure 115 that the observed LSC wave velocity in the presence of solid target boundaries is not highly sensitive to either the value of k_o or to the magnitude of its pressure dependent exponent α. (Increasing magnitudes of k_o and α always increase LSC wave velocities.) Experiments in which LSC waves are ignited from solid targets do have initial velocities which are about a factor of 2 lower than the results given in figure 115[77]. The asymptotes in figures 115 and 116 are obtained by solving equation 99 in the limit of weak shocks.
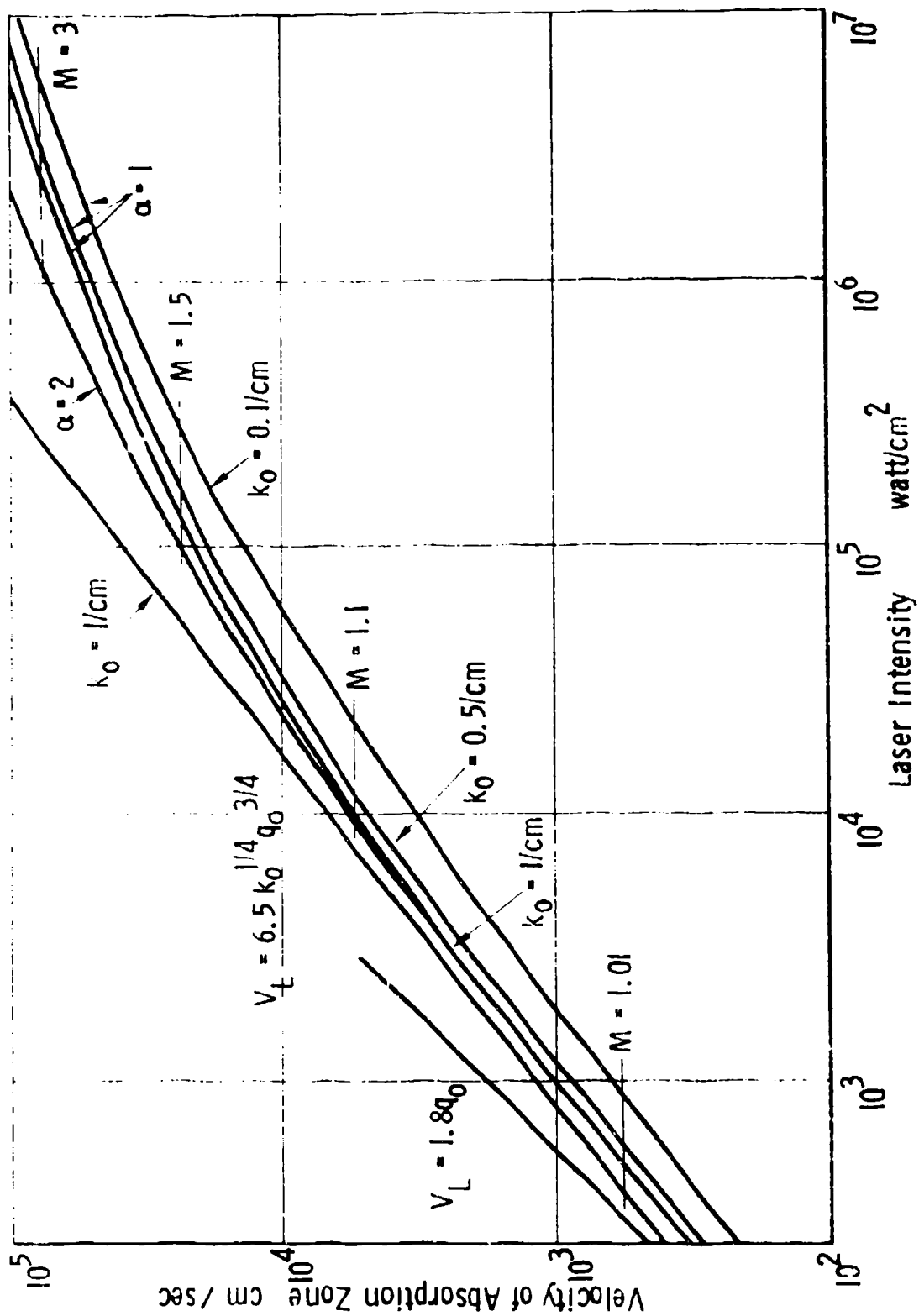
Figure 115: VELOCITIES OF ONE-DIMENSIONAL LSC WAVES V_L IN THE LABORATORY REFERENCE FRAME AS A FUNCTION OF THE LASER INTENSITY q_o FOR THREE ABSORPTION COEFFICIENTS k_o

Figure 116: VELOCITIES OF ONE-DIMENSIONAL LSC WAVES V WITH RESPECT TO THE SHOCKED GAS AHEAD OF THE WAVE AS A FUNCTION OF THE LASER INTENSITY q_0 FOR THREE ABSORPTION COEFFICIENTS k_0

where
$$M = 1 + \epsilon$$
$$\epsilon < 1$$
(101)

By substitution of equation 101 into equation 99 and performing various manipulations, one obtains

$$\epsilon = \frac{g b \kappa_0 T_0 (1 + \epsilon) \sqrt{2} \, u}{8 \rho_0 a c_0 T_{00} \sqrt{1 + \sqrt{4\theta + 1}}}$$
(102)

which leads to an equation relating LSC wave velocity and laser flux

$$V_L = \frac{g b \kappa_0 T_0 \theta}{\sqrt{2} \, \rho_0 a T_{00}} \frac{1}{\sqrt{1 + \sqrt{4\theta + 1}}}$$
(103)

For large laser intensities $(\theta \gg 1)$, one finds

$$V_L = \left(\frac{g}{\rho_0 a T_{00}} \right) \left(\frac{b k_0}{2 T_0^2} \right)^{1/4} q_0^{3/4}$$
(104)

while for smaller intensities $(\theta \ll 1)$, the result

$$V_L = \frac{g \, q_0}{\rho_0 T_{00} a T_0}$$
(105)

is found.

The numerical relationship between the shock Mach number, LSC wave velocity, and the required laser intensity is determined to be (using the previously indicated gas properties

$$q_o = 399 \left(\frac{\epsilon}{.01}\right)^{4/3} \text{watts/cm}^2$$

$$V_L = 579 \left(\frac{\epsilon}{.01}\right) \text{cm/sec}$$

(106)

for $k_o = 1.0$ cm^{-1}. The general dependence of LSC wave velocity at high laser intensities ($\theta \ll 1$) is found to be

$$V_L = 6.5 \, k_o^{1/4} \, q_o^{3/4} \text{cm/sec}$$

(107)

which is indicated on figure 115. One concludes that the asymptotic relationship (equation 107) is valid over a wide range in laser intensity until the shock Mach number becomes appreciable. This tendency can be seen in figures 115 and 116 by the constant Mach number curves drawn for $M = 1.01$, 1.1, 1.5 and 3.0. The curve labeled, $V_L = 1.8 \, q_o$, in figure 115 corresponds to the low laser intensity assymptote ($\theta < 1$).

7.7 SHAPE OF THE FRONT OF AN LSC WAVE

In general, one doesn't expect that LSC waves will propagate with their surfaces perpendicular to the laser beam. This occurs in actual experimental situations in which there is always a radial distribution of laser intensity and from which one expects a corresponding variation of the normal LSC propagation velocity. Our calculations below are based on the assumption of a small laser absorption length compared to the beam radius for which one can use one-dimensional calculations to compute approximate two-dimensional effects. It should be noted that most present

experiments do not necessarily fulfill this analytical requirement and hence the obtained results may not be directly applicable[72,77].

An LSC wave, propagating at an arbitrary angle to the laser beam direction, is shown in figure 117 where the x_1 coordinate system is normal to wavefront. While the laser beam propagates in the x direction, the continuity and energy equations are evaluated across the LSC wave boundary (in the x_1 direction). Noting that

$$x_1 = x \sin \phi \tag{108}$$

one obtains from equation 36

$$\frac{dq}{dx_1} = - \left(\frac{k}{\sin \phi} \right) q \tag{109}$$

the perpendicular component of velocity is similarly

$$V_n = V \sin \phi \tag{110}$$

One thus observes that the previously determined eigenvalue equation is made valid for LSC waves propagating at an arbitrary angle to the laser beam merely by replacing k by ($k/\sin \phi$) and V by $V \sin \phi$.

$$\theta_\phi = \beta_\phi (\beta_\phi + 1) \tag{111}$$

where

$$\left. \begin{array}{l} \theta_\phi = \dfrac{2 \, q_o \sin \phi}{b \, T_o^2 \, k_o} \\[4mm] \beta_\phi = \dfrac{2 \, a \, \rho_o \, V \sin^2 \phi}{b k_o} \end{array} \right\} \tag{112}$$

211

INCIDENT LASER BEAM
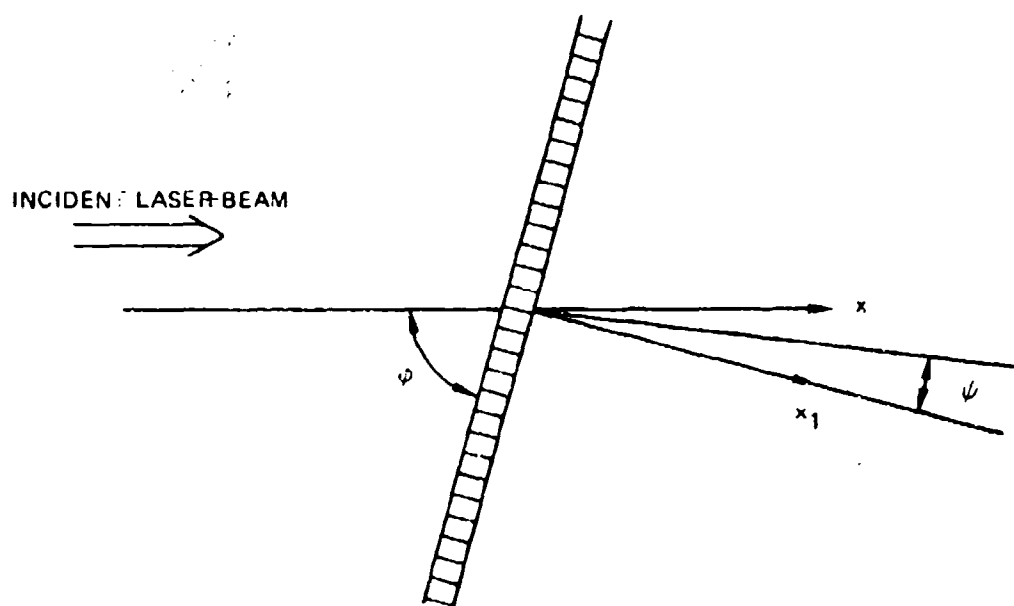
Figure 117. SCHEMATIC OF AN OBLIQUELY INCIDENT LASER BEAM ON A LASER-
SUPPORTED COMBUSTION WAVE.
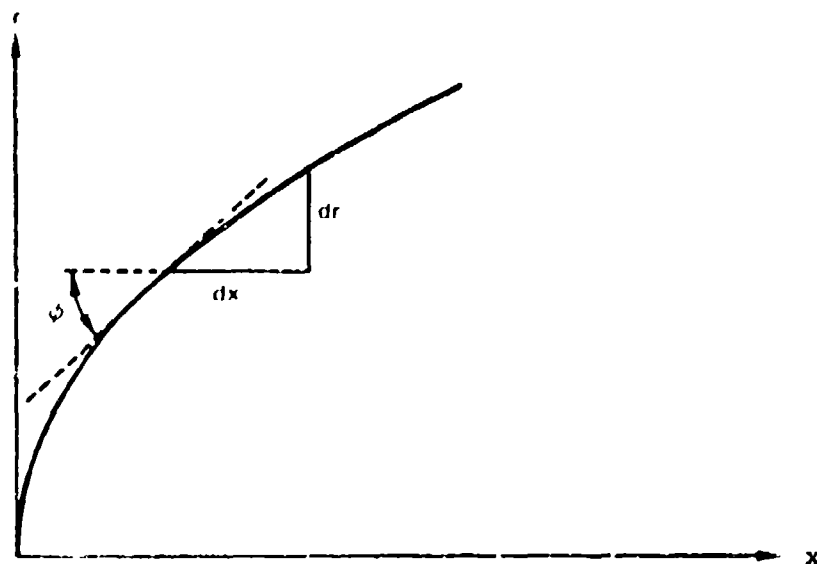
Figure 118 : SCHEMATIC OF A LSC WAVEFRONT.

For large laser intensities ($\beta_\phi \gg 1$), one obtains

$$\rho_o V = \frac{1}{\sin^{3/2} \phi} \sqrt{\frac{q_o k_o \lambda_o T_o}{2 h_o^2}} \tag{113}$$

while for small laser inten ities ($\beta_\psi \ll 1$)

$$\rho_o V = \frac{q_o}{\sin \phi \ h_o} \tag{114}$$

Equation 11! allows us to determine the shape of the front of large diameter LSC waves in which the laser intensity is a function of radius and for those cases in which the beam radius is larger than the absorption length. For most existing laser beams, this requirement is not met since LSC wave have been obtained by focusing down to very small dimensions.

A portion of the LSC wave front is shown in figure 118. The radially symmetric combustion front has a local radius r which is a function of x, the axial distance. One notes that

$$\left. \begin{array}{l} \dfrac{dr}{dx} = \tan \phi \\[2em] \sin \phi = \dfrac{1}{\sqrt{1 + \left(\dfrac{dx}{dr}\right)^2}} \end{array} \right\} \tag{115}$$

If one considers the large intensity combustion wave defined by equation 113, one notes that at all radii (q_o is the axial intensity)

$$\frac{q_o(r)}{\sin^3 \phi} = q_o = \text{constant} \tag{116}$$

213

Substitution of equation 115 into 116 leads to the differential equation determining the shape of the LSC wavefront.

$$\frac{dx}{dr} = \sqrt{\left(\frac{q_o}{q_o(r)}\right)^{2/3} - 1} \tag{117}$$

Equation 117 is difficult to solve for a Gaussian laser beam, however, a useful approximation to such an intensity profile is

$$\frac{q_o(r)}{q_o} = \left[1 + \frac{(r/h)^2}{\left\{1 - \left(\frac{r}{ch}\right)^2\right\}^4}\right]^{-3/2} \tag{118}$$

where, of course, the radial distance r is restricted to values r<ch. The approximation given by equation 118 is compared with a Gaussian beam defined by

$$\frac{q(r)}{q_o} = \exp\left(-\frac{3r^2}{2h}\right) \tag{119}$$

in figure 119 where no discernable difference is to be found. (The parameter c = 2.82 was chosen for a best fit.)

For the above laser intensity, one obtains from equation 117 the shape of the front of the combustion wave.

$$\frac{x}{h} = \frac{1}{2} \frac{\left(\frac{r}{h}\right)^2}{\left(1 - \left(\frac{r}{ch}\right)^2\right)} \tag{120}$$

$$\frac{q(r)}{q(o)} = \exp\left(\frac{-r^2}{\delta^2}\right) \approx \left[1 + \frac{r^2/h^2}{(1-r^2/(ch)^2)^4}\right]^{3/2}$$

$$\delta^2 = \frac{2}{3}h^2$$

$$c = 2.82$$

DIMENSIONLESS RADIUS

LASER-INTENSITY

r/h
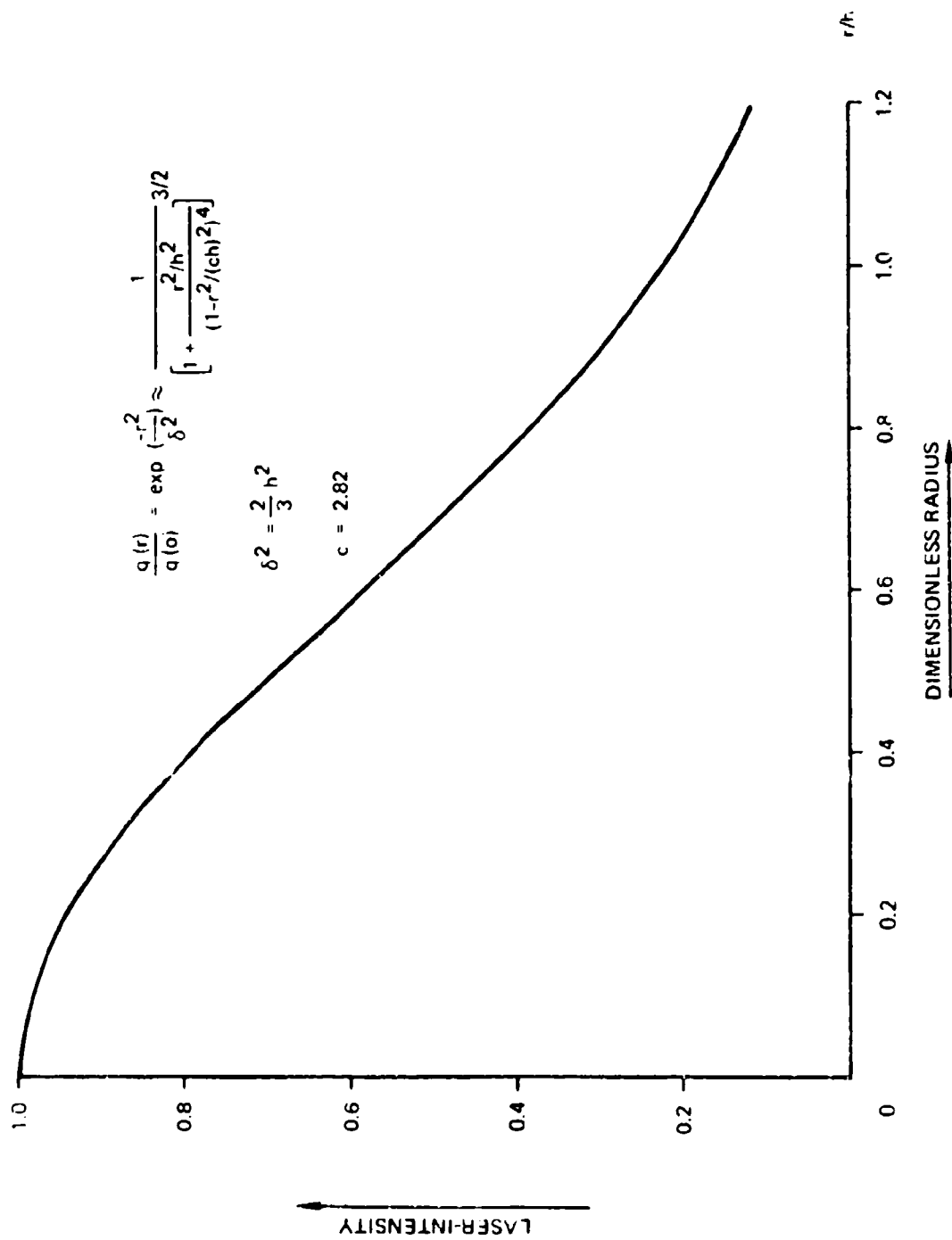
Figure 119: *LASER INTENSITY q_0 (r) AS A FUNCTION OF RADIUS r IN THE BEAM.*

215

This profile is plotted in figure 120 where the parabolic front is evident. Note that the above determined profile is valid only in the part of the laser beam such that $\beta_\phi \ll 1$. When the angle ϕ becomes too small, a different differential equation determines the combustion wave profile. For $\beta_\phi \ll 1$, one finds

$$\left.\begin{array}{l} \dfrac{q_0(r)}{q_0} = \sin \phi \\[20pt] \dfrac{dx}{dr} = \sqrt{\left(\dfrac{q_0}{q_0(r)}\right)^2 - 1} \end{array}\right\} \tag{121}$$

A full solution of this problem would 'connect' smoothly to the previous solution for $\beta_\phi \gg 1$.

The direction ψ of the hot gas behind the combustion wave can be determined from the continuity of mass and from the tangential continuity of flow velocity. From figure 117, one obtains

$$\text{Tan } \psi = \frac{\rho_2}{\rho_1} \, \text{Cot } \phi \tag{122}$$

where (ρ_2/ρ_1) is dependent on both geometry and the eigensolutions of equation 111. Assuming constant pressure, nearly full ionization, an initially diatomic gas so that $g = 4$ and large laser fluxes $(\beta_\phi \gg 1)$, one obtains

$$\text{Tan } \psi = \sqrt{\frac{b \kappa_0}{32 \, a \, \rho_1 \, V}} \quad \frac{\cos^2 \phi}{\sin \phi} \tag{123}$$

$$\frac{x}{h} = \frac{\frac{1}{2}\left(\frac{r}{h}\right)^2}{1 - \left(\frac{r}{ch}\right)^2}$$

$$c = 2.82$$
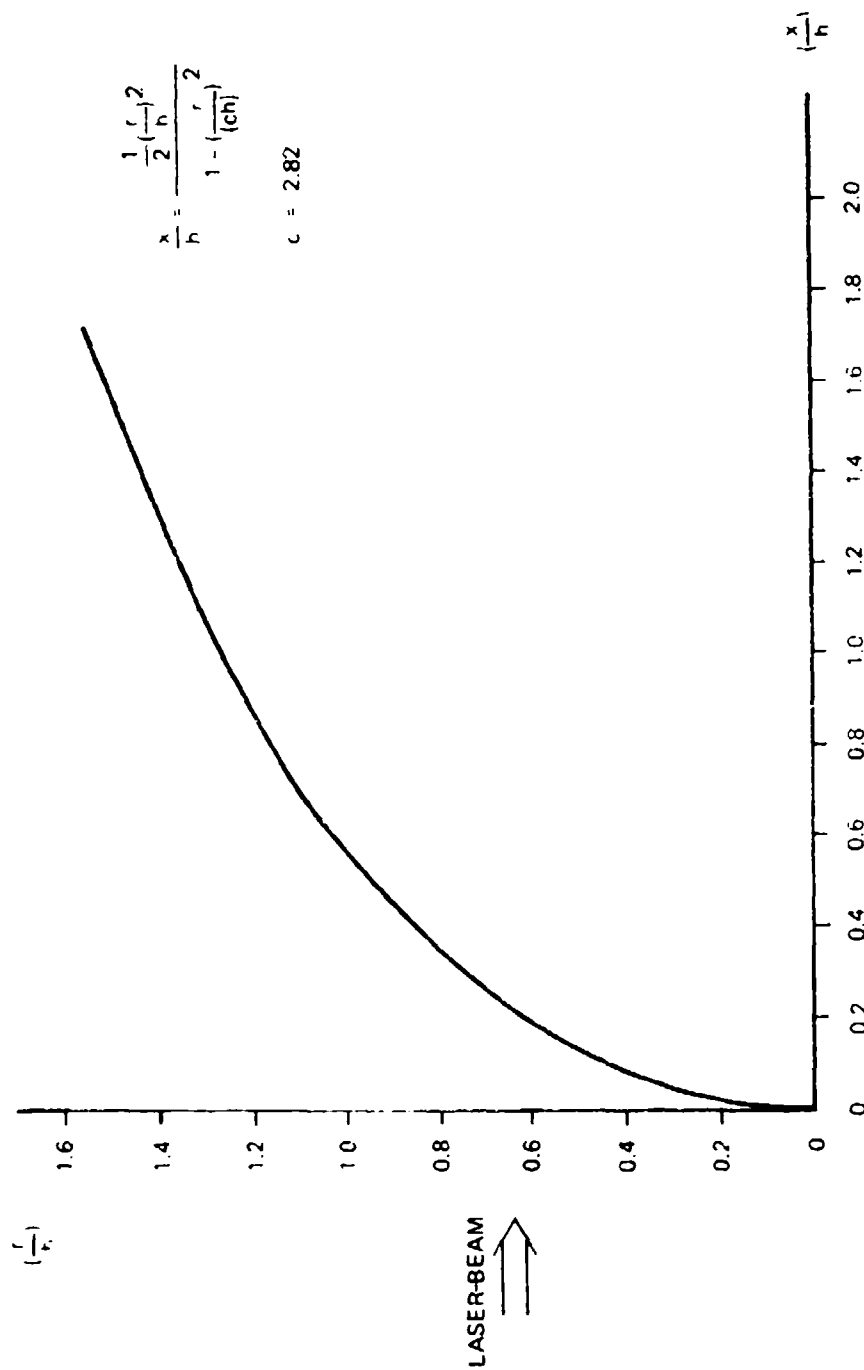
Figure 120 : CALCULATED SHAPE OF A LSC WAVEFRONT WITH AN APPROXIMATELY GAUSSIAN LASER BEAM INTENSITY PROFILE.

LASER-BEAM

7.8 SUMMARY

One-dimensional calculations on an analytical model show that the velocity of the laser-supported absorption zone (LSC wave) is proportional to the 3/4 power of the laser intensity when boundaries are present. Under these circumstances the temperature of the hot gas behind the absorption zone is proportional to the 1/4 power of the laser intensity.

Both heat conduction in the radial direction and radiation loss from Bremsstrahlung and recombination decrease the thickness of the absorption zone, decrease the maximum temperature, and decrease the velocity of propagation of the absorption zone up the laser beam. They both give a critical laser intensity below which the combustion wave cannot be supported. If some of the lost radiation is reabsorbed immediately ahead of the absorption zone, the velocity of propagation increases.

APPENDIX

In order to determine laser-supported detonation wave thresholds, it is necessary to have an adequate knowledge of the laser power density profiles as a function of time. This appendix describes those measurements made on the output of the Boeing Marx Bank Laser.

Measurements have been made on both the incident laser beam as it leaves the laser mirror and on the focused beam. These measurements included energy density profiles and power density profiles obtained with a five-detector array. In addition, the total beam energy and power-time history have been obtained by use of a calibrated beam splitting technique. The results of these measurements indicate that focal diameters of 3 mm are obtained with a 16-inch focal length mirror. A 28-cm focal length mirror or lens has a focal spot diameter of 2.4mm. The peak laser intensity at the beam center has corresponding values of 2.5 x 10^7 and 3.8 x 10^7 watts/cm^2, respectively at a time of 3.1μsec after the beginning of the laser pulse. The energy density profiles indicated that no local hot spots of significant size exist and that the peak laser intensity is near the beam center. From the above minimal dimensions, one calculates that the laser has a beam divergence of 4.4 x 10^{-3} radians - equivalent to 28 times diffraction limited.

1.0 BEAM PROFILE MEASUREMENTS

Accurate beam profile measurements are required for correct assessment of the detonation wave characteristics, particularly for conditions near threshold. There are two extreme conditions where it is possible to obtain the minimum spot diameters required for the detonation wave experiments. These are the near-field and the far-field. The near-field profile appears at the exit aperture of the laser and at any image of the laser aperture. The pattern is magnified or diminished by the ratio of image distance to object distance. The far-field pattern appears near the focal

APPENDIX

In order to determine laser-supported detonation wave thresholds, it is necessary to have an adequate knowledge of the laser power density profiles as a function of time. This appendix describes those measurements made on the output of the Boeing Marx Bank Laser.

Measurements have been made on both the incident laser beam as it leaves the laser mirror and on the focused beam. These measurements included energy density profiles and power density profiles obtained with a five-detector array. In addition, the total beam energy and power-time history have been obtained by use of a calibrated beam splitting technique. The results of these measurements indicate that focal diameters of 3 mm are obtained with a 16-inch focal length mirror. A 28-cm focal length mirror or lens has a focal spot diameter of 2.4mm. The peak laser intensity at the beam center has corresponding values of 2.5 x 10^7 and 3.8 x 10^7 watts/cm^2, respectively at a time of 3.1µsec after the beginning of the laser pulse. The energy density profiles indicated that no local hot spots of significant size exist and that the peak laser intensity is near the beam center. From the minimum focal dimensions, one calculates that the laser has a beam divergence of 4.4 x 10^{-3} radians – equivalent to 28 times diffraction limited.

1.0 BEAM PROFILE MEASUREMENTS

Accurate beam profile measurements are required for correct assessment of the detonation wave characteristics, particularly for conditions near threshold. There are two extreme conditions where it is possible to obtain the minimum spot diameters required for the detonation wave experiments. These are the near-field and the far-field. The near-field profile appears at the exit aperture of the laser and at any image of the laser aperture. The pattern is magnified or diminished by the ratio of image distance to object distance. The far-field pattern appears near the focal

point of a lens or mirror. The dimensions of the pattern are proportional to the effective focal ratio (focal distance to beam diameter) of the focusing system. In these measurements, the geometry was chosen so that the near-field and far-field patterns were quite large, of the order of 6 cm diameter. The data can easily be extrapolated to other spot diameters.

Figure 121 is a plan view of the setup used for measuring beam profile characteristics. The figure shows the pulsed laser and turning mirror in the screen room. The laser beam passed through a KCl prism beam splitter, then was focused with a 10-meter focal length mirror. The five-element gold-doped germanium detector array was located at the position of minimum spot diameter. This position was also the location of the far-field pattern of the laser beam. It should be noted that the far-field pattern was approximately 3 meters inside the focal point of the 10-meter mirror, due to a slight convergence in the main beam as it exited from the laser tube.

The KCl beam splitter prism is wedged at $\theta = 13^{\circ}$. The prism was oriented to cause minimum deviation in the incident beam. In this position, the first and second surface reflections made approximately equal angles of magnitude $n\theta \approx 19^{\circ}$ with the incident beam, as shown in figure 122 (n is the KCl index of refraction).

The first surface reflection was focused at the entrance aperture of a IRG thermopile calorimeter which was used to monitor the pulse energy. The calorimeter output was amplified with a Keithley Model 150A microvolt ammeter and then recorded on a chart recorder. The second surface reflection was focused on a 1-cm thick diffuser cell filled with table salt. The diffused radiation was sensed with a fast gold-doped germanium detector coupled to an oscilloscope which monitored the pulse shape.

Figure 121: BEAM PROFILE MEASUREMENT SETUP

MAIN BEAM

SECOND SURFACE
REFLECTION

FIRST SURFACE
REFLECTION

β

α

θ

KCl WEDGE,
n = 1.454
AT 10.6 MICRONS

$\alpha = 2 \sin^{-1} (n \sin \frac{\theta}{2}) \cong n\theta$

$\beta = \sin^{-1} (n \sin 2\theta) - \alpha \cong n\theta$

TRANSMITTED
BEAM
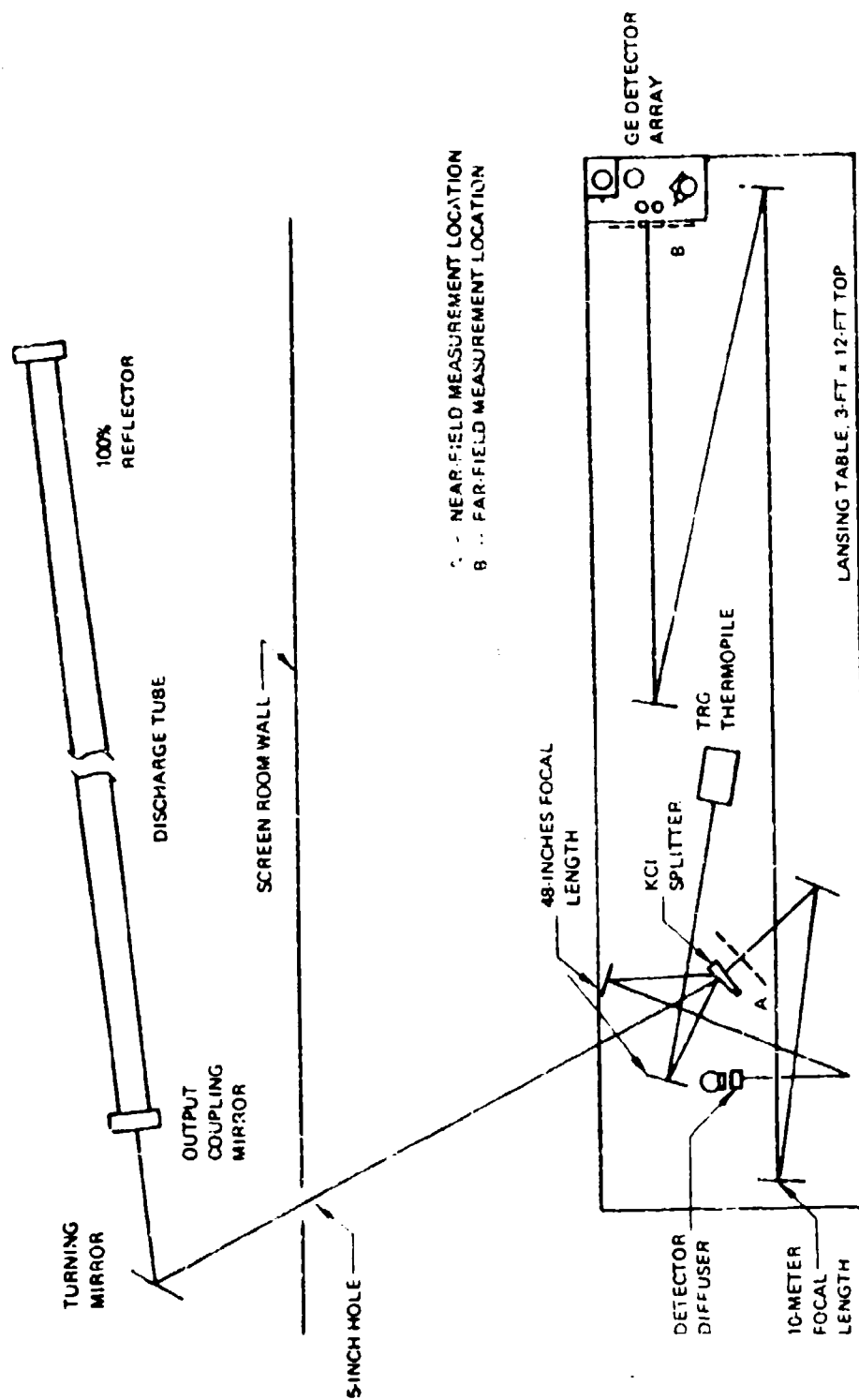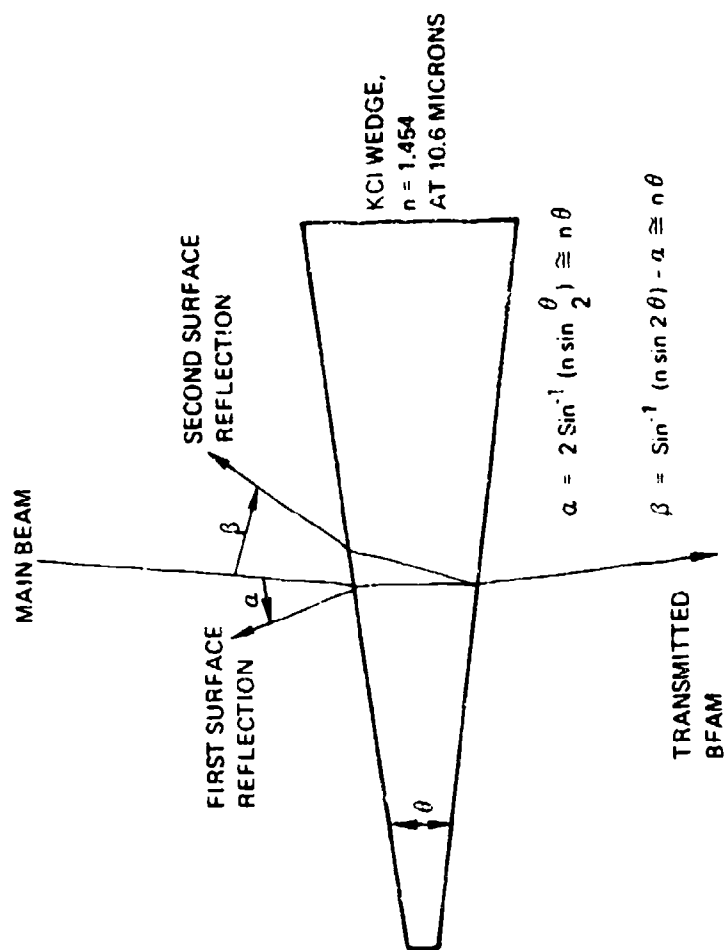
Figure 122 : *KCl PRISM BEAMSPLITTER GEOMETRY*

The germanium detector array consisted of five detectors optically coupled to a copper plate with five 1/4-inch OD copper tubes. The array of entrance apertures is shown in figure 123.

The following measurements were made with the array

1. The array was masked with copper tape, then each hole was individually uncovered and the laser was pulsed. All channels were monitored to check for cross-talk, while the optimum level of the uncovered channel was set on the oscilloscope amplifier.

2. Measurements were made at both the near-field and far-field positions (as shown in figure 121) with the 5-element array centered in the beam.

3. The center detector only was used to obtain a horizontal scan across the far-field pattern. In this test, the detector assembly was moved 0.2-inches between laser shots.

4. A mask of the array aperture was aligned in front of the array and the germanium detector assembly removed. A carbon block thermopile was then used to sequentially measure the energy passing through each hole.

2.0 ENERGY DENSITY OF INCIDENT LASER BEAM

The energy density profile of the incident laser beam was measured as a function of radius as shown schematically in figure 124. The variable aperture allowed a circular beam to be selected at the calorimeter. In this experiment, we relied on laser repeatability to obtain data as we did not have a suitable beam monitor in place. Later data shown below validate this technique. Figure 125 shows the results of plotting energy reaching the calorimeter as a function of aperture area. If a Gaussian profile of energy density is assumed

$$q = q_0 e^{-r^2/\delta^2}$$

223

OUTLINE OF BURN PATTERN ON
CARBON PAPER
(2-3/8 INCH DIAMETER)

0.170-INCH ID

1-INCH DIAMETER CIRCLE

1   5   3

4
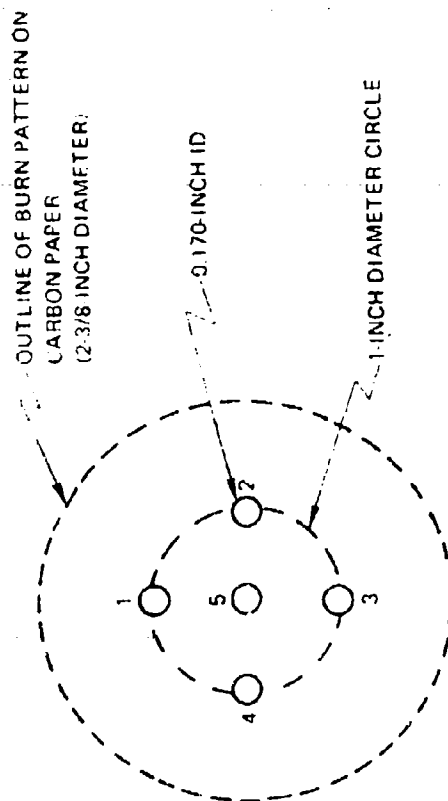
Figure   123.   ENTRANCE APERTURE OF BEAM PROFILE DETECTOR ARRAY

224

INCIDENT
LASER BEAM

APERTURE (VARIABLE)

48-INCH FOCAL
LENGTH MIRRCR
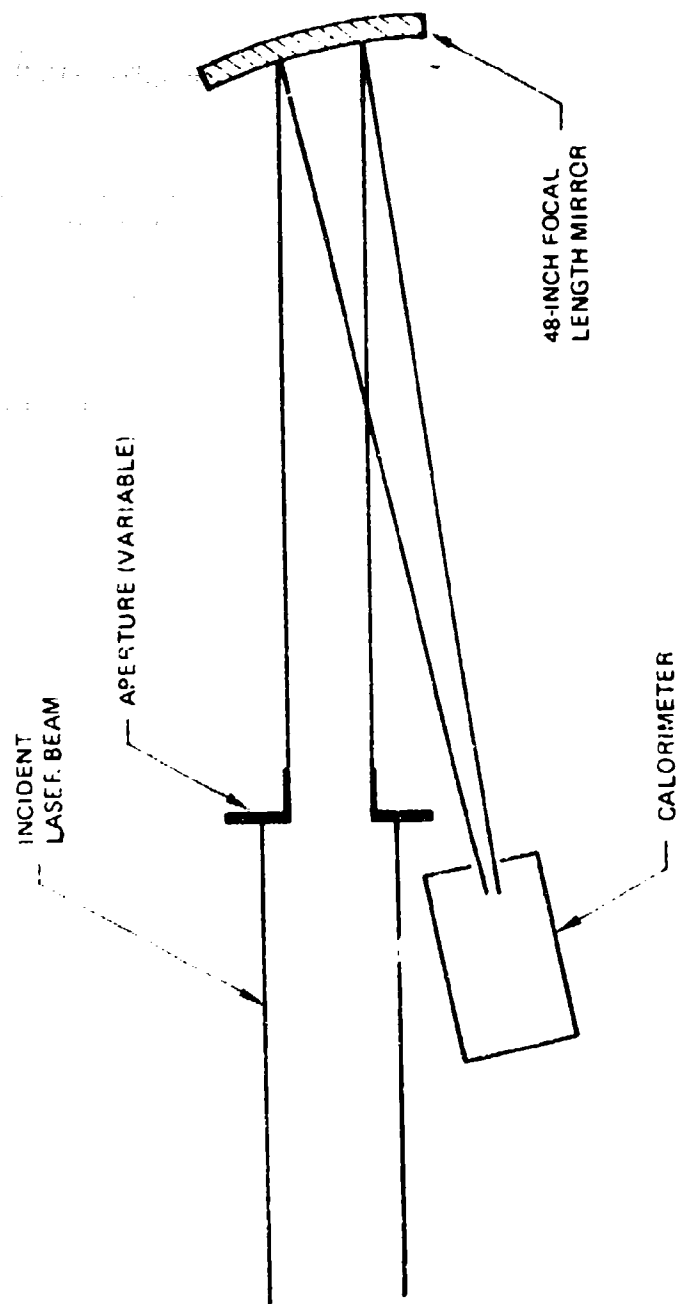
CALORIMETER

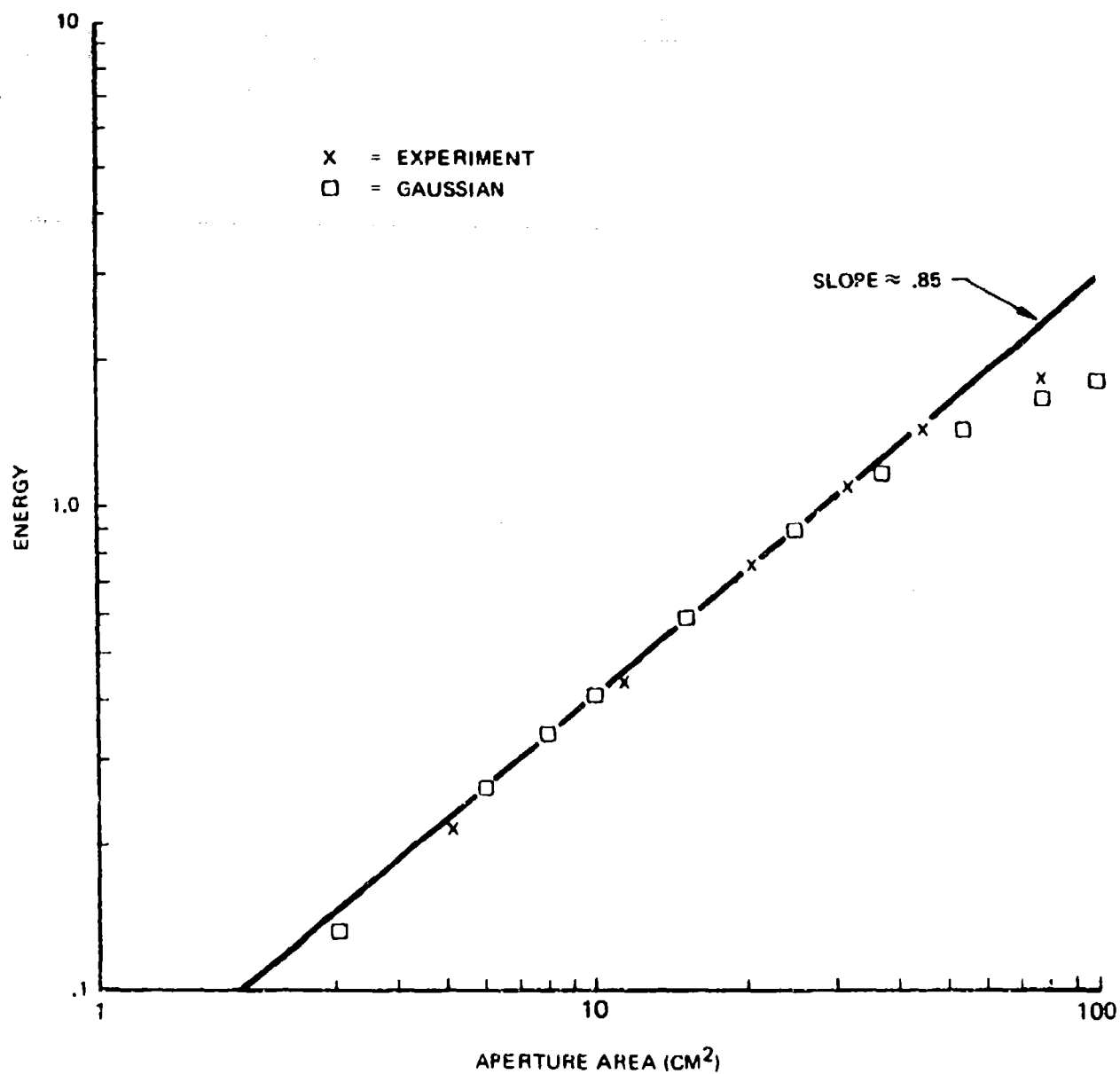Figure 124. SCHEMATIC DIAGRAM OF ENERGY DENSITY MEASUREMENT

Figure 125: INCIDENT LASER ENERGY AS A FUNCTION OF AREA

226

and experiment and theory are fitted at an aperture area of 10 cm^2, one obtains the data also indicated in figure 124 and the value δ = 3.7 cm, which is close to the actual "burn" radius of carbon paper placed in the laser beam path. These measurements indicate that the beam is relatively well behaved on the "average".

3.0 ENERGY DENSITY PROFILE OF FOCUSED BEAM

The energy density measurements of the focused laser were performed in several ways. The methods described here indicate a reasonable agreement with each other.

The first method employed is shown in figure 126a. A TRG thermopile was masked with a .06-inch aperture and moved horizontally across the diameter of the focal plane of a 78-inch focal length mirror. Measurements were obtained every .036 inch, yielding the results shown in figure 127. The points where the energy had dropped to 1/2 the maximum value indicated a beam diameter of 1.31 cm. Using this beam diameter and the focal length of the mirror, we found a beam divergence of 3.2 milliradians.

The second set of measurements were made in the focal plane of a 10-meter focal length mirror in the experimental setup shown in figure 126b. These measurements were made by masking the focal plane with circular apertures and then focusing the transmitted laser beam into a TRG thermopile with a 16-inch focal length mirror. The energy delivered through the various apertures is plotted as a function of the diameter of the aperture. The results are compared to the energy content of a Gaussian laser beam profile in figure 128. The best fit for the Gaussian gives a beam diameter of 4.42 cm corresponding to a beam divergence of 3.2 milliradians.

The third set of measurements of laser energy were obtained by sweeping a small aperture across the focal plane of the 10-meter focal length mirror as shown in figure 126c. The aperture was a
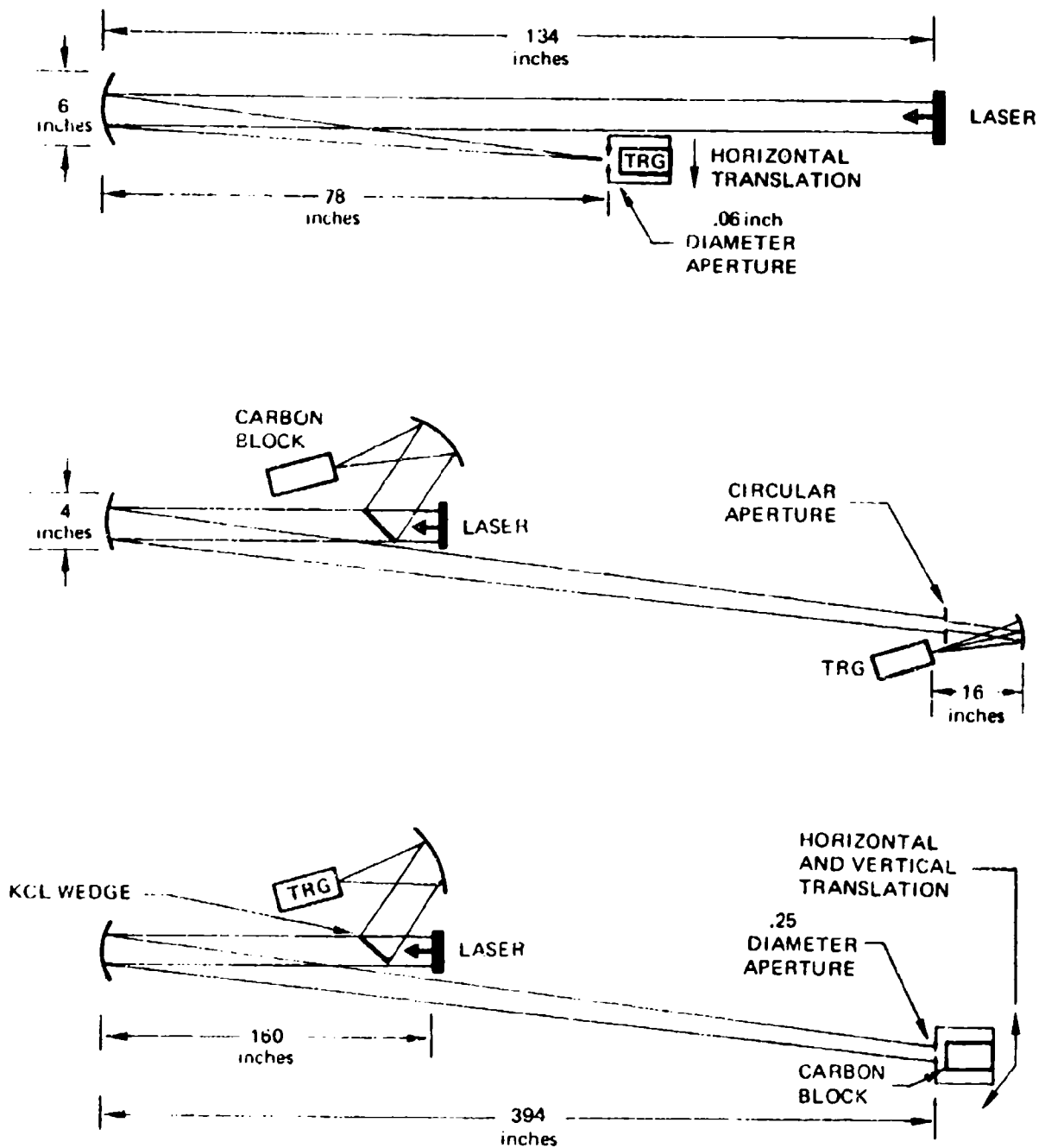
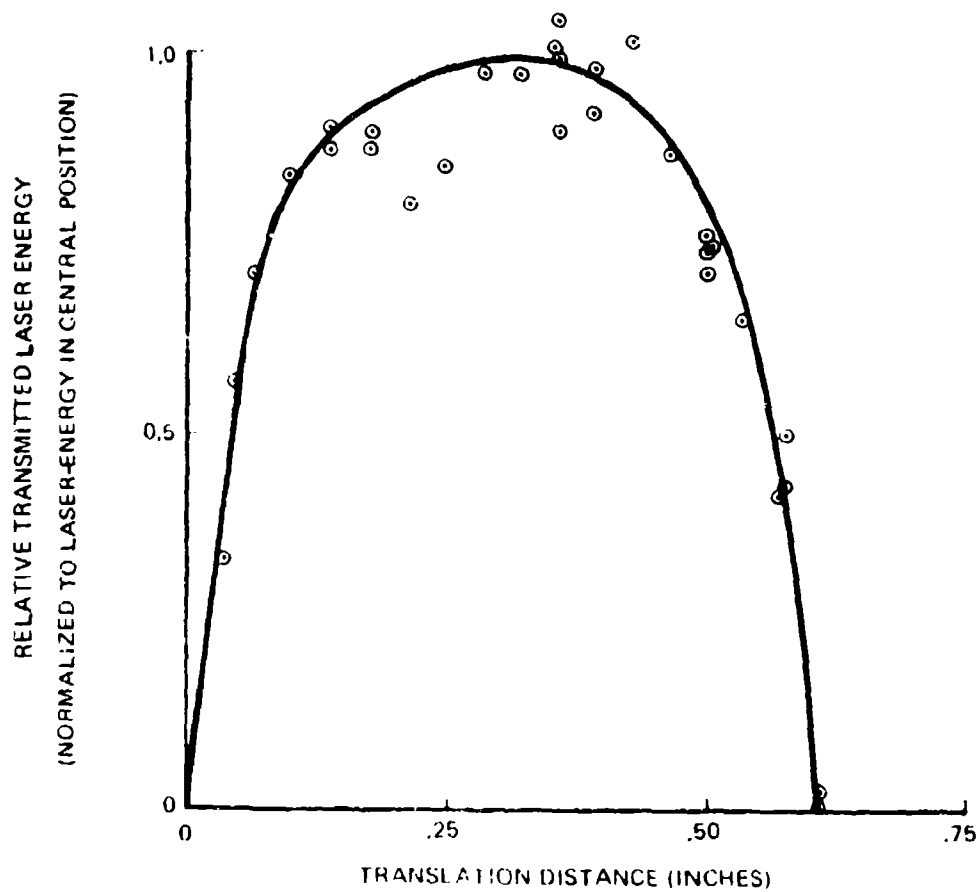Figure 126. EXPERIMENTAL SETUP FOR MEASURING LASER ENERGY DISTRIBUTION

Figure 127: LASER ENERGY MONITORED THROUGH A 0.06" CIRCULAR APERTURE MOVED HORIZONTALLY THROUGH THE FOCAL PLANE OF A 78" FOCAL LENGTH MIRROR
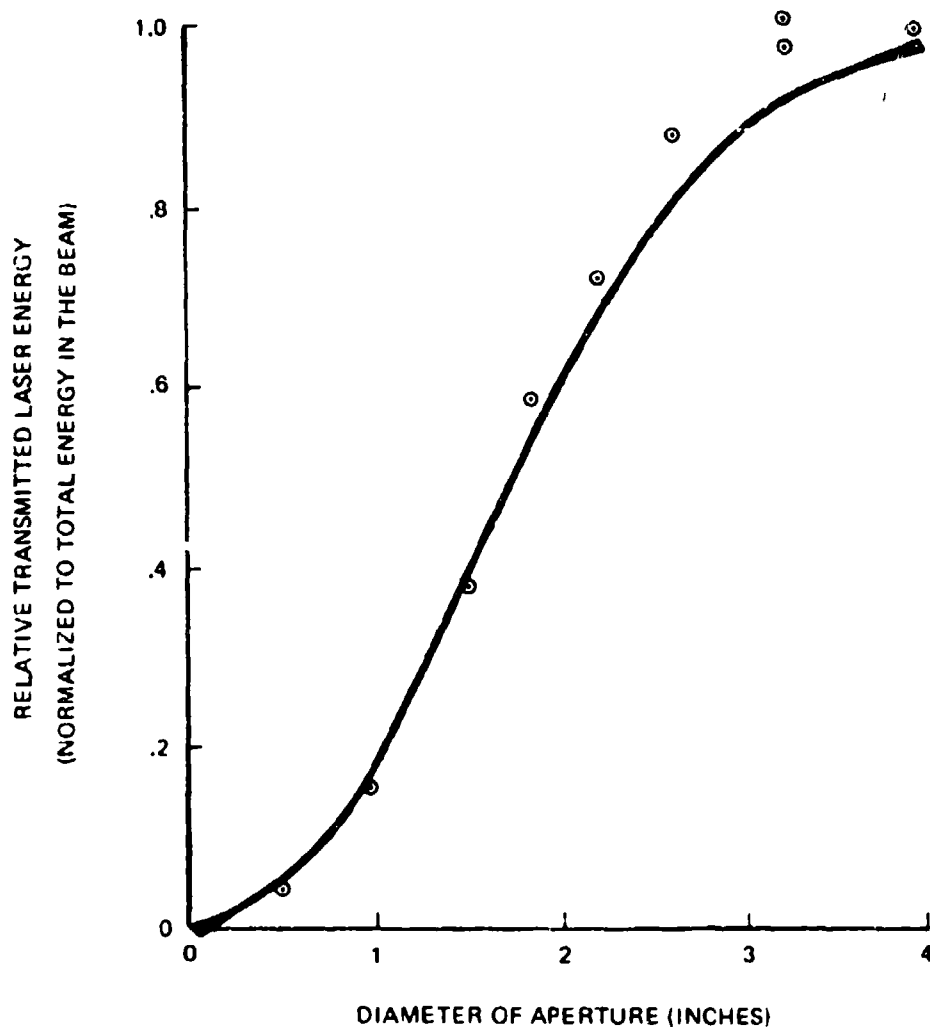
Figure 128: LASER ENERGY MONITORED THROUGH A VARIABLE CIRCULAR APERTURE
AT THE FOCAL PLANE OF 10-METER FOCAL LENGTH MIRROR

1/4-inch circular hole drilled through an aluminum plate which was
attached to a carbon block thermopile. The thermopile was mounted
on a X-Y translation stage so that the aperture could be moved
across the focal plane. A TRG thermopile was used to monitor the
total energy in the laser beam as reflected by a salt wedge with
a 5.6-percent reflection coefficient. A series of 100 measurements
were made with 1/4-inch intervals throughout an area of 2-1/4 x
2-1/4 inches square. It was found during this series of measurements
that the average energy in the laser beam was 17.5 joules with
53 percent of the shots having laser energies between 17 and 18
joules. A three-dimensional plot of these measurements is shown
in figure 129. The beam diameter as measured at the points where
the energy density has dropped to 1/2 is approximately 5.5 cm
corresponding to a beam divergence of 4.0 milliradians.

The three values for beam divergence agree reasonably well.
The two-dimensional scan probably gives the most realistic value
as it does not depend critically on how well the beam is centered
to the energy monitor. The laser beam appears to decrease more
rapidly than a pure Gaussian profile which also makes the third
measurement more reliable.

The focal diameter of the laser beam with this beam divergence
as determined by a 16-inch focal length mirror is estimated to
be 3 mm which is close to burn impressions obtained in lucite.

4.0 INTENSITY PROFILE OF THE FOCAL REGION

The five element detector array (in these tests only four
detectors were working because of the failure of detector No. 5)
was used to determine the temporal and spatial behavior of the
beam. The first sequence of tests, however, utilized a single
detector which was positioned at various stations with respect
to the stationary focal spot. The total laser energy was monitored
for each of these shots and data normalized to account for any

ENERGY MONITORED THROUGH
A 1/4" CIRCULAR HOLE WITH
A CARBON BLOCK THERMOPILE.
TOTAL BEAM ENERGY MONITORED
WITH A TRG THERMOPILE FOR
PROVIDING CORRECTION TO
AVERAGE ENERGY

Laser Energy

0.75

¼"

¼"
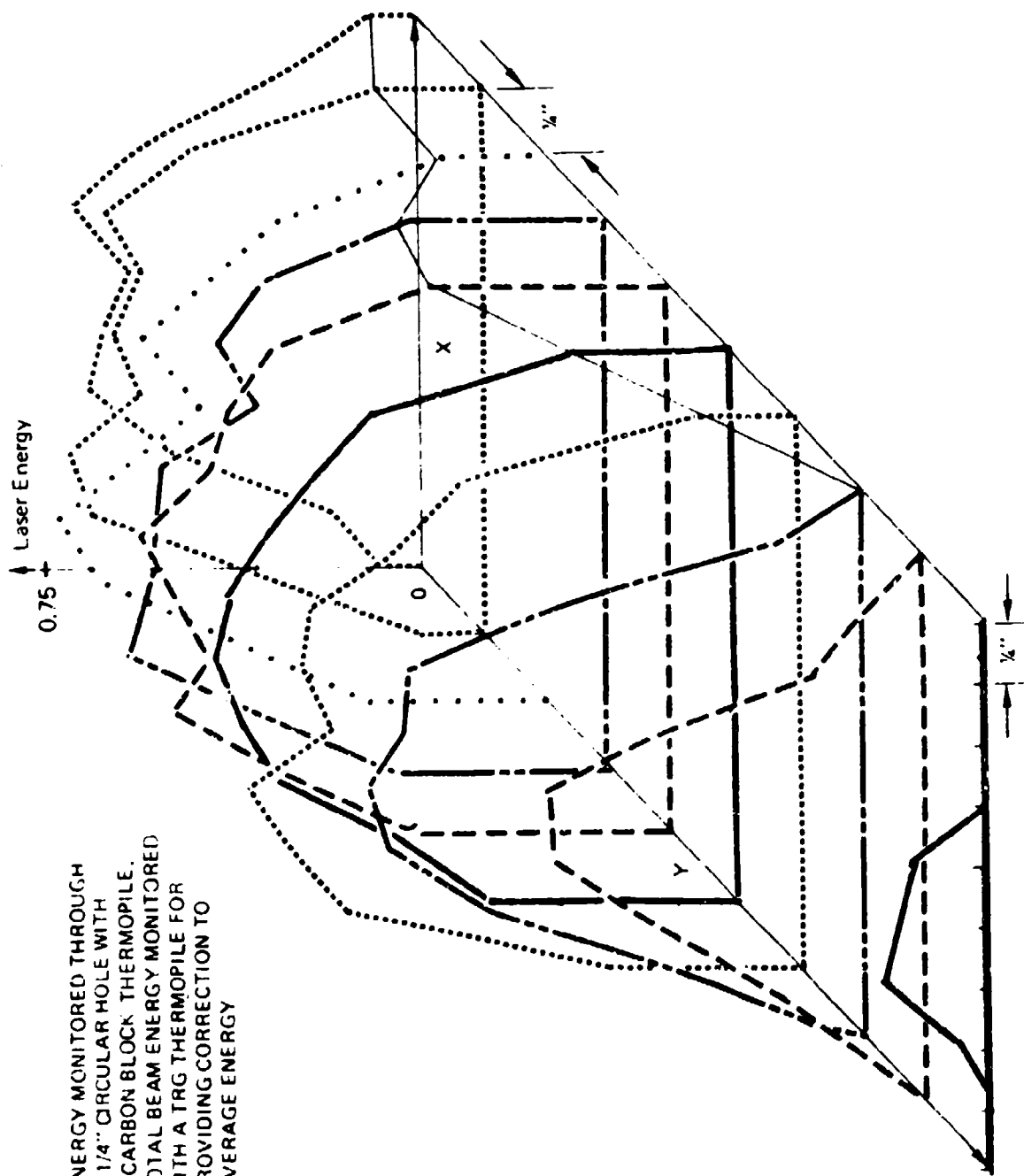
Figure 129: *LASER ENERGY DENSITY PROFILE*

variation. (Over a sequence of approximately 20 laser shots, the energy had a maximum variation of ~10%.)

Figure 130 shows the intensity variation in the focus of the 10-meter focal length mirror. For this data, the laser energy was very nearly 12.5 joules and one can determine the actual intensity at the target. A relative intensity of unity is found to correspond to

$$4.4 \times 10^4 \text{ watts/cm}^2$$

Since this focus was 7 meters from the mirror, one calculates, for a 16-inch focal length mirror, a peak intensity of

$$2.5 \times 10^7 \text{ watts/cm}^2$$

for times less than 4μsec. Figure 130 indicates that off-axis laser modes, in this laser, are the first to decay in time. The "focal" area decreases later in the pulse.

Simultaneous power intensity data taken with the detector array are shown in figure 131. This data shows nearly uniform behavior of the beam as a function of time, indicating that no local hot spots occur.

Figure 132 shows data taken by moving the entire array 1 inch to the right. That is detector No. 4 was now in the same place as detector No. 2 was in the data of figure 131. Comparison of these data shows consistency and in addition clearly shows fast decay of the beam energy at its boundaries as mentioned above. It should be noted that the total beam power (labeled beam monitor) had a somewhat smoother time history than did the intensity at a given radial position.

Figure 130: *INTENSITY PROFILE AS A FUNCTION OF RADIUS*
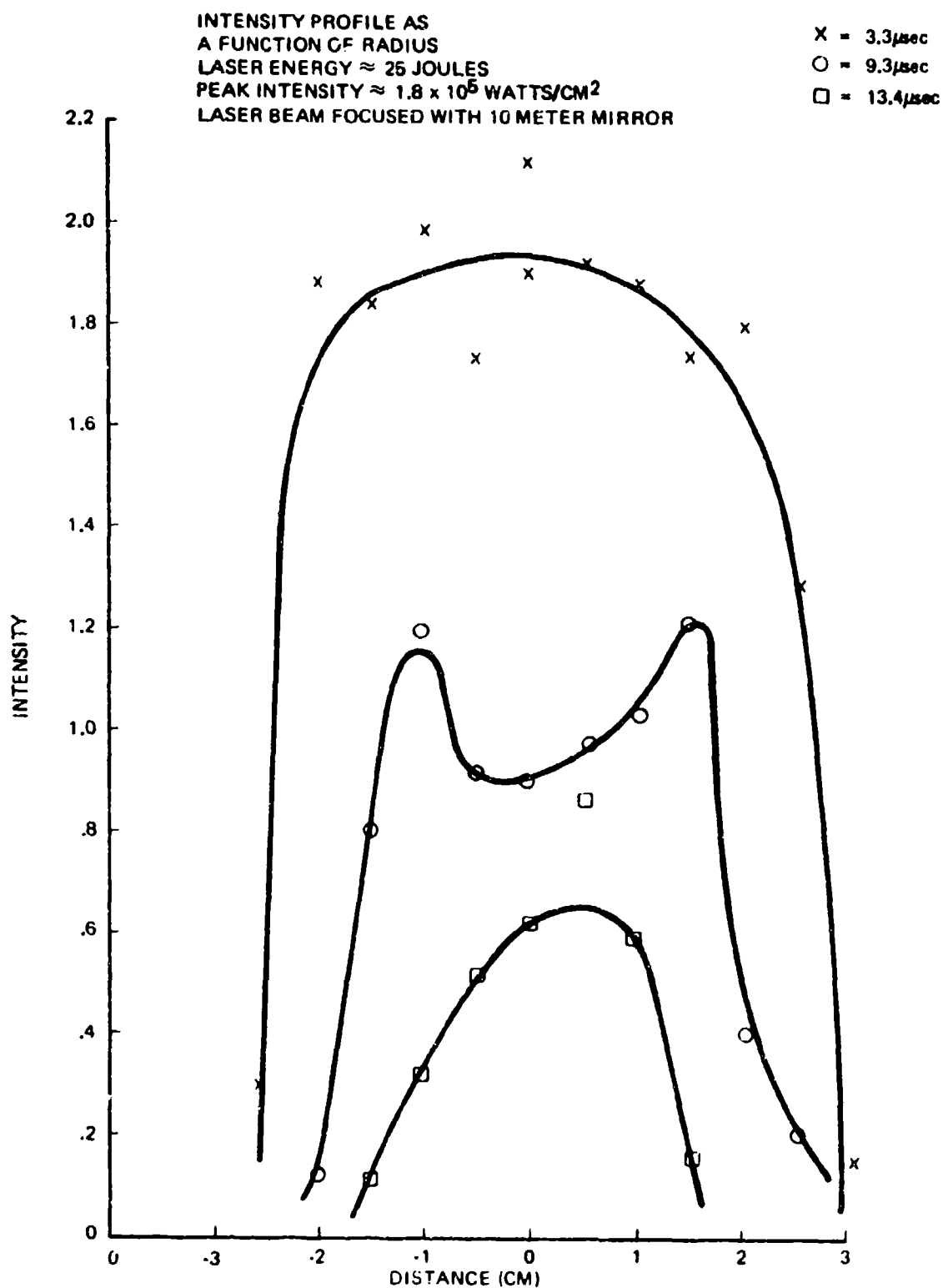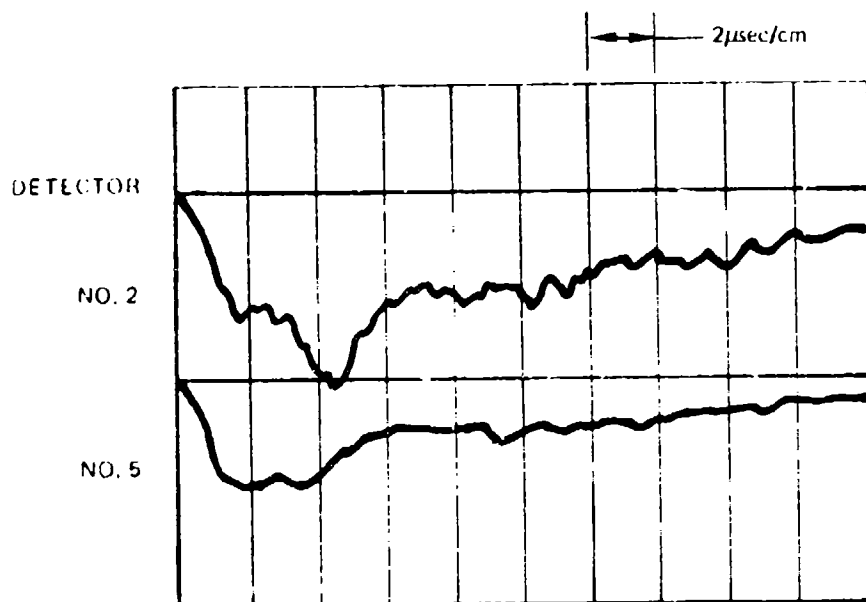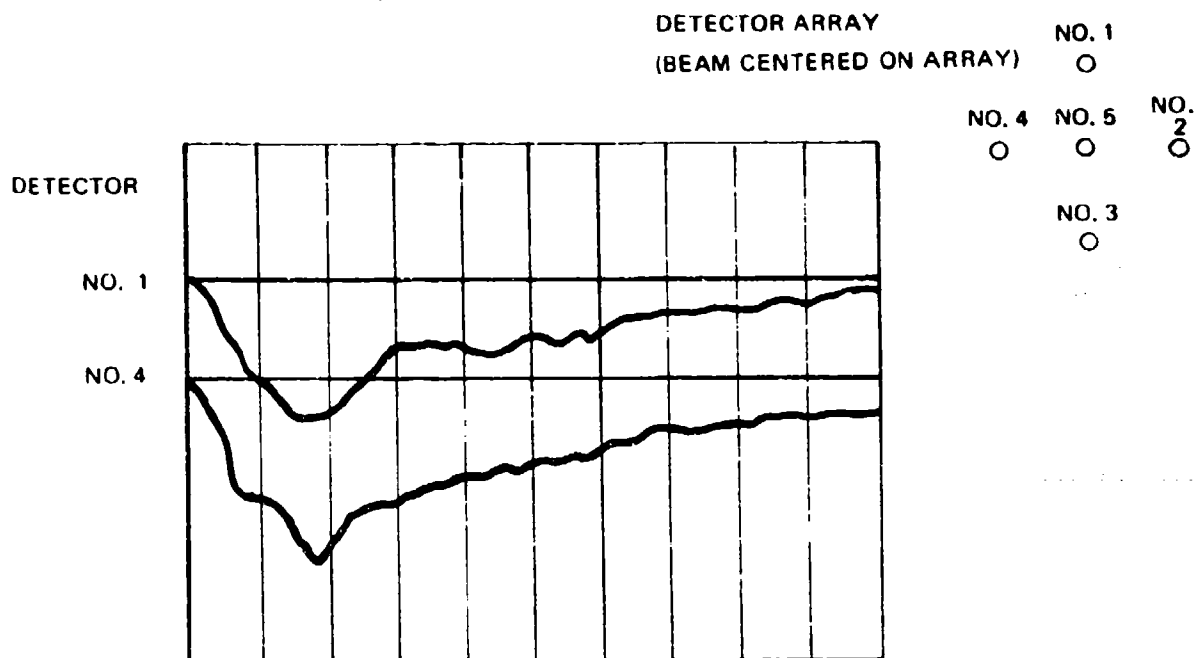
234

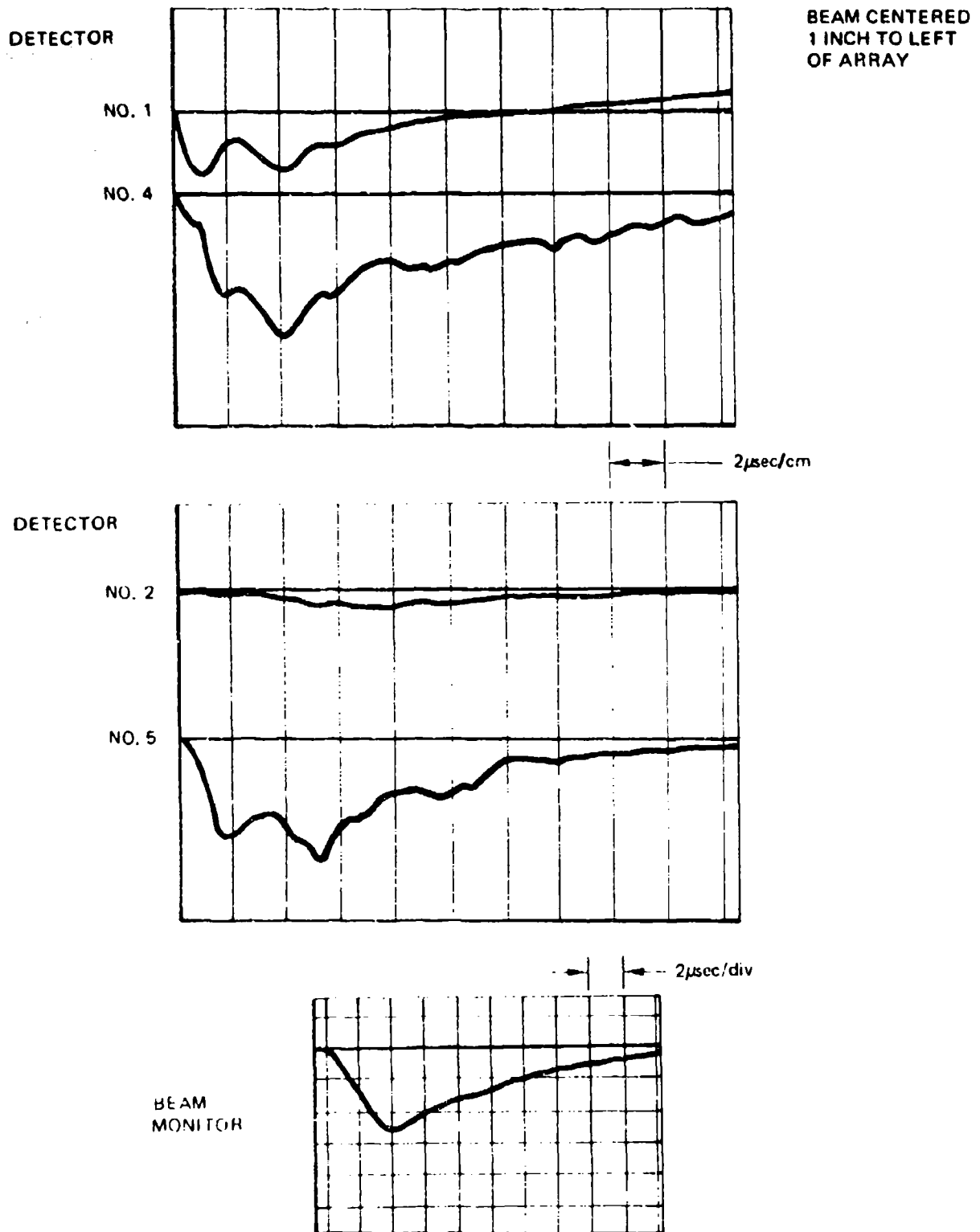Figure 131: SIMULTANEOUS SIGNALS FROM DETECTOR ARRAY

Figure 132. SIMULTANEOUS SIGNALS FROM DETECTOR ARRAY

Data has also been taken of the intensity profile of the unfocused beam by sweeping a single detector across the beam. Data taken at a single instant of time are shown in figure 133. There appears, by comparison of figures 130 and 133, to be a somewhat different intensity profile in the focused and unfocused beam.

The focused beam profile was also determined from laser burn impressions in Lucite targets shown in figure 134.

The fast detector, monitoring the entire laser pulse, is capable of "seeing" 10 nsec pulses, however, we observed no fast variation of either beam intensity or beam power with time.

5.0 MARX BANK LASER WAVELENGTH

The previous beam diagnostic data were all taken with unfiltered gold-doped germanium detectors. This technique led to some ambiguity in knowing the actual total power versus time history of the laser pulse because of the dependence of detector sensitivity on wavelength. In order to resolve this question, we placed a 10.6-micron filter in front of the detector. The filter used had a pass band only .24 micron wide centered at 10.75-micron wavelength. In addition, for wavelengths less than 9.7 micron less than 1 percent transmission occurred. The power versus time oscilloscopic data obtained were essentially identical to those obtained in the absence of filtering. A filter centered at 9.6-micron wavelength on the other hand, in front of the detector element caused no power to be indicated.

As a third diagnostic, we used a copper doped germanium high-speed detector to monitor laser power since it is less frequency (wavelength) dependent than gold-doped detectors. Again, we obtain power versus time data in agreement with our previous work. These results give us confidence that the energy and power measure-
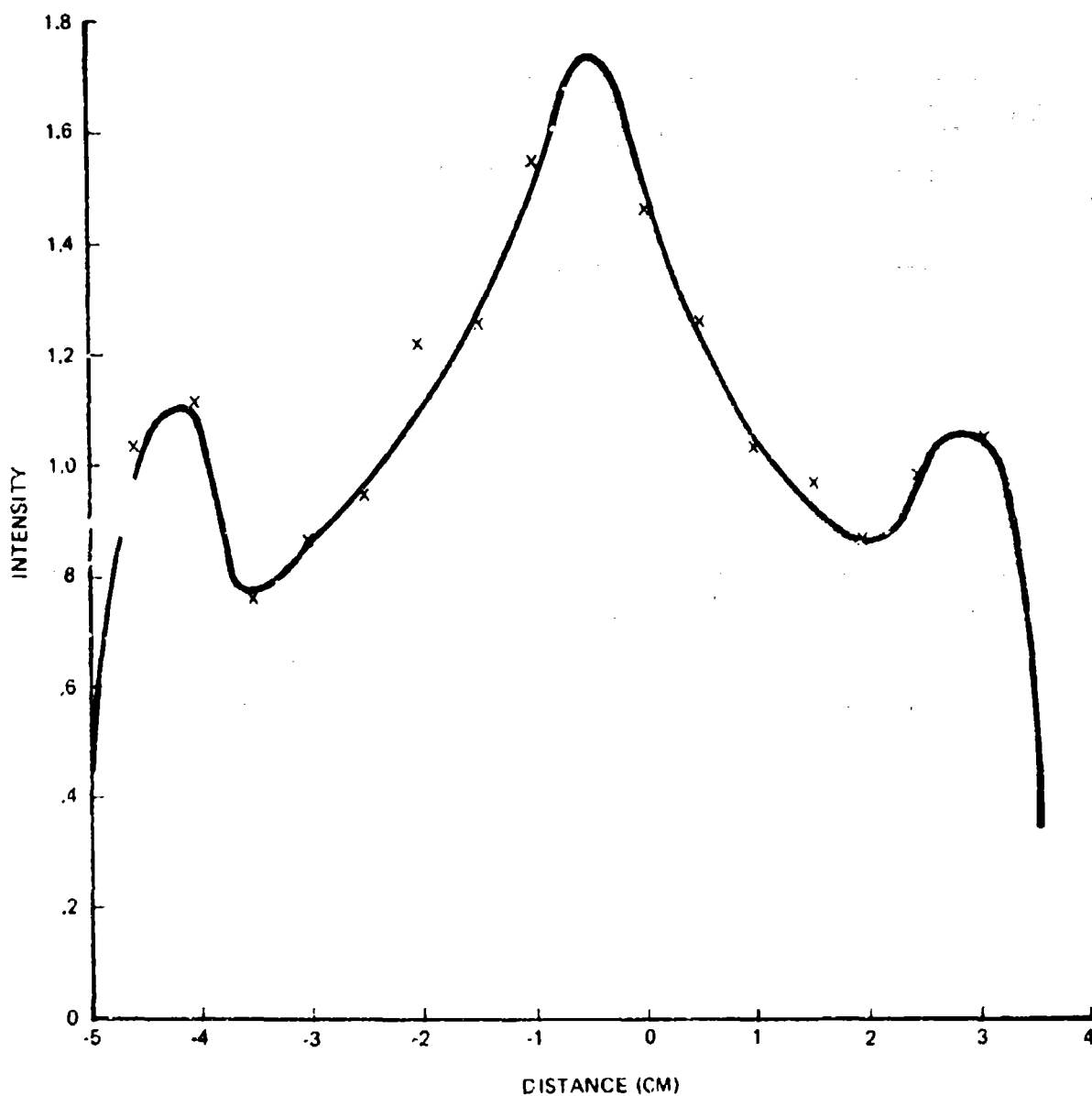
Figure 133: *INTENSITY PROFILE AT 3.3μsec (UNFOCUSED BEAM)*

5 SHOTS
70 JOULES (TOTAL)

|— 2.5 mm —|

10 SHOTS
140 JOULES (TOTAL)

Figure 134: LASER-DRILLED HOLES IN LUCITE, POWER DENSITY (MAX) $\approx 3 \times 10^7$ *WATTS/CM^2*

239

ments are both easily interpretable as 10.6 micron laser radiation.

6.0 RISE-TIME OF LASER PULSE

At a Marx Bank charging voltage of 42 kilovolts, the initial laser spike is approximately 1.4 times the maximum intensity of the slower laser transient. In addition, the laser pulse has a rise-time of about .5 microsecond followed by a 25-microsecond decay as indicated approximately in figure 135.

It is found, in general, that as the Marx Bank charging voltage is increased, the intensity of the initial laser spike rises. All of the experiments discussed in this report were at a fixed voltage (leading to a constant laser pulse shape) of 42 kV.

7.0 ATTENUATORS

In order to accurately determine the intensity thresholds for igniting detonation waves, we maintained constant as many parameters of the laser beam and target geometry as possible. This required the use of variable attenuators that reduced only the amplitude of the laser pulse and did not change its shape. Both absorption and reflection techniques were investigated. A SF_6 absorption cell made of 4-inch diameter pyrex and with Handi-Wrap windows was constructed and tested. Although the technique worked, we found some difficulty in making a practical variable attenuator which could be varied easily over a wide range. All experiments used a reflection attenuation scheme using both multiple sheets of Handi-Warp, each sheet reflecting about 10 percent of the beam energy, and multiple sheets of Tedlar, each sheet reducing the energy by 50 percent. In this way, we have good control on beam power. The attenuator is placed between the beam diagnostic KCl wedge and the laser output aperture. For each shot then, "exact" calibration and positioning of the attenuators is not necessary.
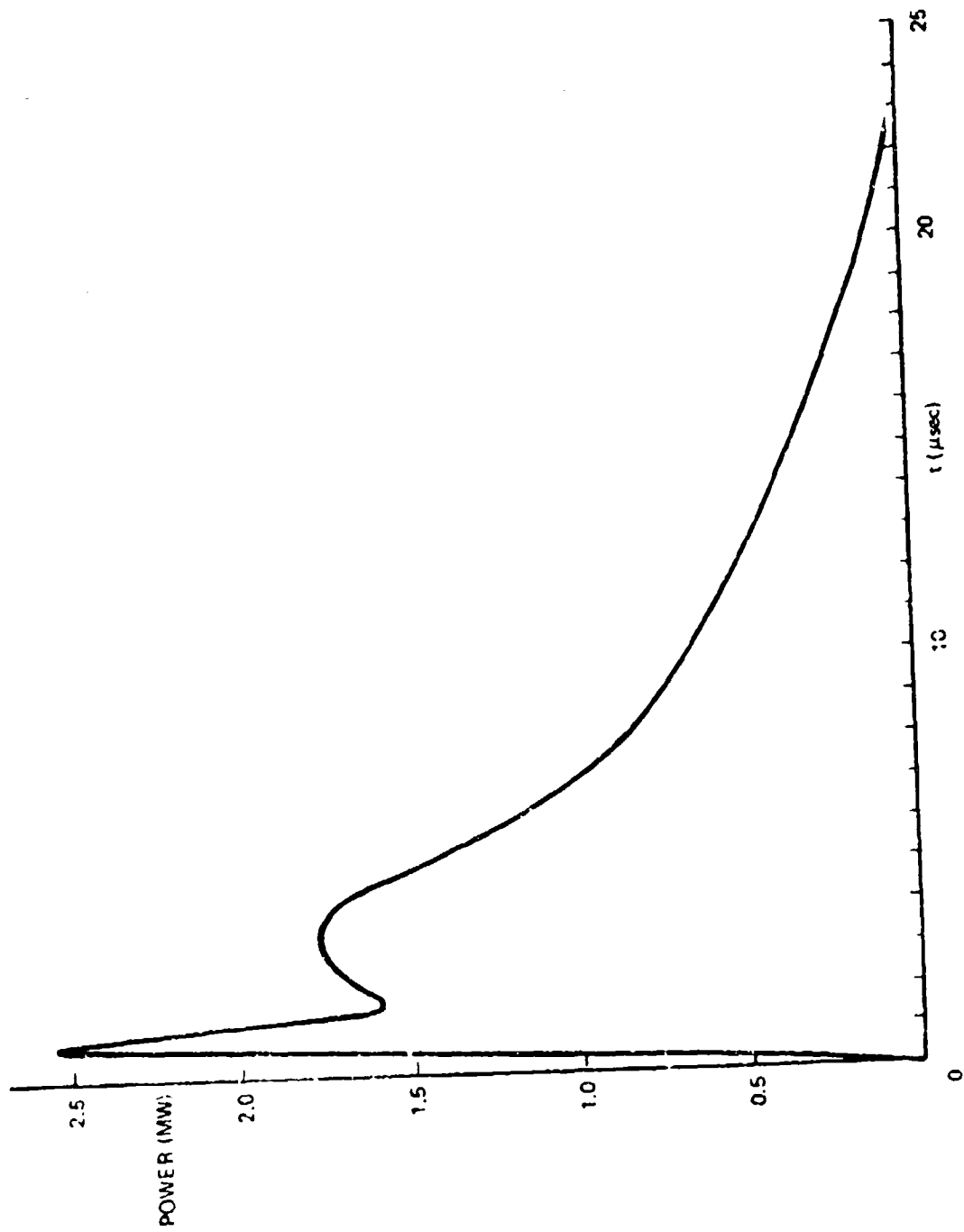
Figure 135: *TYPICAL MARX BANK LASER PULSE. 17.4 J.*

An examination of the far-field pattern of the focused beam
with various numbers of sheets of Handi-Wrap beam attenuators
showed no serious degrading of the beam quality. These measurement
were similar to those reported in Appendix, Section 3, using a
detector array.

REFERENCES

1. Smith, D.C., "Gas-Breakdown Dependence on Beam Size and Pulse Duration with 10.6 μ Wavelength Radiation," _Applied Physics Letters 19_, 405 (1971)

2. Ramsden, S.A. and Savic, P., "A Radiative Detonation Model for the Development of a Laser-Induced Spark in Air," _Nature 203_, 1217 (1964).

3. Bunkin, F.B., Konov, V.I., Prokhorov, A.M., and Fedorov, V.B., _JETP Letters 9_, 609 (1969).

4. Raizer, Y.P., "Heating of a Gas by a Powerful Light Pulse," _Soviet Physics JETP 21_, 1009 (1965).

5. Raizer, Y.P., "Breakdown and Heating of Gases Under the Influence of a Laser Beam," _Soviet Physics Uspekhi 8_, 650 (1966).

6. Raizer, Y.P., "The Feasibility of an Optical Plasmatron and its Power Requirements," _Soviet Physics-JETP_, 195 (1970).

7. Pirri, A.N., Schlier, R., and Northam, D., "Momentum Transfer and Plasma Formation Above a Surface with a High-Power CO_2 Laser," _Applied Physics Letters 21_, 79 (1972).

8. Rudder, R.R., Howland, J.A. and Augustoni, A.L., private communication.

9. Nielsen, P.E., private communication.

10. Daiber, J.W. and Thompson, H.M., _Physics Fluids 10_, 1162 (1967).

11. Raizer, Y.P. _Soviet Physics JETP 31_, 1148 (1970).

12. Harvey, A.J., _Coherent Light_, John Wiley & Sons, New York, New York, 1151 (1970)

13. Gravel, M., Robertson, W.J., Alcock, A.J., Buchl, K., and Richardson, M.C., _Applied Physics Letters 18_, 75 (1971)

14. Alcock, A.J., DeMichelis, C. and Richardson, M.C., _IEEE Journal of Quantum Electronics QE-6_, 622, (1970).

15. Raizer, Y.P., _JETP Letters 7_,55 (1968).

16. Zel'dovich, Y.B. and Raizer, Y.P, _Physics of Shock Waves and High Temperature Hydrodynamic Phenomena_," Academic Press, New York, New York, 188 (1966).

17. Hora, H., Wilhelm, H., "Optical Constants of Fully Ionized Hydrogen Plasma For Laser Radiation,"_Nuclear Fusion 10_ (1970).

18. Cambel, A.B., *Plasma Physics and Magnetofluid-Mechanics*, McGraw-Hill Book Co., Inc., New York, New York, 65 (1963).

19. Born, M., and Wolf, E., *Principles of Optics*, MacMillan Co., New York, New York, 440 (1964).

20. Afanas'ev, Y.V. Bosov, N.G., Krokhin, O.N. Mirochevskii, N.V., and Sklizkov, G.V., *Soviet Physics Technical Physics 14*, 669 (1969).

21. Jarr, W., Keher, G., and Wohr, H., *Marx-Planck-Institute Fur Plasmaphysik Report IPP 1/117* (1971).

22. David, C., Avizonis, P.V., Weichel, H., Bruce, C., and Pyatt, K.D., *IEEE Journal of Quantum Electronics OE-2*, 493 (1966)

23. Jahoda, F.C., in *Modern Optical Methods in Gas Dynamic Research*, Dosanjh ed., Plenum Press, New York, New York, 137 (1971).

24. Richardson, M.C., and Alcock, A.J., *Applied Physics Letter 18*, 357 (1971).

25. Zaidel', A.N., Ostrovskaya, G.V., Ostrovskii, Y.I., and Chelidze, T.A., *Soviet Physics Technical Physics 11*, 1650, (1967).

26. Liepman, H.W., and Roshko, A., *Elements of Gasdynamics*, John Wiley & Sons, New York, New York, 418 (1957).

27. Basov, N.G., Bojko, V.A., Gribkov, V.A., Zakharov, S.M., Krokhin, O.N., and Sklizkov, G.V., *Soviet Physics JETP 34*, 81 (1972).

28. Herzberg, G., *Molecular Spectra and Molecular Structure I. Spectra of Diatomic Molecules*, D. Van Nostrasd Co., Inc., New York, New York, 504 (1950)

29. Bockasten, Kjell, *Journal-Optical Society of America 51*, 943 (1961)

30. Striganov, A.R. and Sventitskii, N.S., "Table of Spectral Lines of Neutral and Ionized Atoms", (IFI/Plenum, New York, 1968).

31. Wiese, W.L., Smith, M.W. and Gelnnon, B.M., "Atomic Transition Probabilities, Vol. 1, Hydrogen Through Neon," (NSRDS, NBS-4, 1966).

32. Pearse, R.W.B., and Grydon, A.G., "The Identification of Molecular Spectra", John Wiley, New York, 3rd edition, (1963).

33. Wei, P.S.P., and Hall, R.B., Journal of Applied Physics 44, (May 1973).

34. JANAF Thermochemical Tables, prepared under the auspices of the Joint Army-Navy-Air Force Thermochemical Panel at the Thermal Research Laboratory, The Dow Chemical Co., Midland, Michigan (issued March 31, 1965).

35. Mayer, J.E., and Mayer, M.G., "Statistical Mechanics", John Wiley & Sons, Inc. New York (1940)

36. White, W.B., Johnson, S.M., and Dantzig, G.B., Journal-Chemical Physics 28, 751 (1958).

37. Zeleznik, F.J. and Gordon, S., Industrial Engineering Chemistry 60, No. 6, 27 (1968).

38. Neumann, Kl. G., Ber Lunsenges. Phys. Chem 66, 551 (1962)

39. Peng, T.C. and Pindroh, A.L., in Magnetohydrodynamics, Proceedings of the 4th Biennial Gas Dynamics Symposium," edited by A.B. Cambel, T.P. Anderson and M.M. Slawsky (Northwestern University Press, Evanston, Illinois, 1962) p. 67.

40. Griem, H.R., "Plasma Spectroscopy", McGraw-Hill, New York, 275 (1964).

41. Zel'dovich, Y.B. and Raizer, Y.P., "Physics of Shock Waves and High-Temperature Hydrodynamic Phenomena", Academic Press, New York, Vol 1, 116 (1966).

42. Chang, D.B., Drummond, J.E., and Hall, R.B., Journal of Applied Physics 41, 4851 (1970).

43. Minck, R.W., Journal of Applied Physics 35, 252 (1964).

44. Mandel'shtam, S.L., Pashinin, P.P., Prokhindeev. A.V., Prokhorov, A.M., and Sukhodrev, N.K., Soviet Physics JETP 22, 1344 (1965).

45. Dalber, J.M. and Winter, T.G., Journal-Optical Society of America 58, 76 (1968).

46. Litvak, M.M. and Edwards, D.F., Journal of Applied Physics 37, 4462 (1966).

47. Evtushenko, T.P., Zaidel', A.N. Ostrouskaya, G.V., and Chelidze, T.V, Soviet Physics-Tech Physics 11, 1126 (1967).

48. Smith, D.C., Journal of Applied Physics 41, 4501 (1970).

49. Maker, P.D., Terhune, R.W. and Savage, C.M., "Ouantum Electronis III", edited by P. Grivet and N. Bloembergen, Columbia University Press, New York, 1559 (1964)

50. DeMichelis, C., "Laser Interaction with Solids-A Bibliographical Review", IEEE Journal of Quantum Electronics QE-6, No. 10, (October 1970)

51. Ready, J.F., Effects of High-Power Laser Radiation, Academic Press, New York, 103 (1971).

52. Chun, M.K., Rose, K., "Interaction of High-Intensity Laser ` ams with Metals", Journal of Applied Physics 41, No. 2, (1970).

53. .ach-Bruevich, A.M., Imas, Y.A., Romanov, G.S., Libenson, M.N. and Mal'tsev, L.N., "Effect of Laser Pulse on the Reflecting Power of a Metal", Soviet Physics-Technical Physics 13, 640 (1969).

54. Basov, N.G., Boiko, V.A., Krokhin, O.N., Semenov, O.G., Sklizkov, G.V., "Reduction of Reflection Coefficient for Intense Laser Radiation on Solid Surfaces," Soviet Physics-Technical Physics 13, No. 1, 1581 (1969).

55. Ujihara, K., "Reflectivity of Metals at High Temperatures", Journal of Applied Physics 43, 2376 (1972).

56. Nevskii, A. ., "Electron Temperature on the Surface of Metals under the Effect of Powerful Heat Fluxes", Teplofizika Vysokikh Temperature, Vol 8, No. 6, 898 (July 1970).

57. Vilenskaya, G.G., Nemchinov, I.V., "Sudden Increase in Absorption of Laser Radiation and Associated Gasdynamic Effects", Soviet Physics-Doklady, Vol. 14, No. 6. 560 (1969)

58. Nemchinov, I.V., Popov, S.P., "Time of Start of Screening of a Surface Evaporating Under the Influence of Laser Radiation", PHETF Pis. Red. 11, No. 9, 459-462, (1970).

59. Handbook of Chemistry and Physics, The Chemical Rubber Co., Cleveland, Ohio, 145 (1968).

60. Pond, R., private communication, The Boeing Aerospace Company.

61. Condon, E.U. and Odishaw, H., Handbook of Physics, McGraw-Hill Book Co., 3-106 (1967).

62. Raizer, Y.P., "High-Frequency High-Pressure Induction Discharge and the Electrodeless Plasmatron," _Soviet Physics-Uspekhi 12,_ (1970)

63. Jacavanco, D.J., "An Experimental Study of the Interaction of Moderate Power Microwaves with Electron Density Gradients", Physical Sciences Research Papers, No. 492, Air Force Cambridge Research Laboratories (1972).

64. Raizer, Y.P., "Propagation of a High-Pressure Microwave Discharge", _Soviet Physics JETP 34,_ 114 (1972).

65. Raizer, Y.P., "Subsonic Propagation of a Light Spark and Threshold Conditions for the Maintenance of Plasma by Radiation", _Soviet Physics JETP 31,_ 1148 (1970).

66. Zakharov, S.D., Tyurin, E.L., and Shcheglov, V.A., "On Monochromatic Radiation Transfer in a Plasma", _Soviet Physics JETP 34_ (1972).

67. Steinhauer, L.C. and Ahlstrom, H.G., "Laser Heating of a Stationary Plasma", Department of Aeronautics and Astronautics-University of Washington, Report 70-4 (1970).

68. Nielsen, P.E., Jackson, J.P., and Canavan, G.H., private communication.

69. Jackson, J.P., Canavan, G.H. and Nielsen, P.E., private communication.

70. Generalov, N.A., Zimakov, V.P., Kozlov, G.I., Masyakov, V.A. and Raizer, Y.P., "Experimental Investigation of a Continuous Optical Discharge", _Soviet Physics JETP 34,_ 763 (1972).

71. Franzen, D.L., "CW Gas Breakdown in Argon Using 10.6μ Laser Radiation," _Applied Physics Letter 21,_ 62 (1972).

72. Conrad, R., private communication, Army Missile Command, Huntsville, Alabama

73. Stegman, R.L., Schriempf, J.T., Hettche, L.R., and Rice, R.W., private communication.

74. Hatch, D.J., "Generalized Program for High Temperature Gas Transport Properties," The Boeing Company, Doc. AS 2112 (1965)

75. Sziklas, E., private communication, Pratt and Whitney Aircraft Corporation.

76. John, R.R., "Theoretical and Experimental Investigation of Arc Plasma Generation Technology", ASD-TDR-62-729, Vol. 1 of Part II.

77. Klosterman, E.L., Bryon, S.R., and Newton, J.F., private communication, Mathematical Sciences Northwest.